THE MICROSTRUCTURAL DEVELOPMENT OF OXIDE SCALES ON LOW CARBON STEELS

By

SORAN BIROSCA

Doctoral Thesis

Submitted in Partial Fulfilment of the Requirements for the Award of Doctor of Philosophy

2006

INSTITUTE OF POLYMER TECHNOLOGY AND MATERIALS ENGINEERING, LOUGHBOROUGH UNIVERSITY

![Loughborough University]

Thesis Access Form

Copy No…………...…………………**Location**……………………………………….……………...…

Author…………Soran Birosca………………………...………………………………………..………

Title…… The Microstructural Development of Oxide Scales on Low Carbon Steels………………………………...

Status of access OPEN / RESTRICTED / CONFIDENTIAL

Moratorium Period:………………………………years,ending…………../…………200………………………

Conditions of access approved by (CAPITALS):……………………………………………………………

Director of Research (Signature)…………………………………………...…………………………………...

Department of……………………………………………………………..…………………………………

Author's Declaration: *I agree the following conditions:*

OPEN access work shall be made available (in the University and externally) and reproduced as necessary at the discretion of the University Librarian or Head of Department. It may also be copied by the British Library in microfilm or other form for supply to requesting libraries or individuals, subject to an indication of intended use for non-publishing purposes in the following form, placed on the copy and on any covering document or label. *The statement itself shall apply to **ALL** copies:*

This copy has been supplied on the understanding that it is copyright material and that no quotation from the thesis may be published without proper acknowledgement.

Restricted/confidential work: All access and any photocopying shall be strictly subject to written permission from the University Head of Department and any external sponsor, if any.

Author's signature………………………………………….Date…………31/03/2006……….…………...……...

users declaration: for signature during any Moratorium period (Not Open work): *I undertake to uphold the above conditions:*			
Date	Name (CAPITALS)	Signature	Address

CERTIFICATE OF ORIGINALITY

This is to certify that I am responsible for the work submitted in this thesis, that the original work is my own except as specified in acknowledgments or in footnotes, and that neither the thesis nor the original work contained therein has been submitted to this or any other institution for a higher degree.

………………………………………… (Signed)

…………………….. ……..……………… (Date)

ACKNOWLEDGEMENT

I would like to express my sincere thanks to the following

Dr. Rebecca Higginson, the project supervisor,

Professor Rachel Thomson, the research director,

EPSRC for financial support,

Universal Steel for supplying steels,

All the academic and technical staffs in IPTME, especially Mr. J. Bates,

All my friends and colleagues in IPTME,

Finally, all my love and heartfelt gratitude to my family in Kurdistan, without their invaluable support, generosity, cheerfulness and imperative encouragement, the completion of this project would not be possible.

Soran Birosca

Abstract

The microstructures of the oxide scale on steels are very complex and their development depends on many factors including time, temperature, oxidation conditions and alloying elements. Classically, steel oxide scales are characterised by a three-layer model: The innermost layer, closest to the steel substrate, with the lowest oxygen content is wüstite (FeO); there is an intermediate magnetite (Fe_3O_4) layer and a final oxygen rich hematite (Fe_2O_3) layer. This classical model is more complicated in reality and its properties change with the factors that affect their development. Microstructure characterisation of the oxide scale helps to obtain a better understanding of the oxidation mechanism. Furthermore, knowledge of the oxide microstructure is critical in understanding how the oxide behaves during the high temperature deformation of steels and more importantly how it can be removed following processing.

An understanding of the oxide scale formation and its properties can only be achieved by careful examination of the scale microstructure. The oxide scale microstructure may be difficult to characterise by conventional techniques such as optical or standard scanning electron microscopy. An unambiguous characterisation of the scale and the correct identification of the phases within the scale are difficult unless the crystallographic structure for each phase in the scale is considered and a microstructure-microtexture analysis is carried out. In the current study Electron Backscatter Diffraction (EBSD) has been used to investigate the microstructure and microtexture of iron oxide layers grown on low carbon steels at different times and temperatures. EBSD has proved to be a powerful technique for identifying the individual phases in the oxide scale accurately. The results show that EBSD can be used to give a complete characterisation of the oxide scale. The microstructural features such as grain size, shape and grain or phase boundaries characteristics has been successfully determined and analysed. The results show that different grain shapes and sizes develop for each phase in the scale depending on time and temperature. Also, a complex relationship between the microstructures and the crystallographic texture of the different scales components has been observed. In the light of new approach of understanding the steel oxidation phenomena from the current study, previous steel oxidation hypothesis and postulations have been reviewed and examined.

CONTENT

INTRODUCTION

Steels are undoubtedly the most successful engineering material. The abundance of iron in the Earth's crust and its ease of extraction makes iron alloys-steels cheaper than other metal. It has a high melting temperature (1534°C) and is available in wide range of mechanical properties, through its ability to respond to heat treatment [Honeycombe, 1981]. However, the tendency for steel to oxidise at high temperatures is relatively high compared to other engineering materials. Yet, it is widely used and in highly demanding engineering applications which creates a challenge for researchers and manufacturers to improve steel surface finish quality.

Steels may be subjected to high temperature oxidation during both manufacturing operation and in service. In service, the oxide scale on steel might be useful to some extent as it can prevent further oxidation which causes damage to the structure and can possibly leads to catastrophic failure. During steel manufacturing, oxide formation on the steel surface is, however, entirely undesirable. Considerable industrial resources have been aimed at an understanding of the oxide scale and how to remove it to improve the surface quality of the finished product.

The method used in the descaling process is an important consideration for the steel manufacturers. Increased environmental awareness means that the use and disposal of either sulphuric or hydrochloric acid, to remove the scale by pickling, has caused a move towards mechanical descaling which has also has the advantage of lower cost [Tominaga, *et al*., 1982]. The descaling process is dependent on the scale properties such as scale thickness, scale composition and the surface quality of the substrate. Mechanical descaling may not, however, remove scales that can be readily removed by pickling [Raman, *et al*., 1998]. Therefore, an understanding of the oxide scale formation, its properties and its behaviour during hot processing can only be achieved by careful examination of the scale microstructures which will lead to the development of a suitable way for removing them from the steel substrate.

Oxide scale microstructures on steels are very complex and their development depends on many factors such as time, temperature, oxidation environment and alloying elements. Generally, iron and steel scales are characterised by a three-layer model: the innermost layer, closest to the steel substrate, with the lowest oxygen content, is wüstite (FeO); there is an intermediate magnetite (Fe_3O_4) layer and a final thin oxygen rich hematite (Fe_2O_3) layer [Taniguchi, *et al*., 2001]. This simple model of oxide scale layers is much more complex in reality, and its properties would change with the factors that affect their development. Furthermore, hot working operations break up this three classical layer scale structure and make characterisation of the individual component of the scale difficult [Nagl, *et al*., 1993].

The properties of the oxide scale such as scale thickness, porosity, adherency to the substrate and mechanical properties vary with factors that affect oxide growth [Tominaga, *et al*., 1982]. It is related to the fact that oxidation at different temperatures leads to the formation of the scales with different thickness and even the ratio between the scale components may change. The presence of alloying elements further complicates the oxidation of steels and the nature of these scales is highly dependent on the scale composition, e.g. each alloying element has a different affect on the development of the oxide scale and therefore leads to change in oxide properties and its microstructure [Sachs, *et al*., 1967]. Moreover, environmental conditions and all other factors that have an affect on the oxide growth should be considered in greater detail in order to develop the mechanism for the complete characterisation of the oxide scales.

The characterisation of oxide scale needs a reliable technique to reveal complete microstructural features. Numerous attempts have been made to obtain direct information about scale microstructure. For thick scales, electron probe microanalysis coupled with x-ray diffraction have been used to identify the phases present, for thin scales, x-ray photoelectron spectroscopy or Auger spectroscopy were utilised [Loretto, 1994]. Laser Raman spectroscopy has been used successfully to identify oxide layers within the scale when coupled with optical microscopy [Raman, *et al*., 1998]. However, none of these techniques gives any direct information on the microstructure within the scale layers themselves. Nowadays, the use of Electron Backscatter Diffraction (EBSD) technique has

allowed a more complete description of the oxide scale to be acquired. EBSD allows diffraction patterns to be acquired and indexed on the surface of a bulk sample [Dingley and Randle, 1992]. The relative ease of sample preparation, its accuracy and fast reliable results puts EBSD at the forefront as an analytical tool. EBSD is extensively used in the present work for grain size measurement, phase identification, phase ratio calculations, grain and phase boundary characterisation, cracks and microstructure consideration, microtexture and misorientation of the oxide scale layers and their correlations. Moreover, throughout this study it has been demonstrated that EBSD can reveal microstructural features within the steel oxide scale more clearly and can eliminate the ambiguity of conventional techniques such as optical or scanning electron microscopy.

The aim of the current study is to increase the understanding of oxide scale microstructural development and how it is affected by the alloying of the steel and the processing conditions. This will lead to a deeper understanding of oxide scales on steels, allowing improved scales to be developed using alloy and process design which will give them the desired properties during processing and descaling. This aim can be achieved by developing a mechanism for the complete characterisation of the oxide scale on steel. Also through determining the effects of steel composition, time, temperature, oxidation conditions, and microtexture of the steel substrate on the oxidation rate, microstructures and microtexture of the scale. From this, the correlations between microstructure, microtexture and the mechanical properties of the scale can be determined and the best microstructure for easy descaling can be defined.

Previous studies regarding oxide scale development on steel surfaces are reported in Chapter 1. The steel applications, grade, phase transformation and heat treatment are described in Part 1. Previous work on the oxidation of steels is documented in Part 2. In Part 3, the EBSD technique is described, which is extensively used in this study for the oxide scale microstructural characterisation and microtexture analysis. The experimental procedures and results from this work are reported in Chapters 2 and 3 respectively. The results from this study are compared with those of previous studies and discussed in Chapter 4 with main conclusions and recommendation for further work are presented in Chapters 5 and 6.

CHAPTER 1   Literature Review

Part 1   Steels and its Microstructure and Properties

1.1.1   Introduction

In this part of the literature review, general steel properties and microstructure are described. While the main objective of this study is to investigate the oxide scales' microstructural development on steel substrates, it is necessary to study the nature of the steel before investigating the oxidation process.

The study of steel is important because of its high availability, good formability and its mechanical properties. It is therefore, not surprising that irons and steels comprise well over 80% by weight of the metal in general industrial use [Honeycombe, 1981]. The general effects of adding various amounts of carbon and other elements to iron have supported the mass market of steels. Steels contain carbon in amounts ranging from very small (about 0.005 wt% in ultra low carbon steel), to a maximum of 2 wt% in the highest carbon tool steel. Iron containing over 2 wt% carbon is classified as cast iron [Sinha, 1989]. Carbon profoundly alters the microstructure and hence properties of iron. Generally, the carbon content is kept low in steels that are required to have high ductility, high toughness and good weldability, but is maintained at high levels when high strength, high hardness, fatigue resistance and wear resistance are required. Furthermore, the performance of a steel component can also be highly dependent upon its thermal treatment as well as other alloying additions [Hill, 1973].

1.1.2 The Iron-Carbon Equilibrium Diagram

In general, phase diagrams are valuable in the understanding of the heat treatment, phase compositions, control of properties and solid-state reactions [William, *et al*., 2001]. The development of the microstructure of an alloy is related to the characteristics of its phase diagram. In addition, phase diagrams provide valuable information about melting, casting, recrystallisation, and other phenomena.

A phase is a portion of a system whose properties, composition, and crystal structure are uniform or homogenous and which is separated from the remainder by distinct bounding

surfaces [Smallman, *et al*., 1995]. In a phase diagram, temperature is plotted vertically and composition horizontally at constant pressure. Figure 1.1.1 shows the iron-carbon equilibrium diagram. The phases present in Figure 1.1.1 are molten alloy (liquid), α-ferrite, γ-ferrite, and cementite, these phases are alternatively called constituents, however, not all constituents like pearlite and bainite are phases, rather a mixture of two phases; ferrite and cementite.
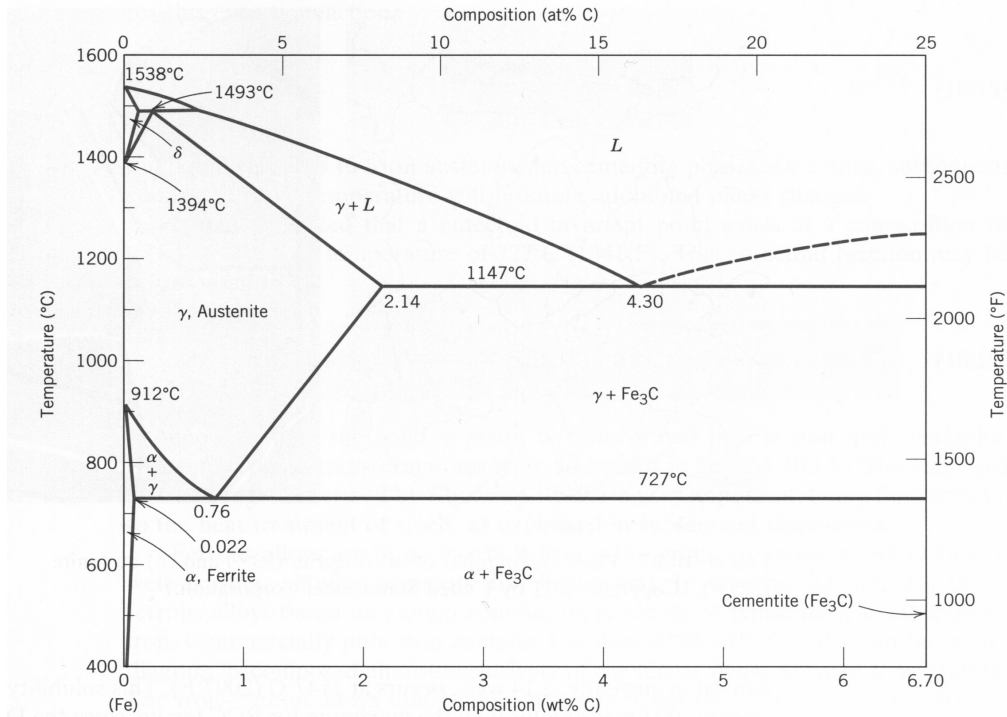
Figure 1.1.1 The iron-carbon diagram (reproduced from ASM International, 1990)

A study of the constituents and structure of all steels must first start with the iron-carbon equilibrium diagram. The much larger phase field of austenite in the diagram compared to ferrite reflects the much greater solubility of carbon in γ-iron, with a maximum value of just 2 wt% at 1147°C. The ferrite field is severely restricted, with a maximum carbon solubility of 0.02 wt%. Ferrite is normally associated with iron carbide in one form or another. Similarly, the δ-iron field is restricted between 1394 and 1538°C and disappears completely when the carbon content reaches 0.5 wt% [Honeycombe, 1981].

There are several temperatures or critical points in Figure 1.1.1. Firstly, there is the 727°C at which the eutectoid reaction occurs [Higgins, 1994]. Secondly, there is 912°C which is when ferrite transforms to austenite in pure iron. However, at this temperature the transformation is progressively lowered by addition of carbon. The third is the temperature at which austenite transform to δ-iron, 1394°C, in pure irons, but this also rises as the

carbon is increased. Is should be pointed out that those transformations are sensitive to the rates of cooling and heating, as well as to the presence of alloying elements [William, *et al.*, 2001].

1.1.3   Structure of Steel

The component elements in steel can be categorised in terms of their crystal structure. A basic knowledge of the practical implications of these crystal arrangements is essential to understand the performance of steel in service. The structures are dependant upon the concentrations of each element, the fashion in which the steel is cooled from furnace temperature, and the amount of cold work preformed on the steel [Higgins, 1994].

1.1.3.1 Ferrite

Ferrite, α-Fe, is the crystal arrangement for pure iron. Pure iron, carbon steels, and other metals such as V, Cr, Mo, and W have body centred cubic (bcc) structure at room temperature. The bcc structure of ferrite has one atom at the centre of the cube and an atom at each corner of the unit cell and constitutes $1 + (8 \times 1/8) = 2$ atoms per unit cell [the 14 different type of crystal system of all solid states are shown the Appendix 1]. The lattice parameter of α-iron at room temperature is 2.86Å [Sinha, 1989]. Ferrite is a more open or less dense structure than other structural modifications of iron, called either gamma iron or austenite. The difference in atomic packing of α- and γ-iron is responsible for volume contraction that takes place on heating low-density ferrite to higher-density austenite [Humphreys, 1986]. Both ferrite and austenite are quite soft and ductile. Their average properties include: tensile strength; 276 mN m^{-2}; elongation, 40%; hardness, 150 Hv. Ferrite is ferromagnetic below 768 °C and paramagnetic in the temperature range 768-912°C [Chan, 1983].

1.1.3.2 Austenite

Austenite, γ-Fe, is a solid solution. All steels exist in this from at sufficiently high temperatures [Smallman, *et al.*, 1995]. Austenite as well as other metals such as Al, Cu, Ni, Ag, Pt and Au has the close-packed face-centred cubic (fcc) structure [see Appendix 1]. Its unit cell has an atom at each corner and an atom at the centre of each face of the unit cell.

Each corner atom is shared by eight unit cells that come together at the corner, while each face atom is shared by two adjacent unit cells, thus there are $(8 \times 1/8) + (6 \times \frac{1}{2}) = 1 + 3 = 4$ atoms per unit cell. The lattice parameter of austenite is 3.57Å, which is larger than that of ferrite [Sinha, 1989]. Gamma iron is the stable form of pure iron in the temperature range of 912-1394°C. Unlike ferrite, austenite is completely paramagnetic.

1.1.3.3 Delta Iron

The third phase that occurs in pure iron is δ-iron that has a bcc structure which is crystallographically similar to alpha iron. Delta iron is stable at temperatures between 1394°C and 1538°C. Its lattice parameter 2.89Å, it is also soft and ductile, and its hardness and elongation are similar to those of ferrite and austenite in their stable forms [Chan, 1983].

1.1.3.4 Cementite

Cementite, iron carbide (Fe_3C) is the hardest and most brittle phase of steel. When carbon atoms can no longer be accommodated in solution of ferrite and austenite (due to an increase in carbon content or reduction in temperature), cementite forms, as it can accommodate more carbon in its crystal structure. Its carbon content is ~ 6.67 weight percent. Its crystal structure is orthorhombic, that is, the sides are at 90 degree to each other, but not equal lengths [Appendix 1]. Cementite is the metastable Fe-C compound with a negligible solubility limit in α-iron. It is ferromagnetic with a Curie temperature of 215°C. It plays an important role in the hardening of many commercial steels [Pollack, 1988].

1.1.3.5 Pearlite

Pearlite is a phase mixture consisting of alternating platelets of ferrite and cementite (α + Fe_3C) which grows by conversion from austenite. Steel containing > 0.77 wt% carbon can consist solely of pearlite if cooled sufficiently slowly from austenite [Smallman, *et al.*, 1995].

1.1.3.6 Martensite

Martensite is commonly found in steel that has been rapidly cooled (quenched) from austenite. It is a particularly hard, brittle arrangement. Essentially it forms because any carbon in solid solution in austenite at high temperatures does not have enough time to be incorporated into cementite when cooled rapidly [Higgins, 1994]. Martensite does not appear on the phase diagram (Figure 1.1.1) as it is not an equilibrium phase.

1.1.3.7 Bainite

If steel is cooled such that the formation of pearlite by the short-range diffusion of iron atoms is not possible, bainite can be produced. The bainite that forms at temperatures just below those at which pearlite forms is termed upper bainite. At lower temperatures, lower bainite forms. Both lower and upper bainite consist of aggregates of platelets or laths of ferrite, separated by regions of residual phases consisting of untransformed austenite or of phases such as martensite or cementite [Higgins, 1994].

1.1.4 Classification of Steels

Steels can be classified by several different systems depending on; the compositions of carbon or alloying elements, the manufacturing methods, the finishing methods, the product shape and the use. However, the chemical composition is the most widely used for designation [Llewellyn, 1995]. Plain carbon steels are essentially iron-carbon alloys. These are subdivided by the range of carbon content into mild or low carbon steel (0.1 - 0.25 wt% carbon), medium-carbon steel (0.25 - 0.6 wt% carbon), high-carbon steel (0.6 - 0.8 wt% carbon) and carbon tool steels (0.8 - 1.1 wt% carbon). In addition, carbon steels contain less than ~ 1.65 wt% manganese, ~ 0.60 wt% silicon, ~ 0.60 wt% copper, and sulphur and phosphorus within specific limits. Small amounts of residuals such as nickel, chromium, and molybdenum are present in all carbon steels [ASM, 1972]. These alloying elements increase the mechanical and/or fabrication properties. Broadly, alloy steels can be divided into; (a) low-alloy steels containing 2 - 5 wt% and (b) alloy steels with more than 5 wt% total non-carbon additions [Smith, 1986].

CHAPTER 1

PART 2   High Temperature Oxidation of Steel

1.2.1 Introduction

A few metals, particularly those in common technological applications, are not stable when exposed to the atmosphere at both high and low temperatures. Consequently, most metals in service today are subject to deterioration, either by corrosion at room temperature or by oxidation at high temperature. Some metals, such as iron, will rust and oxidise very rapidly whereas other metals, such as nickel and chromium, are attacked relatively slowly. In this part the main theoretical and practical aspects of steel oxidation at high temperatures are reported.

1.2.2 Thermodynamic Consideration of Oxidation

For any kind of oxidation reaction, thermodynamic and kinetic approaches should be considered. From the thermodynamic approach, it can be determined whether the reaction would occur or not. However, how fast the reaction can progress depends on its kinetics, and then the mechanism of the oxide growth can be understood [Gaskell, 1995]. Since the conditions most often encountered in high temperature reaction are constant temperature, T, and pressure, the Gibbs free energy, G, can be determined from Equation 1.1;

$$\Delta G = \Delta H - T\Delta S \ldots\ldots\ldots\ldots\ldots\ldots\ldots\ldots\ldots\ldots\ldots\ldots\ldots\ldots\ldots\ldots\ldots\ldots\ldots (1.1)$$

Where H is the enthalpy and S the entropy of the system. It is obvious that at high temperature spontaneous reaction is expected because of $\Delta G < 0$ [Birks, *et al.*, 1983]. When this thermodynamic condition is met, the first process would start, which is the adsorption process. The adsorption process results in a decrease of the surface free energy. In becoming adsorbed on the surface, gas molecules or atoms normally lose some degree of freedom, and therefore the adsorption also results in a decrease in entropy (disorder). A simultaneous decrease in both the free energy and the entropy also implies a decrease of the enthalpy (Equation 1.1), and thus adsorption is normally an exothermic process [Kofstad, 1966].

Often determination of the conditions under which a given corrosion product is likely to form is required, e.g. in selective oxidation of alloys [Birks, *et al.*, 1983]. In this regard, Ellingham diagrams, i.e. plots of the standard free energy of formation versus temperature for the compounds of a type, e.g. oxides, sulphides, carbide, are useful in that they allow comparison of the relative stabilities of each compound. Figure 1.2.1 is such a plot for many simple oxides.
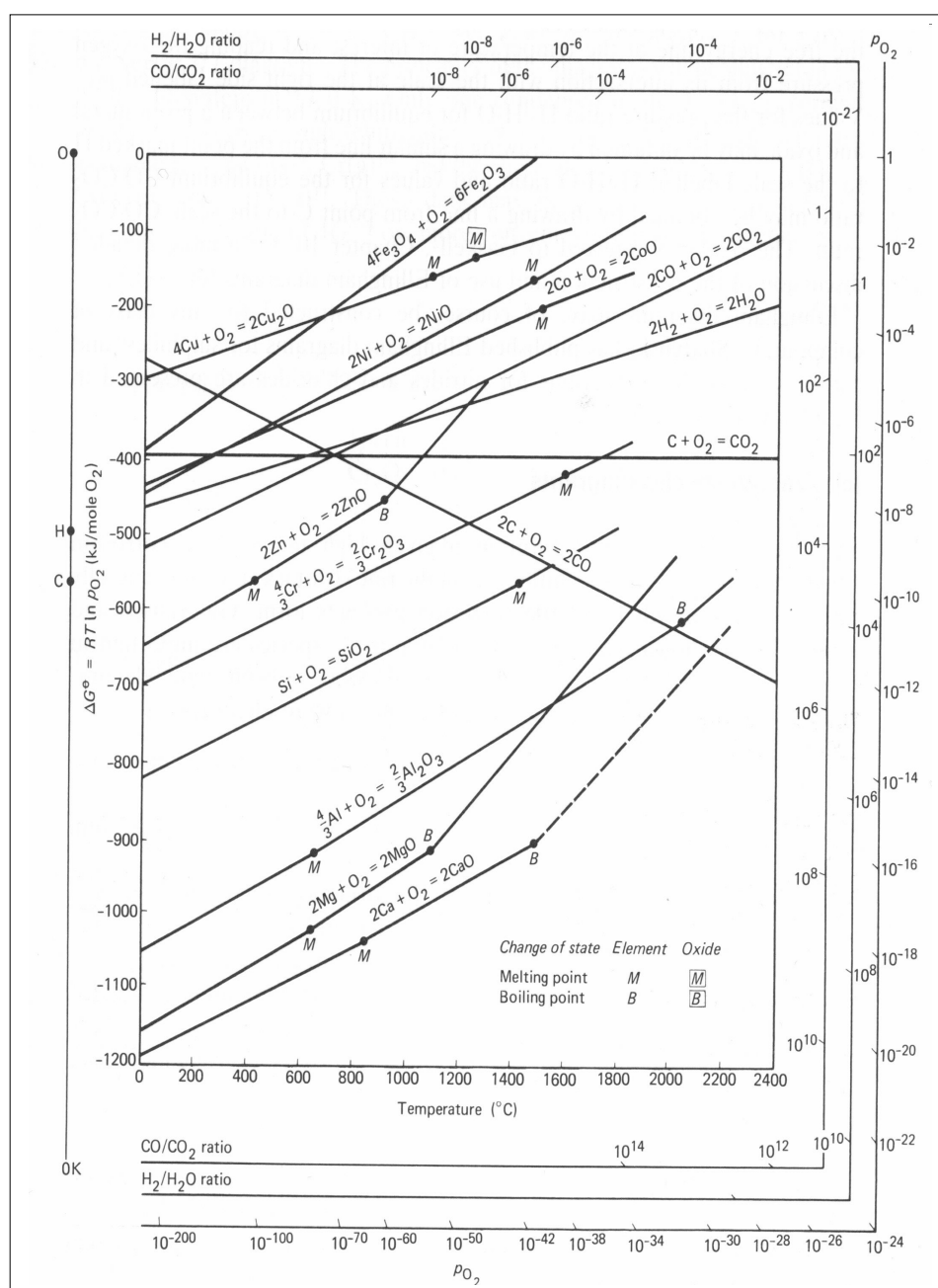

Figure 1.2.1 Standard free energy of formation of selected oxides as a function of temperature (Reproduced from Birks, et al., 1983)

The adsorption of gas on a solid surface leads to the accumulation of gas molecules on the surface. Gas molecules that impinge on a clean metal surface would be

adsorbed. The rate of impingement of gas molecules is proportional to the gas pressure [Kofstad, 1966]. The initial oxide occurs as a two dimensional structures at random positions forming isolated oxide nuclei on the metal surface. After the formation of the random oxide nuclei; the oxidation proceeds through the growth of the individual crystallites until the whole surface is covered with oxide. The rate of reaction during the initial stage increases with time.

The initial crystal growth will be in the shape of whiskers [Kubaschewski, *et al.*, 1967], then blades and platelets, which change depending on time and temperature and oxidation conditions. After the nucleation process is completed through reaction of the steel surface directly with atmosphere, the film formed acts as a barrier between the reactants. Further growth of the oxide film depends on transport, on the atomic level, of either oxygen or metal through the film.

1.2.3 Mechanism of Oxidation and its Kinetics

From consideration of the Equation 1.2;

M(s) + ½ O$_2$(g) = MO(s)……………………………………………………..(1.2)
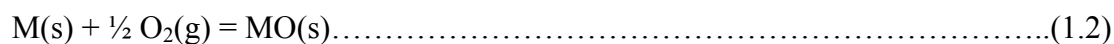
It is obvious that the solid reaction product *MO* will separate the two reactants as shown below;

$$
\begin{array}{c|c|c}
M & MO & O_2 \\
\text{Metal} & \text{Oxide} & \text{Gas}
\end{array}
$$
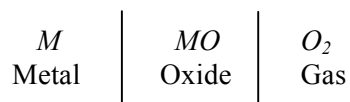
In order for the reaction to proceed further, one or both reactants must penetrate the scale, i.e. either metal must be transported through the oxide to the oxide-gas interface or oxygen must be transported to the oxide-metal interface. Immediately, therefore, the mechanisms by which the reactants may penetrate the oxide layers are seen to be important part of the mechanism by which high temperature oxidation occurs [Birks, *et al.*, 1983 and Hauffe, 1965].

1.2.3.1 Transport Mechanism

Since all metal oxides are ionic in nature it is not practicable to consider the transport of metal or non-metal atoms through the reaction product. Several mechanisms are

available to explain the transport of ions through ionic solids. This can be divided into mechanisms belonging to stoichiometric crystals and those belonging to non-stoichiometric crystals [Kofstad, 1966]. In fact, although many compounds belong firmly to one or the other group, the correct view is probably that all of the possible defects are present to some extent in all compounds, however, in most cases certain types of defects predominate as explained in the following sections.

1.2.3.1.a Stoichiometric Ionic Compounds

Predominant defects in these compounds, which represent one limiting condition, are *Schottky* and *Frenkel* defects [Birks, *et al.*, 1983]. There definitions are as below;

Schottky defects: - Ionic mobility is explained by the existence of ionic vacancies. In order to maintain electroneutrality, it is necessary to postulate an equivalent number, or concentration, of vacancies on both the cationic and anionic sub-lattices.

Frenkel defects: - The case where only the cation is mobile can be explained by assuming that the anion lattice is perfect but that the cation lattice contains cation vacancies and interstitials in equivalent concentrations to maintain electroneutrality for the whole crystal.

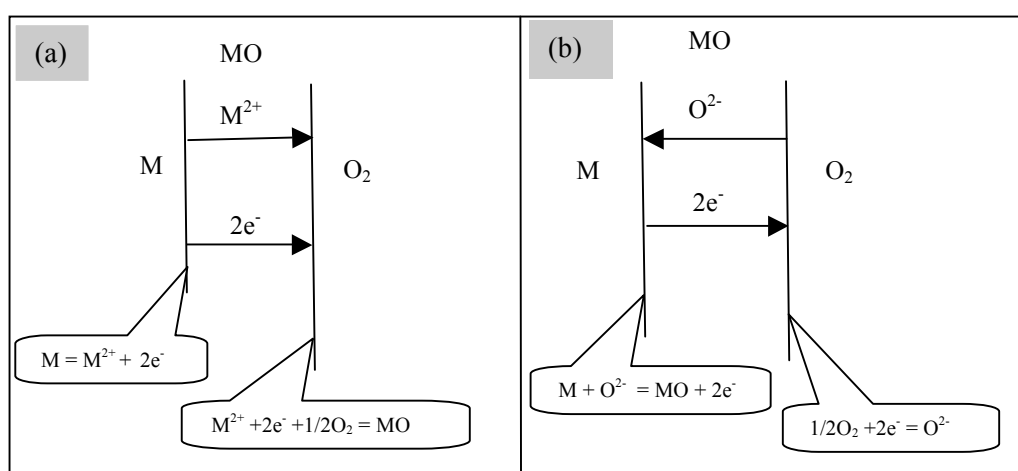*Figure 1.2.2 Interface reactions and transport processes for high temperature oxidation mechanism (a) cation mobile and (b) anion mobile.*

A diagrammatic representation of the oxidation process is shown in Figure 1.2.2. It is seen that either neutral atoms or ions and electrons must migrate in order for the reaction to proceed. In these cases the transport step of the reaction mechanism links

the two-phase boundary reactions as indicated. It is an important distinction between scale growth by cation migration and scale growth by anion migration, the cation migration leads to scale formation at the scale-gas interface whereas anion migration leads to scale formation at the metal-scale interface [Kubaschewski, *et al.*, 1967].

1.2.3.1.b Non-Stoichiometric Ionic Compounds

In order to explain simultaneous migration of ions and electrons it is necessary to assume that the oxides which are formed during oxidation are non-stoichiometric compounds [Birks, *et al.*, 1983]. Non-stoichiometry implies that the metal to non-metal atom ratio is not exactly that given by the chemical formula, even though the compound is electrically neutral. These can only be reconciled by assuming that either the anions or the cation exhibits variable valency on the sub-lattice. It is much more likely that the metal or cation shows variable valency. Non-stoichiometric ionic compounds are classified as semiconductors and may show negative or positive behaviour [Stott, 1987]:

1) N-type or negative semiconductors: The classification refers to the fact that electrical charge is transferred by negative carriers. This may arise, by having either an excess of metal or a deficit of non-metal.
2) P-type or positive semiconductors: In this case charge is transferred by positive carriers. This may arise from either a deficit of metal or an excess of non-metal.

1.2.4 Rate of Oxidation

a) Linear Rate Law

Under certain conditions the oxidation of a metal proceeds at a constant rate and is said to obey the linear rate law, i.e. $x = k_l t$, where x is the scale thickness and k_l is the linear rate constant. The units of k_l depend on the method used to follow the reaction, but the appropriate linear rate constant would have units of g cm^{-2} s^{-1}[Wood, 1970], see Figure 1.2.3 (a).

b) Transition from Linear Law to Parabolic Law

Initially, when the scale is formed and is very thin, diffusion through the scale will be rapid establishing a virtual equilibrium with the metal at the scale-gas interface. In other words, the metal activity at this interface will be maintained at a high value, initially close to unity by rapid diffusion within the scale. Under these conditions the rate of the reaction is likely to be controlled by one of the parameters; oxygen concentration, gas partial pressure, gas flow rate, active species…etc. [Birks, *et al.*, 1983]. As the reaction proceeds at a constant rate the scale layer thickens and at the same time the flux of ions though the scale must be equivalent to the surface reaction rate. To maintain this constant flux, the activities of the metal at the scale-gas interface must fall as the scale thickens. Eventually it will approach an equilibrium value with the increase in scale thickness resulting in a reduction in the metal activity gradient across the scale [Wood, 1970]. At this point the transport of ions across the scale becomes the rate controlling process and the rate falls with time according to a parabolic rate law, see Figure 1.2.3 (b).

The three graphs show, from left to right:

(a) $x = k_l t$ — **Linear**

(b) $y^2 = k_p t$ — **Parabolic**

(c) $Y = k \log (t + t_0) + A$ — **Logarithmic**

with axes labelled *Scale Thickness* (vertical) and *Time* (horizontal).
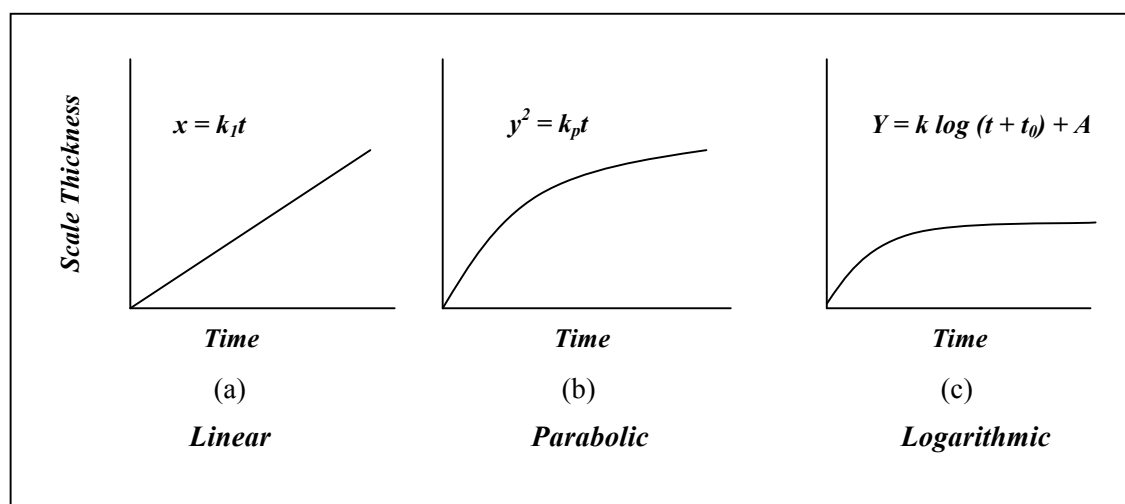
Figure 1.2.3 Schematic illustration of the change in scale thickness with time for the various type of oxidation (following Stott, 1987)

c) Logarithmic Rate Law

When metals are oxidised under certain conditions, typically at temperatures of up to ~ 400°C, the initial oxide formation, up to the 1000Å range, is characterised by an initial rapid reaction that quickly reduces to a very low rate of reaction [Birks, *et al.*,

1983]. Such behaviour has been found to conform to rate laws described by logarithmic functions, see Figure 1.2.3 (c).

1.2.5 Oxidation of Iron

Depending on oxidation conditions, when iron oxidises in air at high temperatures it grows a scale consisting of layers of FeO (wüstite), Fe_3O_4 (magnetite) and Fe_2O_3 (haematite) and thus provides a good example of the formation of multi-layered scale.

From the phase diagram of the iron-oxygen system, shown in Figure 1.2.4, it is clear that the wüstite, FeO, does not form below 570°C. Thus iron oxidised below this temperature would be expected to form a two-layered scale of Fe_3O_4 (magnetite) and Fe_2O_3 (haematite) with the magnetite next to metal. Above 570°C the oxide layer sequence in the scale would be all three layers, with FeO next to the metal.
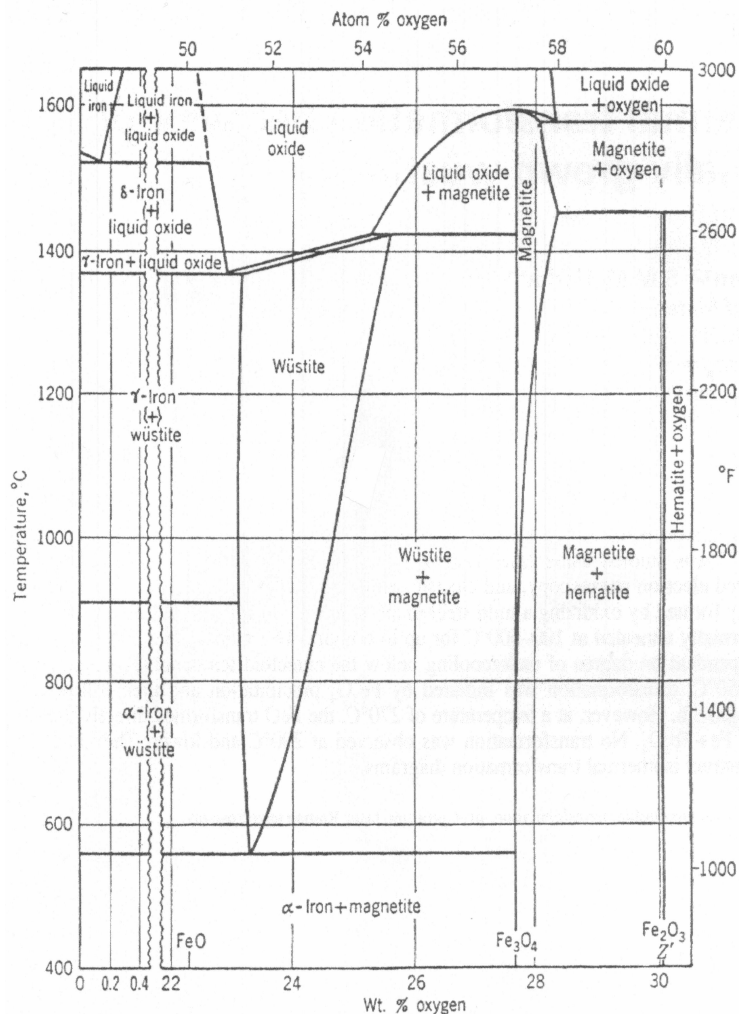
Figure1.2.4 the iron-oxygen phase diagram (Reproduced from Gleeson, et al., 2000)

The basic oxidation mechanism of iron to form a three-layered scale, wüstite, magnetite and haematite above 570°C showing diffusion steps and interfacial reaction is illustrated in Figure 1.2.5.
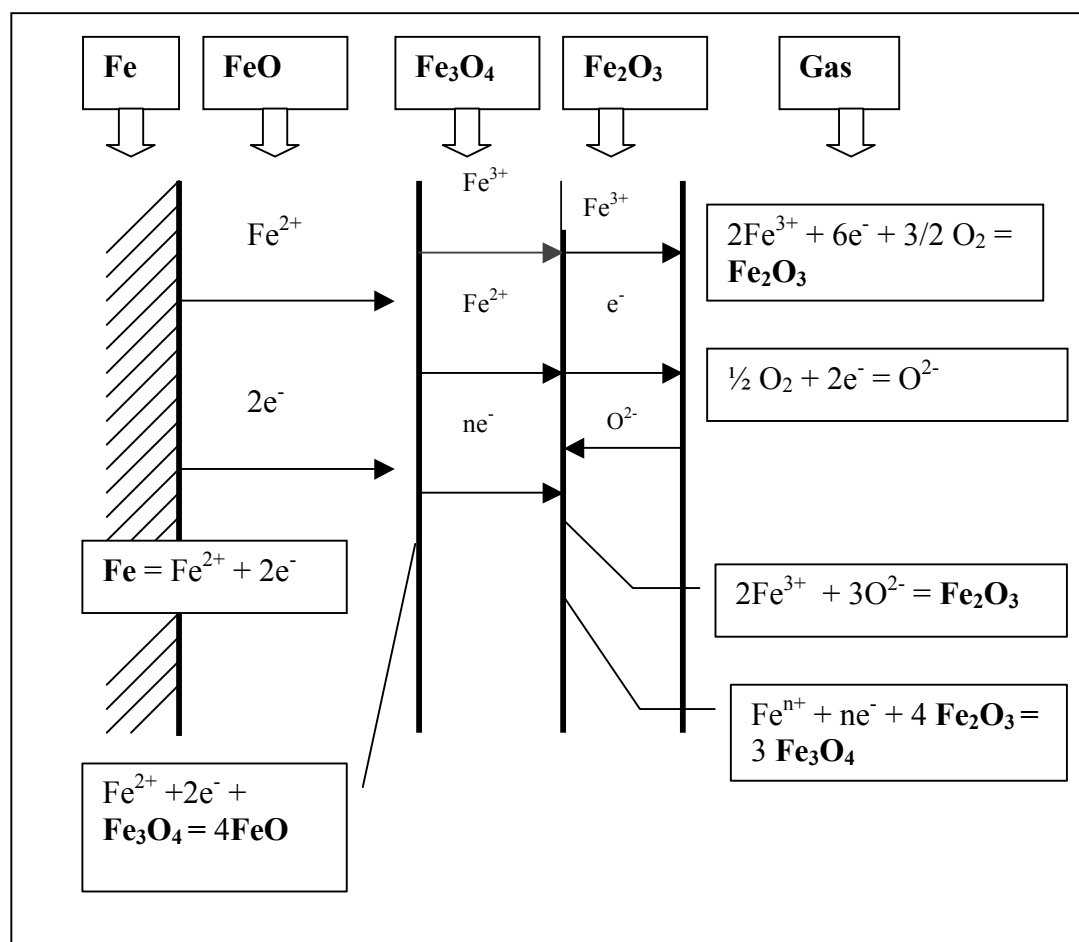
Figure 1.2.5 Oxidation mechanism of iron to form a three-layered scale, wüstite, magnetite and haematite above 570°C showing diffusion steps and interfacial reaction (reproduced from Birks and Meier, 1983).

A simple mechanism can be proposed to represent the oxidation of iron as shown in Figure 1.2.5; at the iron-wüstite interface, iron ionises according to

$$Fe \; = \; Fe^{2+} + 2e^{-} \dots\dots\dots\dots\dots\dots\dots\dots\dots\dots\dots\dots\dots\dots\dots\dots\dots\dots(1.3)$$

The iron ions and electrons migrate outwards through the FeO layer over iron vacancies and electron holes respectively. At the wüstite-magnetite interface, magnetite is reduced by iron ions and electrons according to

$$Fe^{2+} + 2e^{-} + \; Fe_3O_4 \; = \; 4FeO \dots\dots\dots\dots\dots\dots\dots\dots\dots\dots\dots\dots\dots\dots(1.4)$$

Iron ions and electrons surplus to this reaction process outward through the magnetite layer, over iron ion vacancies on the tetrahedral and octahedral sites and over electron holes and excess electrons respectively [Birks, *et al.,* 1983]. At the magnetite-haematite interface, magnetite is formed according to

$$Fe^{n+} + ne^- + 4Fe_2O_3 = 3Fe_3O_4 \dots\dots\dots\dots\dots\dots\dots\dots\dots\dots\dots\dots(1.5)$$
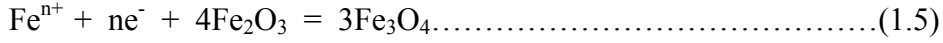
The value of n being 2 or 3 for Fe^{2+} or Fe^{3+} ions, respectively. If iron ions are mobile in the haematite they will migrate through this phase over iron ions vacancies together with electrons and new haematite will form at the Fe_2O_3–gas interface according to

$$2Fe^{3+} + 6e^- + \frac{3}{2} O_2 = Fe_2O_3 \dots\dots\dots\dots\dots\dots\dots\dots\dots\dots\dots\dots(1.6)$$

at this interface also, oxygen ionises according to

$$\frac{1}{2} O_2 + 2e^- = O^{2-} \dots\dots\dots\dots\dots\dots\dots\dots\dots\dots\dots\dots\dots\dots(1.7)$$
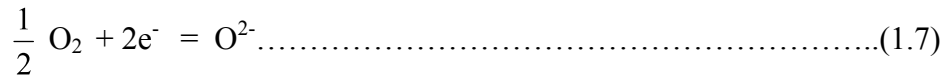
If oxygen ions are mobile in the haematite layer, the iron ions and electrons, in excess of requirement for reduction of haematite to magnetite, will react with oxygen ions diffusing inwards through the Fe_2O_3 layer over oxygen vacancies forming new Fe_2O_3 according to

$$2Fe^{3+} + 3O^{2-} = Fe_2O_3 \dots\dots\dots\dots\dots\dots\dots\dots\dots\dots\dots\dots(1.8)$$
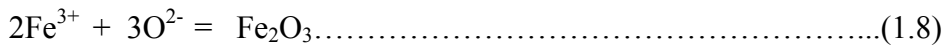
The corresponding electrons then migrate outwards through the Fe_2O_3 to take part in the ionisation of oxygen at the $Fe_2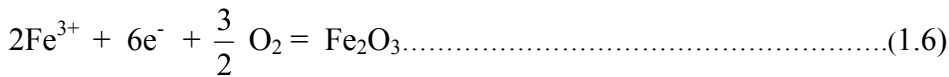O_3$–gas interface. As there is a much greater mobility of defects in wüstite, this layer will be very thick compared with the magnetite and haematite layers [The above mechanism and equations are reported by Kofstad, 1966, Birks, *et al*., 1983, Hauffe, 1965 and Kubaschewski, *et al*., 1967]

Since the scale formed on iron above 570°C is predominantly wüstite, growth of this layer controls the overall rate of oxidation. However, since the defect concentrations in wüstite at the iron-wüstite and wüstite-magnetite interfaces are fixed by the

equilibrium achieved there, for any given temperature, the parabolic rate constant will be relatively unaffected by the external oxygen partial pressure. Increasing the oxygen partial pressure in the gas phase should theoretically lead to an increase in the relative thickness of the haematite layer. However, since this layer only accounts for about 1% of the total scale thickness, any variation in rate constant with oxygen partial pressure will be difficult to detect [Kofstad, 1966].

Generally this simple mechanism illustrated above is more complicated in reality as it is affected by many factors described in the following sections.

1.2.6 Iron Oxide Scale Microstructure

The microstructures of the oxide scales on steels are very complex and their development depends on many factors including time, temperature, oxidation environment and alloying elements. As described earlier, classically iron and steel scales are characterised by a three-layer model. The microstructure characterisation of the oxide scale and verifying its phases helps to obtain a better understanding of the oxidation mechanism. Furthermore, knowledge of the oxide microstructure is critical in understanding how the oxide behaves during the high temperature deformation of steels and more importantly how it can be removed following processing.

Theory concerning the oxidation characterisation of pure metals and alloys, the mechanism and the rate of scale growth is well documented. Related experiments have been documented in numerous independent studies in the 1950s and 1960s. Subsequent studies in the 1960s of the mechanism of scale growth on pure iron and low alloy steel have been reviewed by Sachs and Tuck, 1970. They made a careful analysis of many experimental observations.

Characterising microstructural features within the oxide scale in the literature has mainly concentrated on the porosity, phases present and their ratio. Sheasby, *et al.*, 1984, carried out some experiments on quenched samples, oxidised at 1200 °C, and showed that wüstite was the only oxide phase that formed in the early stage of oxidation (~300 seconds). Haematite and magnetite layers formed at oxidation times longer than 600 seconds. In the early stage of oxidation, the molar flux of iron through the scale will be greater than the flux of gaseous oxygen through the gas/film

boundary layer, such that only wüstite can form [Sheasby, *et al.*, 1984]. When the oxide layer becomes thicker, the molar flux of oxygen through the gas/film boundary layer exceeds the rate of diffusion of iron in the wüstite layer leading to the formation of the magnetite and haematite layers. The rapidly cooled samples had FeO, Fe_3O_4, Fe_2O_3 thickness ratios in close agreement with the 95:4:1 ratio established by Paidassi [Kubaschewski, *et al.*, 1967].

Temperature can influence the fraction of the three phases within the scale. Figure 1.2.6 shows work by Tominaga, *et al.*, 1982 and Hauffe, 1965, who determined the distribution of the three major phases with temperature for steel and iron. From both studies, at low temperatures (<600°C) the magnetite phase dominates the scale. At higher temperatures the wüstite phase becomes more dominant with the haematite layer remaining low at all temperatures. As shown in Figure 1.2.6, there is a difference in the phase ratios between the two studies. Is should be noted that Hauffes work was on iron sheet and Tominagas is on low carbon steel.
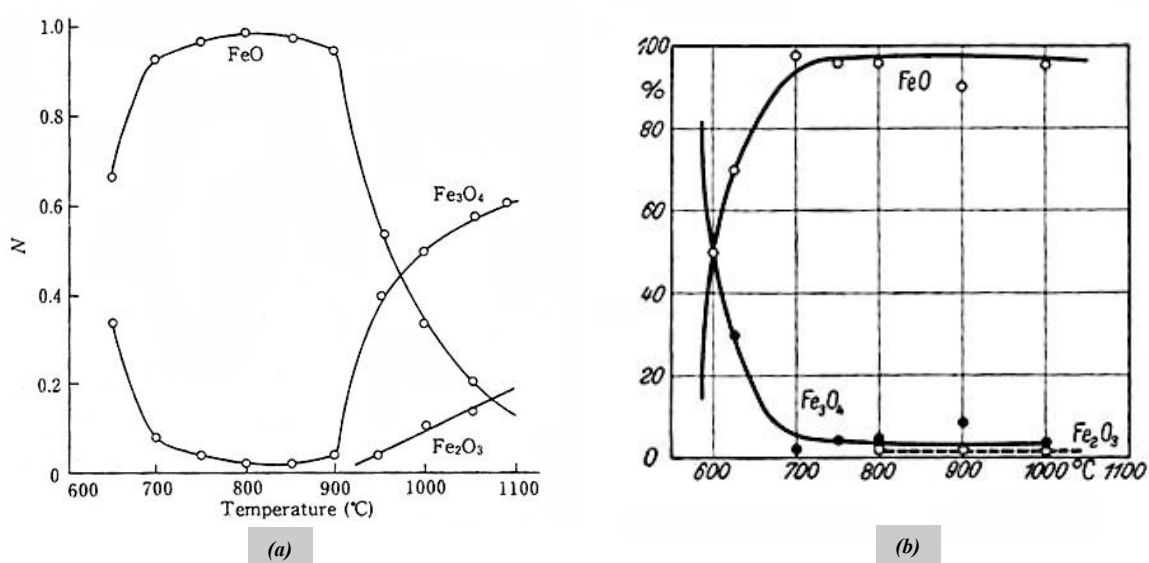
Figure 1.2.6: Volume Fraction of wüstite, magnetite and haematite as a function of temperatures (a) Tominaga, et al., 1982, (b) Hauffe, 1965.

Work has shown that during cooling the wüstite phase is not stable and can transform to magnetite [Kofstad, 1966 and Hauffe, 1965]. Magnetite precipitates on the wüstite due to a saturation of oxygen during cooling from the oxidation to room temperature. This precipitation can further complicate the distribution of the phases within the scale.

Abuluwefa, *et al.*, 1996, studied the effect of time on phase ratio. They monitored the oxide scale during growth on a (0.4 wt% C and 0.02 Si wt %) mild steel surface with time. They showed that the predominant oxide phase was magnetite, followed by haematite and wüstite. This can be explained by chemical equilibrium of the oxides during their growth. If the scale layers are uniform and remain intact during the course of oxidation, chemical equilibrium between the oxides is maintained. However, if oxygen has access to the lower layers of the oxides, through porosity and cracks within the scale, this would affect the growth rates. In such cases, oxidation of the various phases of iron at random locations within the scale can exist, hence, giving rise to the faster growth of the higher oxides with their proportions depending on the accessibility of oxygen on the various reaction sites, see Figure 1.2.7.
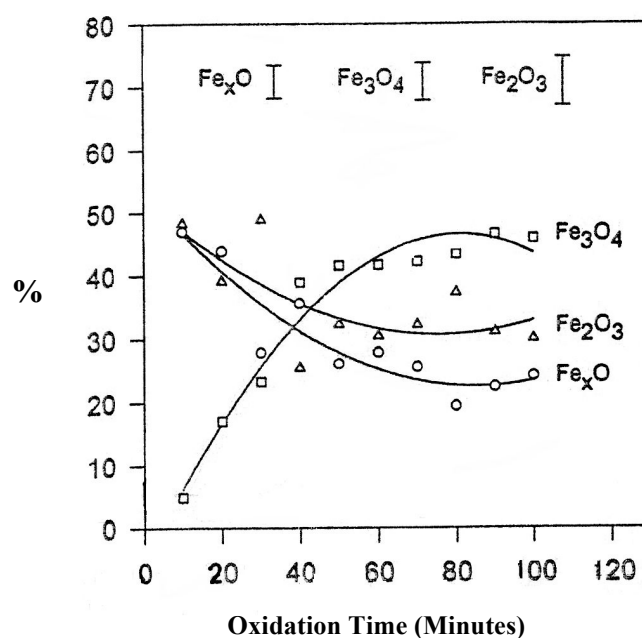
Figure 1.2.7 Variation of the scale composition, wüstite, magnetite and haematite during oxidation in air at 1127°C (Reproduced from Abuluwefa, et al., 1996).

The oxidation behaviour of low carbon, low silicon mild steel has been investigated by Chen, *et al.*, 2001, in ambient air at 450 - 900°C, to simulate steel strip oxidation during finish hot rolling and coiling. They claimed that the oxide scale that developed at 880 - 900°C after a very short time (12 seconds) had a structure similar to that formed on pure iron, but with a greater thickness ratio between the magnetite and wüstite layer. However, the scale structure after oxidation for a longer period, 200 seconds at 900°C, deviated significantly from that reported for pure iron. This difference was attributed to the loss of scale-steel adhesion at some locations. Oxide scales formed in the range of 580 - 700°C after oxidation for more than 7200 seconds

also differed from those reported for pure iron. The scale structure was irregular, comprising mainly of haematite and magnetite with very little or no wüstite, while the thickness ratio of these two layers differed considerably at different locations. They also reported that the scale formed at 450 - 560°C was relatively uniform with a two-layered haematite and magnetite structure; however, the thickness ratio of these two layers varied for different oxidation temperatures and different oxidation times. They also showed that the scale-steel adhesion improved with limited oxygen supply (zero air flow). The thickness ratio of haematite, magnetite and wüstite at 700 - 1250°C was consistent with that for pure iron in air, at about 1:4:95 [Chen, *et al.*, 2002].

Schmid, *et al.*, 2001, studied the oxidation of iron at elevated temperatures in pure oxygen and water vapour and also studied the decomposition of the wüstite using in-situ experimentation in an Environmental Scanning Electron Microscopy (ESEM). They showed that at 700°C in a hydrogen/argon/water vapour mixture that the oxide nucleation occurred rapidly. Oxide grains grew in different orientations and had varying sizes. They showed that further growth of the oxide grains was determined by their original orientation relative to the metal surface. In terms of thickness, wüstite contributed about 90%, magnetite to 7 - 10%, and haematite about 1 - 3% of the total oxide layer thickness when iron was oxidised in air at 650°C. With thickening of the scale, surface diffusion becomes more dominant, although lattice diffusion is still considerably fast. Thus oxide scale changes its growth mode and establishes a pyramidal growth structure. Senkevich, *et al.*, 2000, studied growth of oxide films on low carbon steel at 500°C by impedance spectroscopy; they claimed that the maximum thickness of haematite and magnetite was 0.15 μm and 5.5 μm respectively. They showed that the parabolic kinetics for oxidation of low carbon steel in air at 500°C is equal to 6.3×10^{-5} g/cm^2. min$^{1/2}$.

Raman, *et al.*, 1998, investigated the characterisation of iron oxide scale on low carbon steels grown at 1200°C for 2400 seconds, using Laser Raman Spectroscopy (LRS) which is capable of providing phase identification within thick scales. The technique was shown to be capable of unambiguously distinguishing the three iron oxide layers, however, it gives no information on the microstructures of the scale layers.

The complex microstructural development of the oxide scale on low carbon steel makes the analysis of the scale microstructures difficult. As reported earlier most of the studies in the literature focused on phase ratio and the factors that affect their changes with little attention to the grain boundary characterisation, misorientation, oxide grain size and shape and related features.

1.2.7 Iron Oxide Scale Components

1.2.7.1 Wüstite

Wüstite has a face-centred cubic lattice structure. The wüstite phase, FeO, is a p-type metal semiconductor that can exist over a wide range of stoichiometry. With such a high cation vacancy concentration, the mobility of cations and electrons (via vacancies and electron holes) is extremely high [Stott, 1987]. Its composition varies between its Fe and Fe_3O_4 boundaries [Toft, 1972]. The cubic lattice constants for wüstite at the Fe and Fe_3O_4 boundaries at room temperature are 4.3108 and 4.2774 Å, respectively [Ralph, 1963]. Wüstite only exist at temperatures above 570°C. On cooling from temperatures above 570°C, the wüstite layer will, in theory, undergo a eutectoid reaction. However, if the cooling rate is relatively rapid, the wüstite layer may be retained to a temperature range well below 570°C before the onset of the eutectoid reaction. The unstable wüstite layer might gradually be oxidised to magnetite during the continuous cooling process at temperature below 570°C, the overall reaction is;

$$3FeO + \frac{1}{2}O_2 = Fe_3O_4 \quad \text{……………………………………………………..(1.9)}$$
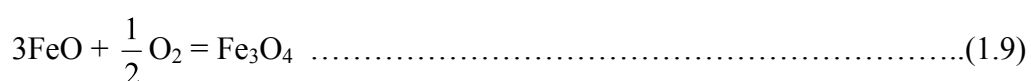
Even at lower temperatures the wüstite may undergo the eutectoid reaction forming a mixture of magnetite and iron via equation 1.10 [Chen, *et al*., 2001];

$$4FeO = Fe_3O_4 + Fe \quad \text{………………………………………………………(1.10)}$$

1.2.7.2 Magnetite

The phase magnetite, Fe_3O_4, is an inverse spinel structure, which has divalent ions, Fe^{2+}, occupying octahedral sites and half of the trivalent ions, Fe^{3+}, occupying tetrahedral sites [Birks, 1983]. Defects occur on both sites and consequently iron ions may diffuse over both tetrahedral and octahedral sites. The composition of magnetite is known to correspond very closely to its stoichiometric composition, Fe_3O_4. The cubic unit cell has a lattice constant of 8.396Å at 25°C [Abuluwefa, *et al.*, 1996]. Half of the octahedral sites and one-eight of the tetrahedral sites are occupied by cations in the magnetite inverse spinel structure. According to Toft, 1972, there is one Fe^{3+} ion per formula unit at a tetrahedral site with the remaining Fe^{2+} and Fe^{3+} ions randomly distributed at octahedral positions. Magnetite can be a non-stoichiometric compound which exhibits a cation deficiency: the iron to oxygen ratio; Fe:O, lies in the range 0.750 to 0.744 [Harkins, 1984], however, this ratio is dependant upon both the oxygen pressure and the temperature.

1.2.7.3 Haematite

There are two forms of haematite; the α and γ. The α–form has a trigonal structure with the ferric ions occupying octahedral sites. While the γ-form has a structure very similar to magnetite, being a cation-deficient inverse spinel with an iron to oxygen ration in the range 0.67 to 0.72. However, γ-Fe_2O_3 oxidises to form α-Fe_2O_3 above 400°C and only this structure needs to be considered here. α-Fe_2O_3, has the trigonal structure with *a* and *c* for the hexagonal unit cell of haematite being; 5,035 and 13.72 Å, respectively at room temperature [Ralph, 1963]. Senkevich, *et al.*, 2000, claimed that haematite has high electrical resistivity (10^9 Ω m) compared to that of magnetite (5×10^{-5} Ω m).

Haematite is much harder than magnetite and wüstite. The magnetite layer is very brittle and therefore easier to remove mechanically than scales containing wüstite [Burke, *et al.*, 2000]. Schimd, *et al.*, 2001, reported that iron develops a porous outer haematite scale. Interface reactions in the multi-layer scale play an important role and vacancy annihilation at the magnetite-haematite interface causes porosity of the outer scale layer.

1.2.8 Effect of Alloying Elements on Oxide Scales

The formation of oxide scales on the steel is complicated by several factors when compared with the simple theoretical model described earlier. When the steel is oxidised, the carbon content and the small quantities of manganese, silicon and sulphur normally present also cause modification to the oxidation process. Therefore, there is no consistent diffusion path as assumed in the derivation of the parabolic growth law. The affect of small amounts of alloying elements on oxidation rate, kinetics and related microstructure is not well understood, however, some experimental and theoretical studies concerning this aspect are summarised in the following sections.

1.2.8.1 Elements Less Noble than Iron

a) **Carbon-** Generally the scaling rate of high carbon steels is lower than low carbon steels. Also the possibility of steel decarburisation increases with increasing amounts of carbon [Sachs, *et al*., 1968]. This was first noticed where the oxidation rate of steel was slower than that of pure iron. The same reference suggested that a small amount of impurity from the steel substrate, including carbon, might inhibit dislocation movement in the scale and favour the formation of a series of micropores or gaps at the steel-scale interface resulting in a reduction in the iron flux crossing the interface. Other studies e.g. Caplan, 1979, observed a thin layer of graphite at the scale-steel interface during oxidation of Fe-C steels in the range of 600 to 800°C. According to Sachs and Brown, 1958, carbon in the steel can also be oxidised to form CO or CO_2 at the scale/substrate interface resulting in a loss of contact between the oxide scale and the substrate and hence reducing the iron flux from the steel substrate into the scale.

b) **Silicon-** Taniguchi, *et al.*, 2001, showed that the scale thickness decreases with an increase in the Si content at 1143°C. This is explained in terms of accumulation of the Fe_2SiO_4 grains at the scale/substrate interface and the formation of a row of large micropores. The Fe_2SiO_4 grains accumulated at the interface slow the diffusion of iron from the substrate to the scale, since the diffusion of iron through Fe_2SiO_4 is much slower than through FeO. In addition, the formation of a row of large micropores decreases the diffusion paths for iron ions towards the outer scale surface. On the other hand, the scale thickness dependence on the Si content was shown to be very

weak at 1203°C. Their work was carried out on 1.5 % Si low carbon steel at 1143 and 1203°C. It was observed that the scale spallation during cooling from 1143°C increase as the Si content increases, while it is almost constant for cooling from 1203°C.

Marston, 2001, stated that an additional oxidation product, fayalite ($2FeO.SiO_2$) can be produced and this can form a eutectic with wüstite that melts at about 1177°C. When the steel cools immediately, fayalite can act as a "glue" to bind the wüstite grains to the steel surface. Therefore, complete scale removal is more difficult, and the layer of scale adjacent to the steel remains attached even after the most intensive descaling operation. Chen, *et al.*, 2002 showed that with 1.8% Si, as in spring steel, the resulting fayalite produces a very thick scale that is difficult to remove by high pressure hydraulic descaling.

The silicon content in high temperature oxidation strongly affects the microstructure of the oxide layer. Work on 0.4% and 2% Si-steel carried out by Kim, *et al.*, 2002, showed that four layers could be seen by EBSD microstructural analysis; magnetite, wüstite, a thin black layer and the steel substrate. Among these layers, the third layer was a composite of wüstite and SiO_2. According to the theory of steel oxidation with differing silicon content, iron ion diffusion in low Si-steel can continue throughout the first silicon oxide layer and subsequently makes the usual three-oxide layers, namely, wüstite, magnetite and haematite. However, a thick SiO_2 layer can impede iron diffusion in the high silicon steel. Fe_3SiO_4, a mixture of wüstite and fayalite, may exist after oxidation of high Si-steel between the haematite and wüstite layers. From this, Kim, *et al.*, 2002, concluded that the main factor to control the microstructure is the alloying element content of the steel rather than substrate crystallographic texture.

1.2.8.2 Elements More Noble than Iron

a) **Nickel-** Nickel, tin and copper do not diffuse into the FeO layer easily unless the alloy contains very high amounts of them. Thus, they are rejected at the metal scale interface where they either accumulate or diffuse back into the steel [Fukugawa, *et al.*, 1994]. For nickel steels, the enriched layer is more resistant to oxidation than the core which results in entanglement of nickel in the scale. What appear to be metal filaments extend back to the steel substrate. Such entanglement renders it more difficult to remove the scale and defects from impressed scale may form during

rolling. Nickel affects on the oxide scale on steel surfaces has been shown by [Burke and Higginson, 2000] to promote the growth of fibrous scales that entangle the metal scale interface.

b) **Sulphur-** Sulphur is also an important constituent in the exhaust gas present in reheat furnaces in the form of SO_2. In a reducing atmosphere iron sulphide is formed. Sulphur can also be provided at the steel scale interface from the steel, especially resulphurised steels. Iron sulphide forms as a low melting point eutectic with wüstite producing an adherent scale. In order to prevent this occurring, an excess of oxygen in the furnace atmosphere is advocated with sulphurous fuels, and this is probably beneficial for resulphurised steels [Chen, *et al.*, 2002 and Marston, 2003].

1.2.9 Oxide Scale Properties and Microstructural Features

1.2.9.1 Porosity

The theoretical densities of Fe_2O_3, Fe_3O_4 and FeO are nearly equal (5.24, 5.18 and 5.70 g/cm^3 respectively), so that an arithmetical average would be nearly equal to the average density of an oxide film without any porosity. Thus, the porosity of an actual oxide film can be determined the using relationship;

$$Porosity, \% = \left(1 - \frac{average.actual, density}{average.theoritical, density}\right).100 \dots\dots\dots\dots\dots\dots\dots\dots\dots(1.11)$$

The average density of an actual film formed on steel can be determined by measuring its average thickness and cross-section area and its weight [Khan, *et al.*, 1969 and Birks, *et al.*, 1983]. However, there is another method for measuring porosity such as statistical measurement of porosity concentration using optical or SEM images. The works by Sachs and Tuck, 1967, Pickens, 1984 and Hauffe, 1965 are examples of measured porosity concentration using this method.

The factors that affect the porosity within the oxide scale are reported in many studies. Sachs and Tuck, 1970, claimed that at higher temperatures and longer times of exposure, the scale would be more porous. Sheasby, *et al.*, 1984, claimed that extensive pore formation in the scale would be observed when iron containing 60 ppm

carbon when oxidised at 950°C, but where the iron contained 32 ppm C the scale formed was free of pores. Pickens, 1984, observed the effect of pores and fissures on the phase transformation and changing phase ratio within the scale. He stated that the upper magnetite layer and central wüstite layer were relatively free of fissures. Also he stated that the fissures present in the wüstite layer were surrounded by haematite at the fissure boundaries so a ring of haematite surrounded the fissure even in the magnetite layer. Generally, in literature the influence of pores on the microstructural development of the oxide scale is controversial and not well understood.

1.2.9.2 Electronic Conductivity

Iron has a very low resistivity and is termed a conductor. Haematite, with a resistivity of the order 10^{12} Ωm, is non-conductor or insulator. Also wüstite is another non-conducting material [Harkins, 1984]. Among the three iron oxides, magnetite has the lowest resistivity and conversely it is the most conductive, see Table 1.3.1.

Table 1.2.1 The resistivity of iron and its oxide [Lowenheim, 1974]

MATERIAL	RESISTIVITY Ωm
Iron, Fe	1×10^{-7}
Wustite, FeO	6×10^{3}
Magnetite, Fe_3O_4	1×10^{-4}
Haematite, Fe_2O_3	10^{12}

1.2.9.3 The oxide scale adherency to the steel substrate

There are a number of theories concerning the formation of the gap at the scale-steel interface. It is suggested that the natural velocity of the diffusion of the iron outwards through the scale is greater than the rate of oxidation of the iron core; hence there is a tendency for contact to be lost between the scale and the core [Kubaschewski and Hopkins, 1967]. Carpenter and Ray, 1973, stated that impurities and inclusions accumulate at the metal surface and are believed to act as barriers to oxide subsidence causing extensive separation, blistering and spalling during cooling. Kucera and Hajduga, 1998, attributed the oxide metal separation to vacancy, voids and cavities which were left behind during the oxidation of iron. However, these theories and those related to the different thermal expansion of the oxide scale layers and steel

substrate which might cause non adherent scale, are difficult in technical terms to prove. Nevertheless, they are useful for understanding the gap formation.

One of the most well-known theories was discussed by Chen, *et al.*, 2003, which is the gas formation at the steel-metal interface related to decarburisation in steels. It is believed that carbon from the steel substrate can be oxidised, causing decarburisation of the steel when the rate of oxidation exceeds that of iron. Decarburisation is normally observed above 700°C, particularly for steels containing relatively high levels of carbon [Chen, *et al.*, 2003]. During steel oxidation, carbon reacts with the scale via the following reaction;

$$C + FeO = Fe + CO \dots\dots\dots\dots\dots\dots\dots\dots\dots\dots\dots\dots\dots\dots\dots\dots\dots\dots(1.12)$$

Further reaction between CO and the scale may produce CO_2 via;

$$CO + FeO = Fe + CO_2 \dots\dots\dots\dots\dots\dots\dots\dots\dots\dots\dots\dots\dots\dots\dots\dots\dots(1.13)$$

The reaction can progress only when CO and CO_2 can escape through the scale. It was proposed that these gases could escape through micro-crack channels. Also it may cause blistering or rupture of the scale.

Below 700°C, the rate of carbon oxidation may be lower than that of iron oxidation. Carbon has virtually no solubility in the scale and so this may lead to carbon enrichment at the metal-scale interface causing solid carbon (graphite) precipitation. A complete description of decarburisation can be found elsewhere [Birks and Jackson, 1970, Sachs and Brown, 1958, Birks and Meier, 1983].

As explained by Sachs and Jay, 1960, the gap at steel-oxide interface might heal or migrate during oxidation or the cooling process. This makes the observation of the gap and its influence on the oxidation rate and related microstructure of the oxide scale difficult. Overall, the theories mentioned in this section can explain the oxide adherency on the steel substrate and gap formation, however, the main factors that manipulate the gap formation are controversial in the literature.

1.2.9.6 Crack Formation within the Oxide Scale

Oxide scales can be beneficial in high temperature application because they act as hard resistance surface layers, which increase the wear resistance of the materials. Oxides are chemically stable and act as a barrier, which reduces the rate of further attack. However, in most practical applications these protective layers are stressed, either by externally applied load, by oxide growth stresses or by thermal stresses induced by the mismatch of the thermal expansion coefficients of oxide layers and substrate. Oxide scales are therefore prone to mechanical failure. The diffusion barrier function is destroyed when oxide failure occurs which allows the oxygen to regain direct access to the metal. This has the most severe consequences when delaminating and spallation of large areas of oxide exposes a clean metal surface leading to a sharp increase in the oxidation rate and breakaway kinetics [Nagl, *et al.*, 1993].

It is almost impossible to achieve both good mechanical stability of the oxide and a low oxidation rate or a low rate of material consumption, because high mechanical stability requires good deformation properties, i.e. high creep rates. The creep rate is determined by the slower moving elements in the scale, whereas the oxidation rate is determined by the faster moving element. Therefore, the task is to arrive at the best trade-off between good deformation properties and low rate of material consumption in order to achieve a maximum component lifetime [Stack, *et al.*, 1991].

Growth stresses arise mainly from the volume change during formation of the oxide. It is suggested that if the ratio of volume of oxide to that of metal which it replaces, i.e. the Pilling-Bedworth ratio, exceeds unity, the oxide grows under compressive stress, or vice versa. This only applies to oxides formed at the metal/oxide interface. Growth stresses are mainly compressive because most materials exhibit a volume expansion during oxidation [Tien, 1974]. The other most common sources of stresses in oxides are thermal stresses due to cooling/heating or thermo-cycling as a result of differences in thermal expansion coefficients of metal and oxide. Thermal stresses are also induced under thermal shock condition or when a heat flow is removed. Similarly the substrate geometry can cause stresses, in particular at corners. Also mechanical stresses can arise in the oxide from axial loading or bending [Nagl, *et al.*, 1993]. Currently there are no methods available to measure the stresses in oxides during mechanical deformation, however, x-ray diffraction has been used widely to

determine the residual and growth stresses present within the oxide scales. Other methods are based on the extension of a sample during oxidation or the deflection of a thin metallic strip oxidised on only one surface [Nagl, *et al.*, 1993].

As a result of the stress generated within the oxide scale cracks can be formed. It is believed that the cracks inevitably form due to the difference in thermal contraction between the iron base and the scale upon cooling and the internal residual stress. The condition of the crack formation depends on the scale thickness, scale strength, and other factors. The number and interval of such cracks are important factors for descaling process [Tominaga, *et al.*, 1982].

Different oxide phases within the steel oxide scale respond differently to stress, for example, wüstite forms discrete grains, and permits lateral cracks and other porosity to develop within the scale. Lateral cracks can be expected to inhibit diffusion of ions, whereas vertical crack can provide a diffusion path for gas [Marston, 2003]. Generally, is believed that cracks can affect the oxidation rate and microstructural development of the oxide scale, thus crack influence on oxidation process should be considered in any oxidation study.

1.2.10 Iron Oxide Crystallographic Texture Formation

An understanding of the oxide texture formation is critical in the understanding of how and to what extent the oxide film can protect the alloy from further oxidation. Among many factors affecting oxide growth rate at high temperatures in a corrosive environment and its resistance to spallation, the crystallographic texture of the metallic substrate plays an important role [Czerwinski and Szpunar, 1999].

It is believed that oxide grain orientations form at the early stage of the oxide formation. Also it is believed that during the growth, some oxide grains grow faster laterally than their neighbours and become bigger. This competition of growth causes the formation of an oxide texture and a different microstructure [Hualong, *et al.*, 1999]. Kofstad, 1966, claimed that the chemisorption and initial oxide nucleation and growth are greatly dependant on substrate orientation. The effect of orientation also extends to larger oxide film thickness. Review work by Kubaschewski and Hopkins, 1967, reported that Sewell and Cohen, 1964, studied the oxidation of iron single

crystals at around 200°C by means of electron diffraction, electrochemical, and gravimetric methods, and found that both the oxide composition and thickness were highly dependant on orientation. The oxide was found to consist of both haematite and magnetite, but no discrete phase boundaries were observed. For low index planes close to (001), (011) and (111) the oxide films had a large proportion of magnetite, while a smaller percentage was observed for high index planes. Mehl, *et al.*, 1984, carried out a detailed study of the orientation relationship between wüstite and $\propto$-iron. It was found that the (100) plane in FeO lies parallel to the (100) in iron, and the [110] direction in the (100) plane in FeO lies to the [100] direction in the (100) plane in iron.

It is also believed that the orientations of the oxide scale on steel surface depend on the oxidation rate [Kubaschewski, *et al.*, 1967]. Pfeil, *et al.*, 1931, who used cold-rolled iron sheets for their experiments, found that the scale crystals corresponded exactly in size, shape and position with the ferrite crystals of iron, and that they also corresponded in orientation. They also claim that $\propto$-Fe_2O_3 produced by short-time oxidation of iron in air tends to orient itself on the surface in a similar way to that found after more advanced oxidation. Garber, 1959, stated that the oxide is initiated as whiskers, which develops into platelets after an immediate linking. If this whisker growth is analogous to that observed on metals, then the oxide nucleation and initial growth must develop with the spiral growth of a screw dislocation from the surface of the metal. He added that the oxide growth is epitaxial and occurs at the surface of the metal along crystallographic planes, which have a definite relationship to the orientation of the individual metal grains at the surface.

The idea of establishing a texture relationship between iron and steel with its oxide is not universally accepted. Kim, *et al.*, 2001, explained that there are two reasons for the columnar structure of the wüstite that is developed in high temperature oxidation; the increase of texture strength is a consequence of the competition in grain growth. The {001} texture component of wüstite is most likely to win this competition because it has a lower surface free energy than other texture components. Another reason may be the massive lattice diffusion of iron ions through wüstite layer at high temperatures. At this point, however, the role of magnetite should be considered on oxidation processes because wüstite is nucleated at the interface between magnetite and steel. The nucleation and growth of wüstite must be affected by magnetite. They

showed that an orientation relationship between steel and oxide was observed at higher temperature: {001} steel // {001} wüstite // {001} magnetite. Also they claimed that during the oxidation process, a strong fibre texture was developed and the number of low angle grain boundaries in wüstite increased as the oxide grew. A year later, Kim, *et al.* 2002, reported that despite a difference in texture and grain size of the substrate, the wüstite layer has a columnar cell structure with a <001>// GD texture (GD stands for growth direction of oxide normal to the sample surface) and magnetite also has a cubic-type cell <001>//GD texture. They showed that the different steel substrates have no influence on the microtexture and microstructure of the oxide scale. Moreover their work on hot-rolled low carbon steel showed that there was no crystallographic relationship between substrate and iron oxide textures, however, the intensity of the substrate texture was not strong. They found that the relationship between substrate and oxide orientations become weaker when the oxide grains nucleate and grew away from the substrate. Certain elements such as carbon and silicon in low carbon steel, may also distort this orientation relationship, but the alloying element role is not well understood.

Higginson, *et al.*, 2002, studied the texture development in oxide scales on steel. They reported that oxidation at 760°C for 7200 seconds of IF steel gave the substrate and the wüstite layer a strong {100}<001> (Cube) texture. The magnetite also contained {100}<001> component with {110}<001> (Goss texture) component. There was clearly a strong relationship between the textures of the two layers in the oxide and that the texture of the substrate increased in strength slightly as the oxidation temperature increased. Low carbon steel was oxidised at 900 and 1000°C and the texture of the wüstite and magnetite were both weak and showed little correlation. The same authors showed that at the higher temperatures, 1050°C, both oxide scales layers show a strong texture, the wüstite ~ 29% {100}<001>, and the magnetite ~ 37% {100}<001>. Clearly, as the oxidation temperature increased the strength of the crystallographic texture in the oxide layers increased. They also noted, when the oxidation temperature increased, the porosity in the scale decreased. There appeared to be a correlation between the porosity of the scale and the preferred orientation of the oxide layers, i.e. as the porosity decreased the strength of the orientation in the scale layers increase, the lower porosity the stronger the texture. Experiments on silicon and nickel containing steels showed that only a small relationship between the crystallographic orientations of the oxide layers existed. From the literature, there is

little agreement on the role of texture on oxidation rate and microstructure. Furthermore, the factors that affect oxide texture formation and its development with oxidation conditions are not well understood.

1.2.11 Oxide Scale Descaling during Steel Manufacturing

During the manufacture of steel components at high temperature the surface quality of the finished product depends on the oxide scales and the ability of the manufacturer to remove them after hot deformation. The behaviour of these scales during processing is also of importance to steel manufacturers as they affect the friction, heat transfer and tool wear during hot working [Higginson, *et al.,* 2002].

Steel manufacturers are under continual pressure to improve the surface finish of product, whether it is flat products such as strip and plate or long products. The process route for strip involves cold rolling to produce a mirror-like surface for the best-painted finish. Although plate and long products are sold in the hot rolled condition, many customers require a painted finish, which would be unacceptable if the surface were rough as a result of an irregular embedded layer of scale [Chen, *et al.*, 2001]. A consistent surface finish requires a planned, objective approach to scale removal, with the descaling condition tailored to the nature of the scale, which in turn depends on the type of steel and reheating conditions.
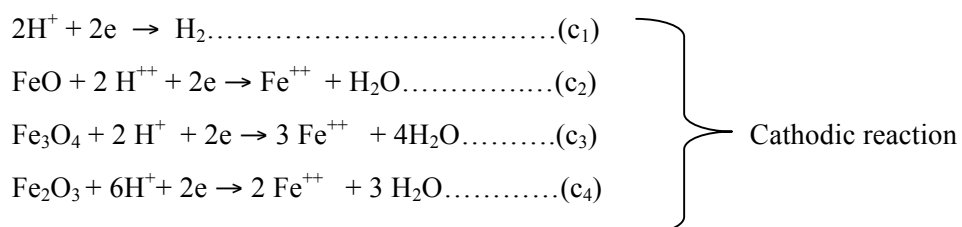
Developing a strategy for the easy removal of scale without sacrificing the mechanical properties of the product is a major priority for the steel manufacturer. In hot-rolled products, the formation of mill scale is unavoidable in the process of cooling from a high temperature just after deformation to an ambient temperature. Pickling has so far been mainly employed to descale wire rods prior to drawing. However, because of the severe pollution control regulations concerning waste acid treatment, mechanical descaling has been put into industrial use and there is a tendency towards the spread of this process since it provides advantages in terms of operating cost [Militzer, *et al.*, 2000 and Tominaga, *et al.*, 1982]. However, in industry, there are many methods for descaling the oxide scale on the steel surface. The main methods of descaling have been summarised in the following sections:

1.2.11.1 Pickling

Descaling the oxide on the steel surface is highly dependent on the mechanical properties of the scale. Furthermore, each oxide layer in the scale has different mechanical properties. For example, wüstite, which exerts the greater effect on the properties of the mill scale, always shows a crystal structure that lacks Fe and is expressed as $Fe_{1-y}O$. Thus, wüstite always has 5 to 16% defects of Fe-atoms. This suggests that wüstite is the softest and the most acid-soluble of all phases of the scale.

Pickling has long been the principal means of descaling. In an acid solution, the solubility of FeO is highest, that of Fe_3O_4 next, and the Fe_2O_3 scarcely dissolves. According to the basic scale model the haematite is on the top of the scale and magnetite is the intermediate layer, when wüstite at the bottom of the scale, dissolution takes place in the order of Fe_2O_3, which is most insoluble, Fe_3O_4 and FeO [Tominaga, *et al.*, 1982]. In general, however, this concept is not accepted. As mentioned before, the scale is not perfect and microcracks are formed in it during cooling and handling. When these cracks reach the iron base, a local cell composed of oxides, an acid solution and iron is formed and the iron base is considered to dissolve first.

The dissolution of the iron base is followed by the reduction and dissolution of the oxides. In connection with this the following reactions need to be considered:

$Fe \rightarrow Fe^{++} + 2e$…………………………………………………(a) Anodic reaction

$2H^+ + 2e \rightarrow H_2$…………………………………(c$_1$)

$FeO + 2 H^{++} + 2e \rightarrow Fe^{++} + H_2O$……….…..(c$_2$)

$Fe_3O_4 + 2 H^+ + 2e \rightarrow 3 Fe^{++} + 4H_2O$……….(c$_3$)   Cathodic reaction

$Fe_2O_3 + 6H^+ + 2e \rightarrow 2 Fe^{++} + 3 H_2O$…………(c$_4$)

In ordinary pickling operations, it may be considered qualitatively that the dissolution takes place in the order of a, c$_1$, c$_2$, c$_3$ and c$_4$. In the case of relatively thick scales, the oxides dissolve in an acid solution according to the above reactions and descaling takes place [the equations above are reported from Tominaga, *et al.*, 1982]. The pressure of H_2 generated by reaction c$_1$ contributes to the mechanical peeling of scale.

Therefore, scale can be said to have a good pickling property when it has the following characteristics; a large fraction of FeO and little Fe_2O_3, many cracks, poor adhesion and a thin scale.

1.2.11.2 Mechanical Descaling

As mentioned earlier, appropriate scale removal is required prior to hot rolling of steels. In practice the complete removal of scale at the scale/substrate interface is impossible. A thin layer or some parts of the scale remain on the substrate surface. Descaling is important as unsuitable descaling sometimes causes surface defects and causes degradation of surface finish. At present, only three mechanical descaling processes are in use; Reverse Bend Process (RBP), Shot Blast Process (SBP) and Air Blast Process (ABP) [Tominaga, *et al*., 1982]. However, details of each these methods are out of the scope of this study.

Generally, for a good mechanical descaling a scale should have the following characteristics; a thick scale with a few cracks, the transformation to Fe_3O_4 does not take place, internal stresses are large and poor adhesion.

1.2.12 Summary

In summary, it has been shown that oxidation temperature, time, environment, alloying elements and oxidation conditions affect the nucleation, growth, kinetics, microstructure, mechanical properties and descal-ability of the oxide scale on steel. At the same time, emphasis on the factors that have only recently been measured, such as texture, leads to a review and the establishment of new principles regarding the oxide growth and descaling processes. It is thought that more research is needed in order to develop a mechanism for the complete characterisation of the oxide scales. This includes relating microstructure and microtexture with the mechanical properties of the oxide scale.

CHAPTER 1

PART 3   **Electron Backscatter Diffraction**

1.3.1 Introduction

Electron backscatter diffraction (EBSD) has been recognised as a powerful technique for studying the local crystallographic properties of a number of microstructures [Gourgues, *et al*., 2000 and 2002]. The development of the EBSD technique began in the early 1980s, allowing crystallographic data to be generated in a microstructural framework for bulk specimens [Randle, 1996]. The evolution of this technology has today become what is known as "Electron Backscatter Diffraction" or "Backscatter Kikuchi Diffraction" and is an add-on package to Scanning Electron Microscopy (SEM). The essential features of EBSD are its unique capabilities of diffraction to give crystallographic data and imaging in real time with spatial resolution of ~0.5 μm, combined with the regular capabilities of a SEM, such as capacity for large specimens, option of chemical analysis, and the abilities to image rough surfaces [Liu, *et al*., 1992].

Already EBSD is fulfilling its early promise to revolutionise texture analysis, and has generated a whole new area of science known as "microtexture" the conjoining of microstructure with crystallography, or texture analysis [Randle, 1989]. Closely allied to microtexture comes the capability to apply EBSD to phase identification, access interfacial (grain boundary) parameters and monitor plastic strain. EBSD has a wide range of applications for many materials. These applications arise from three types of information contained in Electron Backscatter Diffraction Patterns; orientation, misorientation, phase and strain identification [Dingley and Randle, 1992].

Full automation of EBSD in 1991 led to mapping of crystal orientations over entire sample surfaces and to new metallography, termed "Orientation Imaging Microscopy". It was this innovation that gave rise to the current rapid growth of the technique and its full commercialisation. The full history of electron diffraction patterns, however, begins with

the work of Kikuchi in 1928 on observation of electron diffraction through a thin mica crystal. This is the first recorded observation of convergent beam diffraction patterns and description of the technique that now quite properly carries his name [Dingley, 2000]. In this part the basic principles of theoretical and practical background of EBSD are reviewed.

1.3.2 Formation of Electron Backscatter Diffraction Patterns

When the beam in an electron microscope is directed onto a material, different scattering events give rise to a variety of signals, with part of the primary electron signal scattered [Loretto, 1994]. These backscatter electrons can be used for imaging purposes and crystallographic analysis of the sampled volume. The last named is achieved via evaluation of the diffraction patterns, which result when the primary electrons are diffracted by lattice planes in the sample volume of the specimen. In order to obtain sufficient intensity in the EBSD pattern, the specimen surface must make a small angle (~20°) with the electron beam [Randle, 2000].

The diffraction pattern is the fundamental vehicle of EBSD analysis. It is therefore pertinent to have some knowledge of how this pattern arises and how it is interpreted. Figure 1.3.1 shows the classical construction for diffraction from lattice planes. It is shown that the angle θ at which diffraction occurs depends on both the wavelength λ and the interplaner spacing of the scattering atoms d. To derive this dependency, diffraction of radiation at the individual atoms in a crystal can be considered to be reflection of radiation at a set of mirrors at a spacing d. These mirrors are formed by atomic planes, i.e., the lattice plane $\{hkl\}$. Figure 1.3.1 shows a section through a lattice with three atomic layers A, B and C with ray's incident upon these planes in the direction LM at the angle θ. A small portion of the incident radiation will be reflected at the angle 2θ at plane A, whereas the rest continues travelling into the lattice until it will be reflected at a layer further below the surface [Randle and Engler, 2003].

The line L-L2 is drawn perpendicular to the incident beam. In this example, the path difference between the two reflected beams L-M-N and L1-M_I-N_{1B}, i.e., the distance PM_1Q, is either one wavelength λ or a multiple of it. i.e., where n is the order of reflection

and n = 1 for the EBSD case [Dingley and Baba-Kishi, 1986]. The diffraction process may be conveniently visualized as reflection by (*hkl*) crystal planes spacing $d_{(hkl)}$. The diffracted beam corresponds to reflection for particular angles θ between the incident beam and the crystal plane for which

$$n\lambda = 2d \sin \theta \ldots\ldots\ldots\ldots\ldots\ldots\ldots\ldots\ldots\ldots(1.14)$$

Where *d* is the spacing of the (*hkl*) plane and λ is the wavelength. This law known as Bragg's law [William, *et al.*, 2001]. Bragg's law is fundamental for EBSD since for radiation of known wavelength, lattice planes can be identified from measurement of the Bragg angles through which the waves are diffracted. It is convenient to distinguish between the reflecting planes, written with parentheses {*hkl*}, and the corresponding reflected beam *hkl* written without parentheses [Randle, 2000]. For the bcc crystal structures *h+ k+ l* is odd. For fcc crystal structures, the individual Miller indices *h, k* and *l* of the reflecting planes are either all odd or all even [Randle, 2000].
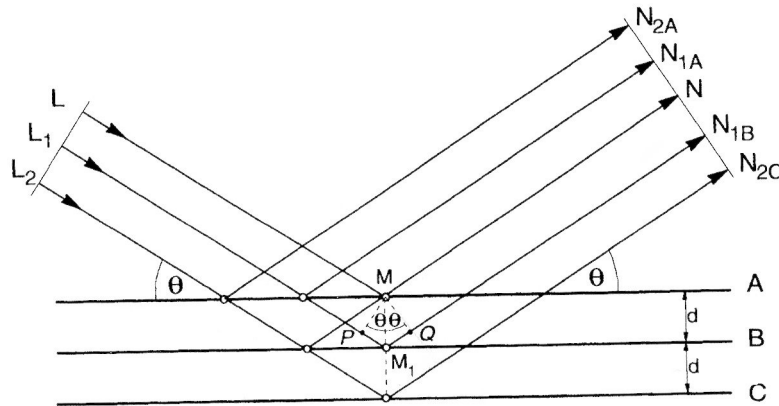
Figure 1.3.1 Diffraction from lattice planes, indicating the geometry that leads to the derivation of Bragg's law (Reproduced form Randle, 2000)

EBSD patterns are essentially Kikuchi patterns; they are formed in the SEM when a stationary probe is focused on the specimen. Initially the incident beam is scattered elastically through a large angle within the specimen; so that electrons diverge from a point source just below the specimen surface and impinge upon crystal planes in all directions

[Michael, 2000]. The subsequent elastic scattering of the divergent electrons by the crystal planes forms an array of Kikuchi cones whenever the Bragg condition is satisfied as illustrated in Figure 1.3.1. Inelastic scattering events also occur and these contribute to a diffuse background. There are two diffraction cones for each set of crystal planes, one from diffraction from the upper side and one from diffraction from the lower side of the planes. If the distribution of diffracted intensities is recorded by the interception of the Kikuchi cones by photographic film or a recording screen, the resulting EBSD patterns can be viewed [Dingley and Randle, 1992 and Humphreys, 2001].

1.3.3 Information Contained in the Electron Diffraction Pattern

In order to determine the structural information quantitatively, it is necessary to know how the structure of the specimen is defined. This involves some knowledge of crystallography. It is important to define some of the crystallographic terms in order to understand diffraction pattern acquisition and its analysis. For example, a crystal in general has a characteristic polyhedral shape, bounded by flat faces. A crystal consists of atoms arranged in a pattern that repeats periodically in three dimensions. An object or figure is said to have symmetry if some movement of the figure or operation on the figure leaves it in a position indistinguishable from its original position [Sand, 1969 and Steadman, 1982]. There are fourteen crystal lattice types in all; these are illustrated in Appendix 1.

The information about crystals can be obtained from diffraction patterns such as *d*- spacing, lattice planes, and lattice parameter [Michael, 2000]. If some prior knowledge of the elemental analysis of the material is available, it may possible to determine the exact structure of the unknown material. Frequently the composition of the material under examination is well known, and then the electron diffraction pattern can be used to determine the orientation in which the specimen is lying with respect to the incident electron beam. Clearly there is a large amount of information that can be extracted from specimens, if it is possible to determine *d*-spacings from available diffraction patterns [Dingley, 2000 and Flewitt, *et al.*, 1985]. Generally, as reported by Randle, 1992 and 2003, the following phenomena can be explored from EBSD electron diffraction patterns:

- Phase relationship and identification.

- Local property effects, exact crystallographic descriptions of crystal defects produced by deformation, irradiation.

- Morphological/geometrical grain parameter, .i.e., size, shape, location

- Orientation variation within individual grains

- Misorientation, i.e. grain boundary orientation.

- Microtexture correlation and direct ODF measurement

In this study EBSD diffraction patterns were used mainly to explore phase identification, grain size measurement, grain and phase boundary characterisation and microtexture correlations. Further investigation into misorientation using EBSD helped to understand the microstructural features within the scale.

1.3.4 Automated EBSD

There are two modes of operation for the EBSD system: manual and automatic. Manual functioning involves operator interaction with the system during data collection to select individual locations on the specimen from which orientation measurements are to be made. The manual mode only needs to be used for specialised investigation, for example those involving complex crystal structures. The automated EBSD mode permits a sampling location to be pre-programmed and located by either beam or stage control in the microscope. Early systems required an operator skilled in crystallography to manually identify features in a captured pattern in order to determine the corresponding orientation. The computer would then determine the orientation from manually supplied data. Modern automated systems use image-processing techniques to identify the features needed to determine the crystallographic orientation from diffraction patterns without any operator intervention [Rolland, *et al*., 2000]. If a representation of the orientation at each grid point is plotted, a crystallographic map of the microstructure is obtained. This is usually known as crystal orientation mapping or Orientation Imaging Microscopy (OIM) [Randle, 2000]. OIM as Randle, and Engler, 2003 stated, is a landmark innovation in the field of EBSD and microtexture because it links orientation directly to the microstructure. In other words the crystal orientation map portrays faithfully the orientation components, i.e. those concerned

with crystallography, of the microstructure in an analogous manner to the mapping of chemical elements in the microstructure via energy dispersive spectroscopy in the SEM.

1.3.4.1 Automated EBSD Data Acquisition

For orientation mapping, the pattern quality has to be good enough so that the diffraction lines can be found by the pattern processing software. Three parameters can be used to do this: the electron beam current, the camera gain, and the integration time. CCD (Charge-Coupled Device) cameras offer a very good combination of sensitivity and low noise. High gain of low noise can be obtained from low beam current and short integration times [Rolland, *et al*., 2000]. The bands in diffraction patterns represent planes in the crystal. Modern commercial systems attempt to determine the orientation based on the geometrical arrangement of bands in the diffraction patterns. The widths of bands are a function of the *d*-spacing of the corresponding crystallographic planes. In addition, the angles between bands in the patterns are directly related to the interplanar angles in the crystal lattice. Once the planes associated with a pair of bands have been identified, then the orientation of the crystal can be calculated [Wright, 2000].

At each point in an automated EBSD scan, several parameters are recorded; the orientation in terms of Euler Angles, an Image Quality (IQ) parameter describing the quality of the diffraction patterns, a confidence factor and a number identifying the phase for scans in multiphase materials. In addition, x-ray spectra can also be recorded [Randle and Engler, 2003]. The operator can also choose to save critical information on the patterns themselves. At each point in the scan the Hough transform is used to locate the bands in the diffraction patterns. The bands appear as peaks in the Hough transform. The location of the peaks describes the angle and position of the bands; the height of the peaks is a measure of the intensity of the bands and the width of the peaks is directly related to the width of the bands. This transformation is the minimum required to reconstruct and index a diffraction pattern. By collecting and recording this information, the user can perform the orientation determination off-line. Collecting the Hough peaks also makes the system more forgiving, for example, if an operator were to make mistakes configuring the material structure required for indexing the patterns, the scan could be re-analysed with the corrected material

structure without having to rescan the sample in the microscope [Wright, *et al.*, 2000].

1.3.4.2 Automated EBSD Data Interpretation

The most visually striking automated EBSD results are the images generated by mapping. Various parameters can be derived from the EBSD patterns onto a colour or grey scale map. Modern automatic EBSD systems have tools for colour-coding the orientation or image quality or other parameters derived from the diffraction patterns associated with each point in the scan to form colour images [Dingley, *et al.*, 2000]. These images provide a direct and quantitative visualisation of the spatial distribution, for example orientation in the sample. Grain boundaries can be overlaid on to these maps by comparing adjacent measurements on the scan grid. If the misorientation between two points exceeds some user-prescribed value, then a line segment is overlaid on the map indicating the presence of a grain boundary [Randle, 2004]. Discrete plots of individual orientations can be constructed as pole figures or in the standard stereographic triangle. Orientations and misorientations can also be plotted in various representations such as Euler angles, axis/angle pairs, or Rodrigues vectors [Wright, *et al.*, 2000]. Tools are generally available for analysing the statistical distribution of orientations and misorientations. These include tools for calculating the orientation distribution function (ODF) and misorientation distribution function (MDF) as well as capabilities for plotting these functions as appropriate. Here only microtexture and mesotexture representations are reviewed.

1.3.4.2.a Representations of Microtexture

1) Pole Figure (PF)

Preferred orientations are usually described by means of pole figures. These are simple stereographic projections, which show the distribution of particular crystallographic directions in the assembly of grains that constitute the material [Humphreys, 2001 and Dingley, *et al.*, 1986]. Thus, orientation can be plotted as two-dimensional projections in pole figures. Such figures can be useful for simplifying the analysis of the orientation distribution. A pole figure shows the position of a pole (a normal to lattice plane) relative to

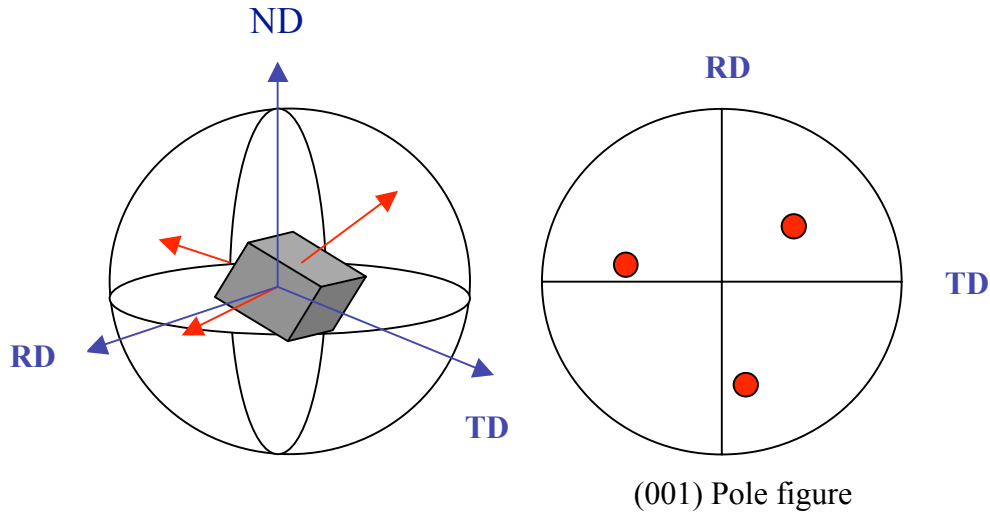the sample reference frame as shown in Figure 1.3.2.

Figure 1.3.2 General description of a pole figure

Stereographic projections plot the normal of crystallographic planes onto great circles, which serve as the representation of the pole. The angular distribution between the normal is determined by specific symmetry of the crystal system and the spatial arrangement between poles which will change depending on the geometry of the projection [Mckie and Mckie, 1986]. The intersection of crystallographic poles with the surface of the sphere is the basis of the stereographic projection method. The two dimensional projections directly map out angular relationships between projected normal and hence give a graphical representation of orientation relationship [Rajan, 2000].

Consider a sample with sheet geometry and cubic crystal symmetry as shown in Figure 1.3.2. With orientation data from ten grains, we can represent the orientations of all these grains together by plotting the position of their {100} poles on a single stereographic projection plane parallel to the sheet surface as shown in Figure 1.3.3. Since each grain has three {100} poles, there will be a total of $3 \times 10 = 30$ poles plotted on the projection. If the grains have a completely random orientation, these poles will be distributed uniformly over the projection. For a random orientation, there will be equal number of poles in each area on the surface of a reference sphere centred on the specimen. There will not be an equal

number, however, on equal areas of the pole figure, since equal areas on the reference sphere do not appear equal in the stereographic projection. Hence, there is an apparent clustering of poles at the centre of the pole figure for randomly oriented grains, since distances representing equal angles are much smaller in this central region than in other parts of the pole figure [Randle, 1992 and 2000].

If a preferred orientation does exist however, the poles will tend to cluster together into certain areas of the projection, leaving the other areas virtually unoccupied. For instance a {100} or cubic texture, arises if each grain is oriented with its (100) planes nearly parallel to the sheet surface and the [001] direction in these planes nearly parallel to the rolling direction, Figure 1.3.3. [Rajan, 2000].
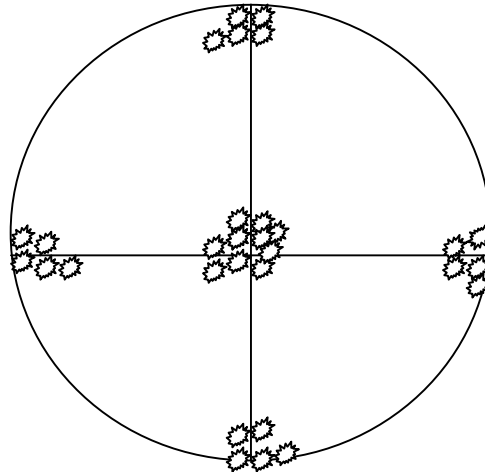
Figure 1.3.3 Schematic of (100) pole figure showing regions of stereographic projection with clustering around { 100} poles illustrative of cubic texture (Reproduced from Rajan, 2000).

In EBSD, the analysis of the geometry of the experimental diffraction patterns allows one to directly map texture onto a stereographic projection by simply monitoring and studying the statistics of the number of grains with a specific orientation.

2) Inverse Pole Figure (IPF)

As indicated by its name, the inverse pole figure is a sort of 'opposite' to the pole figure. While the pole figure shows how the specified crystallographic direction of grains are

distributed in the sample reference frame, the inverse pole figure shows how the selected direction in the sample reference frame is distributed in the reference frame of the crystal. For example, normal direction inverse pole figures show which crystallographic directions in the polycrystalline material are most likely to be parallel to the sample normal direction. Thus, rather than representing the orientation of the crystal coordinate system in the specimen coordinate system, i.e., in pole figure, the orientation of the specimen coordinate system can be projected into the crystal coordinate system in the inverse pole figure [Randle, 2003]. Since the properties of many important engineering materials are strongly direction-dependent, the inverse pole figure is very useful in predicting and calculating the average properties of polycrystalline material along a chosen direction [Dingley, *et al.*, 1986 and Rajan, 2000]. Due to the crystal symmetry, a complete inverse pole figure usually contains many areas where the same information is repeated. For example, there are 24 symmetric sections in an inverse pole figure for cubic system, as shown in Figure 1.3.4. Practically, only one section is used. Is should be noted that inverse pole figures are often used to display the microstructure from axial-symmetric specimen, i.e., only one direction in the specimen is significant [Randle, 2003].

A complete inverse pole figure   A partial inverse pole figure
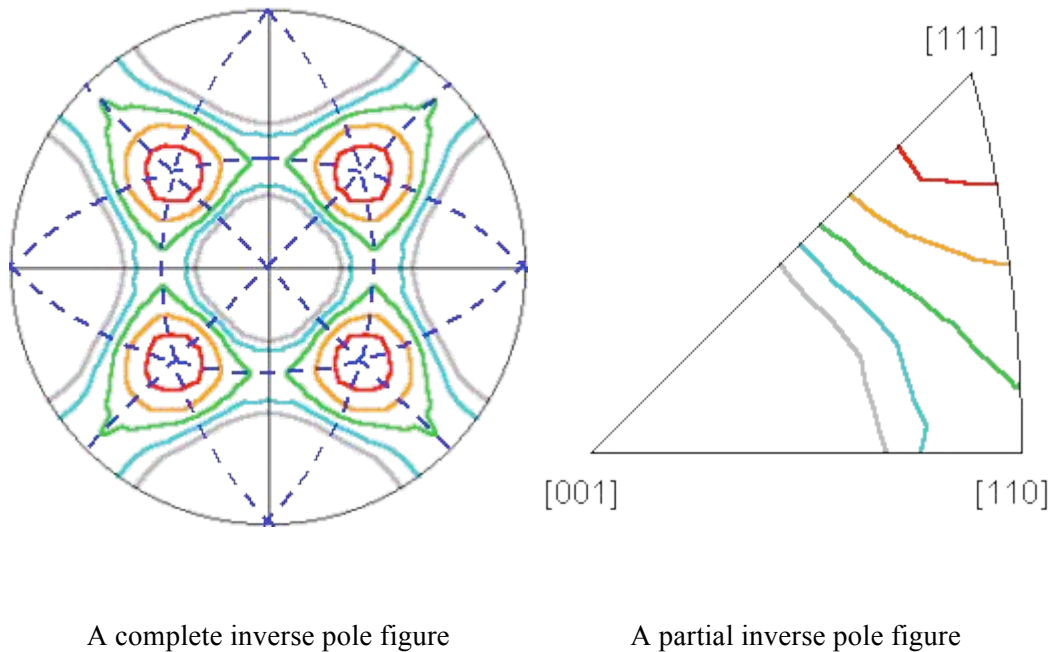
Figure 1.3.4 Partial and complete inverse pole figures as a texture description (ResMat, 2002)

3) Orientation Distribution Function (ODF)

The projection of the three-dimensional orientation distribution onto a two-dimensional pole figure causes a loss in information. So that in turn it is not possible to determine the orientation density of a polycrystalline sample, i.e. its texture, from the experimental pole figures without a certain ambiguity. Thus, for quantitative analysis of microtexture a three-dimensional description (e.g. in terms of the three-dimensional Orientation Distribution Function (ODF)) is required [Randle, and Engler, 2003]. However, unlike pole figures, ODFs cannot directly be measured by means of diffraction techniques, but need to be calculated from the pole figure data. As orientations are inherently three-dimensional, to plot a set of orientations requires a method of representing three dimensions in two [Humphreys, 2001]. This is done using two-dimensional sections through a three dimensional space. To facilitate the description of how this is done, crystallographic orientation can be represented by Euler angles [Bunge, 1986]. The space containing all possible orientations defined as Euler angles is Euler space. The space can be therefore thought of as a bounded rectangular volume. The three axes of the rectangular volume are the three Euler angles [Vainshtein, 1964]. A schematic is shown in Figure 1.3.5 along with sections through the space, in this example the constant angle sections are those along (φ_1).
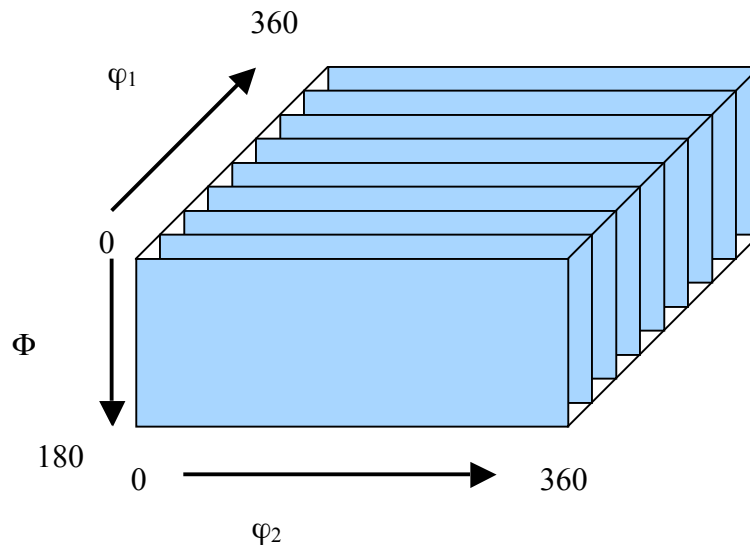
Figure 1.3.5 Orientation representation by plot sections

ODFs permit the calculation of the texture from a limited set of pole figures. The extent of the calculations and the accuracy of the ODFs will vary depending upon the material and its crystal symmetry [Dingley and Randle, 1992]. It should be noted that Euler space is a three dimensional format for representing three dimensional orientation information unlike stereographic projections which are two dimensional in nature and in the process lose some orientational sensitivity. An example of an orientation distribution function is shown in Figure 1.3.6.
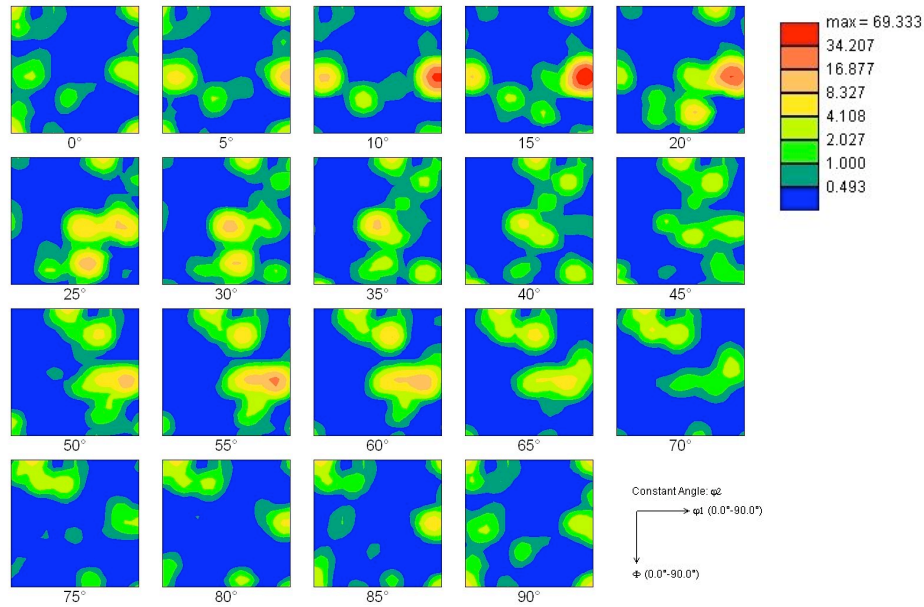
Figure 1.3.6 Orientation Distribution Function (ODF)

1.3.4.2. b Misorientation

An important consequence of measuring orientation using EBSD is that the orientation between crystals can be accessed, in other words, the grain or phase boundaries can be investigated if the orientations on either side of the interface are known [Randle, 1993]. Once a boundary is detected in an EBSD map, the angular relationship between the crystals associated with the boundary is readily calculated because the orientations of the crystals are known. This relationship is commonly expressed in term of angle-axis pairs [Dingley, *et al.*, 1992]. The angle-axis pair defines the angle by which one of the crystals must be rotated about a particular axis so as to bring it into register with the other crystal. It should

be recognised that lattice misorientation and not just lattice orientation is a key metric in describing crystallographic characteristics of a microstructure [Randle, 2003].

The relative orientation between two frames is referred to as microtexture and the relative misorientation between the two lattice frames is referred to as mestexture. The data output from EBSD also includes an axis-angle of misorientation representation [Randle and Brown, 1989 and Rajan, 2000]. Thus, complete misorientation and orientation descriptions can be represented in EBSD.

1.3.5 Summary

In this part of literature review, the basic theoretical and practical EBSD background has reviewed. EBSD is extensively used in this project to investigate the role of oxidation parameters on the microstructural and microtextural development of steels. Many aspects of oxide scale characterisation such as phase identification, grain size and shape measurement, microtexture and mesotexture analyses have relied essentially on EBSD.

More EBSD microstructure and microtexture investigation of specimen are reported and discussed throughout this study. In the light of available literature and the results obtained from this study, the EBSD operation, data acquisitions and analysis, its applications and reliability are discussed further in the following Chapters.

CHAPTER 2   **Experimental Procedure**

The oxidation experiments were carried out on three different grades of steel. All the samples were oxidised under the same oxidation conditions. The sample preparation, oxide scale characterisation, microstructure/microtexture investigations and mechanical property determination, were carried out for all the samples, using the characterisation techniques and analyses as described in this Chapter.

2.1 Materials

Three different grades of steel were used; Interstitial Free (IF) steel, also called Ultra Low Carbon Steel (ULCS) [Caul, *et al*., 1997], which contains very low carbon and other alloying elements as shown in Table 2.1. Also for comparison purposes, two low carbon steels, Alloys A and B were used. Alloy B contained higher C, Si and other alloying elements than Alloy A, except aluminium. The IF steel was received as a hot rolled plate and Alloys A and B as cold drawn and annealed tube. The composition of steels used in this study is shown in Table 2.1.

Table 2.1 Composition of the steels used (wt%)

Sample	C	Si	Mn	P	S	Cr	Mo	Ni	Al	Cu	Sn	V	N
IF Steel	0.0026	0.004	0.004	0.156	0.009	-	-	-	0.05	-	-	-	-
Alloy A	0.10	0.10	0.34	0.005	0.002	0.05	0.01	0.05	0.028	0.08	0.010	0.001	0.007
Alloy B	0.17	0.24	0.63	0.009	0.003	0.14	0.55	0.06	0.008	0.11	0.012	0.001	0.007

2.2 Sample Preparation

In this study, standard metallographic sample preparation was followed for the steel substrate and oxide scale. Samples of the plate 0.8×0.8×0.5 cm were cut using standard techniques and the large surface ground to a final finish of 1200 grit. The samples were oxidised in a furnace at different temperatures, for different times of exposures. A thermocouple was used to determine the exact substrate temperature. Following the removal of the sample from the furnace, visual observations were recorded and a piece of aluminium sheet was adhered to the surface using a

conducting medium, to retain the oxide in position on the substrate surface, see Figure 2.1 (a). The samples were then cooled to room temperature in laboratory air. The optimum method of sample preparation involved mounting the samples in a small aluminium cup in Woods Metal which has a melting temperature of ~80°C [Higginson, *et al*., 2002]. This method minimized any damage to the scale, and gives a completely conductive medium eliminating any charging problems in the electron microscope; see Figure 2.1 (b). The sample assemblies were ground on silica carbide paper finishing with 1200 grit, followed by polishing using 6 and 1µm diamond paste. Quantitative optical metallography was carried out on samples, after etching with 1% HCl in ethanol or 2% Nital, depending on the oxide scale reaction with different etchants. Prior to examination in the SEM, final polishing was carried out using colloidal silica, for a minimum of 15 - 20 minutes just prior to insertion into the microscope.

(a)   (b)
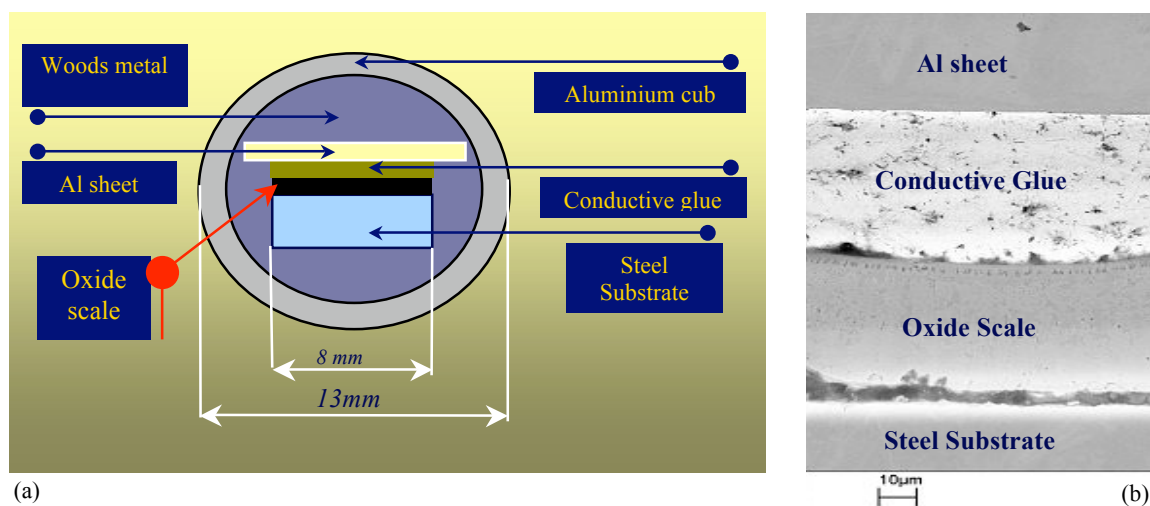
Figure 2.1: (a) A schematic illustration showing sample preparation, (b) An SEM image showing an example of the sample preparation methodology in (a).

One of the major problems was to eliminate the artefacts generated during sample preparation. Due to the brittleness of oxide scale, especially the magnetite layer, grinding the sample caused magnetite grain extraction (pull out) within the scale. Figure 2.2 shows the steps of the sample preparation regarding grinding and polishing methods. Figure 2.2 (a) shows the sample as ground on 1200 grit paper, and then slightly etched with 1% HCl in ethanol. The scale is affected by the grinding which makes the study of the oxide microstructure very difficult. Polishing the sample on 6 µm diamond paste decreases the damage caused by grinding, see Figure 2.2 (b). The artefacts generated during grinding decreased after polishing the sample on

1μm diamond paste especially after 15 minutes of polishing, but there were polishing direction problems when the outermost layer of the oxide scale was affected by the polishing direction, see Figure 2.2 (c) and (d). The longer polishing time on 1μm diamond paste caused distortion of the oxide scale outer layer, which makes it difficult to maintain the exact shape of the oxide, as it had been before polishing. Thus, polishing for more than 20 minutes on 1μm diamond paste had the advantage of decreasing the artefacts generated during grinding, but also the disadvantage of distorting the oxide scale shape. Using 0.5 μm colloidal silica had the advantage of overcoming the oxide distortion problems, but it increased the artefacts within the scale, as shown in Figure 2.2 (e), which made measuring the porosity for the oxide scale inaccurate. Etching the sample in 1% HCl in ethanol, even for 20 seconds, could not reveal the grain boundaries in the oxide scale especially in the magnetite layer, but could discriminate the phases more than with polishing only, see Figure 2.2 (f).

During specimen preparation, care was taken, in order to keep the entire oxide scale on the steel surface, without losing any part or layer of the oxide scale. The scale could be damaged during oxidation procedure, cooling or sample preparation. The oxide scales were susceptible to cracking during cooling, and mechanical damages during sample preparation. Furthermore, most of the scales were not adherent to the steel substrates and suffered from spallation. To retain the complete scale and minimise scale damages, maximum care was taken during sample preparation. Furthermore, to overcome the oxide spallation problem the aluminium-supporting sheet was used as described earlier in this section. For repeatability purposes, two samples were prepared for each oxidation temperature and time of exposure. It should be noted that at some temperatures, the oxide scales were very thin, not adherent, made a large blister or spalled from the substrate surfaces but could be retained entirely on the surface. However, some of those samples were used only for optical microscope examinations to calculate the oxide scale thicknesses, these were complete in some small areas on the substrates, but could not be used for further investigations, such as EBSD characterisation.
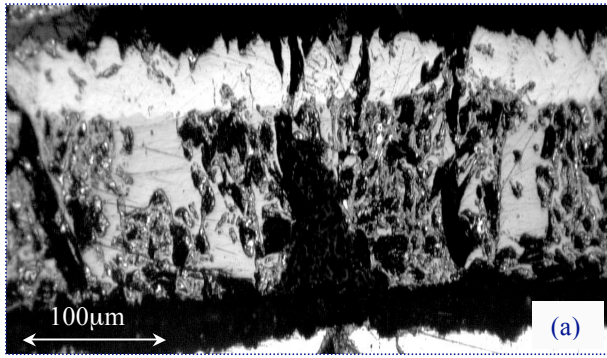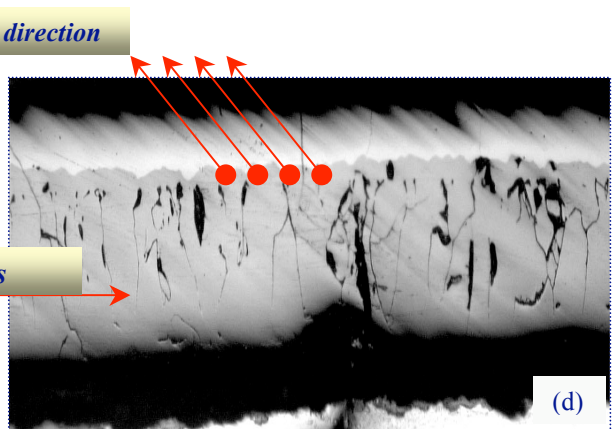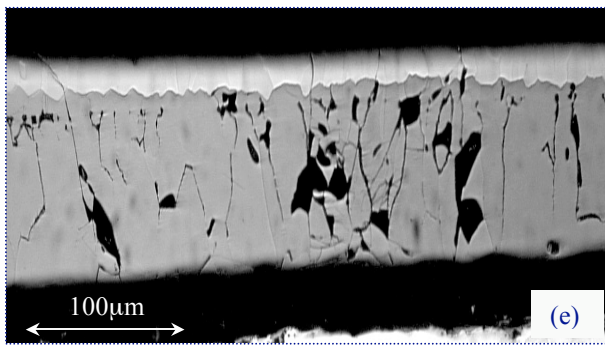
(a) As ground on 1200 grits.   *(b) After 3 minutes polishing with 6µ.m diamond paste*
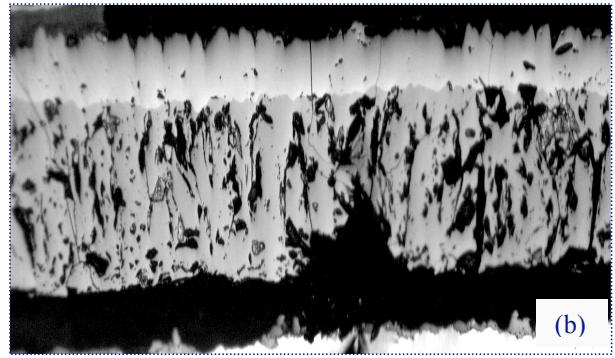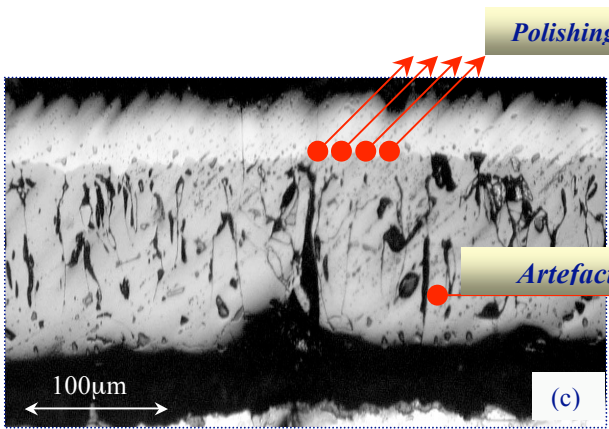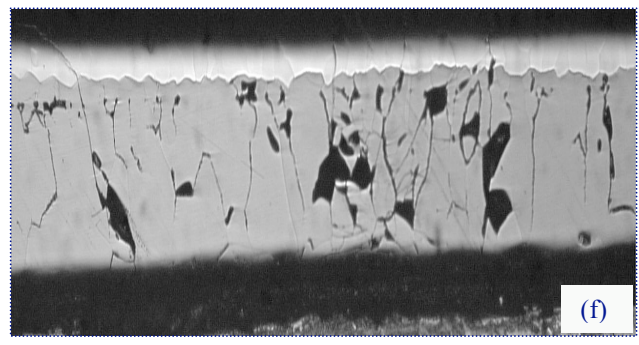
(c) After 5 minutes polishing with 1µ.m diamond paste *(d) After 15 minutes polishing with 1µ.m diamond paste*

(e) After 10 minutes polishing with 0.5 µm colloidal   *(f) After 20 seconds etching with1%HCl in ethanol*

Figure 2.2: Oxide scale formed on Alloy A at 1100°C-3600 seconds.

2.3 Oxidation Conditions

The oxidation conditions were the same for all the types of steel used in this study. The samples oxidised in air at 650, 750, 900, 1000 and 1100°C for 600, 1200, 1800, 3600 seconds, in a standard furnace, using a thermocouple to monitor the exact temperature. The average difference between the furnace's reading temperature and the thermocouple, was ~ 3 ± 2°C. To simulate the actual oxide scale growth on steel substrates during steel manufacturing in industry, the samples were oxidised only in laboratory air without changing oxygen pressure. Following the removal from the furnace, the samples were cooled in laboratory air. The cooling rate for the samples was between 8 to 10°C/second, depending on the oxidation temperature. The samples were prepared and mounted immediately to avoid any damage to the scales. Subsequently, the samples were prepared for optical, scanning electron microscopy and EBSD investigations.

2.4 Characterisation Techniques

Various characterisation and observation techniques were used in this project, in order to obtain detailed microstructure features of the oxide scale. As mentioned in Section 2.2, different techniques required different sample preparation. Certain microstructural details could be obtained from each of the techniques used throughout this study, as cited later in this section. Mainly optical and scanning electron microscopies including EBSD were used for oxide scale microstructure characterisation. The mechanical property consideration of the oxide scale relied on micro-hardness measurements. Each of these techniques and their utilising aims are discussed in the following sections.

2.4.1 Optical Microscopy

Due to the resolution limitations, the optical microscopy was not capable of exposing detailed microstructural features within the oxide scales at very high magnifications. However, optical microscopy was extensively used in this project for morphology observation, oxide scale thickness measurement, crack investigation, substrate and oxide scale adherency and blister considerations. Phase identification and the ratio of oxide scale layers have also been considered, and compared with the results obtained by other techniques. Following sample preparation, all

the samples were examined by optical microscopy before being investigated by other techniques. For comparison purposes, the optical micrographs were taken of the exact EBSD scanning areas. Images were taken using a digital camera attached to a Reichert MEF-3 Microscope. A Kohler illumination system was used to produce a uniformly illuminated field of view, from a small intense light source to optimise the illumination for best resolution and visibility.

2.4.2 Scanning Electron Microscopy (SEM)

Following the optical microscopy observations, the samples were investigated using Scanning Electron Microscopy (SEM). The high resolution capability in SEM allowed further detailed morphology and microstructure observations of the oxide scale such as; magnetite precipitates shape and size, phase ID, grain boundary and porosity considerations. The sample preparation for SEM was the same as for optical microscopy. The SEM used was a Leo 1530 VP field emission gun (FEG) SEM, with an EDAX system, comprising Energy Dispersive Spectroscopy (EDS), also equipped with an ultra-thin window and Electron Backscatter Diffraction (EBSD) system. The operating voltage and working distance were varied. The backscattered, secondary electron and Inlens detectors were used depending on the microstructural feature imaged.

2.4.3 Electron Backscatter Diffraction (EBSD)

The Leo 1530VP FEGSEM is equipped with a TSL-EBSD system as well as Orientation Imaging Microscopy-Data Collection and Analysis (OIM DC and analysis) packages. The software allows simultaneous EDS data to be collected during the EBSD scans. EBSD was extensively used in this work for grain size measurement, phase identification, phase ratio calculation, grain boundary characterisation, cracks and microstructure consideration, microtexture and misorientation analysis of the oxide scale layers and their correlations.

As described in Section 2.2, prior to the EBSD scan, final polishing was carried out using colloidal silica, for a minimum of 15 - 20 minutes without etching. The sample was tilted to 70° in the SEM sample chamber, the diffraction pattern was averaged and the background corrected and then digitised into the computer memory where it was automatically or manually indexed. The operating voltage used was 20 kV to obtain optimum quality of diffraction patterns.

Working distances were varied from 15 to 18 mm. The scanning step size was varied between 0.05 to 0.1 μm depending on the grain size.

The data were analysed by Orientation Imaging Microscopy (OIM analysis), to obtain crystallographic information, microstructure and microtexture information. Prior to data analysis, some data were excluded from OIM analysis through clean up or partitioning data, and cropping the maps. Various maps and charts can be produced from OIM analysis such as Image Quality (IQ), grain size-shape, grain boundary angle, orientation, misorientation, phase and EDS maps. Moreover, the microtexture is represented in the Pole Figure (PF) and Orientation Distribution Function (ODF). Due to the limitation of space, selected maps and charts among large numbers of OIM maps/charts are shown in Chapter 3.

2.4.4 Energy Dispersive Spectroscopy (EDS)

The software provided by the EDAX Phoenix system was equipped with X-ray mapping capability. The software was capable of collecting EDS chemical composition data simultaneously, with the usual OIM orientation data. The OIM software collects the counts from the spectrometer, for a given region of interest. The elements to be mapped can be selected from the periodic table.

2.4.5 Micro-Hardness Testing

An automatic digital Buehler Vickers Microhardness Testing machine was used to determine the hardness of the phases within the oxide scale layers and the steel substrate. The samples were etched before microhardness indentation, to reveal the phases within the scale and steel substrate. The machine was calibrated before the tests, and then the standard hardness procedure was followed. The loading time was 10 - 15 seconds. Various loads were used depending on the scale layer thickness and the grain size. A load of 100 g was used for the steel substrate, and 10 - 25 g for the oxide scale layers. A difficulty arose when there was a high magnetite precipitate concentration within the wüstite layer in some areas. This made it difficult to obtain an accurate reading in the wüstite layer. Following microhardness indentation, an EBSD scan was carried out for some samples to investigate any orientation-mechanical property correlations.

2.5 Quantitative Measurements

The oxide scale thickness and the grain size of the steel substrate and oxide scale layers were measured using different methods including; linear intercept, image analysis software and EBSD grain size calculations. As a double check, the results from all those methods were compared. The grain size and oxide thickness data reported in this study are mainly obtained from linear intercept calculations, and the rest of the measurements from Image analysis and EBSD used as a double check only.

2.5.1: Linear Intercept

The linear intercept method was used to determine the grain size and oxide thickness, full details about the linear interception method can be found in Higginson and Sellars, 2003. The microstructure images had been taken on the optical microscope using a digital camera and printed on A4 paper. Lines were drawn on the print in the rolling direction (RD), and in the short transverse direction (STD) for measuring grain size. The boundaries were marked and counted where they crossed each traverse line. The linear intercept grain sizes are obtained from the count in the RD and STD as:

$$\bar{L} = \frac{\sum L}{M \times \sum x}$$ …………………………………………………………………………...2.1

Where M is magnification and $\sum L$ is the total length of the *n* traverses. $\sum x$ is a sum of the number of counted grain boundaries. The standard error estimated from Equation 2.2 as

$$S(\bar{L}) = \frac{0.65}{\sqrt{\sum x}} \times \bar{L}$$ ……………………………………………………………………2.2

"The mean linear intercept, $\bar{L}$ is the average distance between grain boundaries along lines placed at random on micrographs. In practice, when grains are not equiaxed, it is preferable to measure along straight lines oriented in the three principle direction to obtain $\bar{L}_1$, $\bar{L}_2$ and $\bar{L}_3$, from which the mean linear intercept, $\bar{L}$ can be determined, and additional microstructural parameters

can be derived" [Higginson and Sellars, 2003]. In general, plane strain deformation $\overline{L}_2$ remains

constant and is equal to $\overline{L}$, hence the overall mean linear intercept for the structure is defined as

$$\overline{L} = (\overline{L}_1 \overline{L}_3)^{1/2}$$ ……………………………………………………………...2.3

The mean aspect ratio (e.g. for ferrite grain size) is determined using Equation 2.4:

$$\overline{r} = \frac{\overline{L}_1}{\overline{L}_3}$$ …………………………………………………………………….2.4

The pearlite colony size was also measured; the numbers of boundaries were counted per unit
length along the same traverse lines. The method requires a separate count of the number of
ferrite/pearlite boundaries, $n_{p(i)}$, and the number of ferrite/ferrite grain boundaries, $n_{\alpha(i)}$, to be
made along each of the traverses. The number of pearlite colonies per unit length on each
traverse is

$$N_{p(i)} = \frac{n_{p(i)}}{2P_{p(i)} \times L}$$ …………………………………………………………………….2.5

where L is the length of each traverse. The mean pearlite colony size is calculated using
Equation 2.6:

$$\overline{L}_p = \frac{1}{\overline{N}_p}$$ ……………………………………………………………………….2.6

In a similar way, the ferrite grain size is obtained from the number of ferrite grain boundaries
$n_{\alpha(i)}$, and the number of pearlite colony boundaries $n_{p(i)}$, on each traverse, and the line fraction
occupied by ferrite, i.e., $(1 - P_{p(i)})$ as:

$$N_{\alpha(i)} = \frac{(n_{\alpha(i)} + \frac{1}{2}n_{p(i)})}{(1 - P_{p(i)}) \times L}$$ …………………………………………………………………….2.7

Thus, the mean ferrite grain size is calculated using Equation 2.8

$$\bar{L}_\alpha = \frac{1}{\bar{N}_\alpha}$$ ……………………………………………………………………..2.8

The mean and standard deviations were calculated using Equations 2.9 and 2.10 respectively:

$$\bar{x} = \frac{\sum x}{n}$$ ………………………………………………………………………2.9

$$S^2 = \frac{\sum(x - \bar{x})^2}{n - 1}$$ …………………………………………………………2.10

The standard error is simply related to the standard deviation of the individual measurements such that

$$S(\bar{x}) = \frac{s}{\sqrt{n}}$$ ……………………………………………………………………2.11

Where $\bar{x}$ is the mean with standard deviation s, n is the number of observations is taken from a population. The "c" percent confidence interval is typically 95%. The confidence interval is then given by:

$$\bar{x} \pm t_c \frac{s}{\sqrt{n}}$$ …………………………………………………………………....2.12

t_c varies with the number of degrees of freedom, the value of t_c can be obtained in look-up tables (Can be found in Higginson and Sellars, 2003), such that a = 0.025 and v is given by:

$$v = n - 1$$…………………………………………………………………………..2.13

Measuring the oxide scale thickness was relatively easier than grain size. The lines were drawn on the A4 print paper on the Rolling Direction (RD) only, which represents the Growth Direction (GD). More lines were drawn where the oxide scale was not uniform. The average, standard deviation and errors of the oxide scale thickness, were calculated using Equations 2.9 - 2.13.

In addition to the statistical uncertainties, there are a number of potential sources of systematic errors, which can arise from the preparation of the specimen or observation area, or from the metallographic technique, care was taken to avoid them where possible.

2.5.2 Image Analysis

A commercial Image Analysis (Image-Pro Plus version 5.0) software package was used for some analysis, including measuring the grain size of the steel substrate and the oxide scale and colony volume fraction. Figure 2.3 shows an example of using the image analysis software for grain size and volume fraction determinations. As can be seen from the figure, the software could perfectly differentiate the pearlite colonies from ferrite grains, also the grain boundaries were excluded from the grain size and volume fraction calculations.

Generally, the image analysis tool was used for the linear intercept method and EBSD calculation confirmations. The results from all the methods were very similar. Therefore, the tables and graphs produced by the image analysis tool are not shown in Chapter 3 because of space considerations.
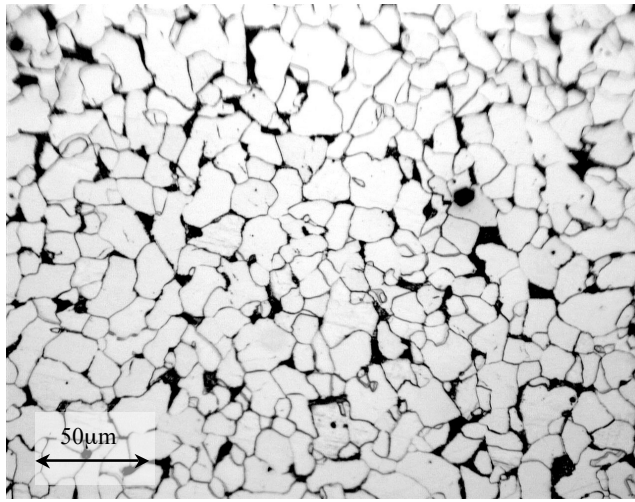
a) Optical microscopy image
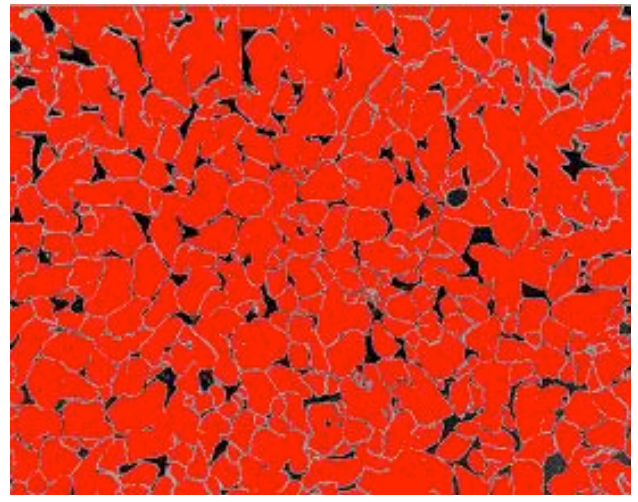
b) Ferrite grain size measurement (red area)
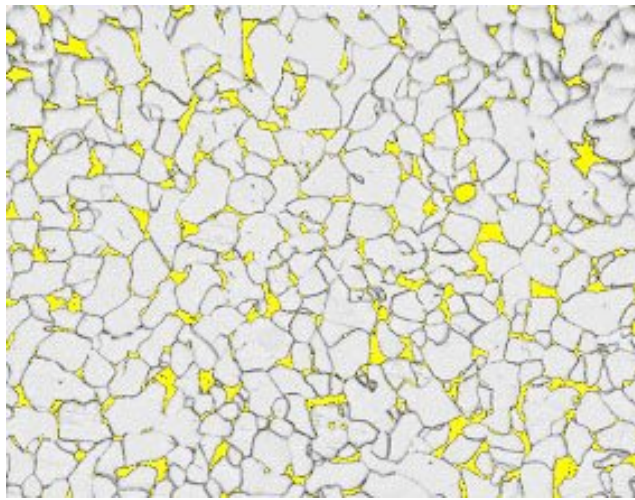
c) Carbide volume fraction measurement (yellow area)
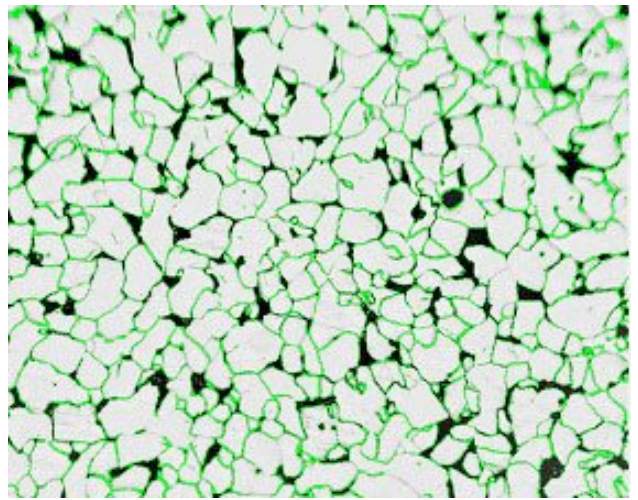
d) The grain boundaries excluded from carbide volume fraction measurements (green lines)

Figure 2.3: An example of ferrite grain size and pearlite volume fraction measurements using Image Analysis software as a double check of the linear intercept hand calculation.

CHAPTER 3   Experimental Results

In this chapter, the results obtained from the present experiments are reported. The results are presented in separate sections, each form a particular investigation and for individual oxidation aspect consideration. Some results relate to specific experiments which were carried out for reproducibility purposes, others for the determination of differences between the characterisation techniques used in this project. In addition to the general results collected from the major experiments, the conclusive results are illustrated in Figures and Tables shown in each section.

3.1 Oxidation Rate and Kinetics

Oxidation rate is expressed as the increase in oxide scale thickness with time. It is believed that the thickness measurement of the oxide scale would give more accurate results than the other methods, such as weight loss or weight gain. As mentioned in Section 2.3, the oxidation of steel was carried out at different temperatures for increasing times of exposure. The measurement of the oxide scale thickness for each sample was carried out using optical microscopy, followed by quantitative measurements of the mean oxide scale thickness and its standard error. Also comparisons were made with the images taken by SEM and EBSD to show the accuracy from one technique to another. Two images were taken of each sample to measure the thickness quantitatively and to allow more accurate standard errors to be calculated.

The oxide scale thicknesses on IF steel, Alloys A and B at different times and temperatures are shown in Appendixes 2, 3 and 4, respectively and the same results are plotted in Figures 3.1.1, 3.1.2 and 3.1.3. Appendix 2 shows the oxide scale thicknesses on IF steel. As expected there is an increase in the oxide thickness with increasing time at temperature. From Figure 3.1.1, the oxidation rate has been observed as follow; at temperature of 650°C it was difficult to know what kind of oxidation rate was followed, however, the oxidation rate tends to be more parabolic than linear or cubic (for comparison purposes see also Figure 1.2.3). At 750°C the thickness reaches a maximum value of ~ 47µm after ~ 600 seconds after which there is little further growth of the scale layer. At 900°C the growth of the oxide layer begins to slow after ~ 1800 seconds

although there is still some growth until 3600 seconds. At other temperatures, the same trend can be seen as shown in Figure 3.1.1. Thus, the results seem to indicate that the oxide scale grown on IF steel develops in a parabolic manner at all temperatures.

The oxide scale thicknesses of Alloy A are less than on the IF steel at 650, 750 and 900°C, but greater in thicknesses at 1000 and 1100°C as shown in Figure 3.1.2 and Appendix 3. The oxide thickening reaches a maximum oxidation rate for all temperatures at 1800 seconds of exposure, except 650°C where it is difficult to say where the maximum oxidation rate is. As shown in Figure 3.1.2, the oxidation kinetic seems to be parabolic at all temperatures. At 650°C, the oxidation rate is very doubtful, however, the data was first considered to be linear, but the data did not fit in with linear rate equation. The results show that even at 650°C the oxidation rate tends to be more parabolic than linear. In fact, at 650°C the oxidation rate is very controversial in the literature as to whether it is linear or parabolic. At the rest of the temperatures, the parabolic equation rate fits with the parabolic kinetics equation as shown in Figure 3.1.2. Furthermore, data at 1100°C was difficult to fit with the parabolic equation.

The oxide thicknesses of Alloy B are less than those on the IF steel and Alloy A samples at all temperatures, as can be seen in Appendix 4. Figure 3.1.3 shows a graph of oxide thicknesses versus time. At 900, 1000, 1100°C, the thicknesses of the scale reach a maximum value after 1800 seconds after which there is a further growth of the scale layers. As shown in the Figure 3.1.3, it is very difficult to know whether the oxidation kinetics at 650 and 750°C are parabolic or linear, or where the oxidation rate reaches its maximum values. However, the data better fitted the parabolic rate equation than others at these temperatures. Thus, at all temperatures the oxidation rate tends to be parabolic. From the same Figure, the oxide thickness increased dramatically with time at 1100°C, whereas at 650 and 750°C the oxide thicknesses are very low compared with IF steel and Alloy A.

The parabolic rate constants for oxidation of steels used in this study are shown in Tables 3.1.1 - 3.1.3. The rate constants are determined from the slope of each line in the graphs, in which the oxide thickness square is plotted against time. The parabolic rate constant determined in term of (m^2/s) unit. The unit of $(g^2cm^{-4}sec^{-1})$ has to be avoided because of

two reasons. First; the conversion factors (α) of K_p (g^2 cm^{-4} sec $^{-1}$) = α K_x (cm^{-2} sec^{-1}) is different in the literature and is also dependent on temperature. For example, O'Neill gave a factor of 1.636, Sheasby derived a factor α = 1.877 and Brown and Assefpour found α to be 1.77 [Chen, *et al.*, 2002]. This controversy in the different values of α can therefore cause more errors in the oxidation rate calculations. Secondly various conversion factors have been proposed in the literature, based on the assumption that the average scale densities are 5.67 $g.cm^{-3}$ for wüstite, 5.18 for magnetite and 5.24 for haematite. Furthermore, the scale layers thickness ratios is assumed to be exactly 95:4:1 of wüstite: magnetite: haematite. In fact the conversion factor should vary from temperature to temperature as the ratio between the oxide sale layers changes. This is especially true of wüstite as its density is not constant as can be seen from iron-oxygen diagram (Figure 1.1.2). Thus, different oxide phase ratios at different times and temperatures make using these kinds of conversion factors not always suitable for oxidation rate calculations.

As shown in Tables 3.1.1 – 3.1.3, the parabolic rate constants are very low at 650, 750, 900 and 1000°C for Alloy B, compared with IF and Alloy A steels. Moreover, the largest parabolic rate constant is for IF steel at all temperatures compared to the other alloys.

At constant ambient oxygen pressure the oxidation rate depends on temperature, which obeys an Arrhenius equation;

$$K = K_o \exp (-Q/RT)\ldots\ldots\ldots\ldots\ldots\ldots\ldots. 3.1$$

where; Q is the activation energy (J/mole), R is the gas constant (8.3144 J/mole. K) and T is the absolute temperature (K).

From the equation above, the activation energy Q is determined by plotting ln K_p as a function of 1/T as suggested by Caplan, *et al.*, 1981, Kofstad, 1966 and Chen, *et al.*, 2002. Arrhenius plots for the experimental data are shown in Figures 3.1.4 – 3.1.6. As expected the activation energy for IF steel has the highest value (-145 KJ/mol), while Alloy B has the lowest value (-214.178 KJ/mole). This indicates that the highest

thickening of the oxide scale can be found in IF steel. There is a big difference in the oxidation rates of Alloy A and B up to 1000°C, but at 1100°C the differences decrease. The oxidation rate of Alloy B is very low until 1000°C then is followed by dramatic increase. This caused the activation energy similar to Alloy A, however, is still lower value than for Alloy A.

Table 3.1.1: Parabolic rate constant at different temperatures, IF steel.

Temperature (°C)	K_p (m^2/s)
650	8×10^{-14}
750	1×10^{-12}
900	1×10^{-11}
1000	2×10^{-11}
1100	4×10^{-11}

Table 3.1. 2: Parabolic rate constant at different temperatures, Alloy A.

Temperature (°C)	K_p (m^2/s)
650	1×10^{-14}
750	2×10^{-13}
900	5×10^{-12}
1000	4×10^{-11}
1100	7×10^{-11}

Table 3.1.3: Parabolic rate constant at different temperatures, Alloy B.

Temperature (°C)	K_p (m^2/s)
650	6×10^{-15}
750	1×10^{-14}
900	2×10^{-12}
1000	3×10^{-12}
1100	4×10^{-11}
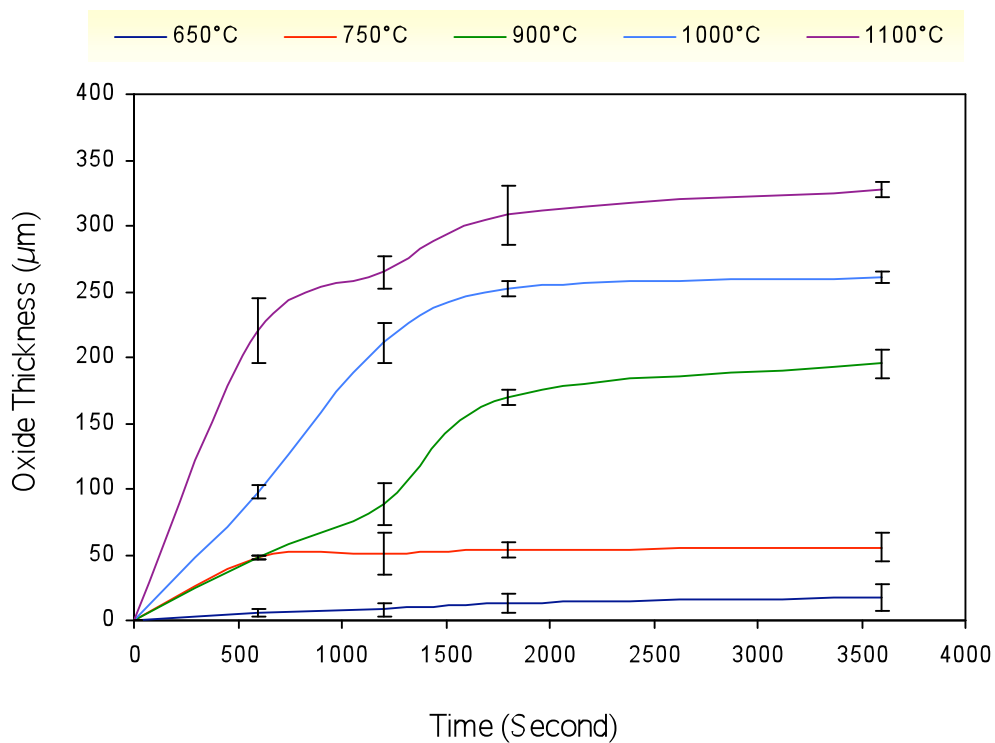
Figure 3.1.1: Oxide thickness vs. time at different temperatures, IF steel.
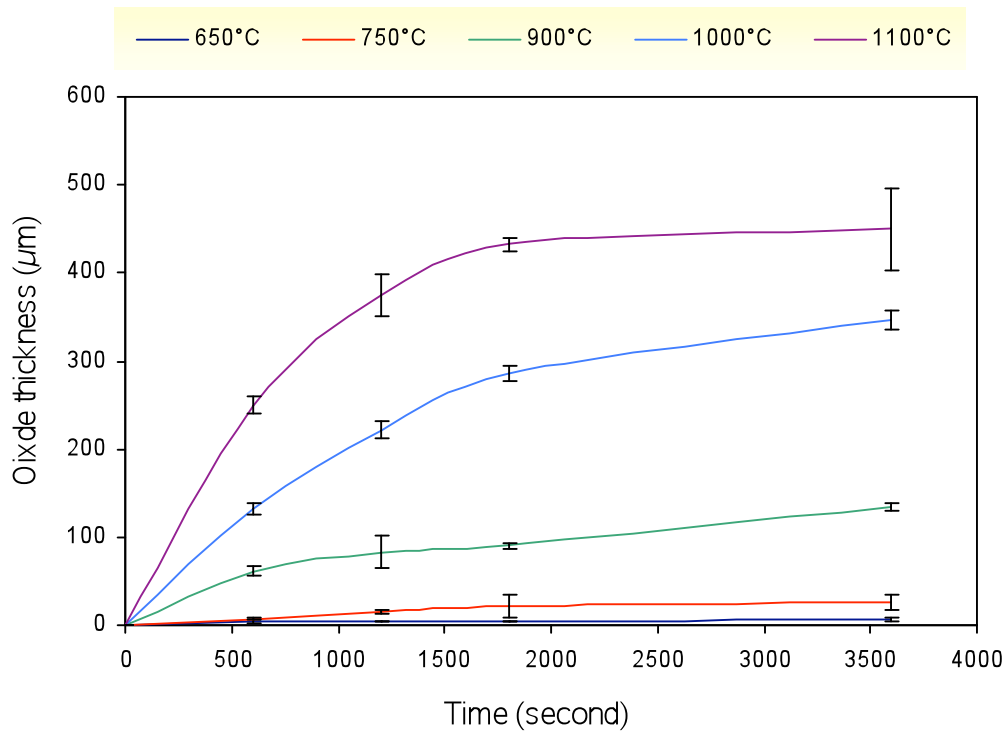
Figure 3.1.2: Oxide thickness vs. time at different temperatures, Alloy A.
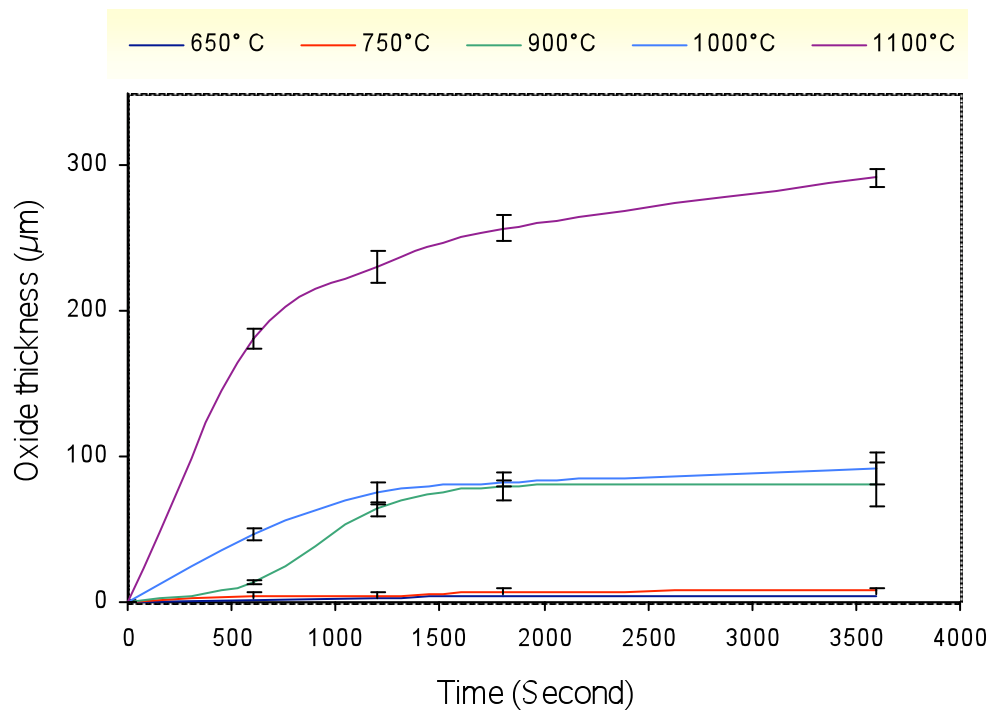
Figure 3.1.3: Oxide thickness vs. time at different temperatures, Alloy B.

$$\ln k_p = -17440 \, 1/T - 10.896$$
$$K_p = 1.85E-5 \exp(-145,003/RT)$$
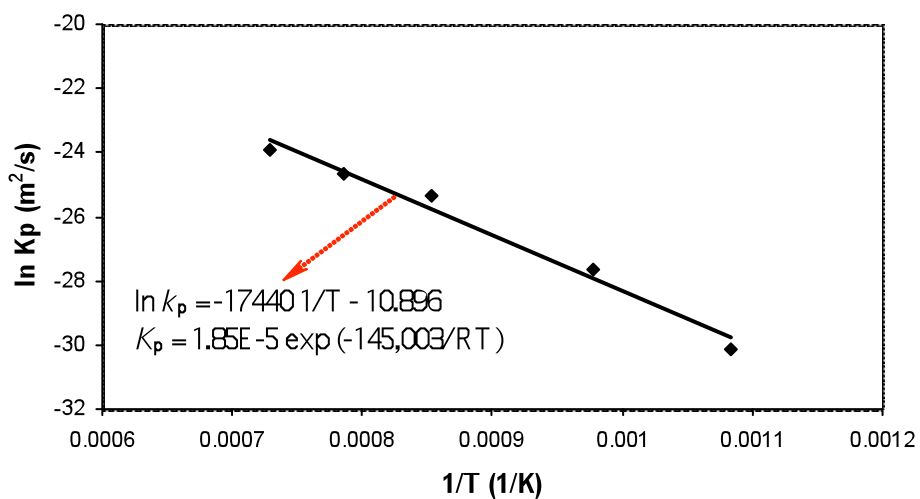
Figure 3.1.4: Arrhenius plot of parabolic rate constant for oxide scale grown of IF steel.
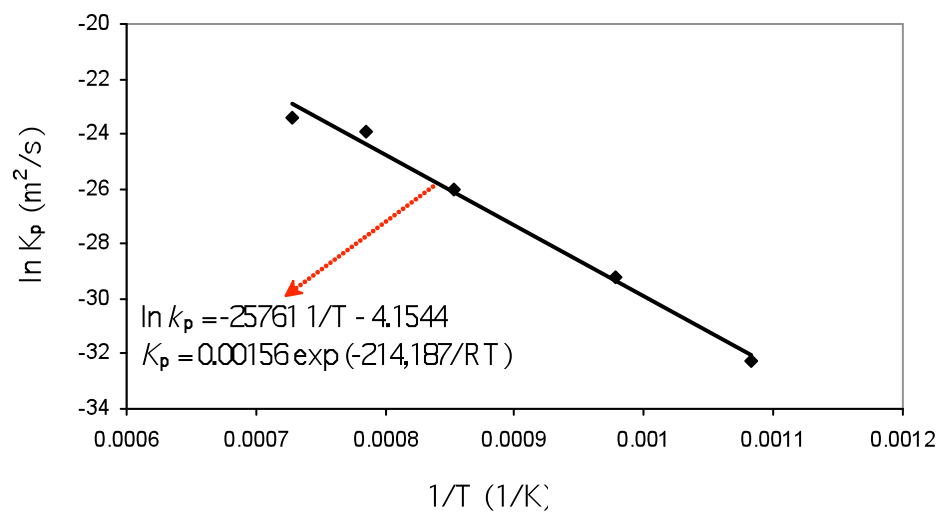
Figure 3.1. 5: Arrhenius plot of parabolic rate constant for oxide scale grown of Alloy A steel.
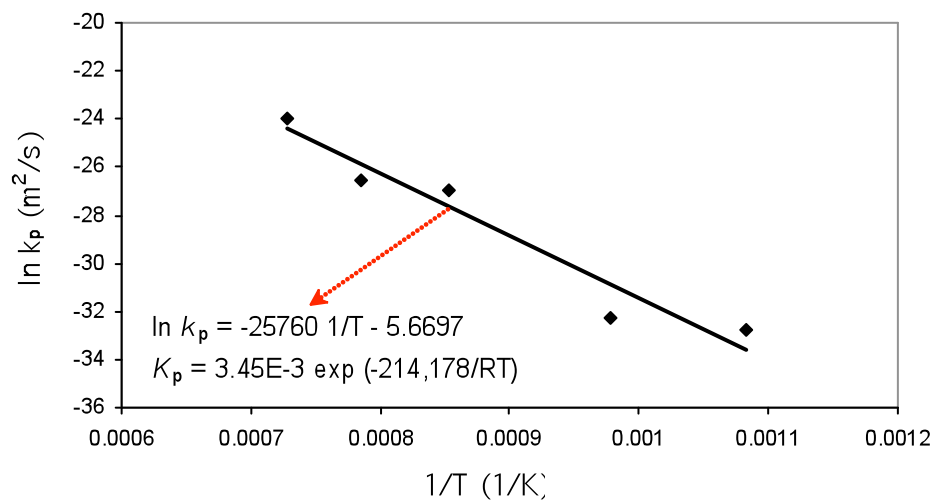
Figure 3.1.6: Arrhenius plot of parabolic rate constant for oxide scale grown of Alloy B steel.

3.2 Steel Substrate Microstructure

The microstructure of the steel substrates that were to be oxidised at different temperatures and times were investigated. The substrate microstructural features that are of concerned in this study are the grain size for the phases in the substrate and the examining any phase transformation at each temperature. As discussed in Sections 2.2 and 2.4, the samples were examined using standard methods for sample preparation and etched in 2% Nital. For statistical and accuracy purposes, four images were taken for each sample using standard optical microscopy. The grain size was measured using the linear intercept method described in Section 2.5. The substrate microstructure was also investigated using EBSD for the grain size measurement as double-checks of the quantitative calculations. However, EBSD was not used for phase identification of the substrate, as distinguishing more than five phases, including those of the oxide is very difficult. Avoiding these difficulties, the phase identification concentrated on the existing phases in the oxide scale layers not on the substrate itself during EBSD scans. EBSD was extensively used for microtexture analysis and grain boundary misorientation determination of the steel substrate as described in later sections. The grain size, aspect ratio and volume fraction of each phase in the steel substrate were checked using Image Analysis software.

As shown in Figures 3.2.1 - 3.2.4, IF steel contains only ferrite after heating to all temperatures. The grain size of IF steel is relatively large compared with other two steels used in this study. The smallest ferrite grain size was 78.98 μm at 650°C after 600 seconds hold time, and the largest was 146.36 μm at 750°C after 3600 seconds hold time. Appendix 5 shows the ferrite grain size and aspect ratio at different temperatures and times. The ferrite grain size varied with temperatures and times of exposure. Figure 3.2.23, shows the ferrite grain size versus temperature at 1800 seconds. As can be seen from the graph, there is no trend in the grain size with increasing temperature. However, generally the grain size increased with increasing time of oxidation at each temperature, see Appendix 5. The aspect ratio varied from 0.84 to 1.11, which indicates that the grain shapes are generally near equiaxed at all temperatures.

Alloy A contains ferrite and pearlite at all temperatures as shown in Figures 3.2.5 - 3.2.10. The ferrite grain size increased with increasing temperature at 1800 seconds as shown in 3.2.24. However, this tendency is not observed with time of exposure as shown in Appendix 6. Overall examination of Alloy A shows the ferrite grain size increases with increasing temperature but is independent of time of exposure. However, there were some exceptions from this trend. The ferrite grain size in Alloy A was much smaller than in IF Steel. The smallest ferrite grain size was 19.01 μm at 900°C and the largest was 31.35 μm at 1100°C. The aspect ratio varied from 0.82 to 1.08, which again indicates that the grain shapes are generally near equiaxed at all temperatures. The pearlite volume fraction and colony size differ with temperature without showing any trends as they varied even from different times of exposure as shown in Appendix 6. The pearlite and carbide segregations were observed at all temperatures as shown in Figure 3.2.10. The pearlite distribution on the substrate surface was not homogenous, which caused difficulties in statistical accuracy of the measurements. Furthermore, in some areas on the substrate there was no pearlite at all as shown in Figure 3.2.9. However, effort had been taken to obtain accurate measurements of pearlite colony size by taking larger areas of the substrate and taking images from different area of the samples. Therefore the final results have bigger standard errors as shown in Appendix 6. Also, the decarbonisation during oxidation was taken into account in the measurements by not calculating pearlite volume fractions in decarbonised areas. As shown in Figures 3.2.5 and 3.2.6 decarbonisation happened near the substrate surfaces. It also appears that pearlite segregates in some areas within the substrate and pearlite free zone near the substrate/oxide scale interface, see Figures 3.2.5 - 3.2.10.

Figures 3.2.11 - 3.2.22 show the microstructure of Alloy B for different heat treatments. The phases contained at each temperature are indicated on the Figures. From 650°C to 900°C ferrite grains dominate large areas on the substrate surface, and pearlite has smaller grain sizes and its volume fraction varied with time and temperature (Figures 3.2.11 and 3.2.12). At 900°C, especially after 1800 seconds of heat treatment, bainite formed occupying large volume fractions (Figures 3.1.15 – 3.1.18). Appendix 7 shows the ferrite and pearlite grain sizes, their volume fractions as well as the bainite volume fraction at each temperature and time of heat treatment. At 1000°C and above bainite has

a bigger volume fraction than the other two phases, while pearlite was hardly observed in some areas as shown in Figure 3.2.21. At 1100°C, the martensite structure is formed, see Figure 3.2.22. It should be noted that the samples after the heat treatment were cooled in air (~9°C/S cooling rate). The ferrite grain size increased with increasing temperature from 650 to 900°C, followed by decrease in size at 1000°C after the formation of bainite, as shown in Figure 3.2.25. The aspect ratio of ferrite grain size varied between 0.66 and 1.07. There are no trends toward increasing or decreasing pearlite volume fraction with temperature as can be seen in Appendix 7. However, pearlite volume fractions at all temperatures were much higher than in other two types of steels used in this study and the ferrite gain size was the smallest. The bainite volume fraction increased with increasing temperature and the whole structure transformed to martensite (0.41 at 900°C up to 0.78 at 1100°C), see Appendix 7. As shown in Figures 3.2.13 and 3.2.15, there was decarbonisation at nearly all temperatures, especially at the edges of the substrate.

The grain size and volume fraction measurements were carried out using the linear intercept method. For further confirmation the Image Analysis tool was used as a double check of these results. The results obtained from the Image Analysis tool were very close to the calculated results. Furthermore, the microstructures of the steel substrates were also observed and examined by EBSD. Most of the EBSD scans covered the oxide scale layers as well as the steel substrate in the same scanning area. Therefore, the EBSD data and analysis of the steel substrates will be discussed with oxide scale analysis in later sections of this Chapter.
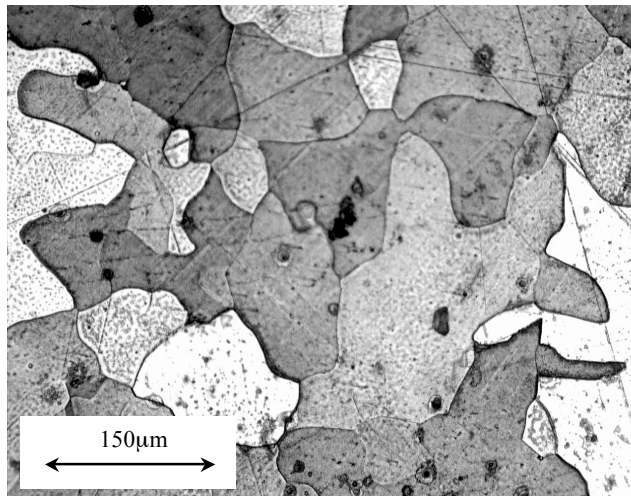
Figure 3.2.1: Optical micrograph of IF steel substrate, heat-treated at 650°C for 600 seconds, cooled in air.
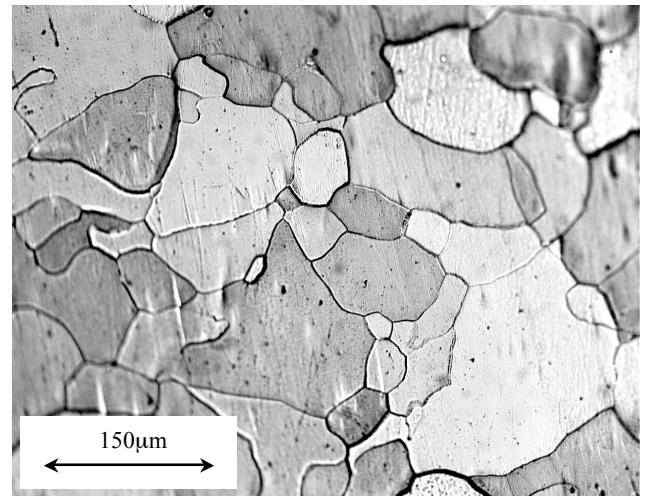

Figure 3.2.2: Optical micrograph of IF steel substrate, heat-treated at 650°C for 1800 seconds, cooled in air.
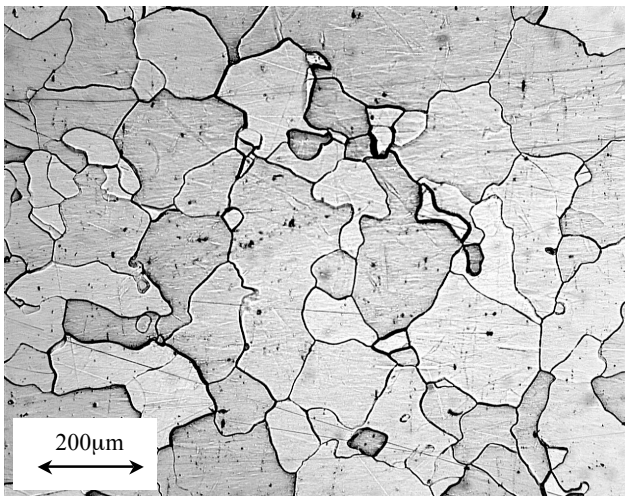

Figure 3.2.3: Optical micrograph of IF steel substrate, heat-treated at 750°C for 1800 seconds, cooled in air.
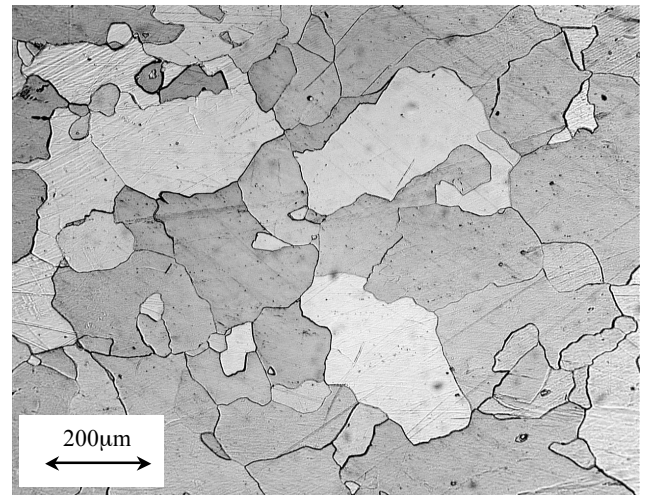

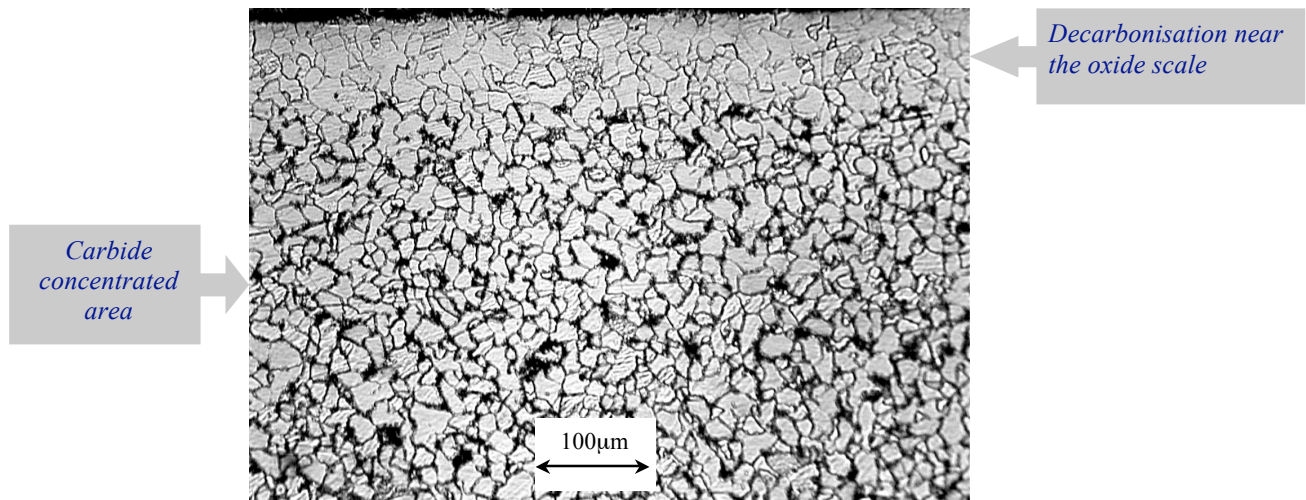***Figure 3.2.4: Optical micrograph of IF steel substrate, heat-treated at 1100°C for 600 seconds, cooled in air.***

Decarbonisation near the oxide scale

Carbide concentrated area

100μm

Figure 3.2.5: Optical micrograph of Alloy A substrate, oxidised at 750°C for 1200 seconds, cooled in air.

Oxide scale

Decarbonisation near the oxide scale

150μm
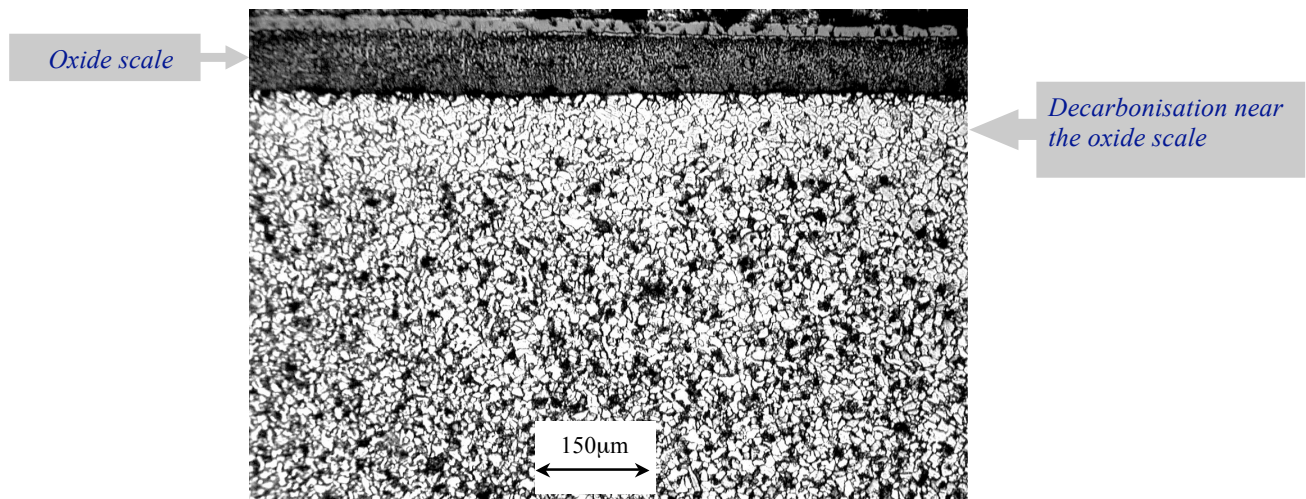
Figure 3.2.6: Optical micrograph of Alloy A substrate, oxidised at 900°C for 3600 seconds, cooled in air.

Pearlite colony

Ferrite grain

50μm
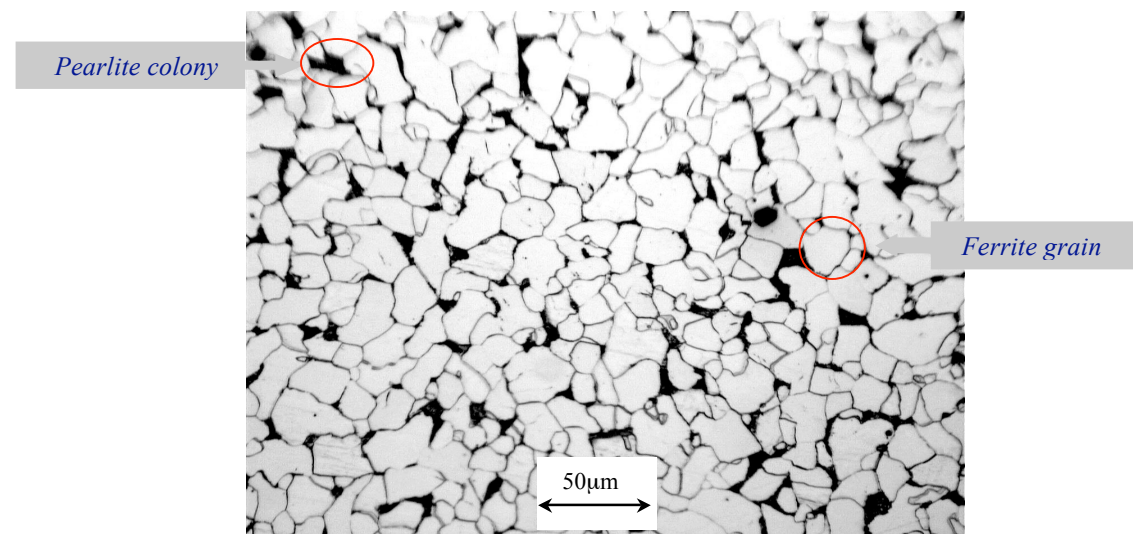
Figure 3.2.7: Optical micrograph of Alloy A substrate, oxidised at 650°C for 1800 seconds, cooled in air.
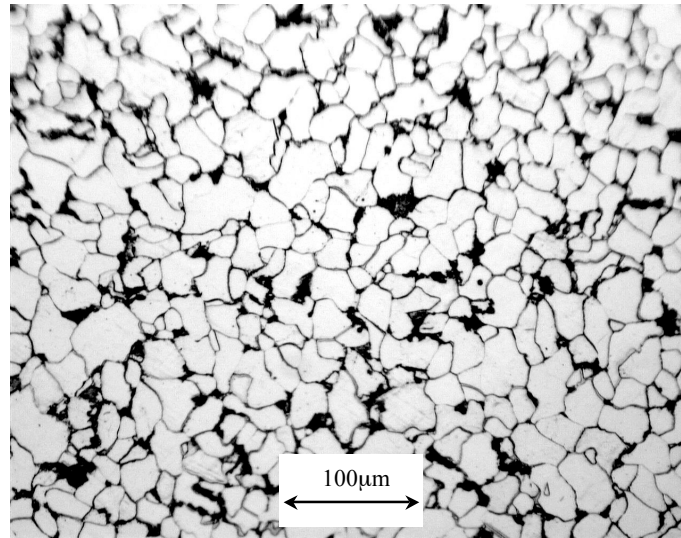
Figure 3.2.8: Optical micrograph of Alloy A, oxidised at 1000°C for 1800 seconds, cooled in air.
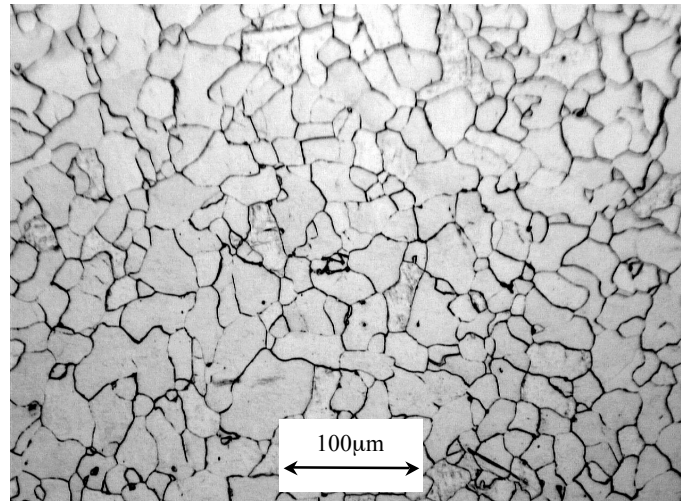
Figure 3.2.9: Optical micrograph of a free pearlite area of Alloy A, same sample as in Figure 3.2.8.
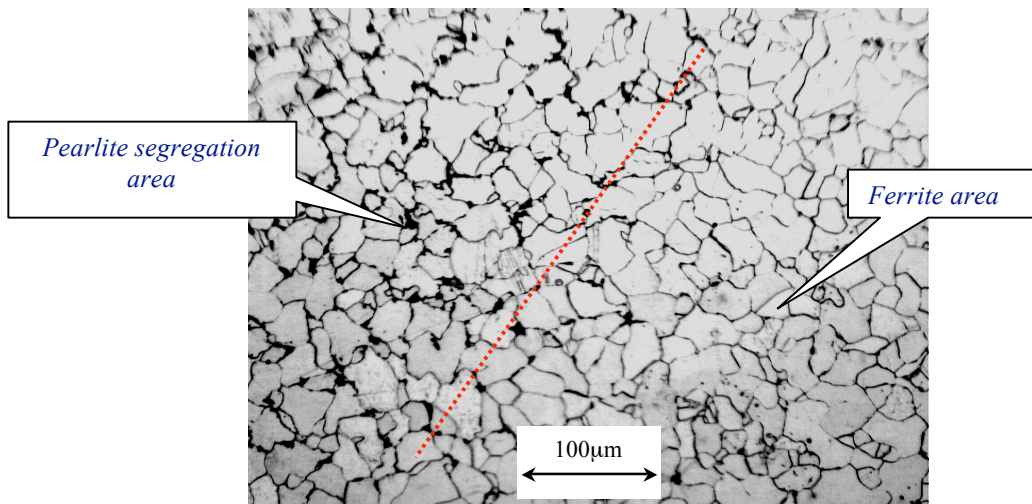
Figure 3.2.10: Optical micrograph of Alloy A, oxidised at 1000°C for 1800 seconds, cooled in air.
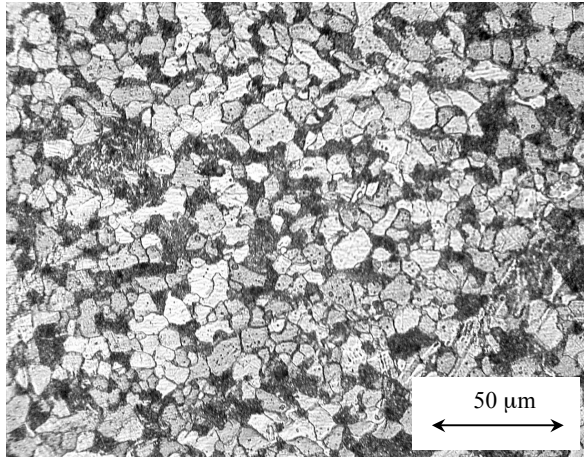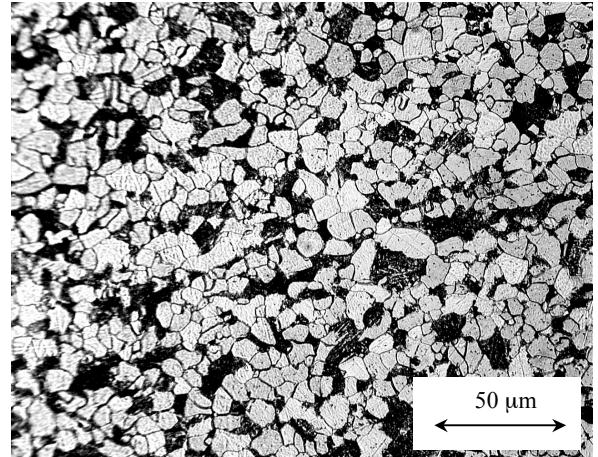
Figure 3.2.11: Alloy B, 650°C-600 seconds

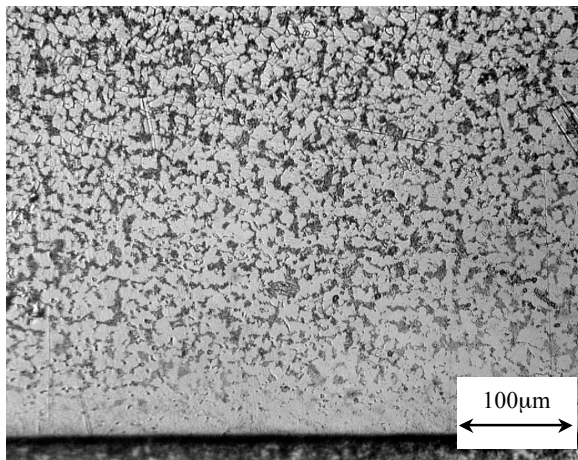*Figure 3.2.12: Alloy B, 650°C- 1200 seconds*

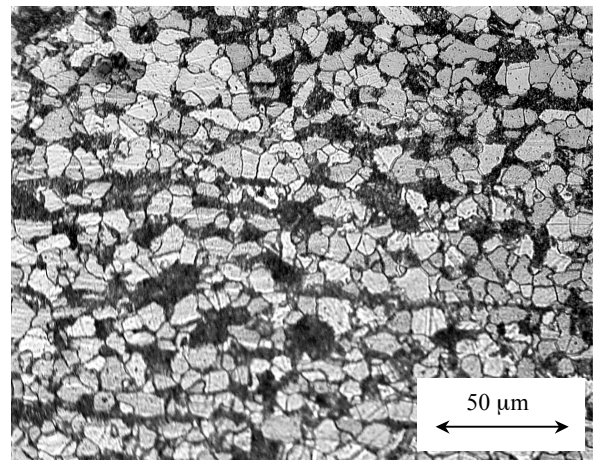*Figure 3.2.13: Alloy B, 750°C-600 seconds*
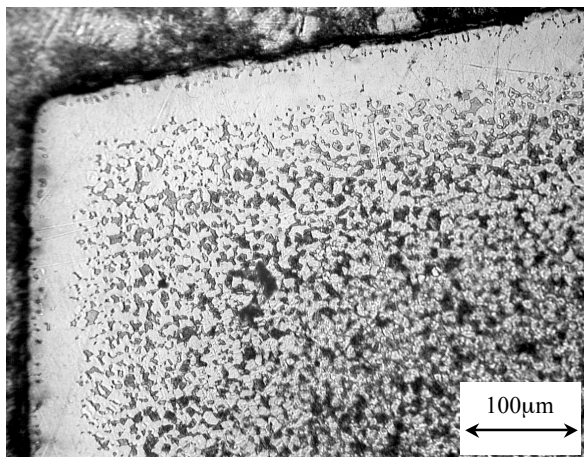

Figure 3.2.14: Alloy B, 750°C- 1200 Seconds
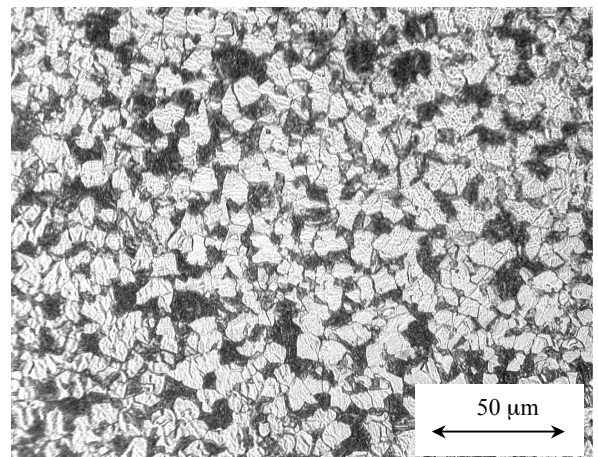

Figure 3.2.15: Alloy B, 900°C-600 seconds

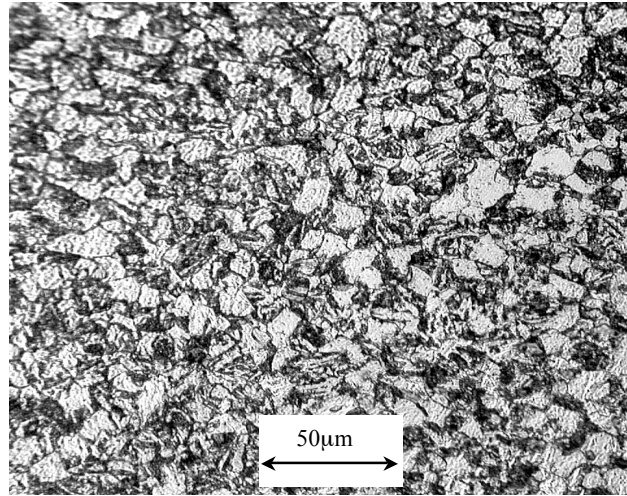*Figure 3.2.16: Alloy B, 900°C- 600 seconds*

Figure 3.2.17: Optical micrograph of Alloy B, heat treated at 900°C for 1200 seconds, cooled in air.
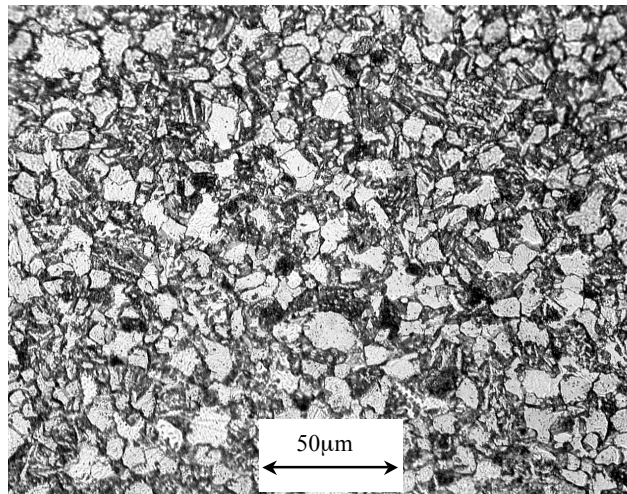

Figure 3.2.18: Optical micrograph of Alloy B, heat treated at 900°C for 1800 seconds, cooled in air.
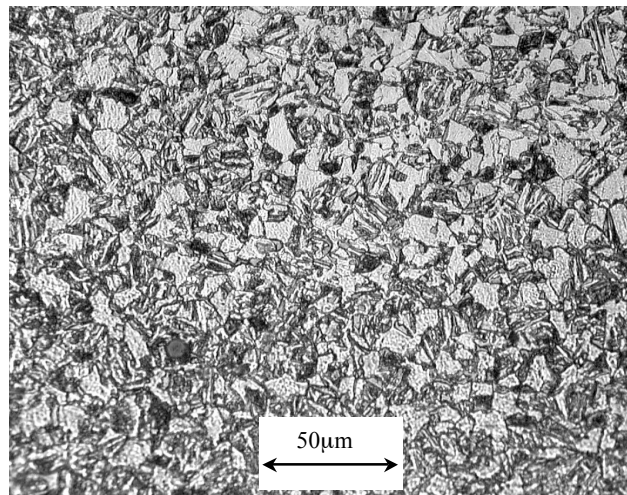

Figure 3.2.19: Optical micrograph of Alloy B, heat treated at 1000°C for 600 seconds, cooled in air.

Carbide

Ferrite

Bainite

50μm
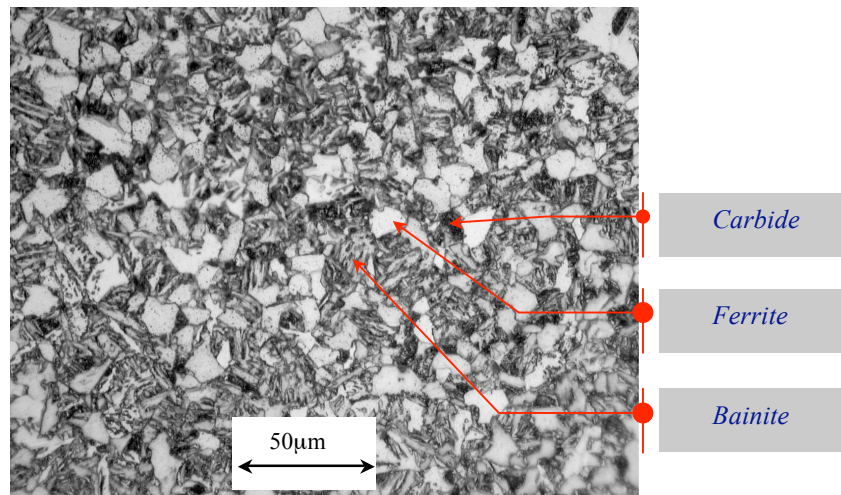
Figure 3.2.20: Optical micrograph of Alloy B, heat treated at 1000°C for 1800 seconds, cooled in air.

Bainite structure

20μm
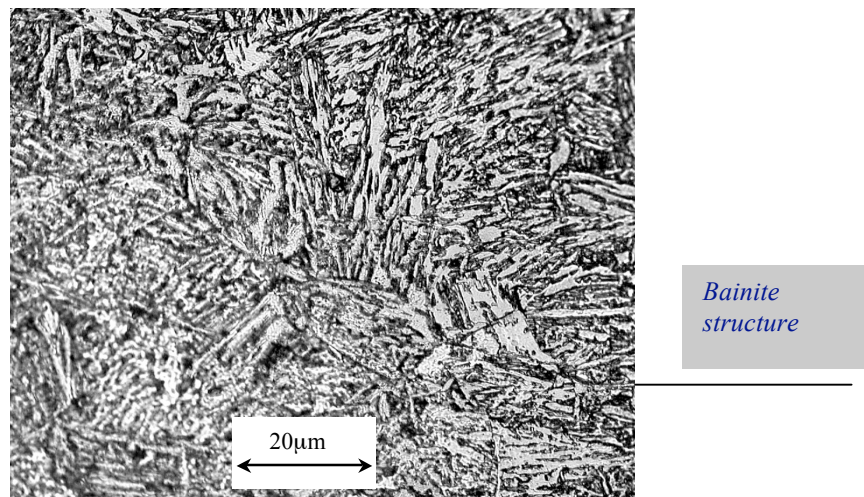
Figure 3.2.21: Optical micrograph of Alloy B, heat treated at 1100°C for 1800 seconds, cooled in air.

Martensite Structure

50μm

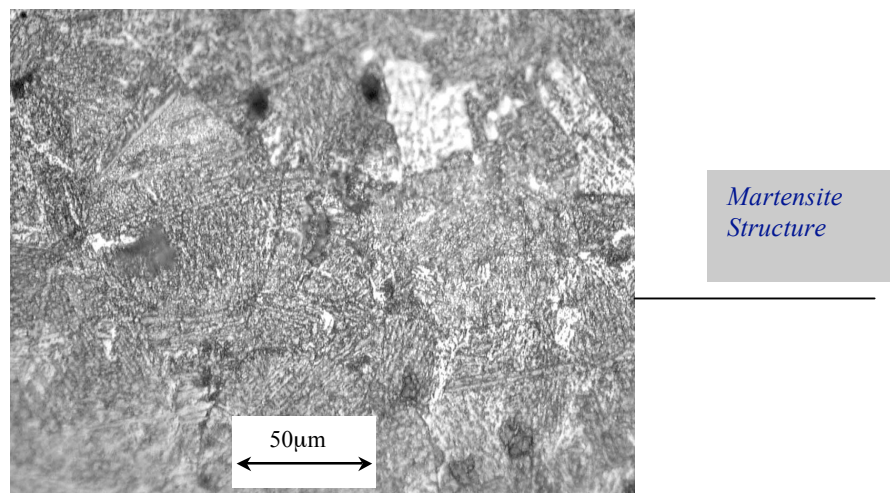***Figure 3.2.22: Optical micrograph of Alloy B, heat treated at 1100°C for 3600 seconds, cooled in air.***
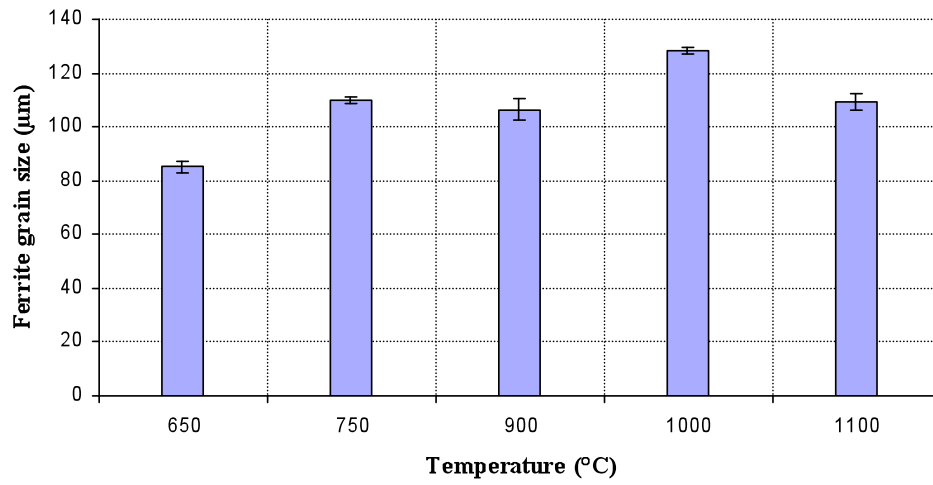
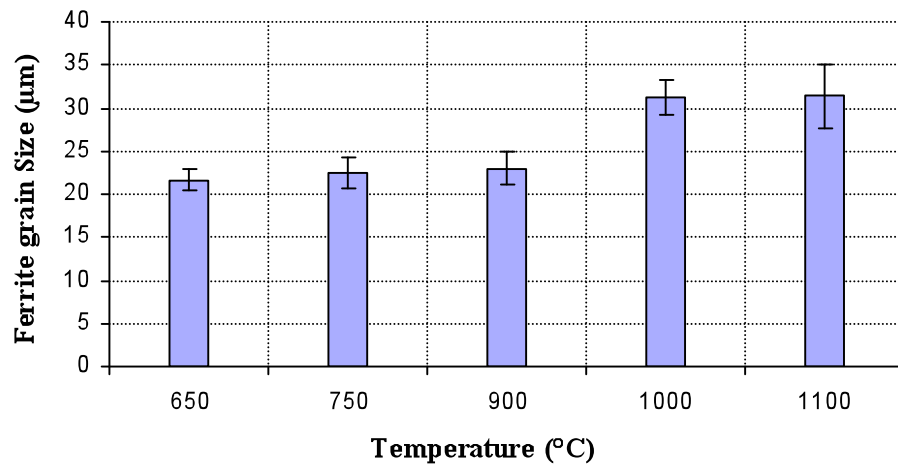*Figure 3.2.23: Ferrite grain size versus temperature of IF steel at 1800 seconds*

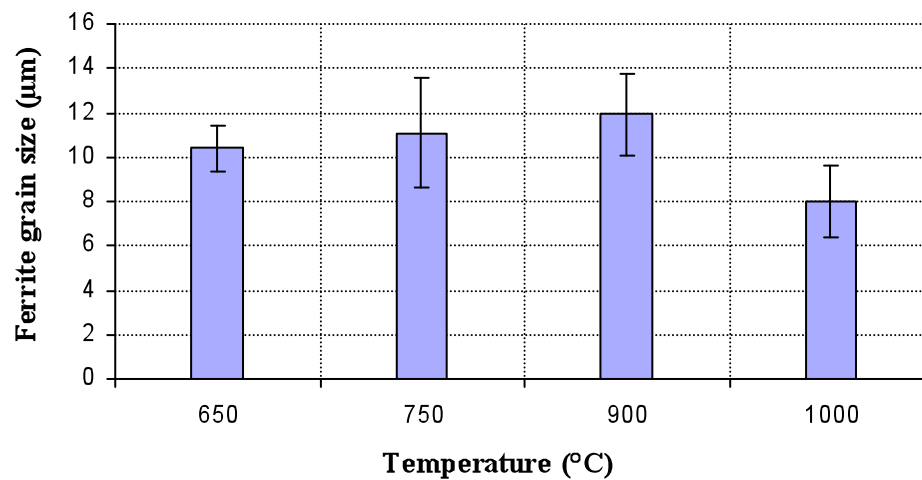*Figure 3.2.24: Ferrite grain size versus temperature of Alloy A at 1800 seconds*

Figure 3.2.25: Ferrite grain size versus temperature of Alloy B at 1800 seconds

3.3 Optical and Scanning Electron Microscopy Observations

The microstructure of the oxide scales formed on the IF steel, Alloy A and Alloy B were examined and investigated using different techniques such as optical microscopy, Scanning Electron Microscopy (SEM), Energy Dispersive Spectroscopy (EDS) and Electron Backscatter Diffraction (EBSD). The visual examination was also recorded during experiments such as general morphology, adherence, colour of the scale and visible cracks and porosity. Optical microscopy was used for the general microstructure investigation, morphology, adherence, porosity, and cracking. Moreover, optical micrographs have been extensively used for oxide growth and thickness measurements from which the oxidation rates for each grade of steel were calculated. Many methods were followed to obtain maximum information of oxide microstructures. These methods included taking images of the oxide scale as polished and etched for different times. Each method has its advantages and the different microstructure details that could be obtained.

Figures 3.3.1 - 3.3.8 show the polished cross sections of selected oxide scales formed on IF Steel at different times and temperatures with different polishing times. For very thin oxide thicknesses such as in Figures 3.3.1 and 3.3.2 polishing on 1 μm diamond paste could not reveal the phases within the scale. The scales were not adherent to the surface and were hardly retained by the conductive glue supported by the aluminium sheet as described in Section 2.1. For thicker oxide scale as shown in Figure 3.3.3, increasing the polishing time to 10 minutes could reveal the phases. Whereas, polishing for 3 minutes on 6 μm diamond paste could not reveal any phases in the oxide scale even for thicker scale as shown in Figures 3.3.4 - 3.3.7. Figure 3.3.8 gives little information about the phases in the oxide scale after the cross section was polished with 1 μm for 3 minutes, as the scale is still too porous and has many polishing artefacts. However polishing on 1 μm and 6 μm diamond paste for short times (2 - 5 minutes) could be used for measuring oxide scale thickness but not for phase discriminations, grain size or porosity measurements.

Figures 3.3.9 - 3.3.14 show the oxide scale formed on IF Steels at various temperatures after polishing on 6 and 1 μm diamond pastes and then etched with 1% HCl in ethanol.

The Figures are arranged in order of the highest temperature to the lowest as all the three oxide scale layers can be seen clearly at higher temperatures. As can be seen from the Figures, etching can reveal the phases in the oxide scale. The lightest layer on the top is haematite and the magnetite is slightly darker, while the darkest phase is wüstite. As shown in Figures 3.3.9 and 3.3.10, magnetite precipitates can also be revealed by etching since they have the same colour as the magnetite layer. The wüstite layer is divided into two different shades, one very dark and another less dark. Figure 3.3.10 shows a vertical crack crossing all the layers in the scale. The crack is within the wüstite grains and magnetite precipitates, not across the grain boundaries. Phase identification by optical microscopy is not easy in some samples as the colours of the phases were similar. Furthermore in the case of only two phases present, it was difficult to say what they are among wüstite, magnetite and haematite, as can be seen in Figures 3.3.11 - 3.3.14. In Figure 3.3.13, it was difficult to say whether the two phases shown are haematite and magnetite or wüstite and magnetite. Even at higher magnification, the phase's colour has changed, and that makes the phases identification more difficult. Etching samples for 20 seconds reveals not only the phases but also some grain boundaries, as shown in Figure 3.3.14. However, the grain boundaries were not revealed completely, especially in the magnetite layer. Further increasing the etching time caused damage and pits in the scale. As show in the Figures 3.3.11 - 3.3.13, the oxide scale etched in the same way as the sample in Figure 3.3.14, but there is no indication of the grain boundaries in the scale.

Figures 3.3.15 – 3.3.19 show the oxide scales formed on Alloy A. The samples were polished for different times, which has an affect on decreasing the polishing artefacts in the samples. The results of Alloy A were similar to those of the IF steels. The descriptions of the sample preparations are given in the figure captions. As shown, polishing the samples for 15 minutes using 1μm diamond paste gives good information about the phases, with etching the samples gave better detail about the phase present. More micrographs of etched samples are show in Appendix 8. The scales on Alloy A were mainly etched with 2% Nital. Where the scale on Alloy A was etched with 1% HCl in ethanol, the phases could hardly be revealed and distinguished. From this, it was concluded that different etches have different affects on the scale formed on different types of steels. For Alloy A, 2% Nital was better than 1% HCl in ethanol etchant for

revealing the phases in the oxide scale layers. However, 2% Nital caused more pits and has more etching artefacts than 1% HCl in ethanol.

As for IF steel, some of the oxide scales formed on Alloy A were not uniform, as shown in Figures 3.3.20 and 3.3.21. At the early stages of this study it was believed that this was due to the adherences of the oxide scale to the substrate surfaces, see Figure 3.3.21. Further investigations showed that the non-uniform oxide scales was observed also even on relatively adherent oxide scale to the substrate, as show in Figures 3.3.11, 3.3.13, 3.3.19 and 3.3.20. As shown in Figures 3.3.21.a, b and c, the oxide scale is thicker where it is adherent to the substrate and thinner where is spalled off. However, this phenomenon is not observed every time. As shown in Figure 3.3.20 the oxide scale is relatively adherent to the substrate, but still the oxide is not uniform. An overall observation indicates that there is no correlation between uniformity of the oxide scale and its adherency with the steel substrate. Further details on this aspect will be discussed in Chapter 4. It has been noted that the oxide scale phases in the thin areas are different from those in the thick areas. As shown in Figures 3.3.20 and 3.3.21 only magnetite exists in the thin area whereas wüstite dominates a large portion of the oxide scale in the thicker areas. Furthermore, at the spallation junction (Figure 3.3.21.c) wüstite stops growing and only magnetite thickness increased.

The phase ratio of the oxide scale is not only related to uniformity and adherency of the scales to the steel substrate, but also to the geometry of the sample. As shown in Figure 3.3.22, the scale formed on the top of the substrate surfaces consists of three layers (wüstite, magnetite and haematite). Whereas, the scale formed on the side on the sample consists of haematite and magnetite layers only. Moreover, the thickness and the phase ratio differs from side to side of the sample surfaces, see the same Figure (3.3.22).

The oxide scale examinations of Alloy B were carried out in the same way as the other two alloys. As show in Figures 3.3.23 – 3.3.25, etching with 1% HCl in ethanol revealed the phase boundaries in the oxide scale. The 2% Nital was too strong for the oxide formed on Alloy B, which caused damage and etch pits. Unlike the IF steel and Alloy A, the wüstite layer on Alloy B appeared very dark and no colour gradients within the

wüstite layer were observed. As shown in Figure 3.3.23, the magnetite precipitates are clearly revealed by etching.
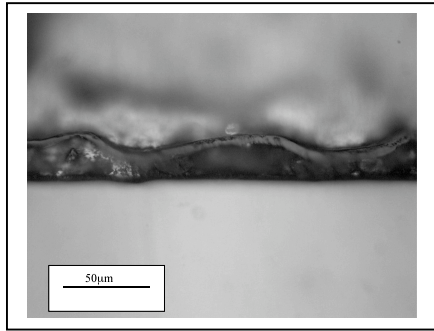

Figure 3.3.1: Optical micrograph of oxide scale grown at 650°C for 600 seconds on IF steel. The scale is very thin, not porous and not adherent to the steel substrate. The scale thickness is 6.40 ± 1.67µm. The sample cross section was polished with 1 µm diamond paste.
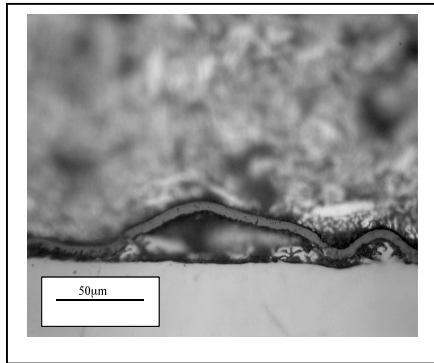
Figure 3.3.2: Optical micrograph of oxide scale grown at 650°C for 1200 seconds on IF steel. The scale is very thin, porous and not adherent to the steel substrate. The scale thickness is 8 ± 0.44µm. The sample cross section was polished with 1 µm diamond paste.
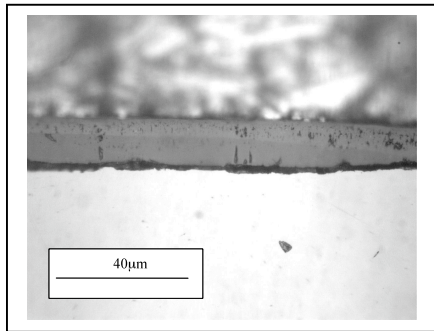
Figure 3.3.3: Oxide scale grown at 650°C for 1800 seconds on IF steel. The scale is thin, relatively non porous and adherent to the steel substrate. The scale thickness is 13.2 ± 1.22µm. The wüstite and magnetite layers can clearly be observed using optical microscopy. The sample cross section was polished with 1 µm diamond paste.
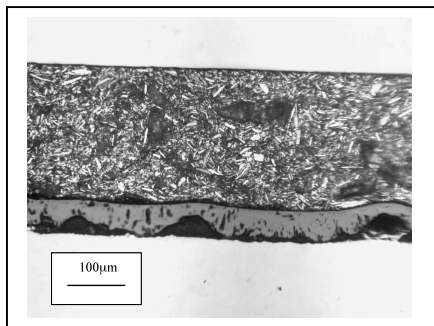
Figure 3.3.4: Oxide scale grown at 750°C for 3600 seconds on IF steel. The scale is relatively porous and not an adherent. The scale thickness is 55.52 ± 10.17µm. The oxide spalled during cooling the sample to room temperature. The image was taken using optical microscopy. The sample cross section was polished with 6 µm diamond paste.
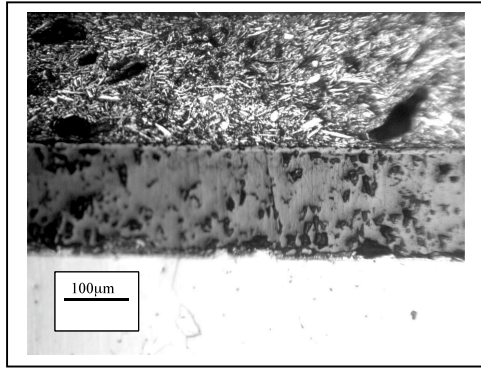
Figure 3.3.5: Oxide scale grown at 900°C for 1800 seconds on IF steel. The scale is porous and adherent to the surface. The scale thickness is 168.9 ± 4.67μm. The oxide remained on the sample surface more readily during cooling the sample to room temperature. The image was taken using optical microscopy, the different oxide layers cannot clearly be observed as shown in the image. The sample cross section was polished with 6 μm diamond paste.
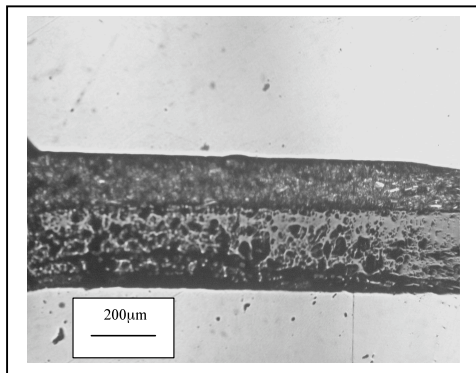
Figure 3.3.6: Oxide scale grown at 900°C for 3600 seconds on IF steel. The scale is very porous and not adherent to the surface. The scale thickness is 195 ± 9μm. The image was taken using optical microscopy, the different oxide layers cannot clearly be observed as shown in the image. The sample cross section was polished with 6 μm diamond paste.
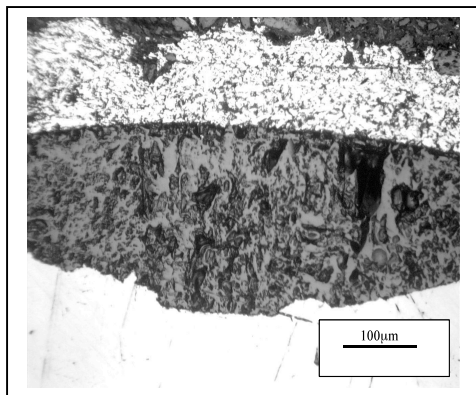
Figure 3.3.7: Oxide scale grown at 1000°C for 1200 seconds on IF steel. The scale is very porous with many cracks and is adherent to the steel substrate surface. The scale thickness is 211 ± 11.93μm. The oxide is not uniform. The oxide looks dark, because the sample mounted in Bakelite that fills the gaps in the pores and the cracks. The sample cross section was polished with 6 μm diamond paste.
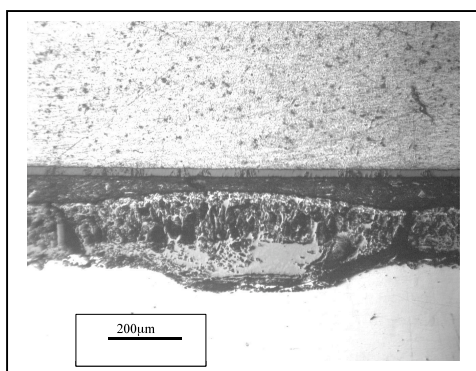
Figure 3.3.8: Oxide scale grown at 1100°C for 600 seconds on IF steel. The scale is not uniform, very porous and adherent to the steel substrate surface. The scale thickness is 220 ± 43μm. The sample cross section was polished with 1 μm diamond paste.

Haematite

Magnetite

Artefact

Pore

Wüstite

Magnetite precipitate

100μm
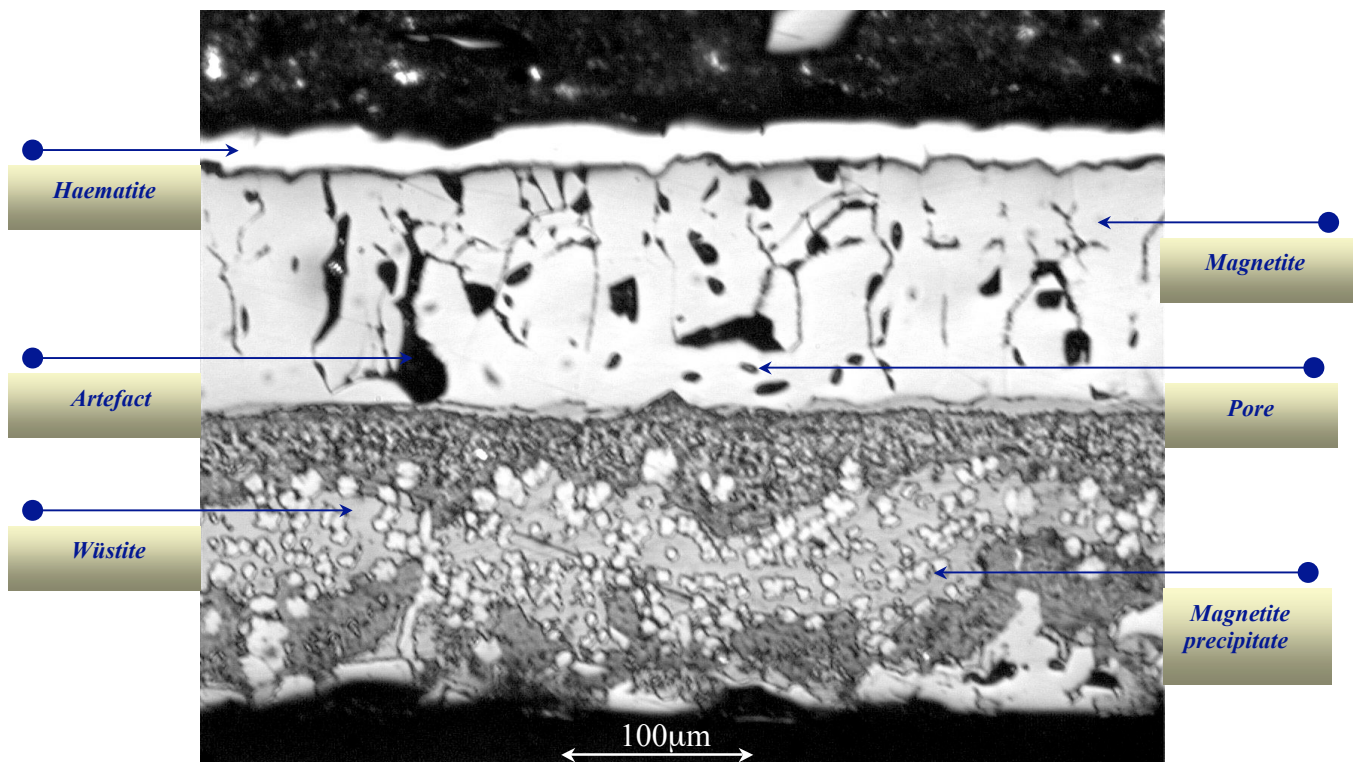
Figure 3.3.9: Optical micrograph of oxide scale formed on IF steel at 1100°C-1800 seconds, etched with 1% HCl in ethanol.

100μm
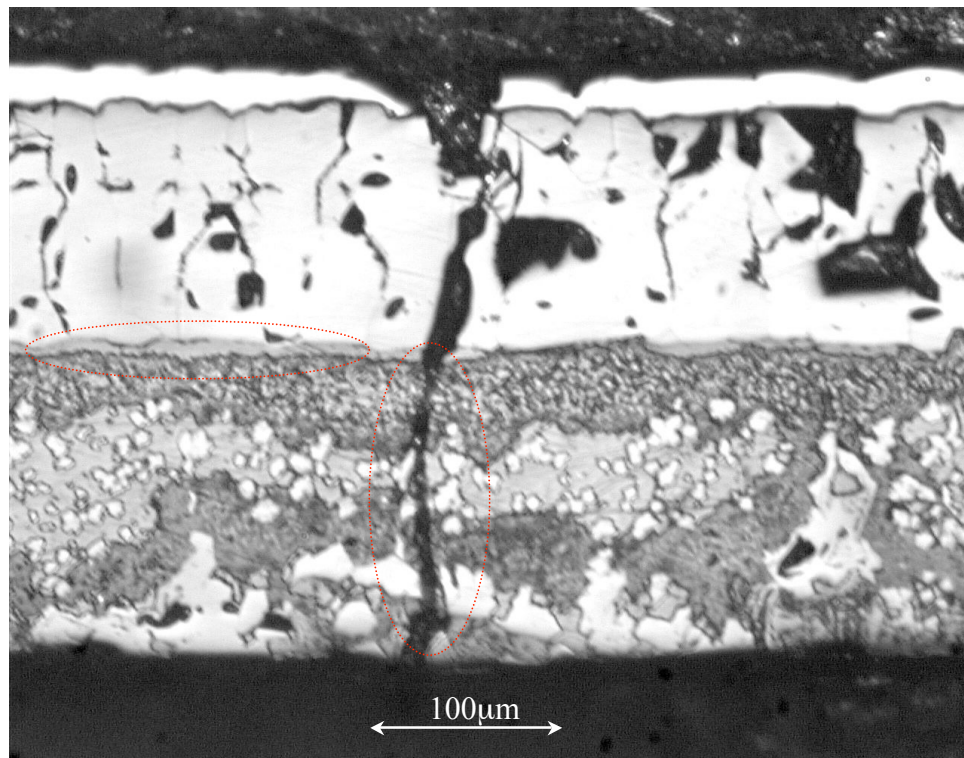
Figure 3.3.10: Different area of the same sample in Figure 3.3.9 showing a crack in the scale.
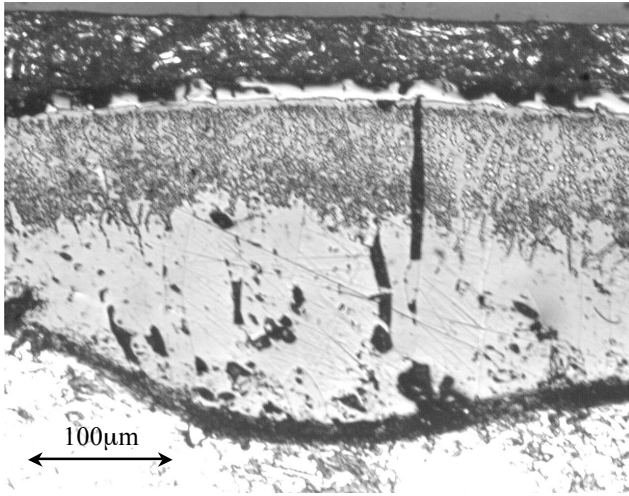
Figure 3.3.11: Oxide scale on IF steel at 1000°C-1800 seconds, etched with 1% HCl in ethanol.
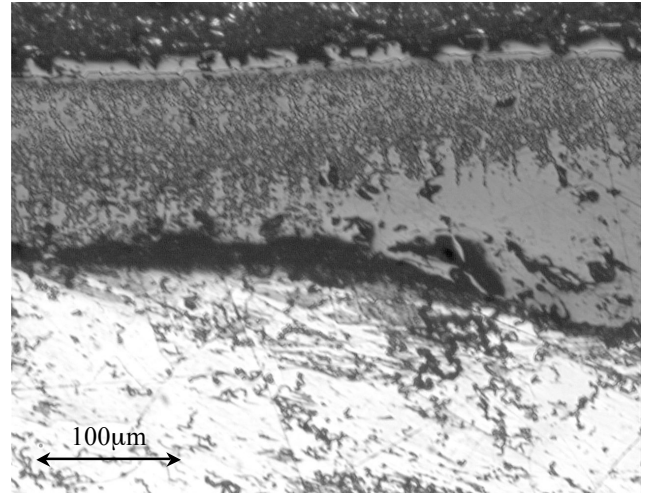
Figure 3.3.12: Oxide scale on IF steel at 1000°C-1800 seconds, etched with 1% HCl in ethanol.
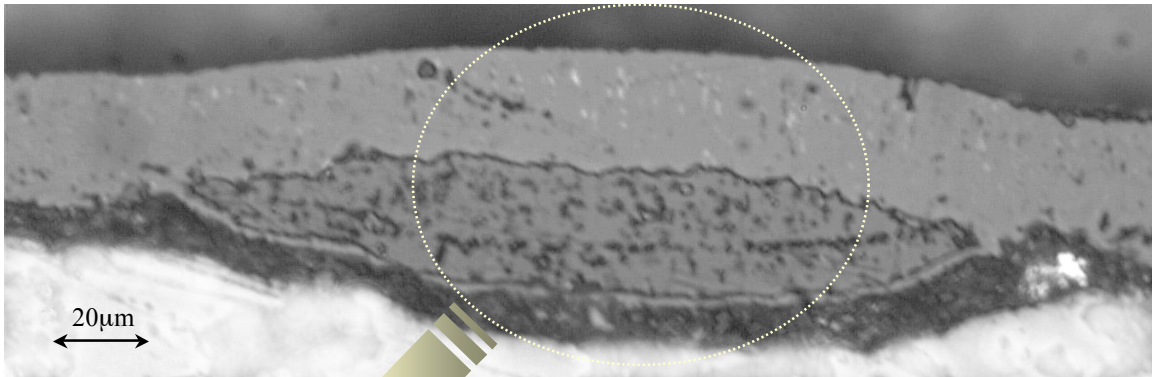
Figure 3.3.13: Oxide scale on IF steel at 750°C-1800 seconds, etched with 1% HCl in ethanol

Magnetite

Wüstite
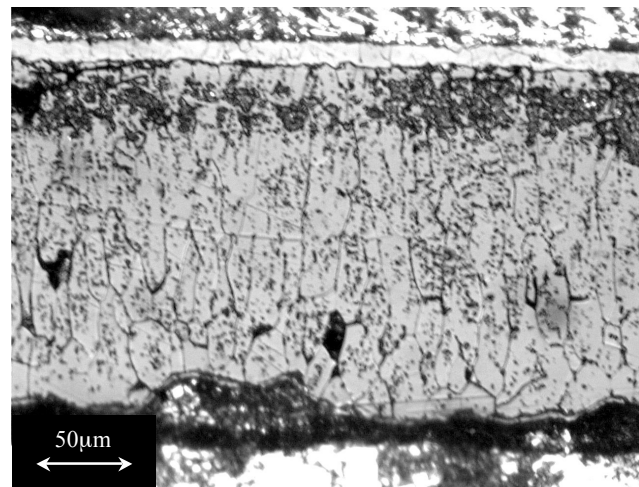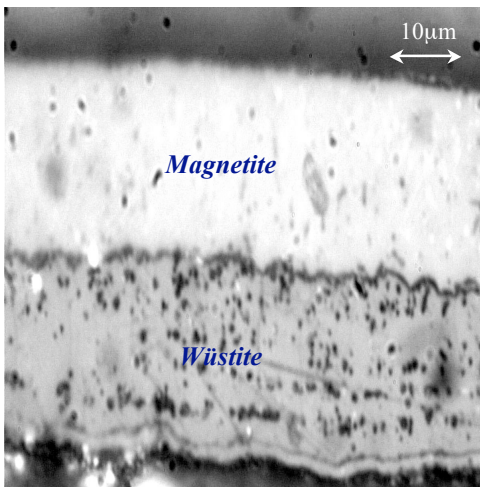
Figure 3.3.14: Oxide scale on IF steel at 900°C-1800 seconds, etched with 1% HCl in ethanol.
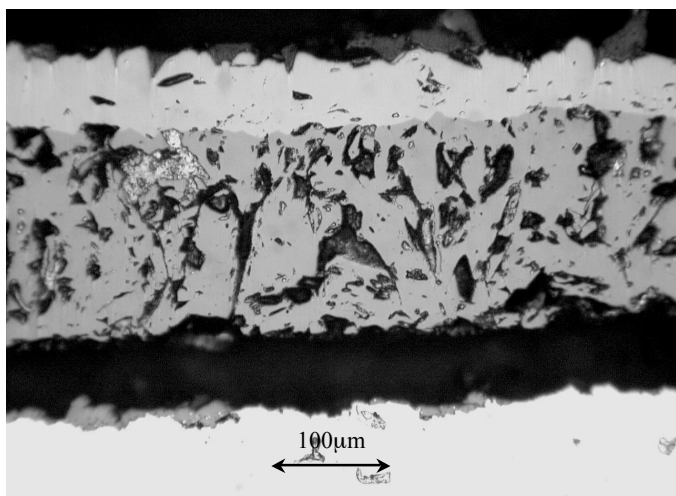
Figure 3.3.15: Oxide scale formed on Alloy A at 1100°C-3600 seconds, polished with 1 μm for 2 minutes and etched.
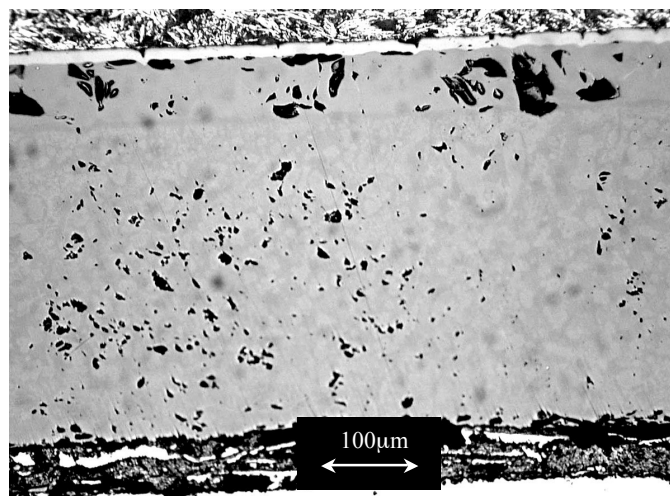
Figure 3.3.16: Oxide scale formed on Alloy A at 1100°C-1200 seconds, polished with 1 μm for 15 minutes.
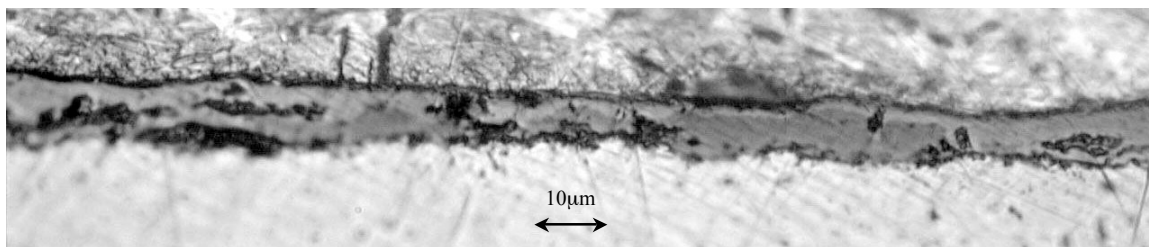
Figure 3.3.17: Oxide scale formed on Alloy A at 750°C-1200 seconds, polished with 1 μm diamond paste.
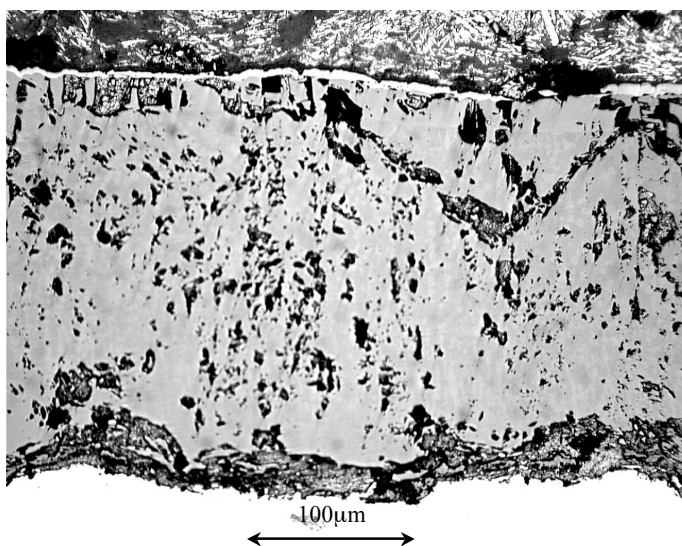
Figure 3.3.18: Oxide scale formed on Alloy A at 1000°C-1200 seconds, polished (1 μm-10 minutes).
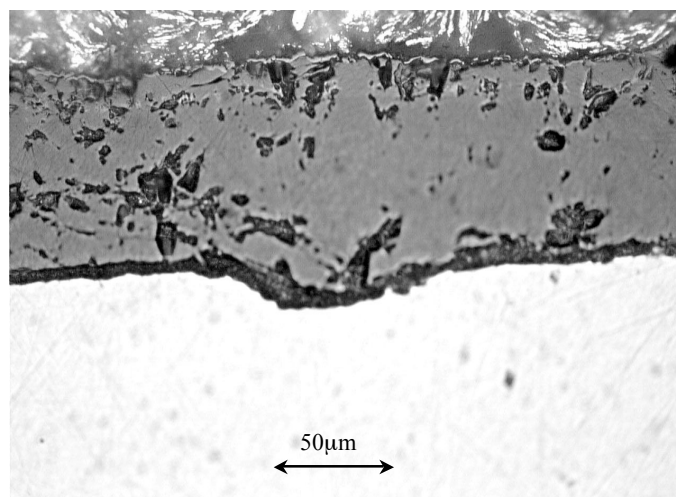
Figure 3.3.19: Oxide scale formed on Alloy A at 900°C-1800 seconds, polished (6 μm-5 minutes).
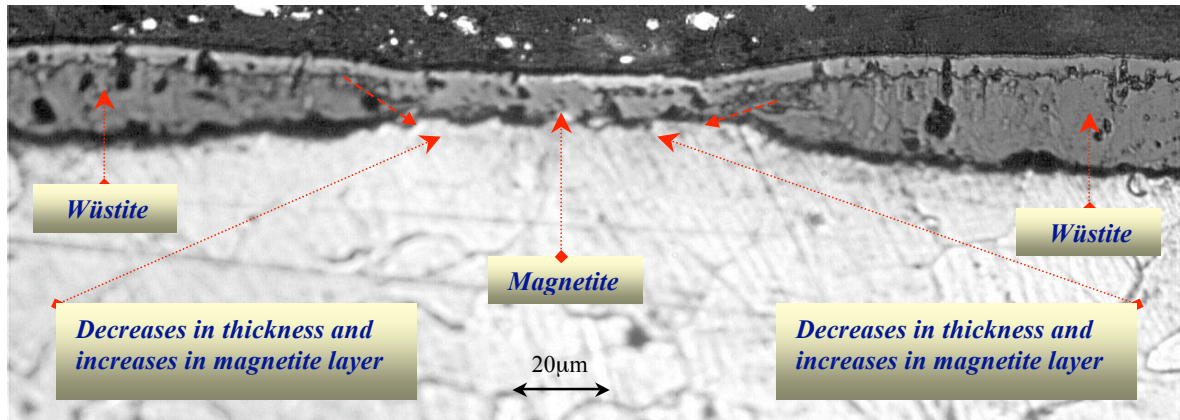
Figure 3.3.20: Non-uniform oxide scale formed on Alloy A at 750°C-1800 seconds, etched.
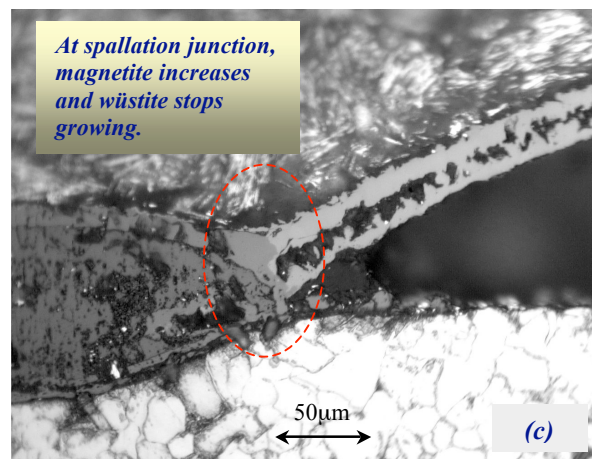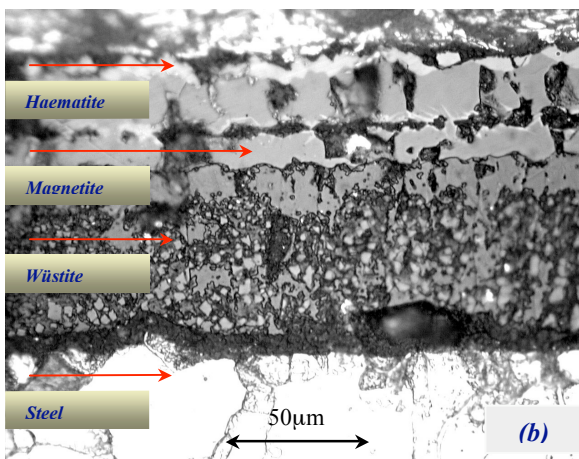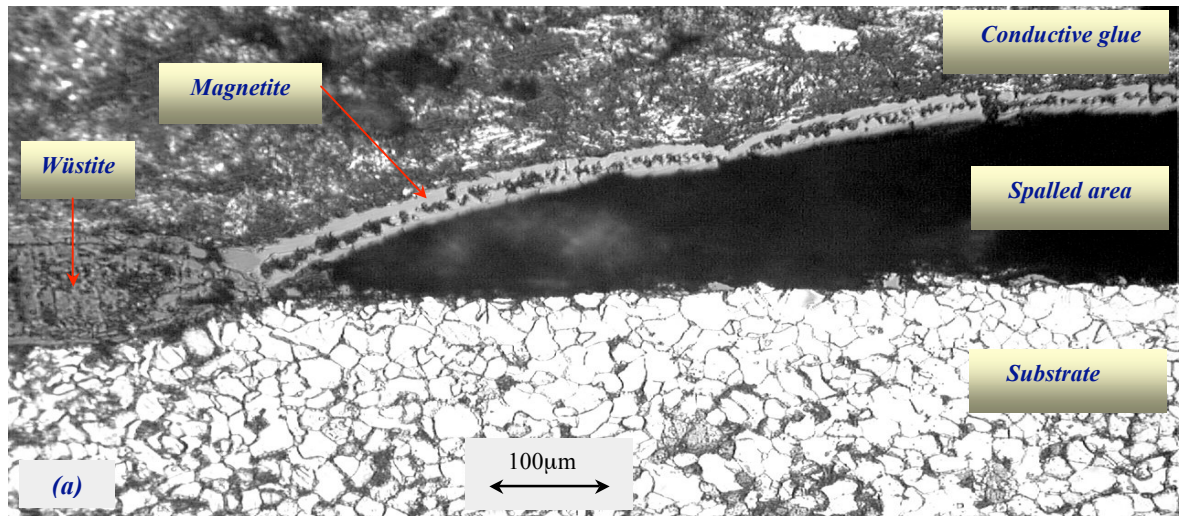
Figure 3.3.21: (a) Oxide scale formed on Alloy A at 900°C-1800 seconds, etched. (b) higher magnification of the adherent area in (a). (c) the spallation junction.

Haematite layer

Magnetite layer

Wüstite layer

200μm

250μm

250μm

Haematite layer

Magnetite layer

100μm
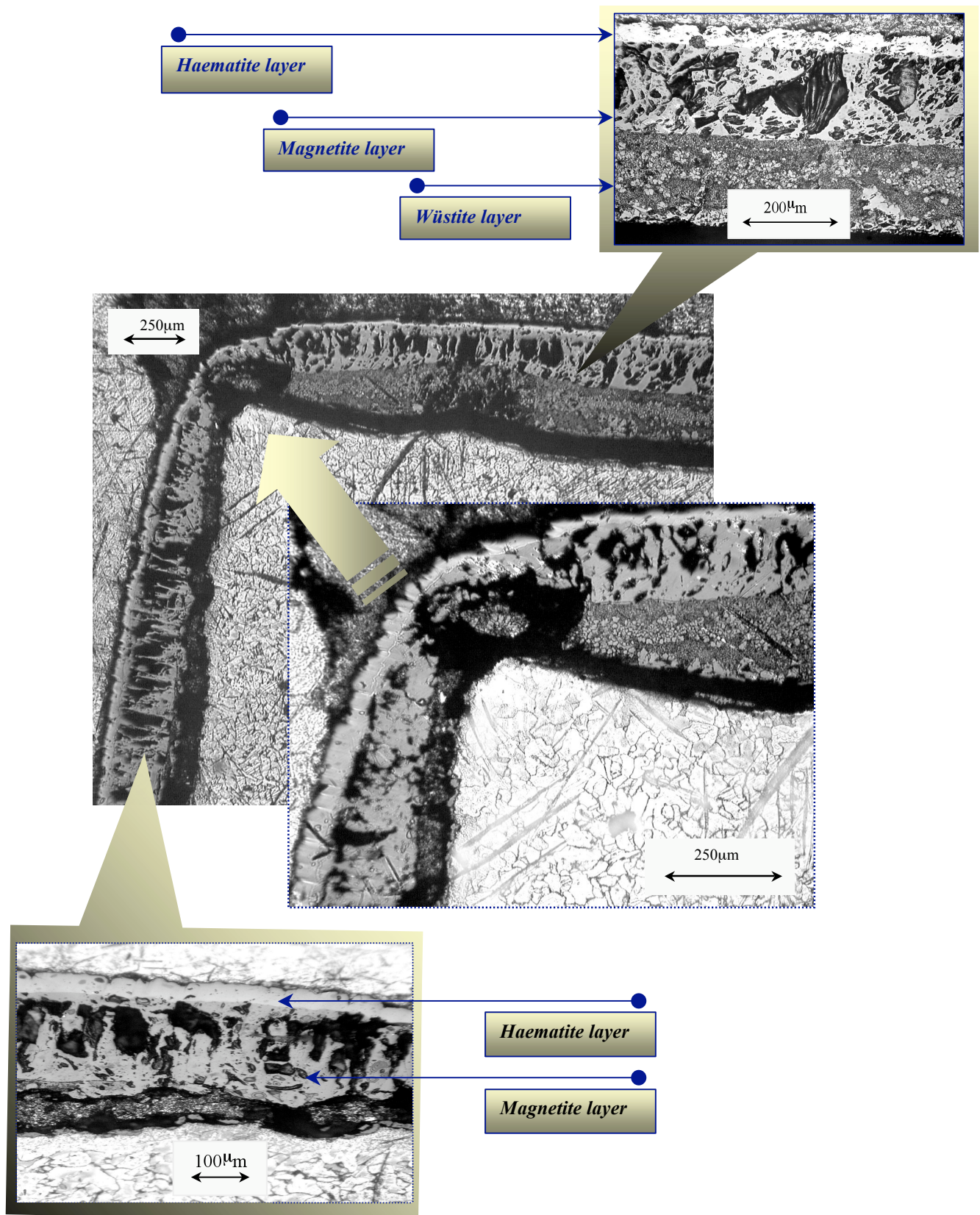
Figure 3.3.22: Oxide scale formed on Alloy A, 1100°C-1800 seconds, etched in 2% Nital.
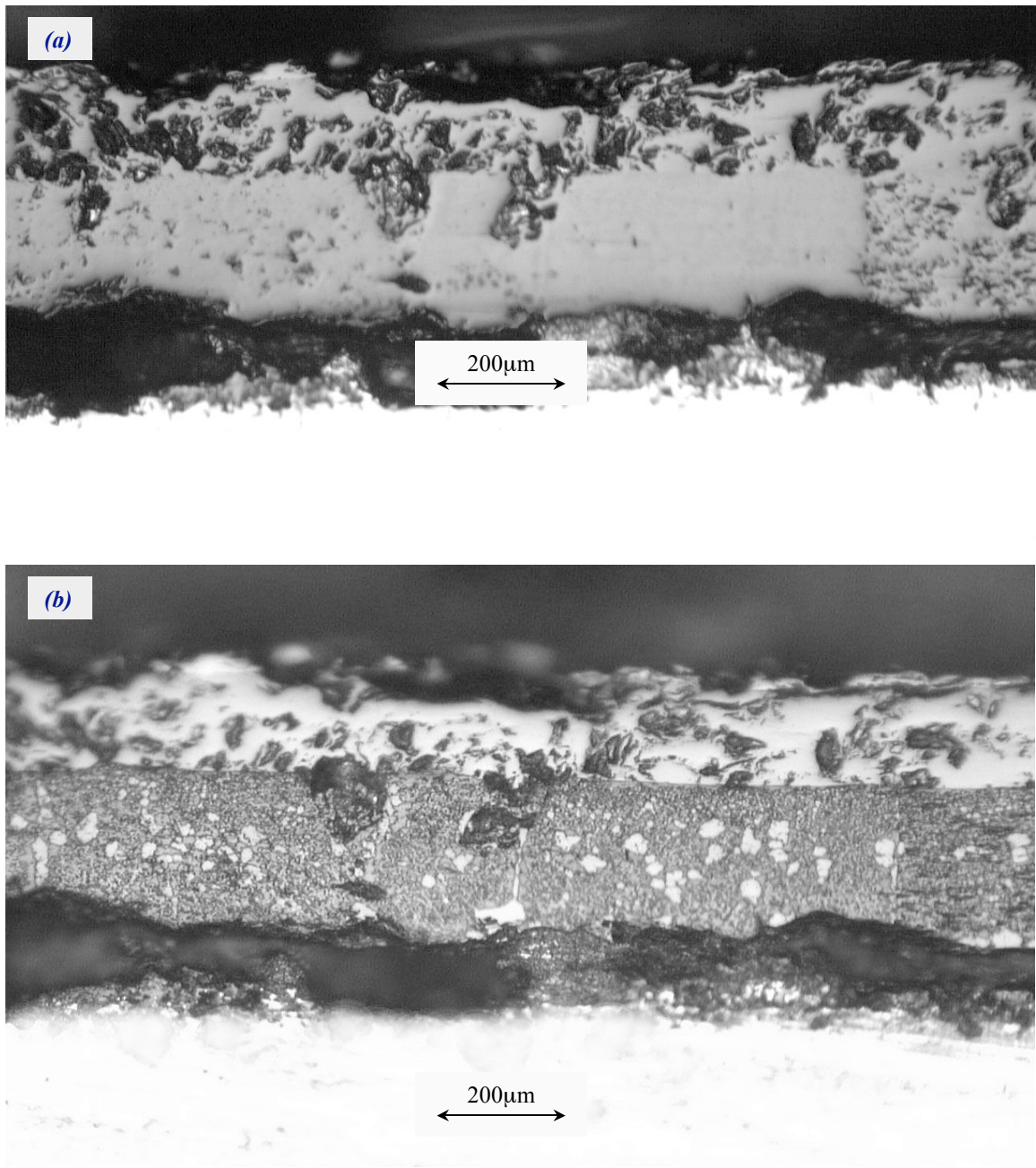
Figure 3.3.23: Optical micrograph of oxide scale formed on Alloy B at 1200-1200 seconds, (a) polished with 1 μm diamond paste for 10 minutes, (b) etched with 1% HCl in ethanol
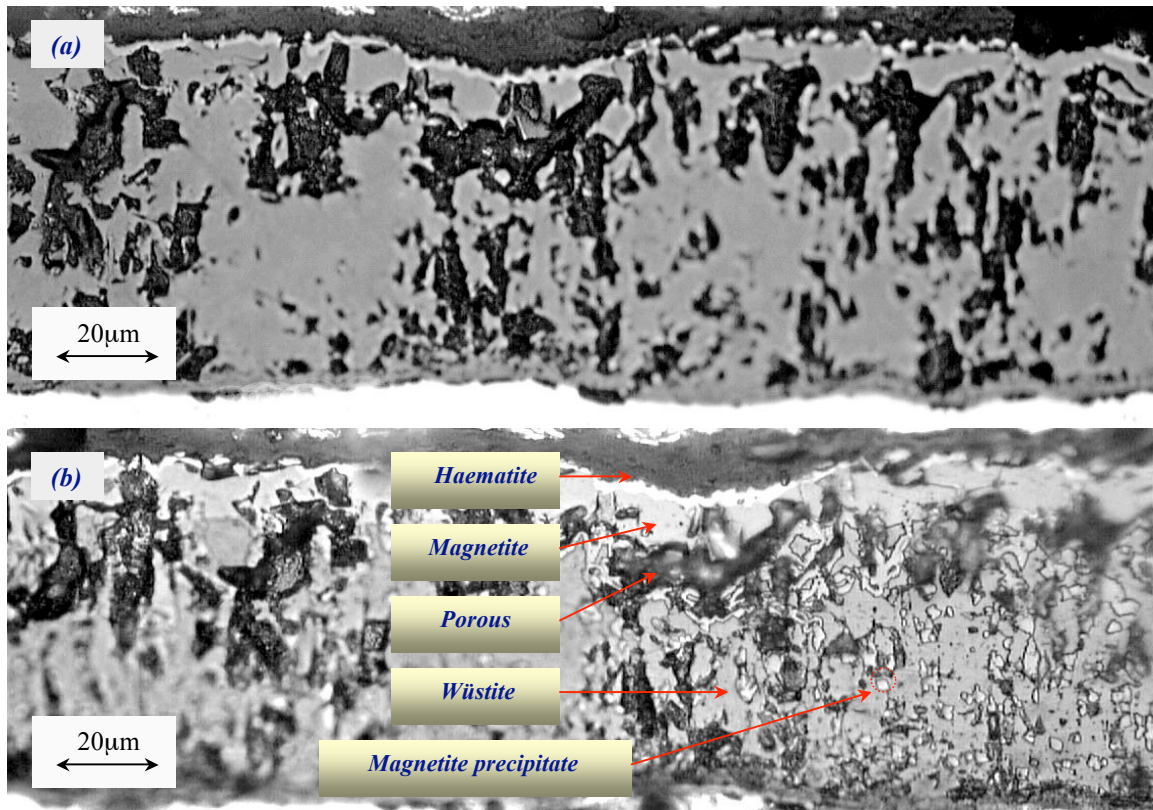
Figure 3.3.24: Optical micrograph of oxide scale formed on Alloy B at 900-1800 seconds, (a) polished with 1 µm diamond paste for 5 minutes, (b) etched with 1% HCl in ethanol.
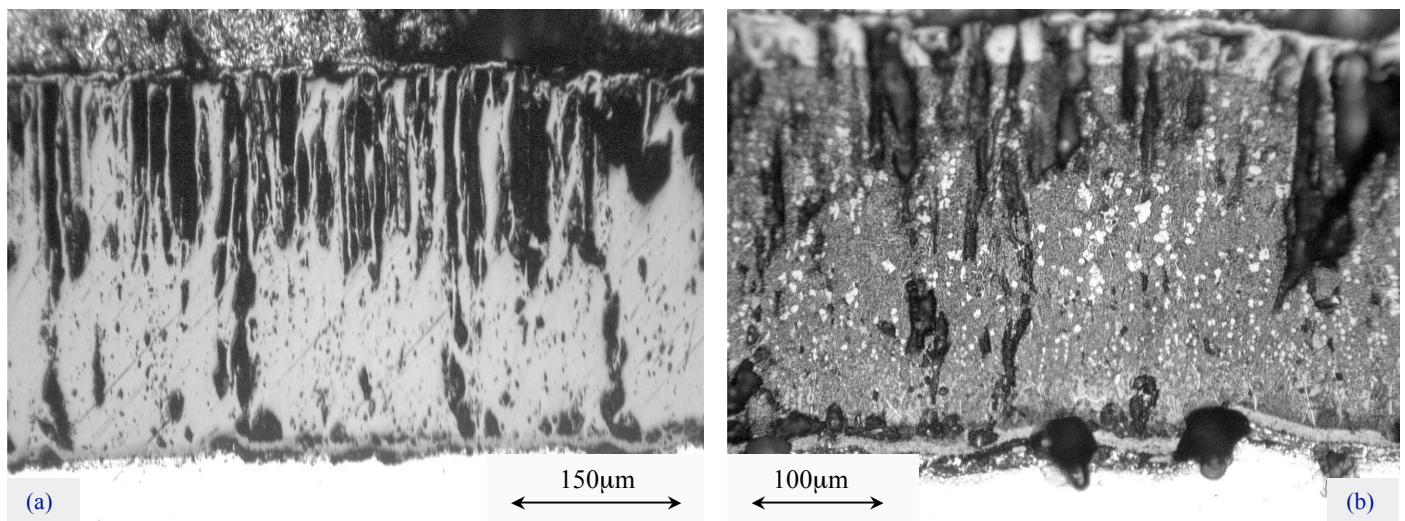
Figure 3.3.25: Optical micrograph of oxide scale formed on Alloy B at 1100-3600 seconds (a) polished only, (b) etched with 1% HCl in ethanol.

The optical microscopy gives information about the oxide scale microstructure features, however, sample preparation artefacts, etching methodology and optical microscopy limitations may mislead the observer. For example, different etches have different effects on the oxide scale layers. Although revealing the phase and grain boundaries is dependant on the etching time, but using different etches for different times could not reveal the grain boundaries of the majority of the samples. To avoid unreliable results, the optical microscope observations were compared with those obtained from other techniques, such as SEM, EDX and EBSD.

The microstructures of the oxide scale on steel surfaces were examined using standard Scanning Electron Microscopy (SEM) following investigation using optical microscopy in order to obtain a better understanding of the oxide scale microstructure. Depending on the purpose of the observations some samples were only polished and others were polished and then etched. Also images were taken only of the EBSD scanning area for comparison purposes, however, those images will be shown with the EBSD maps in later sections of this Chapter. The high magnification capability of the SEM technique helps to characterise the microstructural features of the oxide scale such as adherency, porosity, cracks and individual layer thicknesses within the oxide. Other microstructural features such as phase identity within the oxide scale could be better characterised using optical microscopy than SEM for the etched sample because the colour contrast of the optical micrograph was better than the SEM image.

Figure 3.3.26 shows a backscatter electron (QBSD) SEM image of oxide scale grown on IF steel at 750°C for 1200 seconds. The difference in the colour contrast in the image could be from difference phases, however, the phase discrimination and grain boundaries could not be determined clearly from such SEM images. Referring to the iron-oxygen phase diagram (Figure 1.2.4), the top layer could be magnetite and the bottom layer wüstite for the iron oxidised at 750°C. As shown in the image there is a very thin layer on the top separated from the scale by pores almost forming a lateral defect. Depending on the colour contrast observation, this top layer seems to be magnetite, as there are no colour differences between the top layer and underneath the lateral defect. This phenomenon has been found in other samples, as shown in later Sections, as the

magnetite layer is more susceptible to lateral cracking and pores than other phases. Moreover, the scale in the blistered area contains only magnetite as can be seen from the same figure. Figure 3.3.27 shows an SEM image of the polished cross section of the oxide scale formed on IF steel at 900°C-600 seconds. From the figure, the phases cannot be identified, also it is not clear whether the lateral crack within the scale is in-between two difference phase layers or a crack formed within the same phase layer. As shown in Figure 3.3.27, the oxide scale formed on the steel substrate at 900°C-600 seconds was not uniform. The same phenomenon was observed at 1000°C-1800 seconds; see Figure 3.3.28 (a). The cracks formed in the thick area, as show in 3.3.28 (b), could not be determined to be either transgranular or intergranular as the grain boundaries cannot be seen. It appears from the Figures 3.3.28 (c) and (d) that the junction between the thick and thin areas was more susceptible to cracking. The brittleness of the oxide scale can be seen clearly in the same Figure, which makes sample preparation difficult. As shown previously, the polishing causes grain pull out which makes the surface uneven. This makes distinguishing grain boundaries from cracks difficult.

Etching the sample gives better microstructural details as shown in Figure 3.3.29, which shows the scale grown at 1100°C for 1800 seconds. Secondary electron SEM imaging can distinguish between the phases but not as clear as a backscatter image, see Figure 3.3.29 (a and c). As mentioned earlier one of the advantages of SEM over optical microscopy is the high magnification. A high-magnified electron micrograph of the wüstite area is shown in Figure 3.3.29 (b). The image clearly shows the magnetite precipitates in the wüstite layer. The precipitates look rectangular in shape. In contrast to the optical micrograph, the haematite is the darkest phase in the scale; magnetite less dark and wüstite is the lightest in the SEM images.

The oxide scale formed on Alloy A at 900°C-1800 seconds was examined again using SEM. Comparing the images taken by optical microscopy and SEM, Figures 3.3.21 and 3.3.30, respectively, the SEM images give more details about magnetite precipitate distributions. As shown in Figure 3.3.21 (b), the shape of magnetite precipitates is difficult to recognize, but due to the high magnification in the SEM, the precipitate shapes and their locations within the scale can be clearly seen as in Figure 3.3.30 (b, c

and d). Etching the samples in 2% Nital caused pits to form within the scale making the observation of the magnetite precipitations more difficult, while SEM could overcome that problem. However, the phase discrimination from optical micrographs is easier than from SEM images because of the better optical microscopy image contrast. The grain boundaries of the steel substrate can be seen clearly in both Figures 3.3.21 and 3.3.30, but none of the techniques could completely reveal grain boundaries within the oxide scale layers. In fact a combination of optical microscopy and SEM observation can reveal phase boundaries but not grain boundaries in the oxide scale. As mentioned earlier, colour contrast in backscatter images is easier than in secondary electron images. As shown in Figure 3.3.31 (a), the layers are more visible than in (b). However, in both images, the phase boundaries can be seen but not the grain boundaries. The other SEM images and optical micrographs that related to EBSD maps area are displayed in later sections in this Chapter.
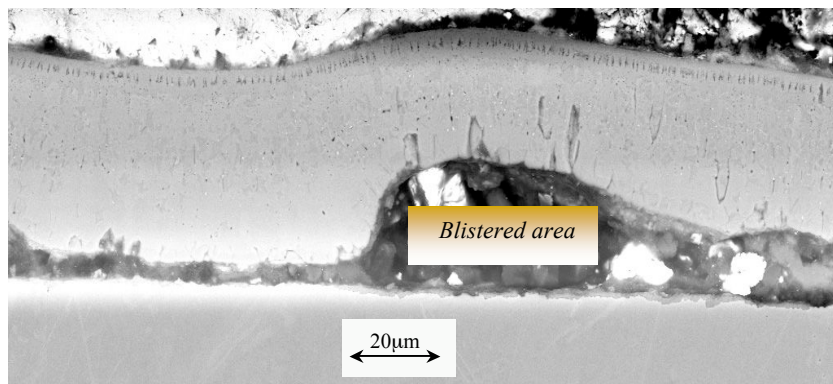
Figure 3.3.26: SEM image of the oxide scale formed on IF steel at 750°C-1200 seconds. Polished sample, 20kV EHT, 11 mm WD, QBSD detector image.
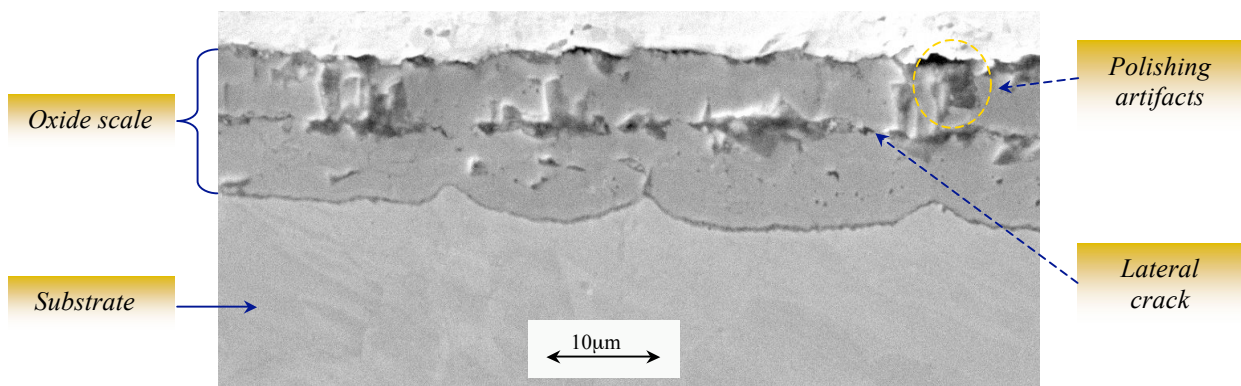
Figure 3.3.27: SEM image of the oxide scale formed on IF steel at 900°C-600 seconds. Polished sample, 20kV EHT, 9 mm WD, SE1 detector image.
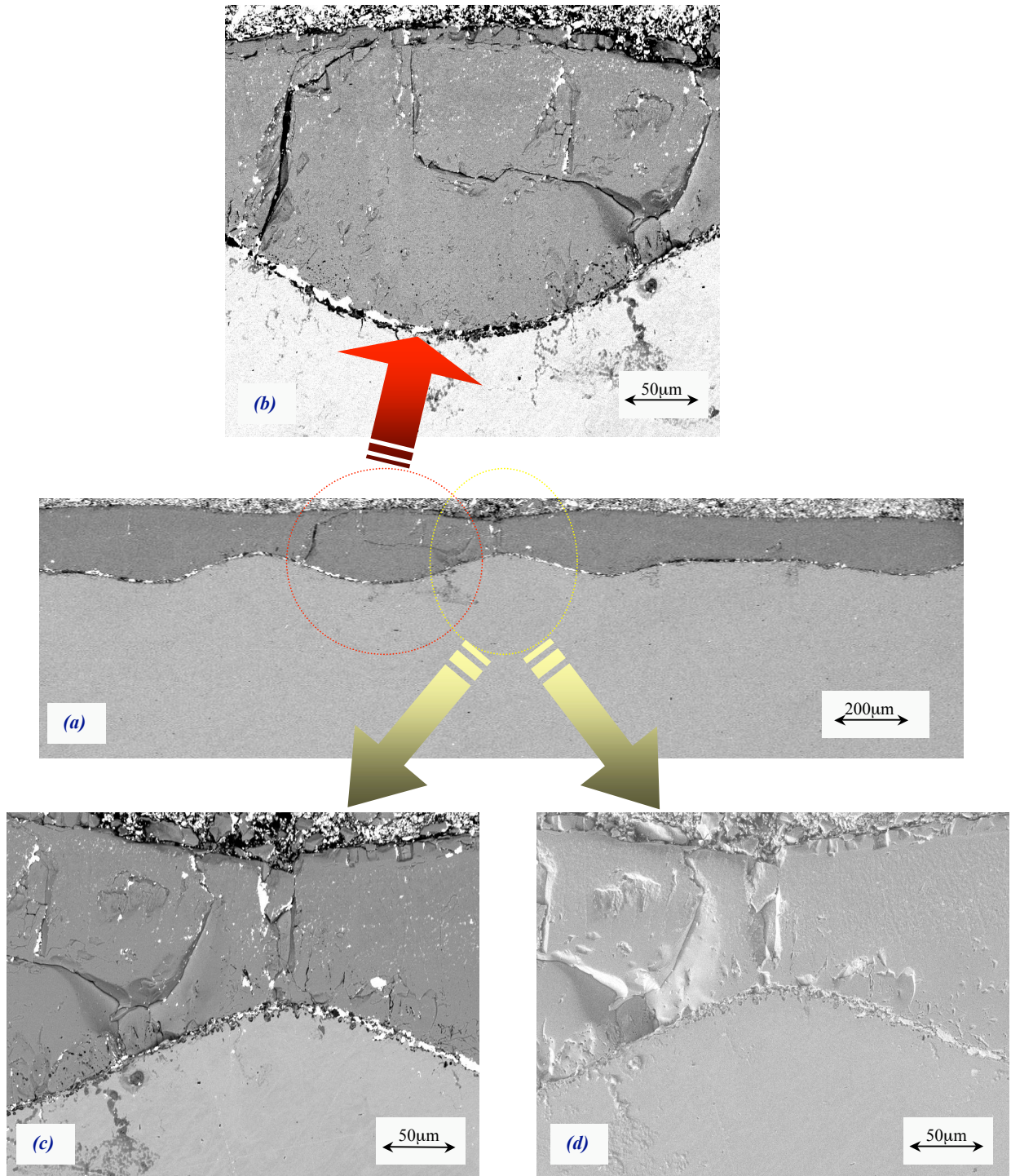
Figure 3.3.28: SEM image of the oxide scale formed on IF steel at 1000°C-1800 seconds. Polished sample, 20kV EHT, 16 mm WD, (a, b and c) QBSD and (d) SE1 detector images.
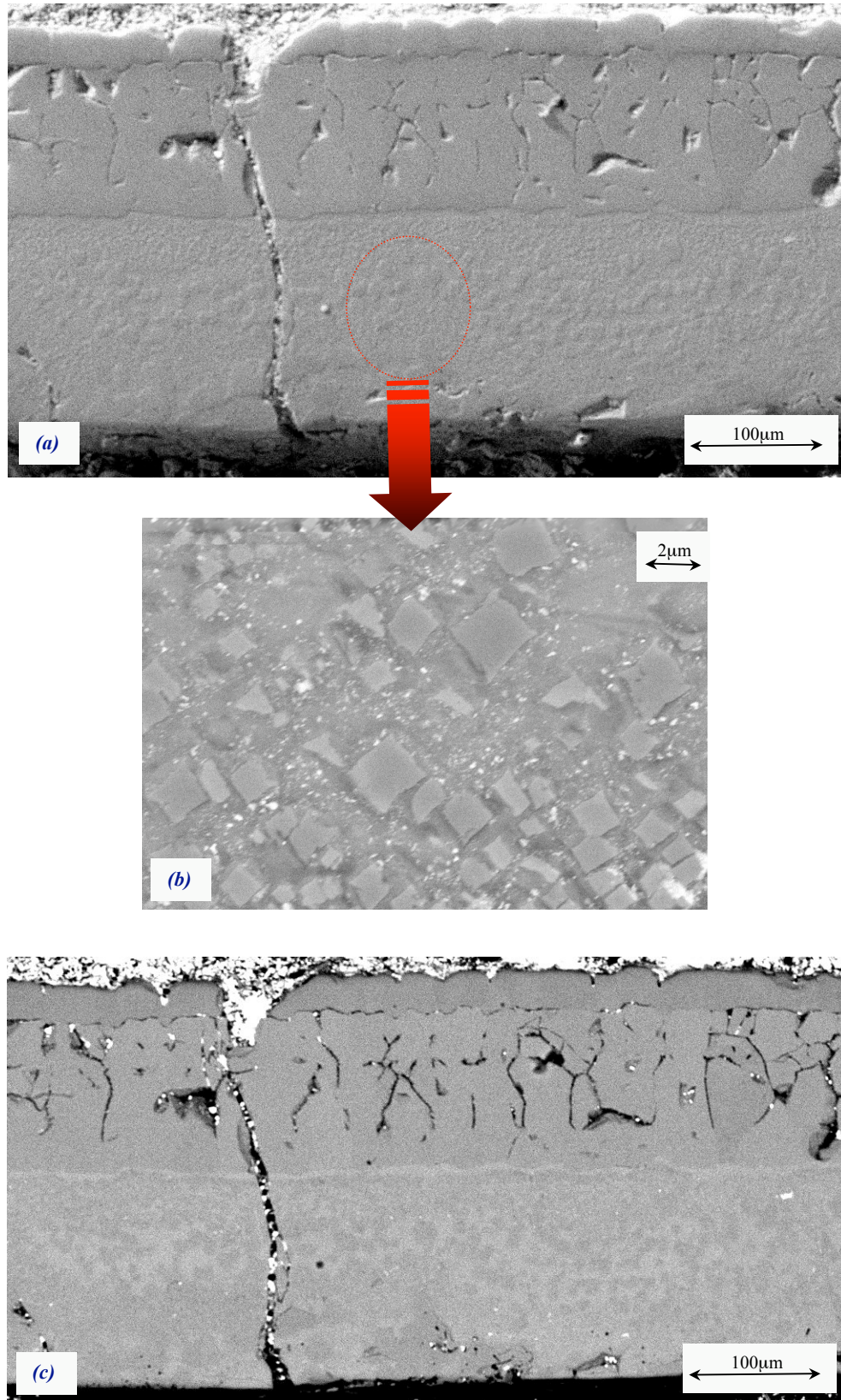
Figure 3.3.29: SEM image of the oxide scale formed on IF steel at 1100°C-1800 seconds, 20kV EHT, 15 mm WD. (a) SE1 image, (b) High magnified area in (a), (c) QBSD detector images.
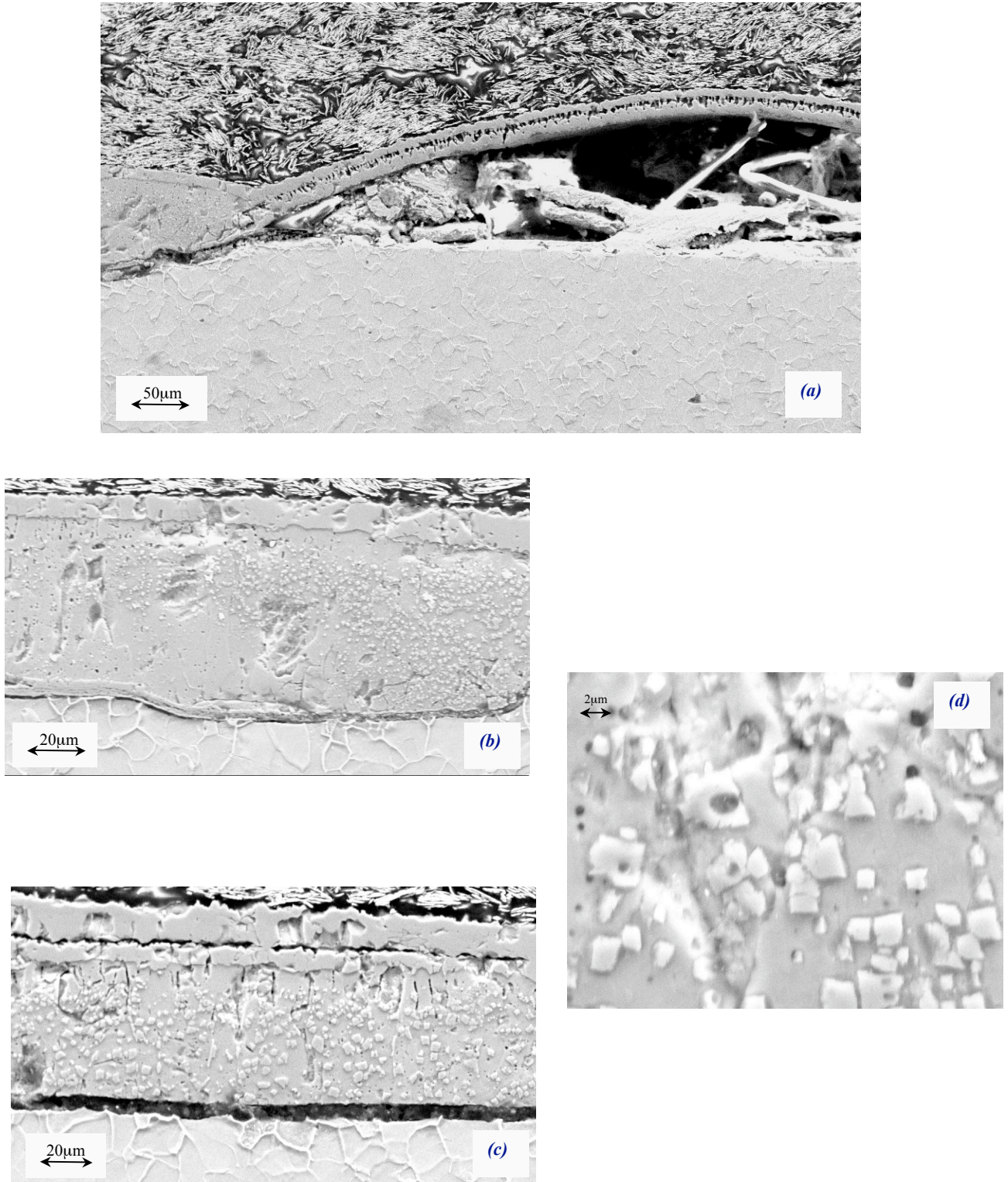
Figure 3.3.30: SEM image of the oxide scale formed on Alloy A at 900°C-1800 seconds as in Figure 3.3.21 (a) SE1 image, 20kV EHT, 18mm WD (b) the adherent area near spallation junction, (c) the adherent area far away from the blister, (d) high magnification of magnetite precipitations.
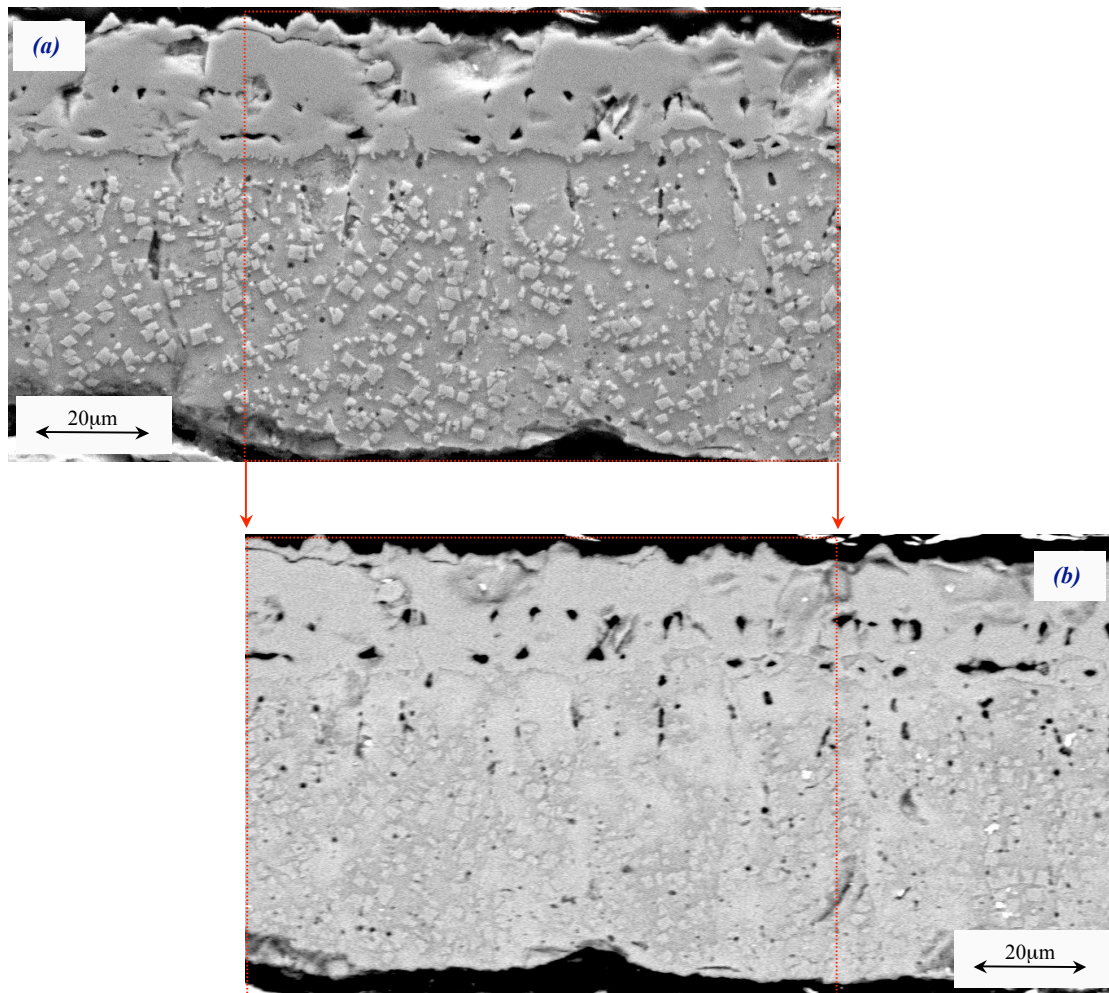
Figure 3.3.31: SEM image of the oxide scale formed on Alloy A at 900°C-1800 seconds. Polished sample, 20kV EHT, 18 mm WD, (a) SE1 and (b) QBSD detector images.

3.4 Oxide Scale Grain Size Measurements

As mentioned in Section 3.3, the optical and SEM microscopy could not reveal the grain boundaries in the oxide scale layers. Using etchants such as 1% HCl in ethanol and 2% Nital could reveal partial but not complete grain boundaries. Furthermore, it was difficult to distinguish between the grain boundaries and small cracks as well as some scratches due to artefact generated from the sample preparation. However, in a number of cases none of the chemical etchants could reveal any grain boundaries within the oxide scale layers. For this reasons it was not possible to measure the grain size in the oxide scale using conventional techniques such as optical or scanning electron microscopy. Electron Backscatter Diffraction (EBSD) can give complete microstructure characteristics as it can expose grain boundaries as well as phase boundaries of the oxide scale. This unique feature in EBSD facilitates grain size measurement for each phase within the oxide scale as well as their shapes.

Figures 3.4.1 – 3.4.6 show the comparisons between optical, SEM and EBSD images. The Figures show the oxide scale formed on IF steel exposed for 1800 seconds at different high temperatures. The classical three layer oxide scale could be seen more clearly at higher temperatures. Thus, for simplicity purposes, the Figures are arranged from highest temperature to the lowest. Figure 3.4.1 shows the oxide scale formed on IF steel at 1100°C-1800 seconds. Figures 3.4.1 (a) and (b) show the optical and SEM micrographs, respectively. The phase boundaries can be clearly seen, but there is no indication of grain boundaries in each phase within the scale. One of the powerful features of the EBSD is the Image Quality (IQ) map which provides better contrast of the grain boundaries than conventional secondary electron SEM. Therefore, obtaining grain size, shape and detailed microstructure of the phases using EBSD characterisation technique is more reliable than other techniques. As shown in Figure 3.4.1 (c), the phase and grain boundaries can be seen clearly in the IQ map. Moreover, grain boundary characterisation can be carried out using the EBSD data. Figure 3.4.2 (a) shows the misorientation map for the same scanning area. The misorientation angle distribution is indicated in the same figure referring to the misorientation chart. Characterising the grain boundaries in terms of rotational angle between two grains is shown in grain boundaries level map, Figure 3.4.2 (b). The grain boundaries in the sample area can be characterized easily, whether low (2 - 15°) or high (15 - 180°) angle. Characterising grain boundary misorientations is important

for grain size measurements as the EBSD user can decided which grain boundaries are to be excluded in the grain size measurements. In this study only high angles (15 - 180°) grain boundaries are included. Figure 3.4.2 (c) shows the Unique Grain Colour (UGC) map, where the grains are shaded with random colours. It should be mentioned here that the colours used in this option do not correspond in any way to lattice orientations. Thus, from this map the grain size can be calculated as well as the grain shape. Figure 3.4.3 shows the EBSD grain size measurements of magnetite and haematite grains within the scale. As can be seen from the figure, ESBD software only calculates the grains separated by high angle grain boundaries. However, this is a user-defined feature in which the user can include or exclude specific grain boundaries from the calculations, see area 1 in Figure 3.4.2 (c). The two grains indicated in area 2 in the same figure are separated by a low angle grain boundary as can be seen in Figure 3.4.2 (b), but the grains are separated in the unique grain colour map. This is related to differences in phase between the two grains (magnetite and wüstite) as will be discussed further in Section 3.5. One of the other powerful features of EBSD grain size measurements is that the software automatically excludes the grains on the edges, as can be seen from Figure 3.4.3 (a) and (b). Thus, the software, wherever it identifies an incomplete grain in the map, will exclude it from the calculations. It should be noted that all the grain size measurements were checked and compared with manually made measurements.

The areas 3 and 4 in Figure 3.4.2 (b) show the EBSDs ability to distinguish the grain boundaries from the artefact generated during sample preparations. As indicated in areas 3 and 4, the scratches in the cross section are not counted as grain boundaries. This feature is very useful and has advantages over conventional techniques such optical or scanning election microscopy. Moreover, micro-scratches or cracks in the specimen could mislead the observer when other techniques are used.

It should be mentioned that magnetite precipitates are excluded from the grain size calculation in both EBSD and in hand calculations using the linear intercept method. As shown in Figure 3.4.2 (a) and (b), the magnetite grains are separated by either low or high grain boundaries depending on their location within the scale. Whilst, magnetite precipitates and wüstite grains are separated by very low grain boundaries and even appear as one grain in the IQ map, Figure 3.4.1 (c). However, in the EBSD

grain size calculations this could be avoided as grain size is measured for each phase separately not the whole sample area. The software automatically excluded other phases during individual grain size measurements for each phases within the scale, Figure 3.4.3.

Figure 3.4.4 shows the microstructure of the oxide scale on IF steel formed at 1000°C-1800 seconds. As can be seen from Figures 3.4.4, the SEM-QBSD image in (a) and SEM-SE image in (b) can reveal phase boundaries due to different electron reflection from the different phases, but no indication of grain boundaries within the scale. However, the QBSD image could reveal the gap between the steel substrate and the oxide scale better than the SE image. The colour contrast between the phases in the scale is far better in the optical micrograph in Figure 3.4.4 (c) than the SEM images. Also the damage due to the artefacts generated during sample preparation and cracks are revealed in the optical micrograph but not in the SEM images (a and b). Etching the cross section in 1% HCl in ethanol could not reveal the grain boundaries even in the optical micrograph. When the sample was etched for a longer time, pits were generated and the microstructure features could not be seen clearly. The sample in Figure 3.4.4 (c) is etched for 10 seconds and pits can be seen. Generally the pits formed, especially near magnetite precipitates, on most of the samples. In order to eliminate these ambiguities, EBSD scans were carried out on the same sample area. Figures 3.4.4 (d, e and f) show the EBSD Image Quality (IQ), Grain Boundary Level (GBL) and Unique Grain Colour (UGC) maps, respectively. From the maps, the grain boundaries were characterised which made the grain size measurements easier and more accurate.

Etching the cross section of the oxide scale formed on IF steel at 900°C-1800 seconds with 1% HCl in ethanol, for 15 seconds was sufficient to reveal some of the grain boundaries within the scale, see Figure 3.4.5. However, grain boundaries revealed in this manner were incomplete in some areas; see area 1 and 2 in the same figure. It should be noted that even etching for 15 seconds caused pit generation in the upper wüstite layer in the scale. EBSD scanning carried out for the same sample area is shown in Figure 3.4.6. The EBSD maps are shown in Figure 3.4.6 (a - d) and the grain size measured in the same manner as previous samples. Appendices 9 and

10 show EBSD images of the oxide scales formed on Alloy A and B, respectively, at different times and temperatures.

Table 3.4.1, 3.4.2 and 3.4.3 show the grain sizes of the oxide scale phases developed on IF, Alloy A and Alloy B, respectively. The samples were exposed to different temperatures for 1800 seconds. All EBSD calculations were compared with linear intercept method measurements as a double check. At most temperatures the grain size, i.e. wüstite, in growth direction was bigger than in transverse direction, therefore, it was more convenient to measure the grain size in both directions rather than depending on grain area measurements.

As shown in Figure 3.4.7 the wüstite and magnetite grain size increased with increasing temperatures on the IF steel. The wüstite grain size showed dramatic acceleration above 1000°C. The magnetite grain size increased steadily with increasing temperature, except in the growth direction at 1100°C. The aspect ratio of the wüstite grains is near to 1 only at 1100°C where the grains are approximately equiaxed, at the rest of the temperatures the wüstite grain shape was columnar, for further details see Appendix 11. Whilst, the magnetite grain aspect ratio is ~ 1 at 1000°C, see Figure 3.4.8 also Appendix 11, the word elongated in Appendix 11 indicates that the grains are elongated along the substrate surface. The magnetite grain shape at 900°C is indicated as elongated, which means the shape is not equiaxed as the length of the grain in transverse direction is bigger than the length in the growth direction. Furthermore, this can be clearly seen in the Figure 3.4.8 where the points in the curve above 1 indicate that the shape is columnar in the growth direction. Whereas, the points under 1 indicate that the grain shape is not equiaxed but elongated in the transverse direction.

Figure 3.4.9 shows the grain size of the wüstite and magnetite grown on Alloy A at 1800 seconds at different temperatures. The same trends as on the IF steel can be seen as the oxide grain size increased with increasing temperature. There is a dramatic escalation of the wüstite grain size at 1000°C, but the magnetite grain size most dramatic increase is at 1100°C. The wüstite grain shape was columnar at 750, 900 and 1000°C and elongated at 1100°C, whereas, the magnetite grain shape was columnar at 750°C and became equiaxed at 900 and 1000°C, then grew laterally

forming an elongated shape at 1100°C, see Appendix 11. Figure 3.4.10 shows the aspect ratio versus temperature graph. The aspect ratio decreased with increasing temperature, which indicates that the grain shape is changing in order of columnar → equiaxed → elongated with increasing temperature.

Figures 3.4.11 and 3.4.12 show the oxide grain size and aspect ratio with temperature graphs for Alloy B, respectively. There was no dramatic change in grain growth for either the wüstite or magnetite at any temperature. The oxide on Alloy B has the same trend as IF and Alloy A steels, where the grain size increased with increasing temperatures. The aspect ratios of the wüstite grains is greater than 1 at all temperatures, see Figure 3.4.12, making the shapes of the grains columnar, see also Appendix 11. The magnetite grain aspect ratio was ~ 1 only at 900°C and then started to grow laterally becoming elongated at higher temperatures.

Figures 3.4.13 and 3.4.14 show the wüstite grain size change in the growth and transverse directions of IF, Alloy A and Alloy B steels with temperature. Figures 3.4.15 and 3.4.16 show the same comparison for magnetite grains. While the IF steel wüstite grain size increases steadily in the growth direction, dramatic growth can be seen in transverse direction at 1000°C, see Figures 3.4.13 and 3.4.14. The more dramatic increase at 1100°C in transverse direction on Alloy A makes the shape elongated. Alloy B did not show any dramatic changes in grain size in either direction. The same phenomenon can be seen in Figures 3.4.13 and 3.4.14 for Alloy A magnetite grains at 1100°C. However, this phenomenon can be related to oxidation growth rate and kinetics as will be discussed in Chapter 4.

Some EBSD scans were performed to observe the effect of the time of oxidation on grain size. A temperature of 1100°C was chosen for this purpose because the three classical layers (wüstite, magnetite and haematite) are thick enough to be characterised easily and more clearly than at lower temperatures. Oxide scales on Alloy A formed at 1100°C were grown for 600, 1200, 1800 and 3600 seconds are shown in Appendix 9. Table 3.4.4 (a) and (b) show the grain size of the oxide scale formed on Alloy A at 1100°C for different times of exposure. The wüstite grain size increased in the growth direction until ~1200 seconds and then started to decrease. Whilst, in transverse direction the wüstite grains grow with time, see Figure 3.4.17

also Appendix 9 and 11. The magnetite grains are equiaxed at 600 and 1200°C, and then grow laterally making them elongated at 1800 seconds. The grain shape of the magnetite becomes columnar where the wüstite phase is completely transformed, allowing the magnetite grains to grow vertically making columnar grains at 3600 seconds. The same phenomenon was observed for haematite, see Table 3.4.4 (a, b) and Appendix 11.
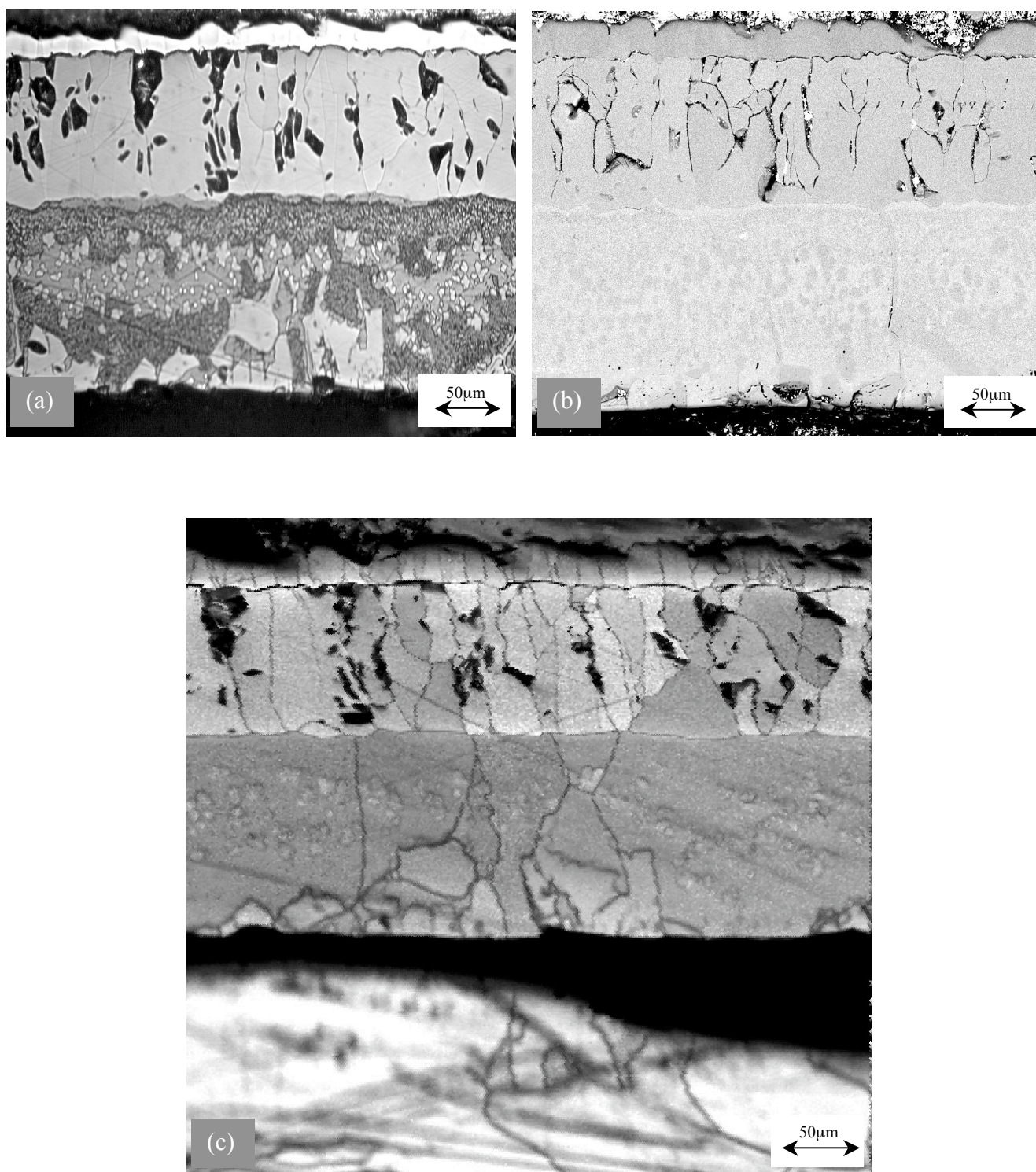
Figure 3.4.1: IF steel oxidised at 1100°C for 1800 seconds. (a) Optical micrograph of etched cross section with 1% HCl in ethanol for 10 seconds, (b) SEM-QBSD detector image, 20kV, 16 mm WD, (c) EBSD Image Quality map, 0.1 scanning step size.
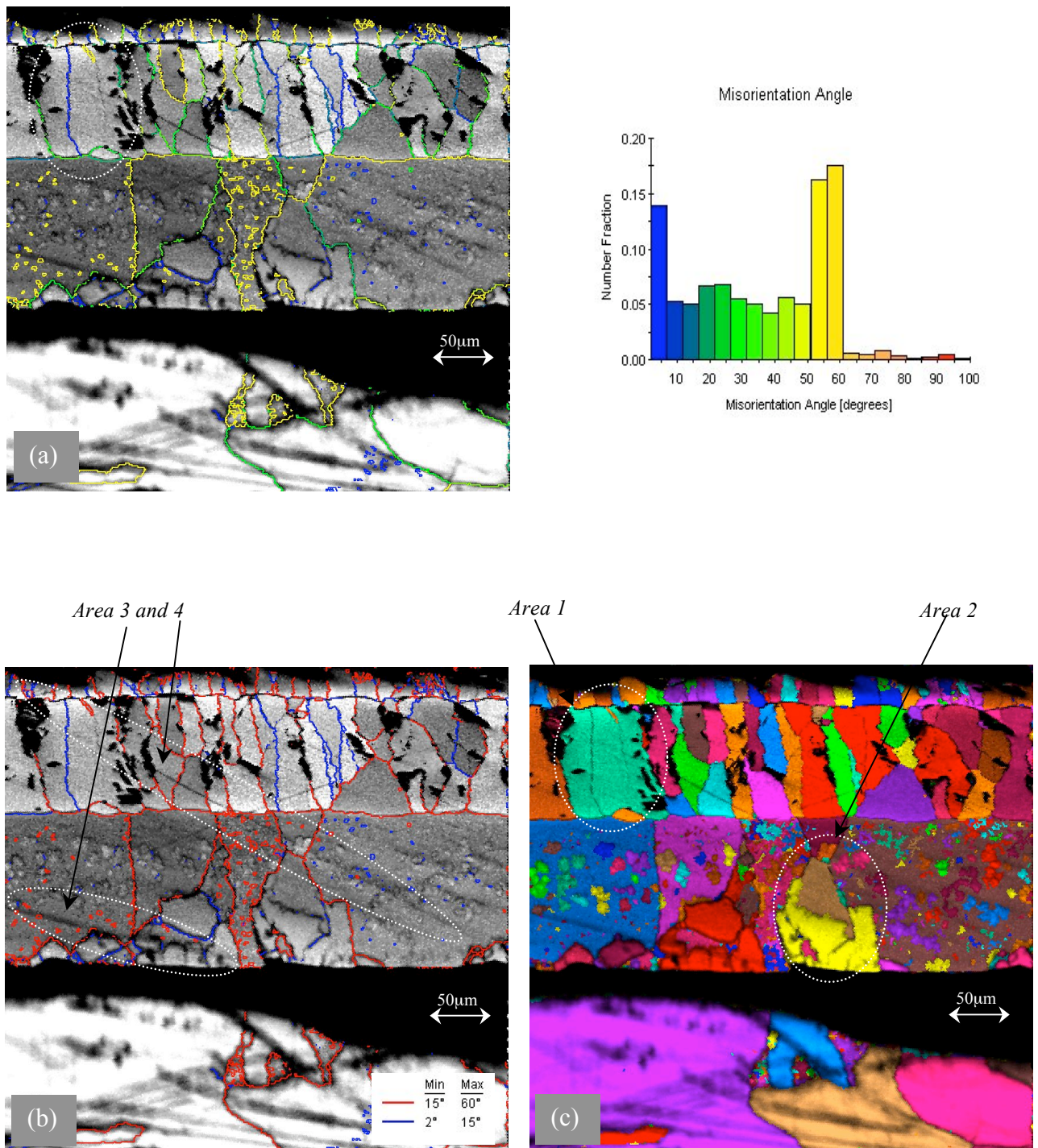
***Figure 3.4.2: IF steel oxidised at 1100°C for 1800 seconds. (a) EBSD-Misorientation map
and misorientation volume factions vs. misorientation angles graph indicates the
misorientation distribution within the map, (b) EBSD-Grain Boundary Level map,
characterising low and high grain boundary angles within the map, (c) EBSD-Unique Grain***
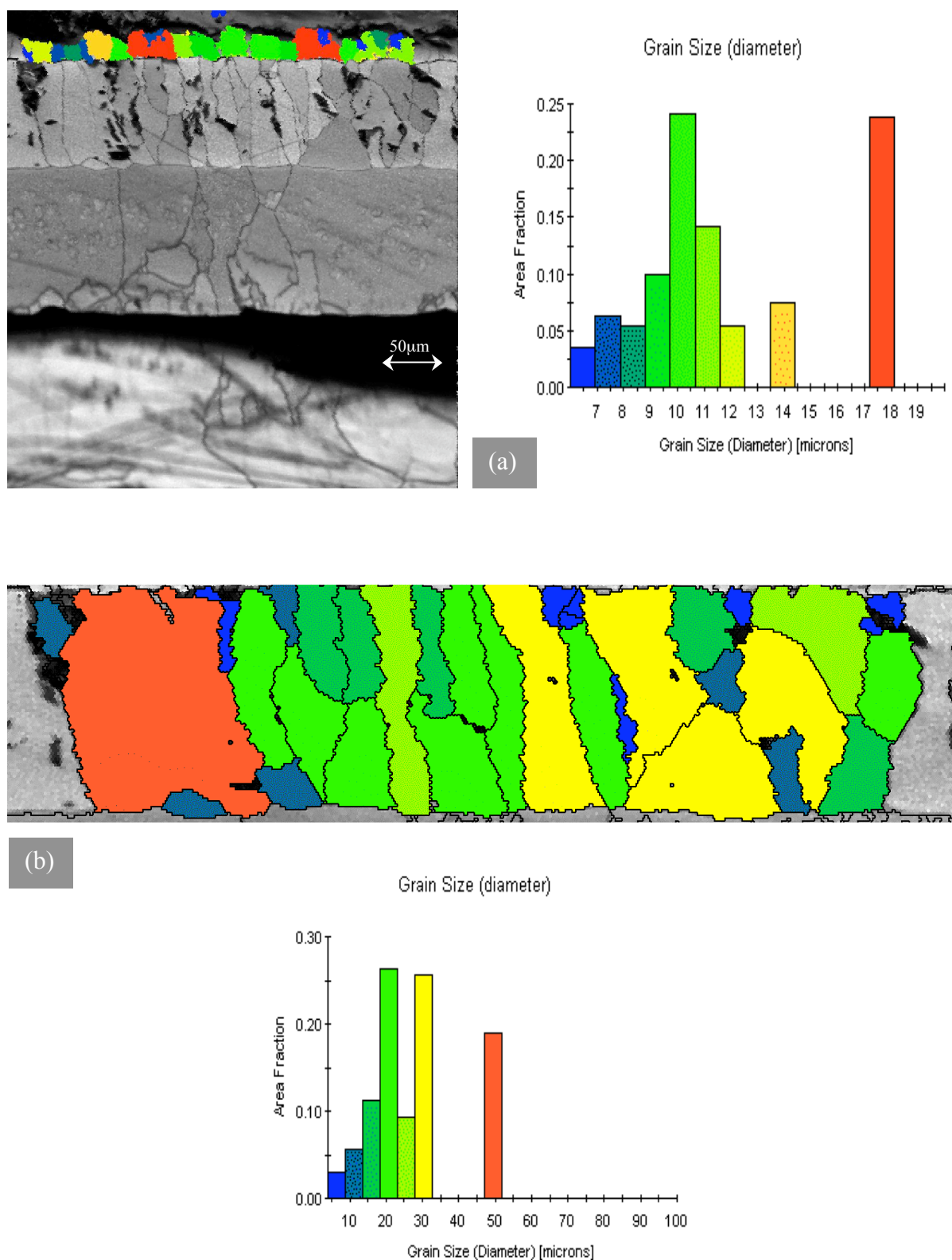
Figure 3.4.3: EBSD grain size measurement for (a) haematite (b) magnetite grains in the scale formed on IF steel at 1100°C after 1800 seconds. The charts with the images showing the area fraction vs. grain size in the map (EBSD calculation).
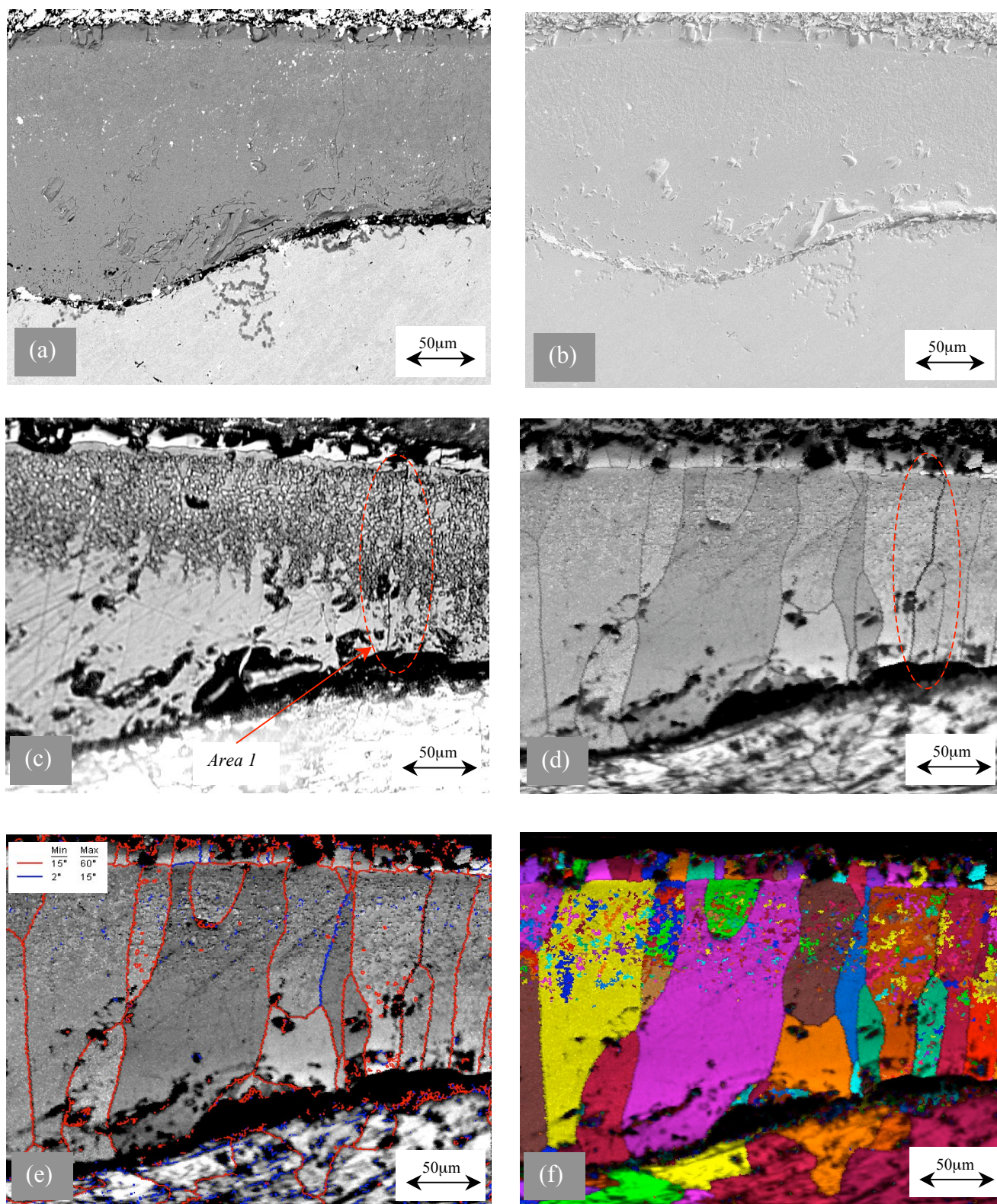
***Figure 3.4.4: IF steel oxidised at 1000 °C for 1800 seconds. (a) SEM-QBSD detector image,
20kV, 16 mm WD, (b) SE SEM image, (c) Optical micrograph of etched cross section with 1%
HCl in ethanol for 10 seconds, (d) EBSD Image Quality map, 0.1 scanning step size, (e)
EBSD-Grain boundary level map, (f) EBSD-Unique grain colour map.***
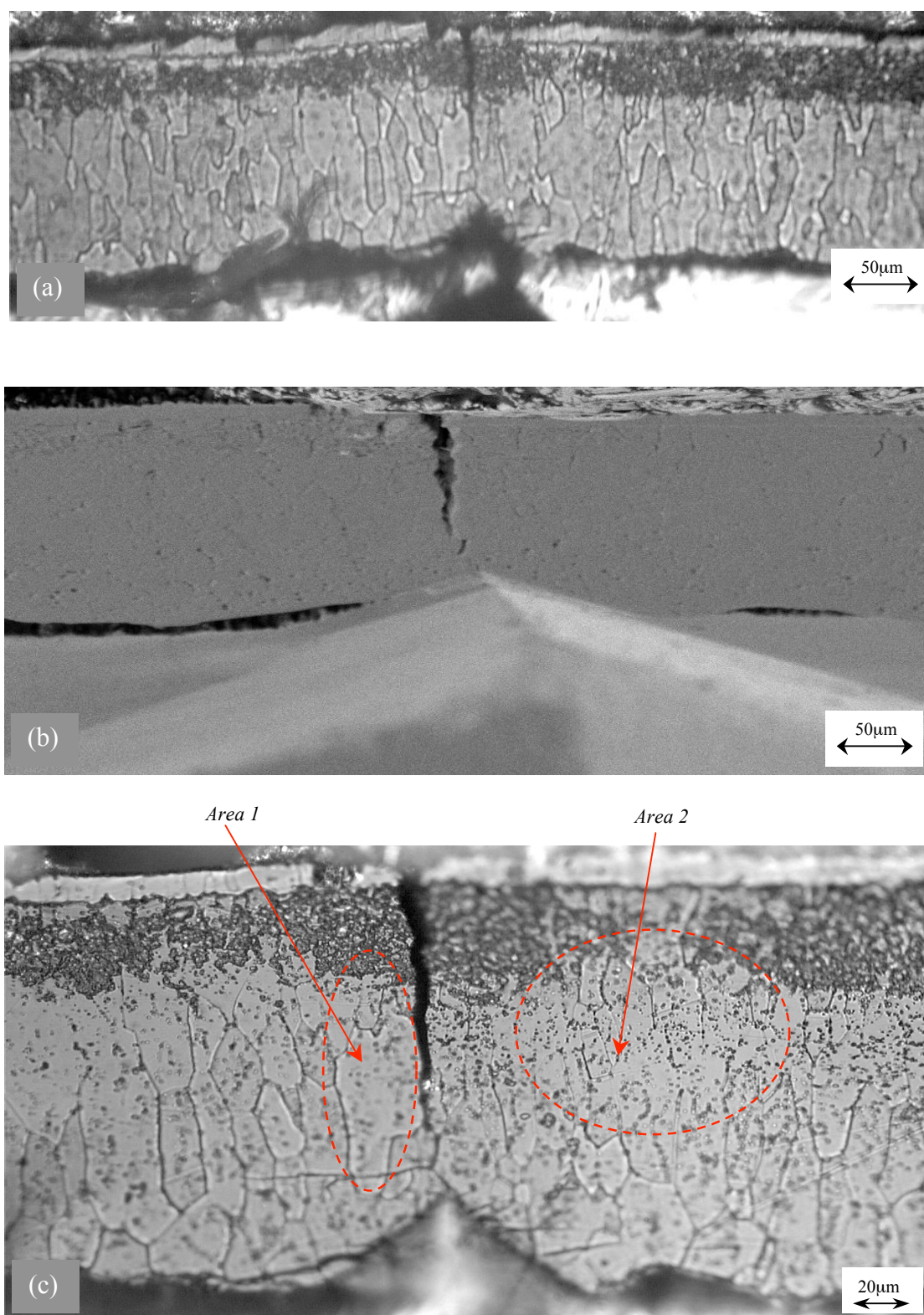
Figure 3.4.5: IF steel oxidised at 900°C for 1800 seconds. (a) Optical micrograph of etched cross section with 1% HCl in ethanol for15 seconds, (b) SEM-SE detector image, 20kV, 18 mm WD, (c) Optical micrograph of higher magnified area in (a).
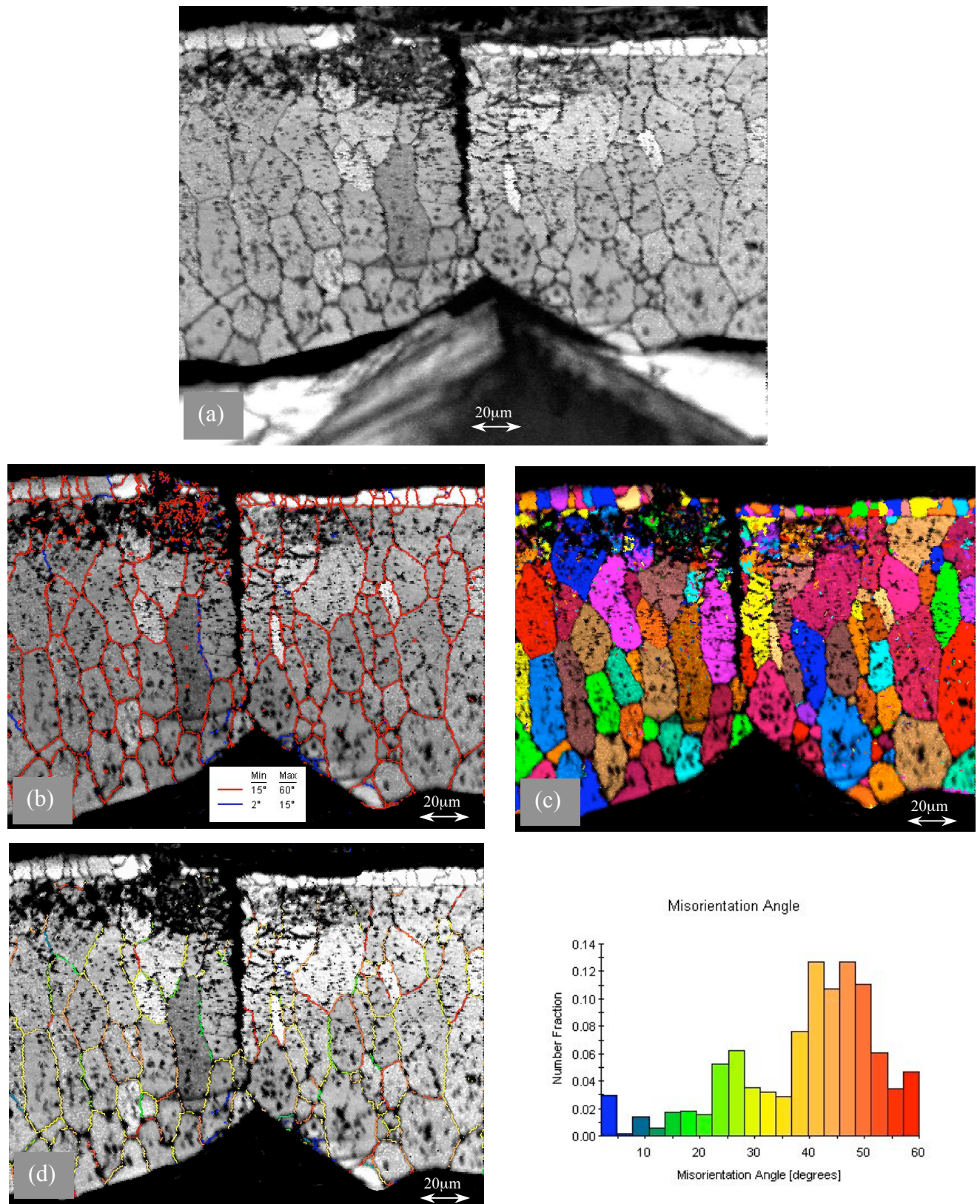
Figure 3.4.6: EBSD maps of IF steel oxidised at 900°C for 1800 seconds, 0.02 step size. (a) EBSD Image Quality map, (b) EBSD-Grain boundary level map, characterising low and high grain boundary angles in the map, (c) EBSD-Unique Grain Colour map, (d) EBSD-Misorientation map and misorientation volume factions vs. angles graph indicates misorientation distribution within the map

IF Steel

Table 3.4.1-a: IF Steel oxide scale phases grain size (µm-diameter) in Growth Direction (GD or ND)

Temperature °C	Wüstite	Magnetite	Haematite
1100	148.64 ± 14.30	77.34 ± 13.11	17.45 ± 2.35
1000	123.03 ± 30.29	17.27 ± 0.69	Not observed
900	36.81 ± 8.96	8.56 ± 1.16	Not observed
750	7.67 ± 3.45	6.48 ± 3.42	Not observed
650	6.45 ± 2.39	3.94 ± 0.71	Not observed

Table 3.4.1-b: IF Steel oxide scale phases grain size (µm-diameter) in Transverse Direction (TD)

Temperature °C	Wüstite	Magnetite	Haematite
1100	165.88 ± 16.76	29.17 ± 11.69	16.61 ± 2.12
1000	48.19 ± 18.36	17.73 ± 1.71	Not observed
900	13.20 ± 10.37	17.68 ± 2.13	Not observed
750	3.65 ± 0.68	1.18 ± 2.49	Not observed
650	2.36 ± 0.95	1. 12 ± 1.85	Not observed

Alloy A

Table 3.4.2-a: Alloy A oxide scale phases grain size (µm-diameter) in Growth Direction (GD or ND)

Temperature °C	Wüstite	Magnetite	Haematite
1100	185.95 ± 3.32	131.74 ± 29.36	52.11 ± 1.23
1000	111.56 ± 25.69	24.21 ± 2.63	Not observed
900	22.89 ± 5.36	7.31 ± 1.68	Not observed
750	8.73 ± 9.84	3.91 ± 2.85	Not observed

Table 3.4.2-b: Alloy A oxide scale phases grain size (µm-diameter) in Transverse Direction (TD)

Temperature °C	Wüstite	Magnetite	Haematite
1100	216.35 ± 9.6	196.63 ± 36.42	41.36 ± 2.69
1000	72.63 ± 12.36	26.84 ± 0.79	Not observed
900	10.73 ± 2.41	6.92 ± 0.96	Not observed
750	1.46 ± 6.35	1.99 ± 2.37	Not observed

Alloy B

Table 3.4.3-a: Alloy B oxide scale phases grain size (μm-diameter) in Growth Direction (GD or ND)

Temperature °C	Wüstite	Magnetite
1100	80.02 ± 12.64	17.68 ± 1.97
1000	49.71 ± 11.65	17.59 ± 2.65
900	39.54 ± 7.29	11.85 ± 0.84

Table 3.4.3-b: Alloy B oxide scale phases grain size (μm-diameter) in Transverse Direction (TD)

Temperature °C	Wüstite	Magnetite
1100	47.05 ± 19.54	25.36 ± 6.31
1000	34.87 ± 5.49	24.52 ± 1.38
900	6.47 ± 4.63	10.24 ± 1.47

Table 3.4.4-a: Alloy A oxide scale phases grain size (μm-diameter) in Growth Direction (GD) at 1100°C for different times.

Time(seconds)	Wüstite	Magnetite	Haematite
600	204.16 ± 15.69	21. 8 ± 7.24	not observed
1200	291.47 ± 19.87	41. 7 ± 17.65	8.3 ± 2.6
1800	185.95 ± 25.69	131.74± 29.36	52.11 ± 1.23
3600	not observed	197.36 ± 17.56	118.66± 3.78

Table 3.4.4-b: Alloy A oxide scale phases grain size (μm-diameter) in Transverse Direction (TD) at 1100°C for different times.

Time(seconds)	Wüstite	Magnetite	Haematite
600	54.16 ± 13.65	23.49 ± 6.58	not observed
1200	141.36 ± 25.69	39.56 ± 6.53	37.73 ± 2.36
1800	216.35 ± 9.6	196.63 ± 36.42	41.36 ± 2.69
3600	not observed	118.66 ± 10.34	59.33 ± 16.89

Temperature (°C)

	650	750	900	1000	1100
■ wustite in GD	6.45	7.69	36.81	123.03	148.64
■ wustite in TD	2.36	3.65	13.2	48.19	165.19
□ magnetite in GD	3.94	6.48	8.56	17.27	77.34
■ magnetite in TD	1.12	1.18	17.68	17.73	29.17
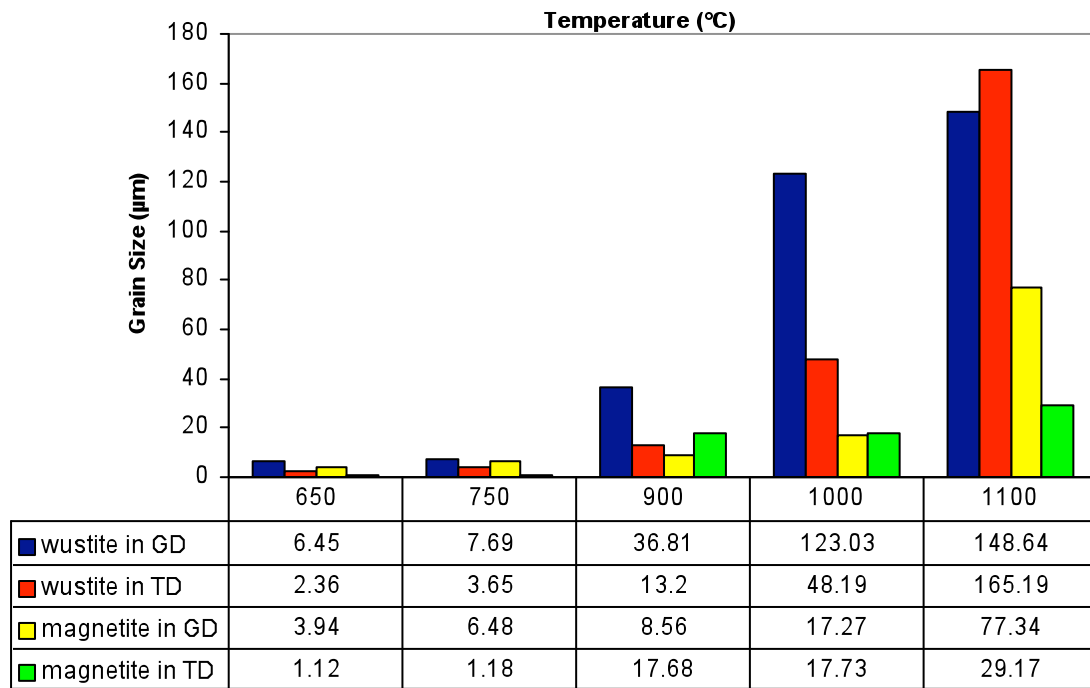
Figure 3.4.7: IF steel oxide phases grain size versus temperature at 1800 seconds in both growth and transverse directions.
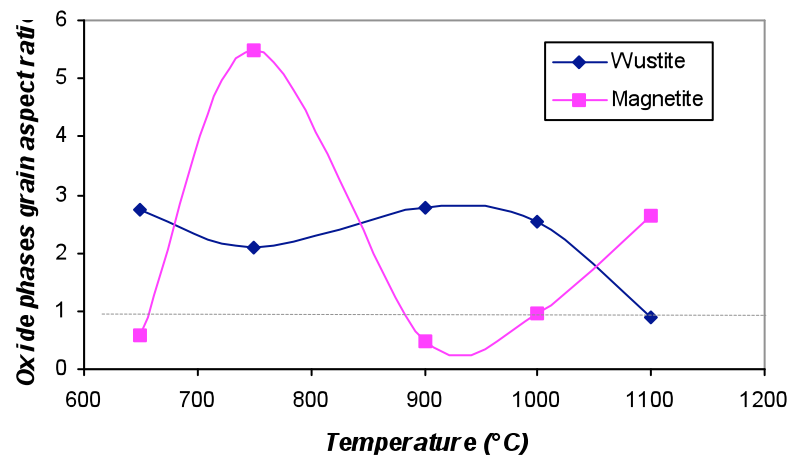
Figure 3.4.8: Wüstite and magnetite grain size aspect ratio of IF steel oxidised at different temperature for 1800 seconds.

Temperature (°C)	750	900	1000	1100
■ wustite in GD	8.73	22.89	111.56	185.95
■ wustite in TD	1.46	10.73	72.63	216.35
□ magnetite in GD	3.91	7.31	24.21	131.74
■ magnetite in TD	1.99	6.92	26.84	196.63
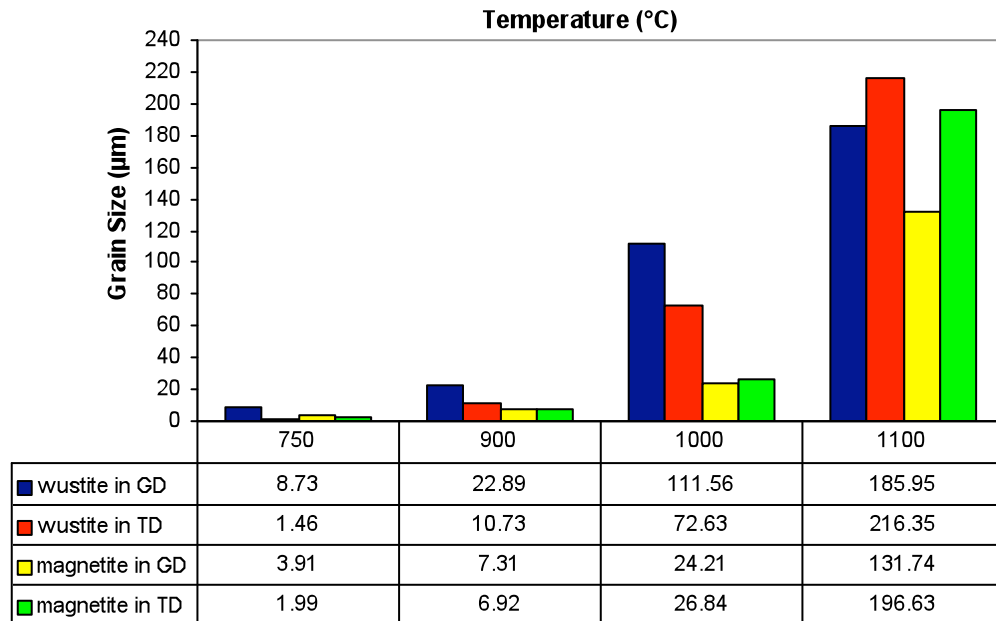
Figure 3.4.9: Alloy A oxide phases grain size versus temperature at 1800 seconds in both growth and transverse directions.
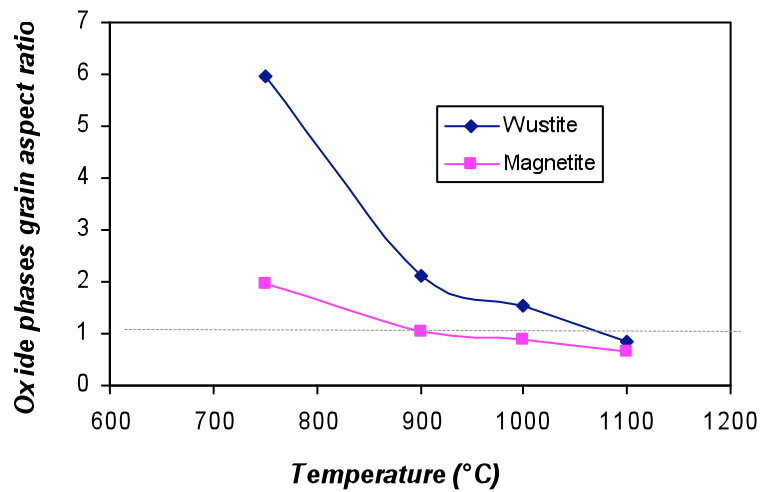
Figure 3.4.10: Wüstite and magnetite grain size aspect ratio of Alloy A oxidised at different temperature for 1800 seconds.

Temperature (°C)	900	1000	1100
■ wustite in GD	39.54	49.71	80.02
■ wustite in TD	6.47	34.87	47.05
□ magnetite in GD	11.85	17.59	17.69
■ magnetite in TD	10.24	24.52	25.36
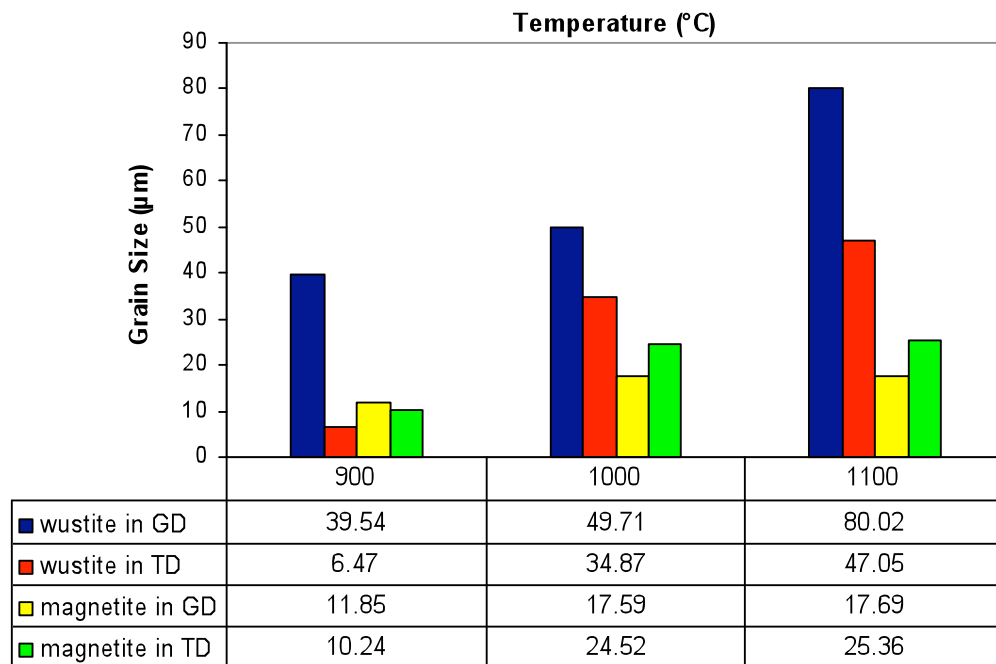
Figure 3.4.11: Alloy B oxide phases grain size versus temperature at 1800 seconds in both growth and transverse directions.
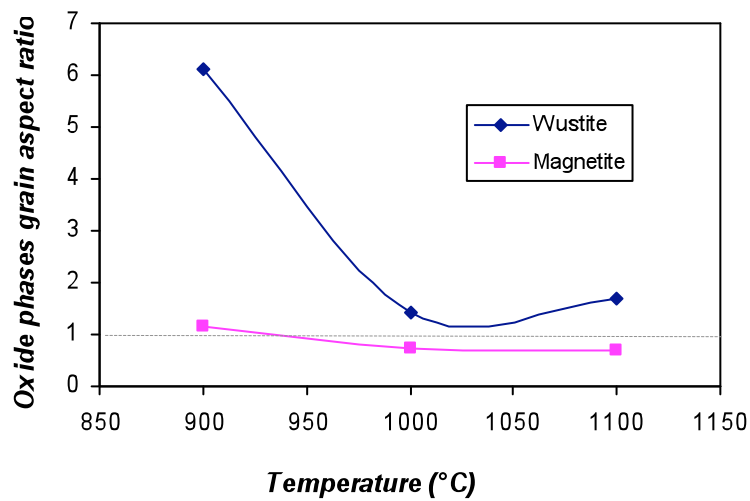
Figure 3.4.12: Wüstite and magnetite grain size aspect ratio of Alloy B oxidised at different temperature for 1800 seconds.
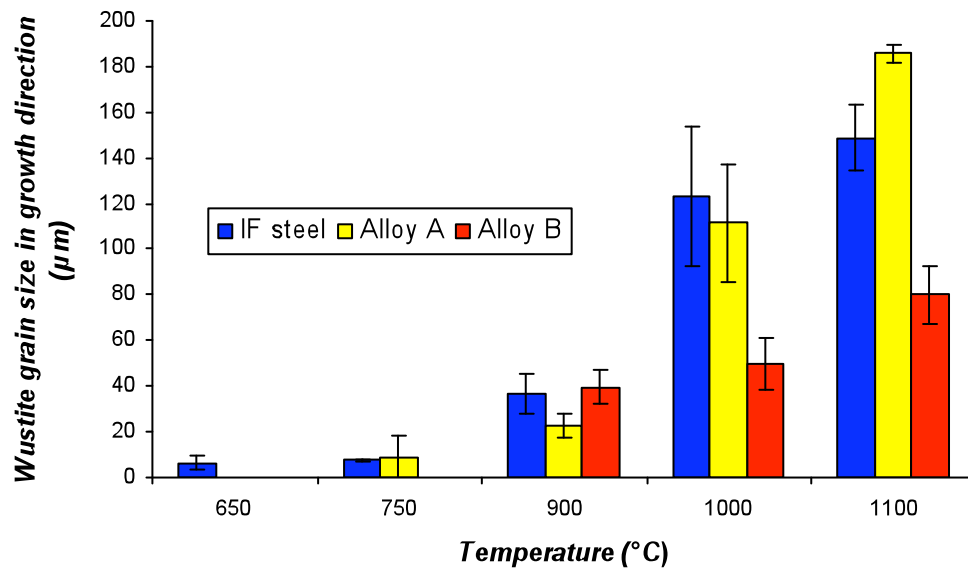
Figure 3.4.13: Wüstite grain size in growth direction of oxide scale on IF steel, Alloy A and Alloy B versus temperature.
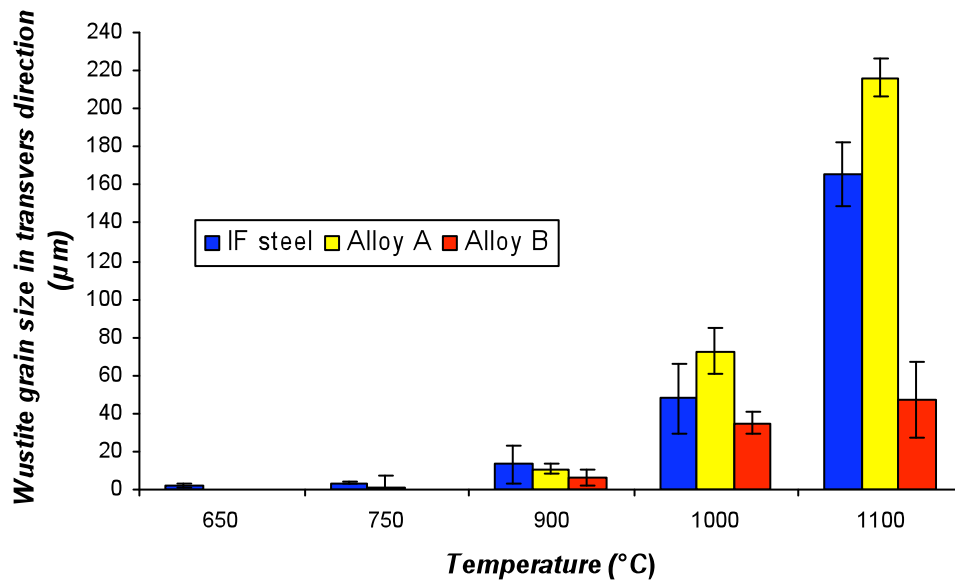
Figure 3.4.14: Wüstite grain size in transverse direction of oxide scale on IF steel, Alloy A and Alloy B versus temperature.
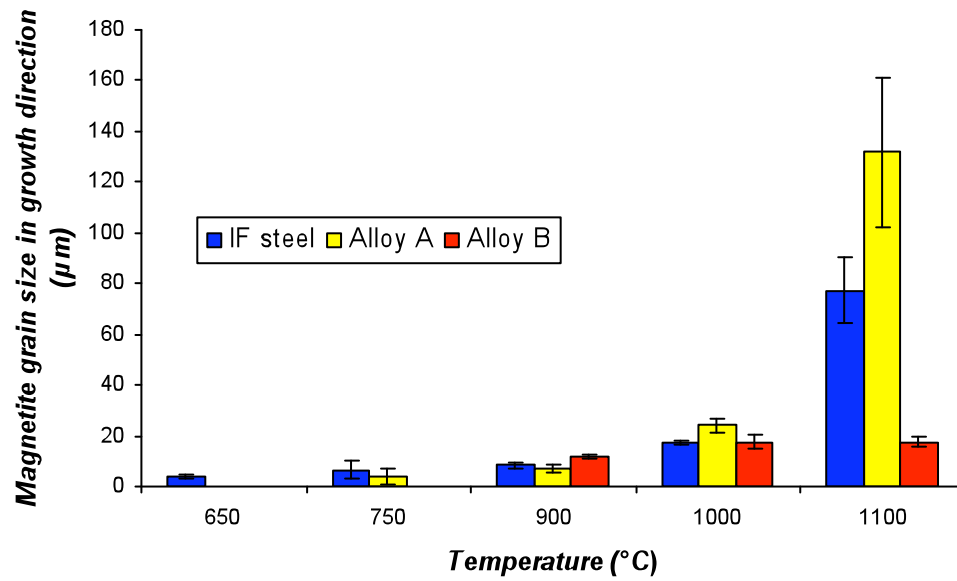
Figure 3.4.15: Magnetite grain size in growth direction of oxide scale on IF steel, Alloy A and Alloy B versus temperature.
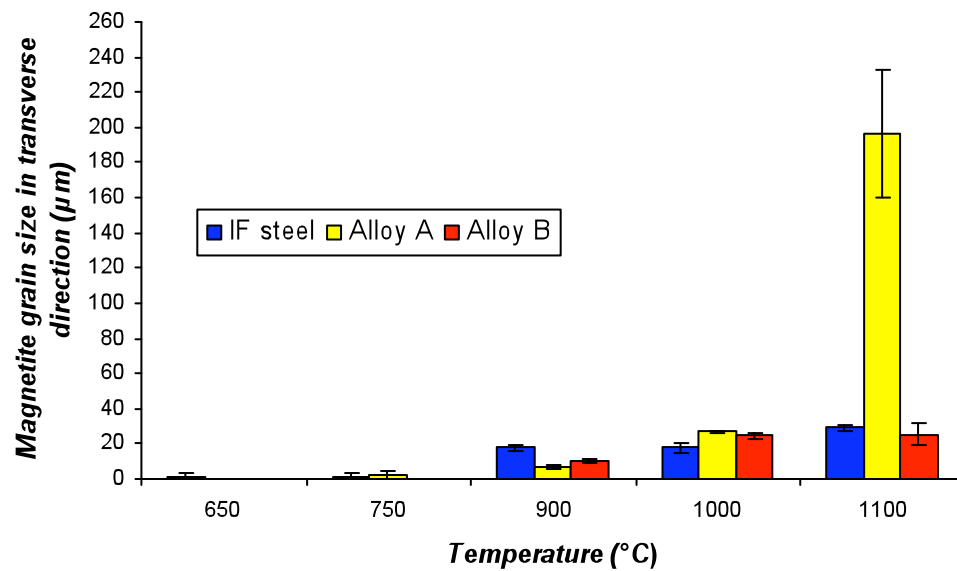
Figure 3.4.16: Magnetite grain size in transverse direction of oxide scale on IF steel, Alloy A and Alloy B versus temperature.
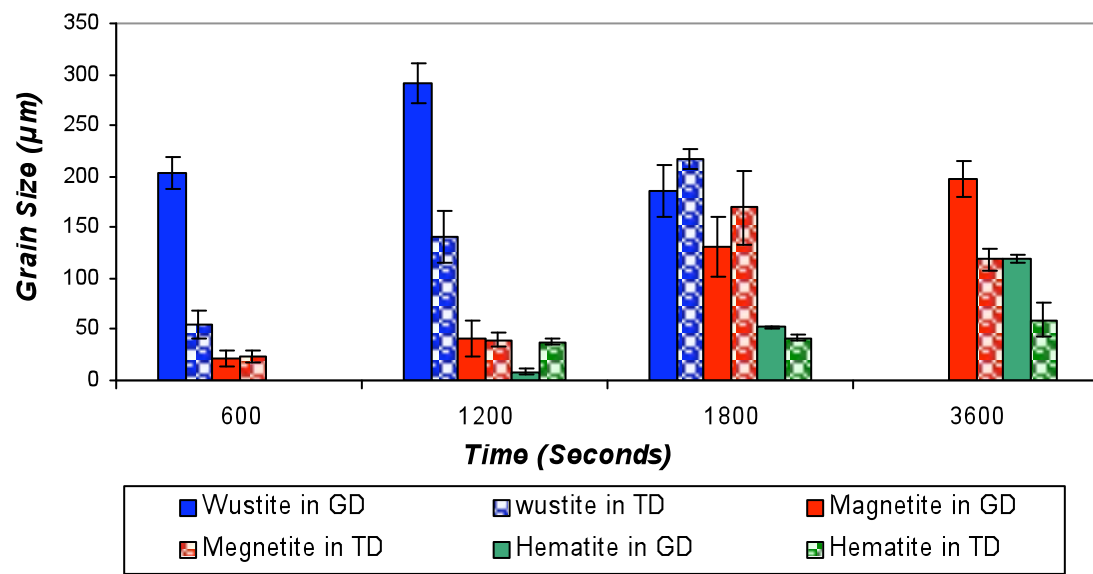
Figure 3.4.17: Alloy A oxide phases grain size versus time at 1100°C in both growth and transverse directions.

3.5 Phase Identification of the Oxide Scale

Traditionally, standard metallographic sample preparation and investigation has been used to identify the phases in the oxide scale by optical or scanning electron microscopy, see Section 3.3. From this method; wüstite appears dark relative to the magnetite, and haematite is the lightest of the etched oxide layers. The magnetite precipitation on wüstite has the same colour as the magnetite layer. This method is not, however, an accurate way of identifying the phase distribution within the scale as is not correlated to crystal structure analysis of the phases within the scale.

EBSD is a technique that can provide identification of unknown crystalline phases. EBSD patterns contain a large amount of information about the crystal structure of the phase such as *d*-spacing, lattice parameters and crystal planes. To distinguish between phases, the selected crystals must either have different structures or have a unit cell parameter differences greater than 10% [Dingley and Randle, 1992]. When these conditions are met, a mapping program can distinguish between the phases (phase discrimination). Figures 3.5.1 - 3.5.4 show the diffraction pattern produced by iron (Figure 3.5.1), wüstite (Figure 3.5.2), magnetite (Figure 3.5.3) and haematite (Figure 3.5.4). For the EBSD system it is easy to distinguish the haematite from the rest of the phases that exist within the oxide scale, as its crystal structure is trigonal while the rest of the phases are cubic. Identifying the other phases depends on the differences in their lattice parameters. As can be seen from Figures 3.5.1 - 3.5.4 the diffraction patterns could be perfectly indexed. The accurate diffraction pattern indexing allows the EBSD data collection software to recognize the crystal planes and then the *d*-spacing could be determined. As shown from the figures, the indices associated with the zone axes (the poles in the Kikuchi pattern formed as a result of intersecting bands) could be identified accurately. The Confidence Index (CI) for the iron diffraction pattern was always high relatively to other phases, while haematite was always the lowest; 0.68 (iron), 0.59 (wüstite), 0.5 (magnetite) and (0.06) for haematite. However, optimising the diffraction pattern indexing is not only dependent on CI, but also on fitting the band widths. For iron, wüstite and magnetite 5 - 7 diffraction patterns band indexing was enough to obtain accurate indexing, as they all are cubic. But to identify the non-cubic (e.g. haematite) it

was necessarily to index more than 10 diffraction patterns and that made optimising the indexing parameters more difficult for all of the phases. Another indexing difficulty arose, as iron, wüstite and magnetite are all cubic and their lattice parameters very close. Therefore, it was necessarily to increase the number of indexed diffraction patterns. The EBSD system was always calibrated before EBSD mapping to avoid misindexing. It should be mentioned that priority of indexing parameters (vote, CI, fit and band width) were changed depending on the diffraction pattern quality, sample conditions, SEM working distance and EBSD calibration. Furthermore, the indexing parameters are optimised and as a double check, images of individual diffraction patterns from each phase were indexed and analysed after mapping. Where there was low CI and poor pattern fit, the data was rescanned using optimised indexing parameters. Some of the scannings were combined with chemical mapping to eliminate ambiguous results obtained from inaccurate indexing.

Figures 3.5.5 - 3.5.12 show phase identification EBSD maps of the oxide scale formed on IF steel. In order for all three classical layers to be shown for explanation purposes, the images are arranged from higher temperature (i.e. 1100°C) to lower temperature (i.e. 650°C). Figure 3.5.5 (a) shows the phase map of the oxide scale formed at 1100°C for 1800 seconds. The phases within the scale and substrate were accurately identified by EBSD as compared to the optical micrograph in Figure 3.5.1 (a). Figure 3.5.5 (b) shows the phase map with phase boundary (white) as an indication of the ability of the EBSD to distinguish phase from grain boundaries. Figure 3.5.5 (c) shows the phase ratio within the oxide scale. It should be mentioned that before the EBSD phase ratio calculation, the substrate area was cropped to avoid any statistical errors. The phase ratio chart and table are shown with each phase ratio map. As can be seen from the Figure 3.5.5 (c), the magnetite phase has the largest volume fraction within the scale (0.62), while haematite has the lowest (0.07). Figure 3.5.6 shows the EBSD–EDS maps for oxygen (a), iron (b), carbon (c) and silicon (d). Comparing the phase map (Figure 3.5.5-a) with Oxygen-EDS map (Figure 3.5.6-a), the oxygen concentration in the magnetite layer is higher than the wüstite layer. The areas indexed as magnetite and wüstite in the phase map match the oxygen concentration in the EDS map. Moreover, the magnetite precipitates appear to have the same oxygen concentration as the magnetite layer. As expected, haematite has a

highest oxygen concentration. Differences in the iron concentration among the oxide phases was less clear than the oxygen, therefore, double-checking of the indexing method in the phase map relied mainly on consideration of the oxygen EDS map. As can be seen from Figures 3.5.6 (c) and (d), there was no indication of high carbon or silicon concentration. Due to the large number of EDS maps for each element in the samples and the limitations of space, only oxygen and iron EDS maps are shown for the rest of the samples, unless specific observation were noted. Using the same method, oxide scale on IF steel grown at 1000°C-1800 seconds was analysed, see Figure 3.5.7. In some samples an indentor point was used to find an exact scanning area for comparison reason with optical and SEM images. As can be seen from Figure 3.5.8, the indentor caused a large crack within the oxide scale, however, the crack did not affect the oxide scale phase identification.

At 750°C-1800 seconds, the oxide scale on IF steel is not uniform, Figures 3.5.9 and 3.5.10. For repeatability purposes two EBSD scans were carried out on different areas on the same sample, however, the phase ratio results from both EBSD scans are very close, see the same Figures. Figure 3.5.11 show an IF steel oxide scale developed at 750°C after 1200 seconds. From the figure, a high magnetite precipitate concentration and magnetite seam can be clearly seen, making up 49% of the scale. At 650°C, the oxide scale is very thin and spalled from the substrate, therefore, it was very difficult to obtain good diffraction patterns. Chi-EBSD scanning was carried out, as the indexing was poor, by combining chemical and EBSD mapping the phases within the scale and substrate could be verified, see Figure 3.5.12. There is a relatively high carbon concentration at the top and silicon at the bottom of the scale, see Figures 3.5.12 (d) and (e) respectively.

Figures 3.5.13 - 3.5.19 show the related phase identification EBSD maps of the oxide scale and the steel substrate of Alloy A at different times and temperatures. The figures start from low temperature (i.e. 750°C) to high temperature. Figure 3.5.13 shows the oxide scale formed on Alloy A at 750°C-1800 seconds. Increased porosity at the wüstite/magnetite interface and within the magnetite layer caused poor indexing of the diffraction patterns in those areas; see Figure 3.5.13 (a). To exclude poor index patterns and ambiguous data, a 60% confident index map was superimposed on the phase map as

shown in Figure 3.5.13 (b). The data of less than 0.2 CI in Figure 3.5.13 (b) appears as black points in the map. On this basis phase ratio has been calculated to avoid any error in the measurements, see Figure 3.5.13 (c). Figure 3.5.14 shows the oxide scale developed at 900°C-1800 seconds. In Figures 3.5.14 (a) and (b) it is difficult to distinguish between the pores and magnetite precipitates in some areas. By distinguishing phase boundaries (white) from grain boundaries (red), as shown in Figure 3.5.14 (c), the magnetite precipitates can be clearly distinguished from the small pores. Through using the same method, the oxide scale phases on IF steel formed at 1000°C-1800 seconds were characterised, see Figure 3.5.15.

Figures 3.5.16-3.5.19 show the oxide scale formed on Alloy A, at 1100°C at different times of exposure. Figure 3.5.16 shows the scale formed after 600 seconds which consists of wüstite and magnetite only. After 1200 seconds of air exposure, haematite appears on the top of the scale and magnetite precipitates have increased, see Figure 3.5.17. The thickness of the haematite layer and the size of the magnetite precipitates increased with increasing times until the haematite layer occupied large areas of the oxide scale at 3600 seonds, see Figures 3.5.18 and 3.5.19. The magnetite precipitation in the wüstite layer increased with increasing time until they joined together making a magnetite layer, leading to the wüstite layer completely disappearing at 3600 seconds, see Figure 3.5.19.

In the same manner, the oxide scales formed on Alloy B have been identified. Figures 3.5.20 - 3.5.22 show the oxide scale and substrate related phase identification EBSD maps of Alloy B at different temperatures for 1800 seconds. As on IF steel and Alloy A, the magnetite precipitations increased in size with increasing temperature on Alloy B.

Figure 3.5.23 shows the oxide phases' ratio versus temperature graph for IF steel oxidised for 1800 seconds. The haematite phase was not observed at lower temperatures (i.e. 650, 750 and 900°C), then appears at 1000 and grows further at 1100°C. Magnetite increased from 650 until 750°C and started to decrease at 900°C and then started to increase again at 1000°C and grow further at 1100°C. Whereas, wüstite decreased from 650 to 750°C and then increased dramatically at 900°C followed by decrease with increasing temperatures. Looking only at three last temperatures 900, 1000 and 1100°C,

is appeared that magnetite and haematite increased with increasing temperatures while wüstite decreases.

Figure 3.5.24 shows the oxide phase's ratio versus temperature graph for Alloy A oxidised for 1800 seconds. The haematite phase was not observed at any temperatures except 1100°C. The magnetite phase volume fraction increased from 750 until 900°C then started to decrease at 1000°C followed by increase at 1100°C. While the wüstite volume fraction decreased from 750 until 900°C, then increased at 1000°C followed by a decrease at 1100°C. Generally there was no trend in variation of the oxide scale phase volume fraction with temperature.

Figure 3.5.25 shows the oxide phase's ratio versus temperature graph for Alloy B oxidised for 1800 seconds. The phase's volume fraction in the oxide scale is changed only slightly with temperature. The magnetite phase volume fraction remained constant at all temperatures, while slight changes occurred in haematite and wüstite. The oxide layers thickness and overall thickness increased with temperature, but the phase ratio remains constant or very small changes were noted.

Figure 3.5.26 shows the oxide phase's ratio versus time graph for Alloy A oxidised at 1100°C. As shown in the figure, the wüstite phase volume fraction decreased with increasing temperatures, and at 1100°C wüstite does not appear in the scale. While magnetite and haematite increased with increasing time, occupying the whole layer at 1100°C.

(a)   *(b)*   *(c)*

(d)   *(e)*
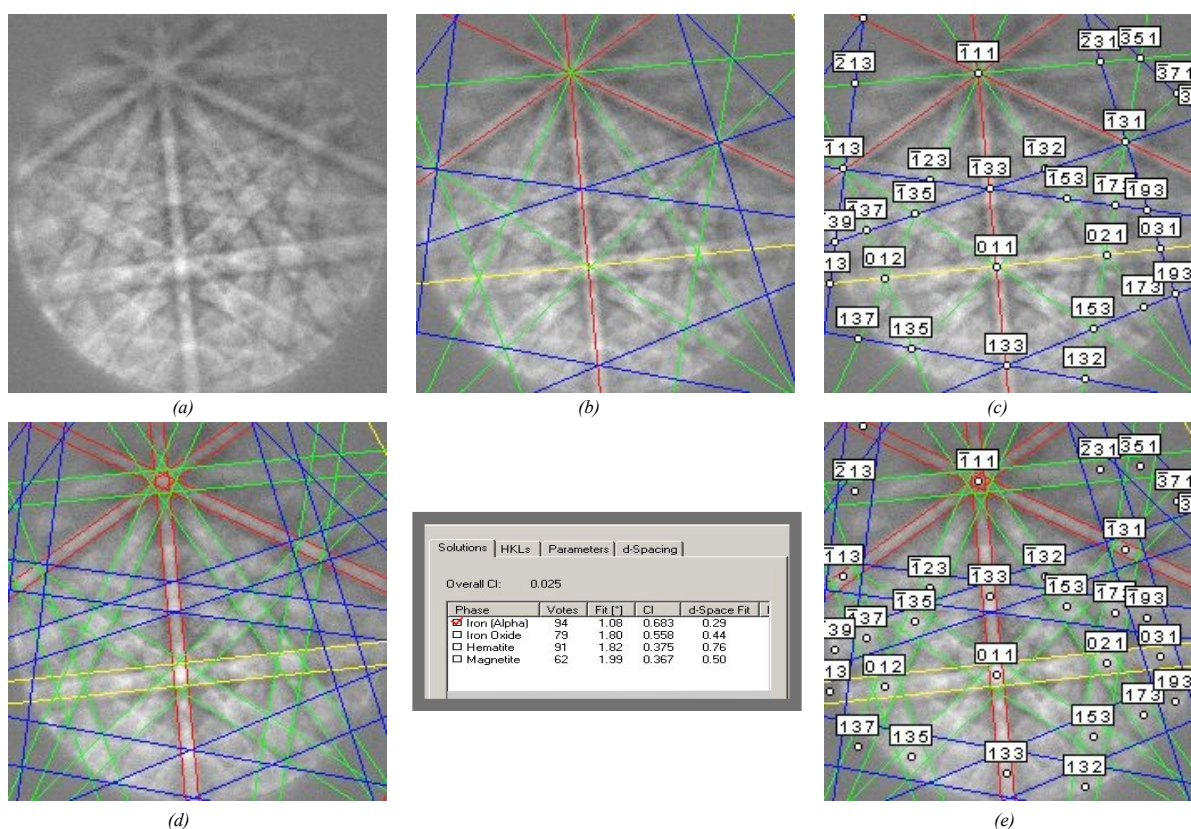
Figure 3.5.1: (a) Iron diffraction pattern, (b) indexed, recognising crystal planes, (c) identifying indices associated with zone axes, (d) determination of d-spacing, (e) indexed diffraction pattern showing band widths and poles.

(a)   *(b)*   *(c)*

(d)   *(e)*
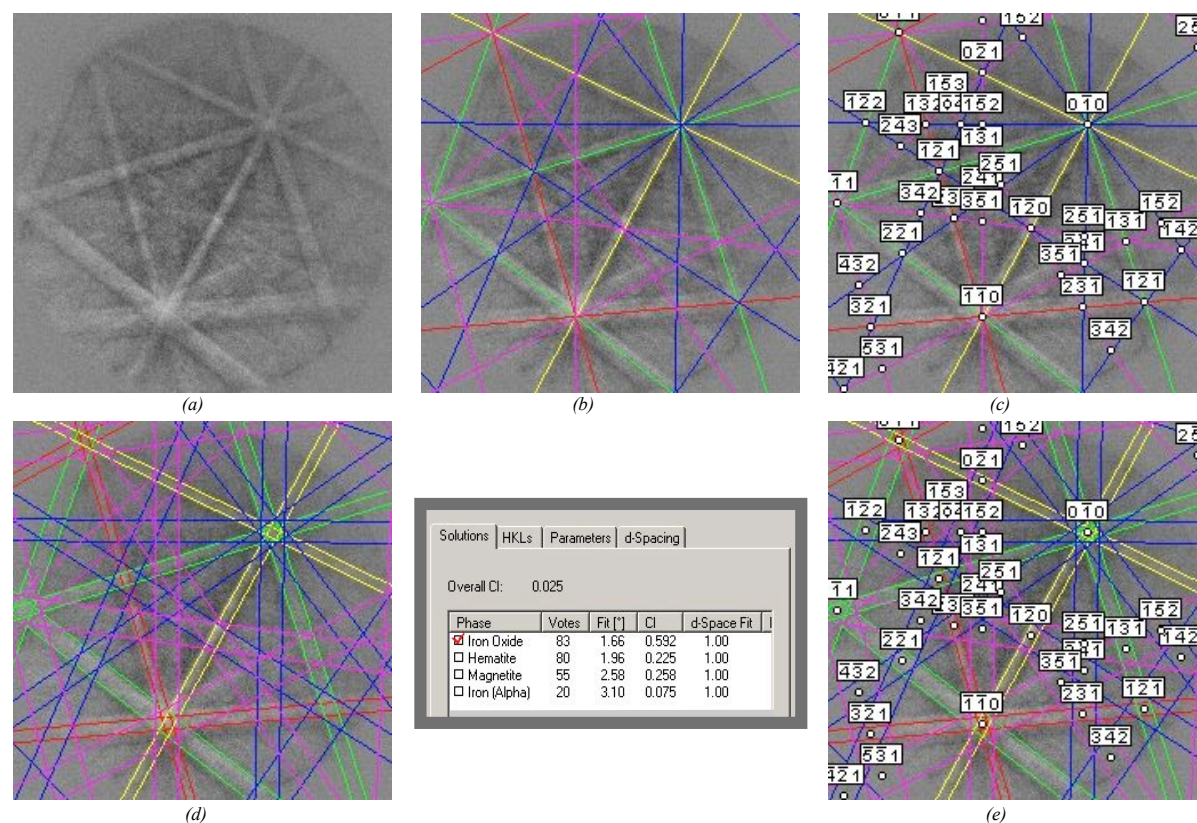
Figure 3.5.2: (a) Wüstite diffraction pattern, (b) indexed, recognising crystal planes, (c) identifying indices associated with zone axes, (d) determination of d-spacing, (e) indexed diffraction pattern showing band widths and poles.
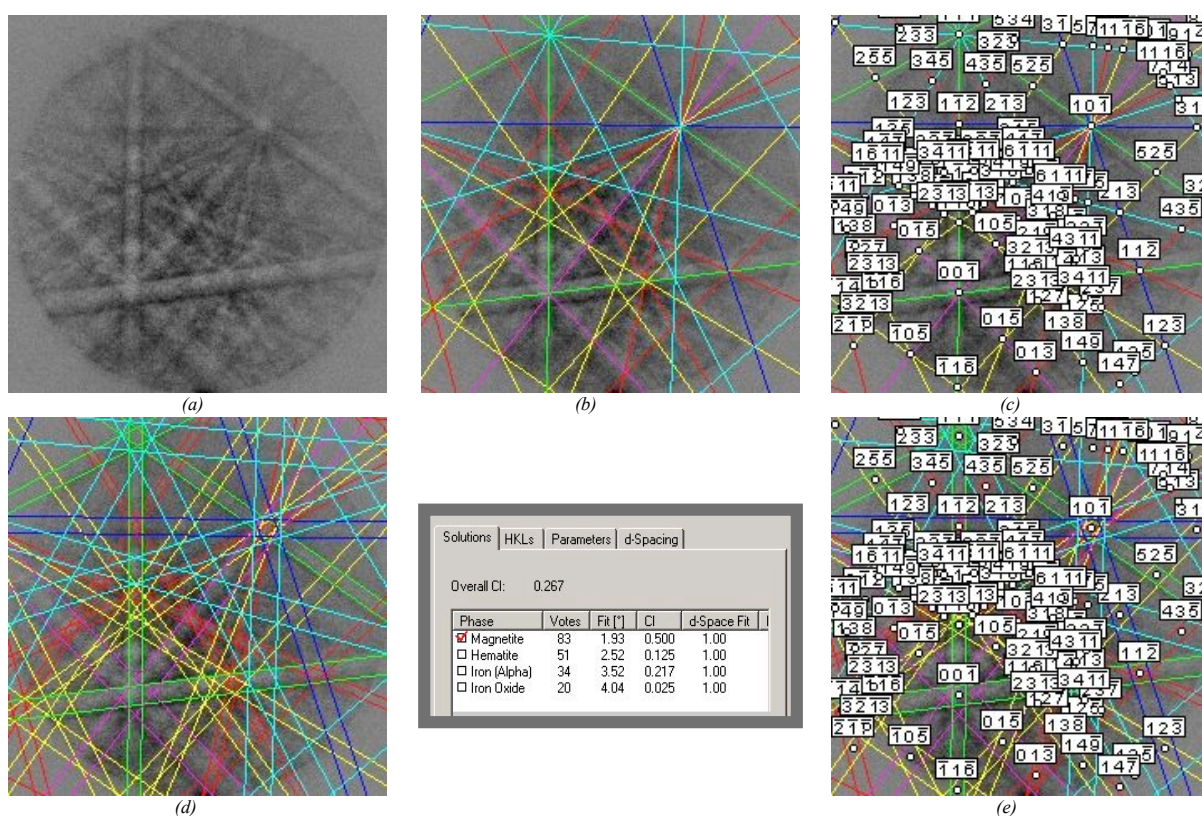
Figure 3.5.3: (a) Magnetite diffraction pattern, (b) indexed, (c) identifying indices associated with zone axes, (d) determination of d-spacing, (e) indexed diffraction pattern showing band widths and poles.
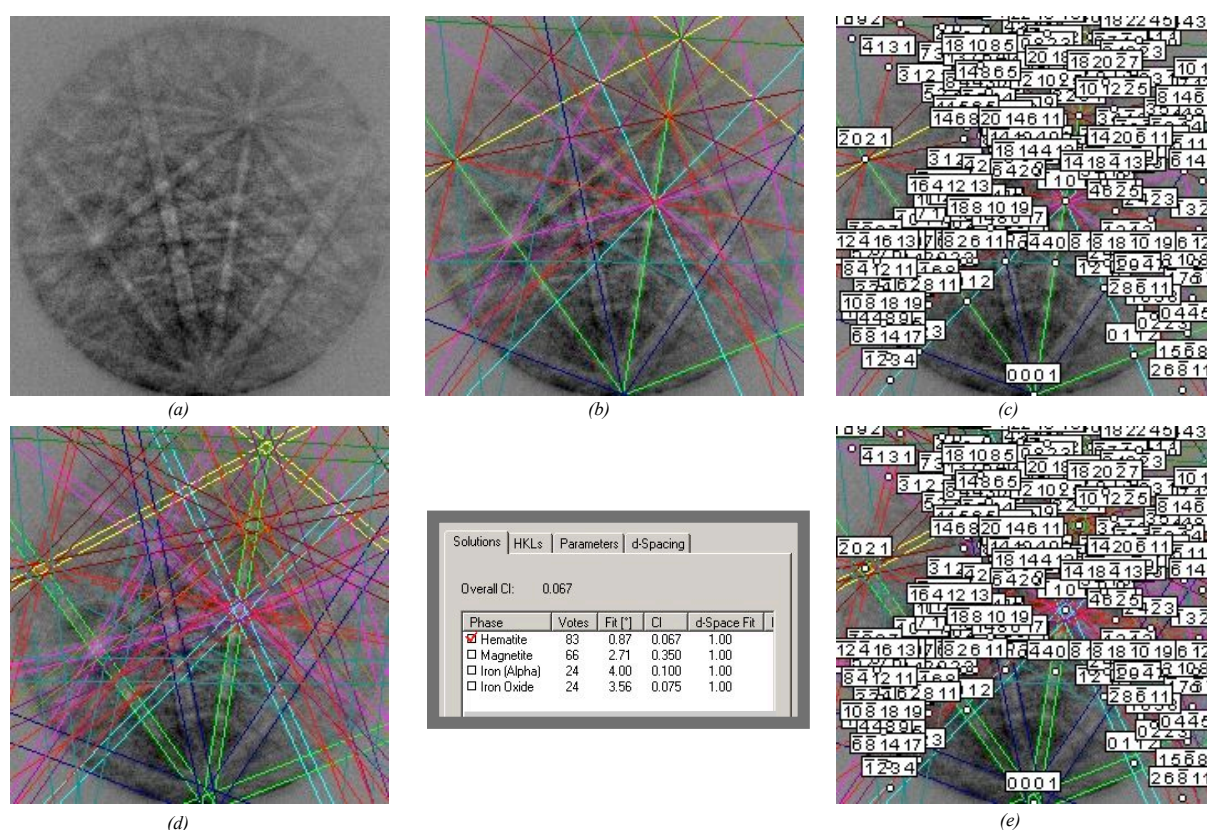
Figure 3.5.4: (a) Haematite diffraction pattern, (b) indexed, (c) identifying indices associated with zone axes, (d) determination of d-spacing, (e) indexed diffraction pattern showing band widths and poles.

IF Steel Related Phase Map Images

Figure 3.5.5: IF steel oxidised at 1100°C for 1800 seconds. (a) phase map, (b) phase map with phase boundary (white), (c) phase ratio chart and map.

Chart: Phase

Phase	Number Fraction
Hematite	0.0763176
Iron (Alpha)	0.00011575
Magnetite	0.622598
Iron Oxide	0.300968

Min. ▮▮▮▮ **Max.**
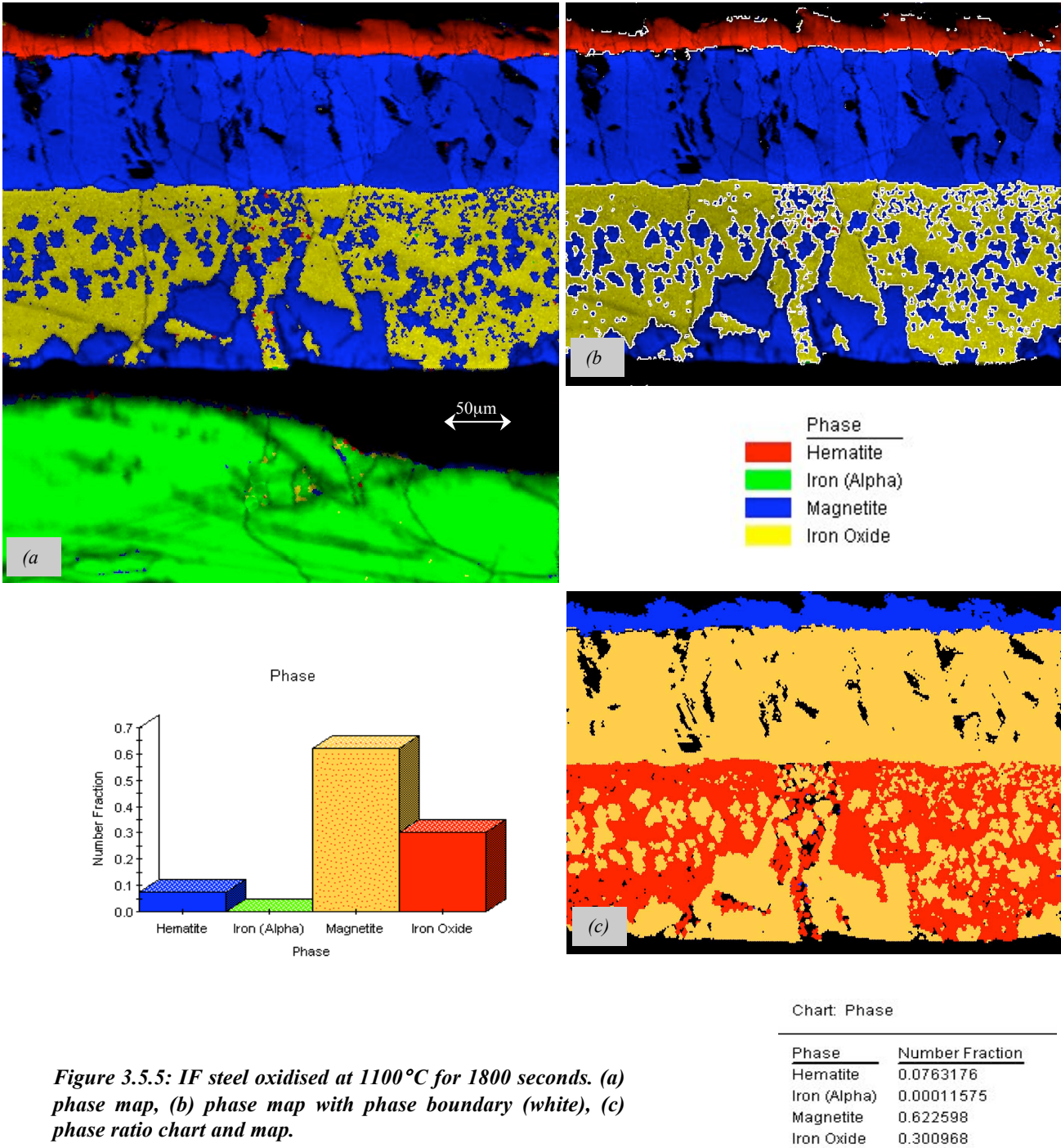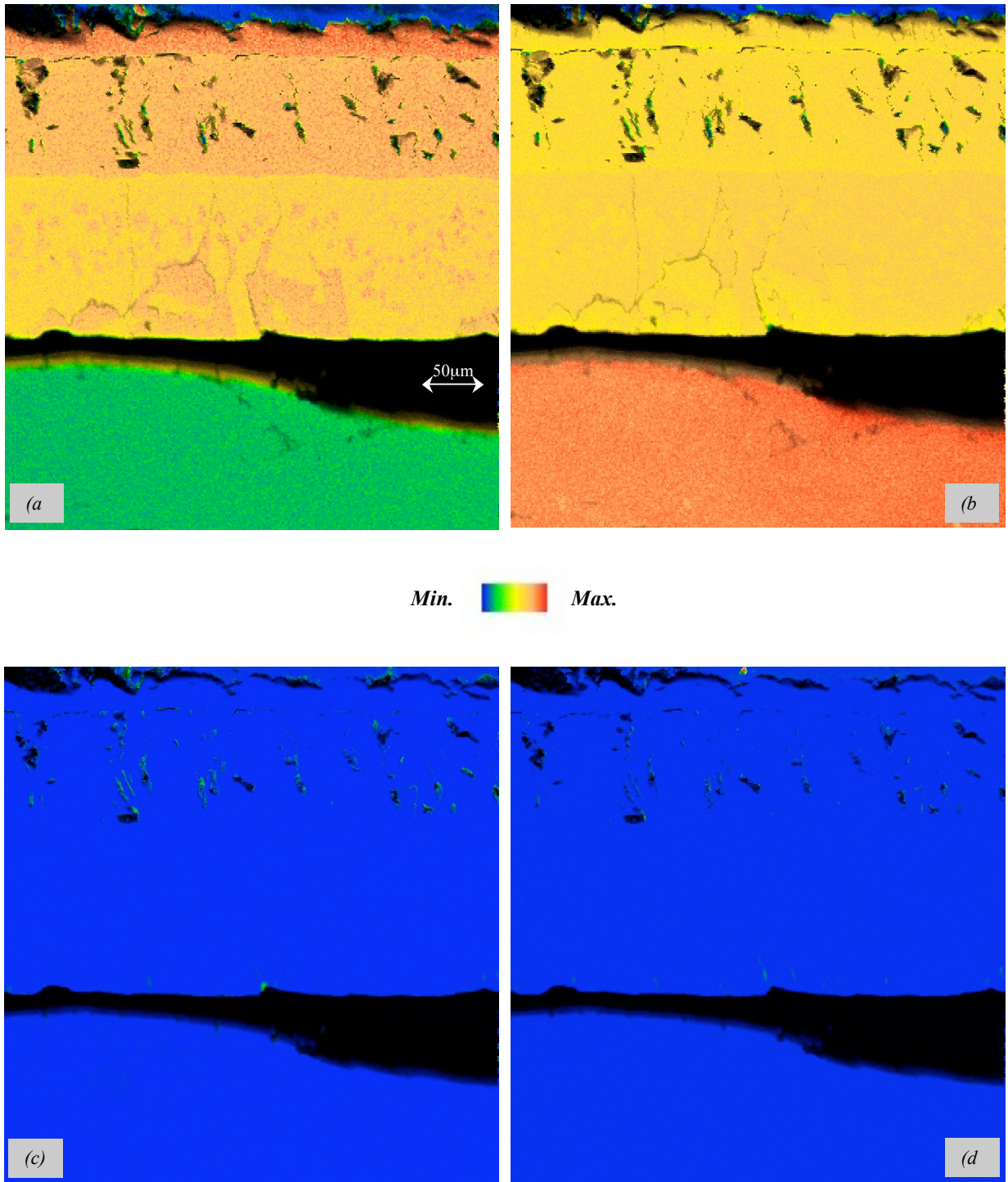
Figure 3.5.6: EBSD-EDS maps for the sample in Figure 3.5.5, (a) Oxygen, (b) Iron, (c) Carbon and (d) Silicon.
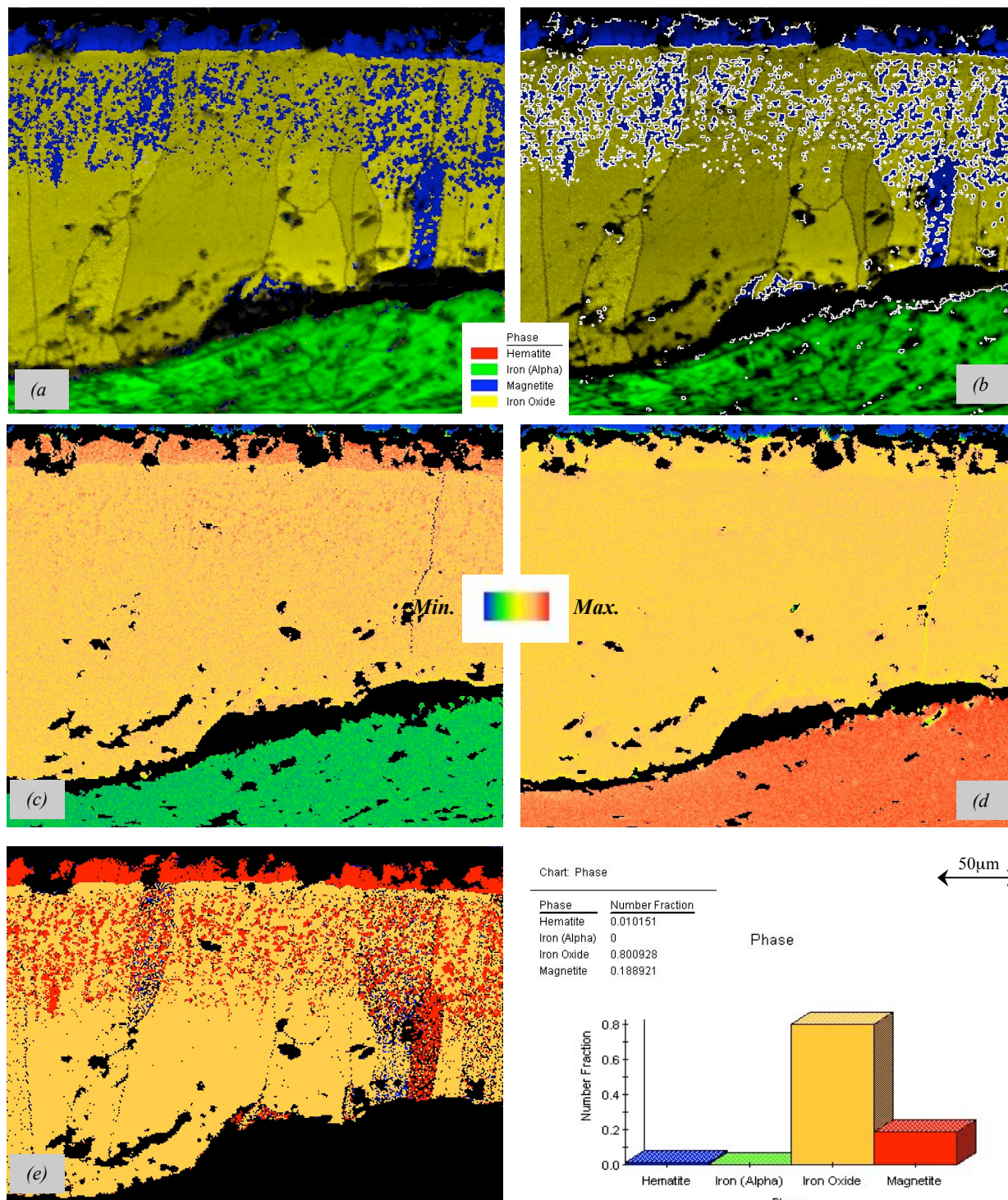
Figure 3.5.7: IF steel oxidised at 1000°C for 1800 seconds. (a) phase map, (b) phase map with phase boundary, (c) oxygen EDS map, (d) iron EDS map, (e) phase ratio map and chart.
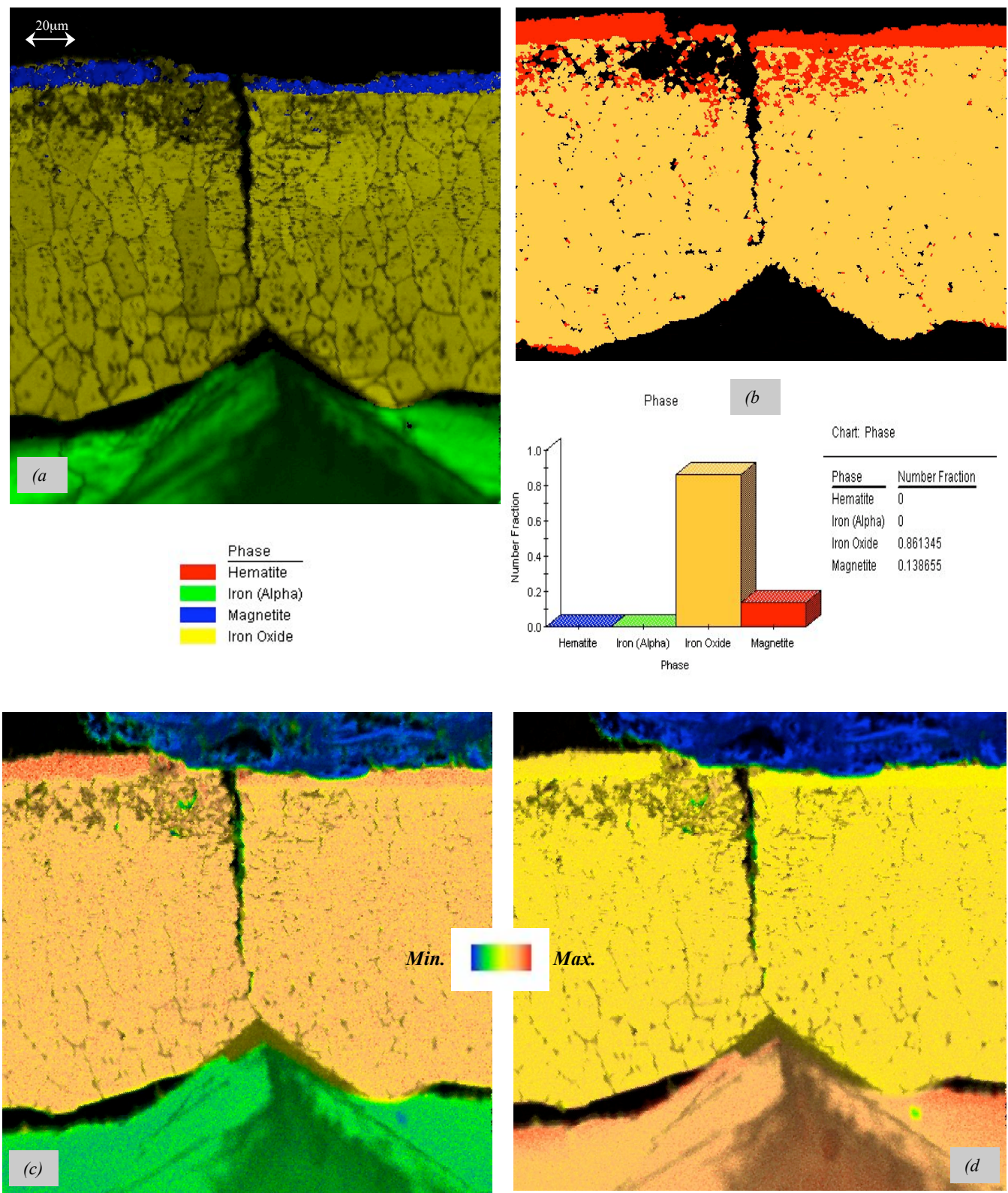
Figure 3.5.8: IF steel oxidised at 900°C for 1800 seconds. (a) phase map, (b) phase ratio map and chart, (c) oxygen EDS map, (d) iron EDS map.
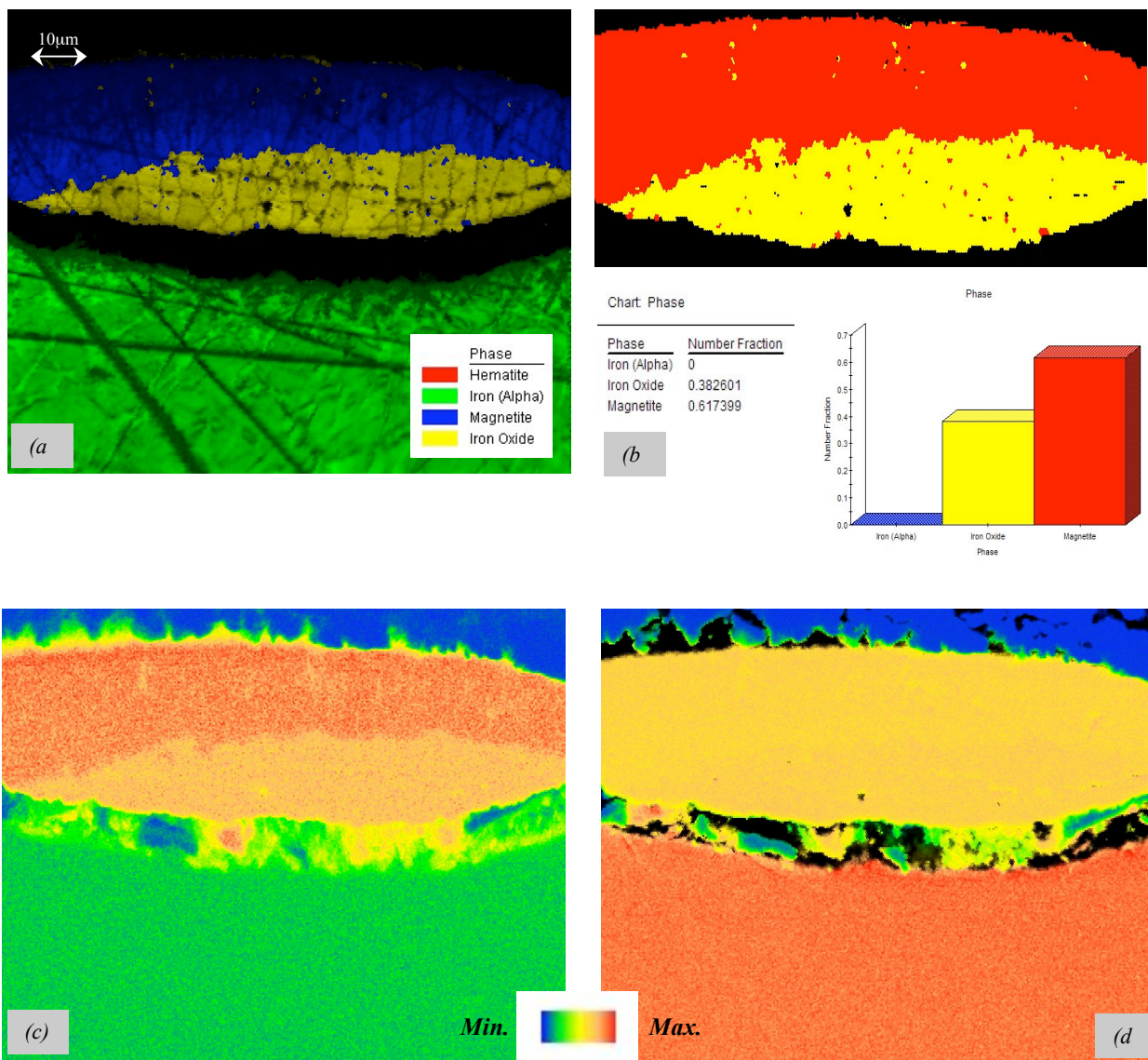
Figure 3.5.9: IF steel oxidised at 750°C for 1800 seconds. (a) phase map, (b) phase ratio map and chart, (c) oxygen EDS map, (d) iron EDS map.
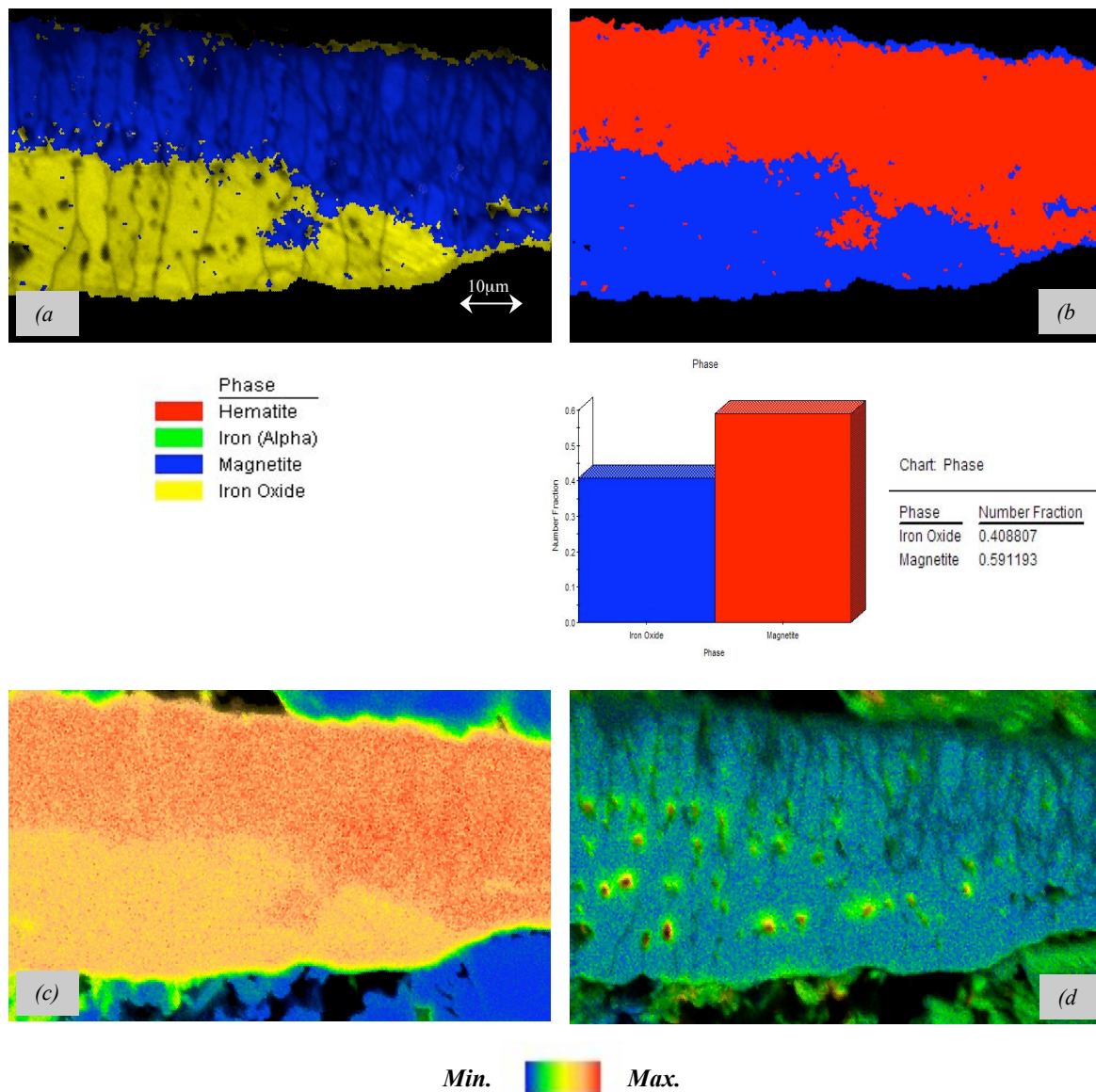
Figure 3.5.10: IF steel oxidised at 750°C for 1800 seconds. (a) phase map, (b) phase ratio map and chart, (c) oxygen EDS map, (d) silicon EDS map.
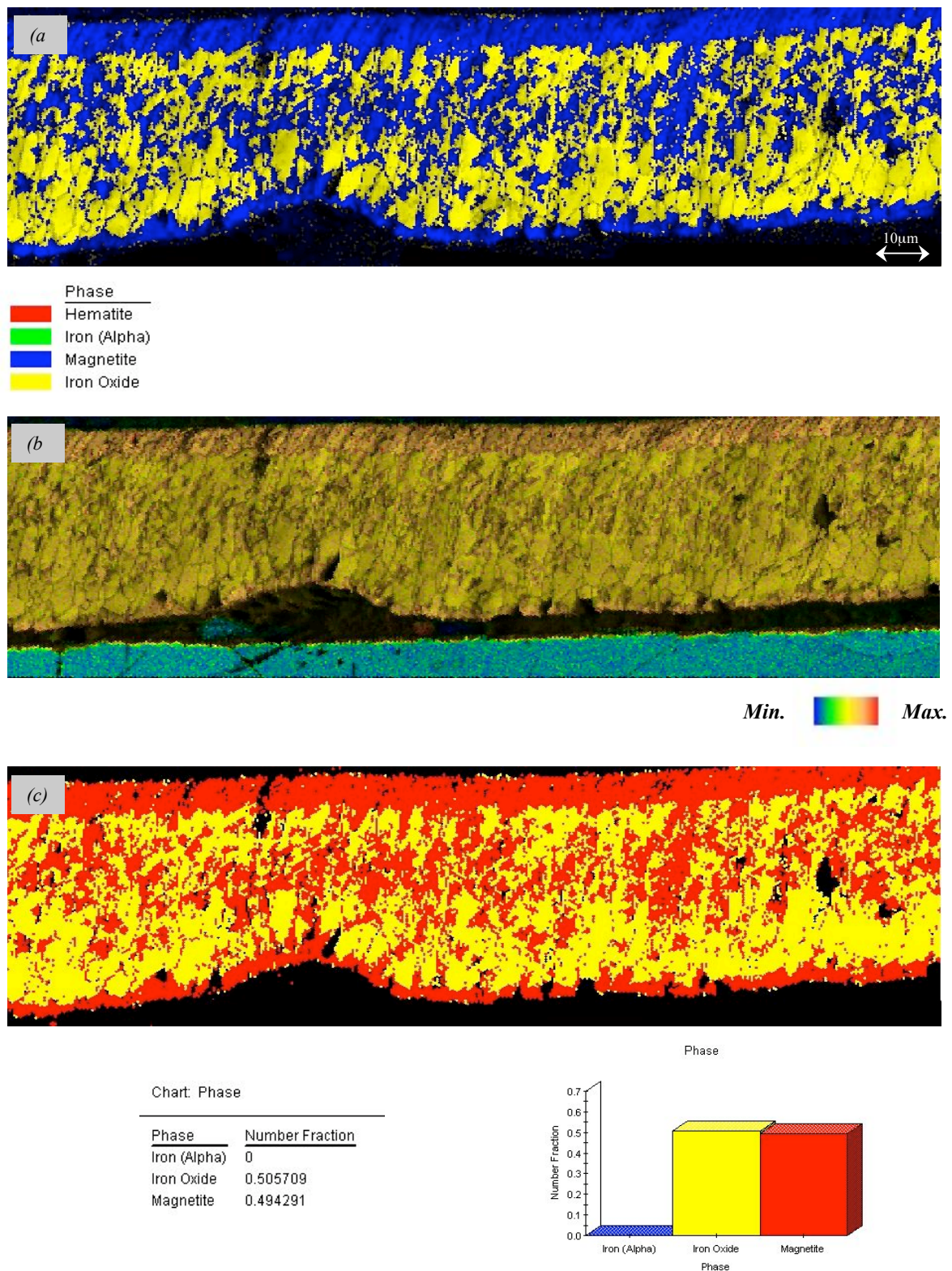
Figure 3.5.11: IF steel oxidised at 750°C for 1200 seconds. (a) phase map, (b) oxygen EDS map superimposed on 60% Image Quality map (c) phase ratio map and chart.
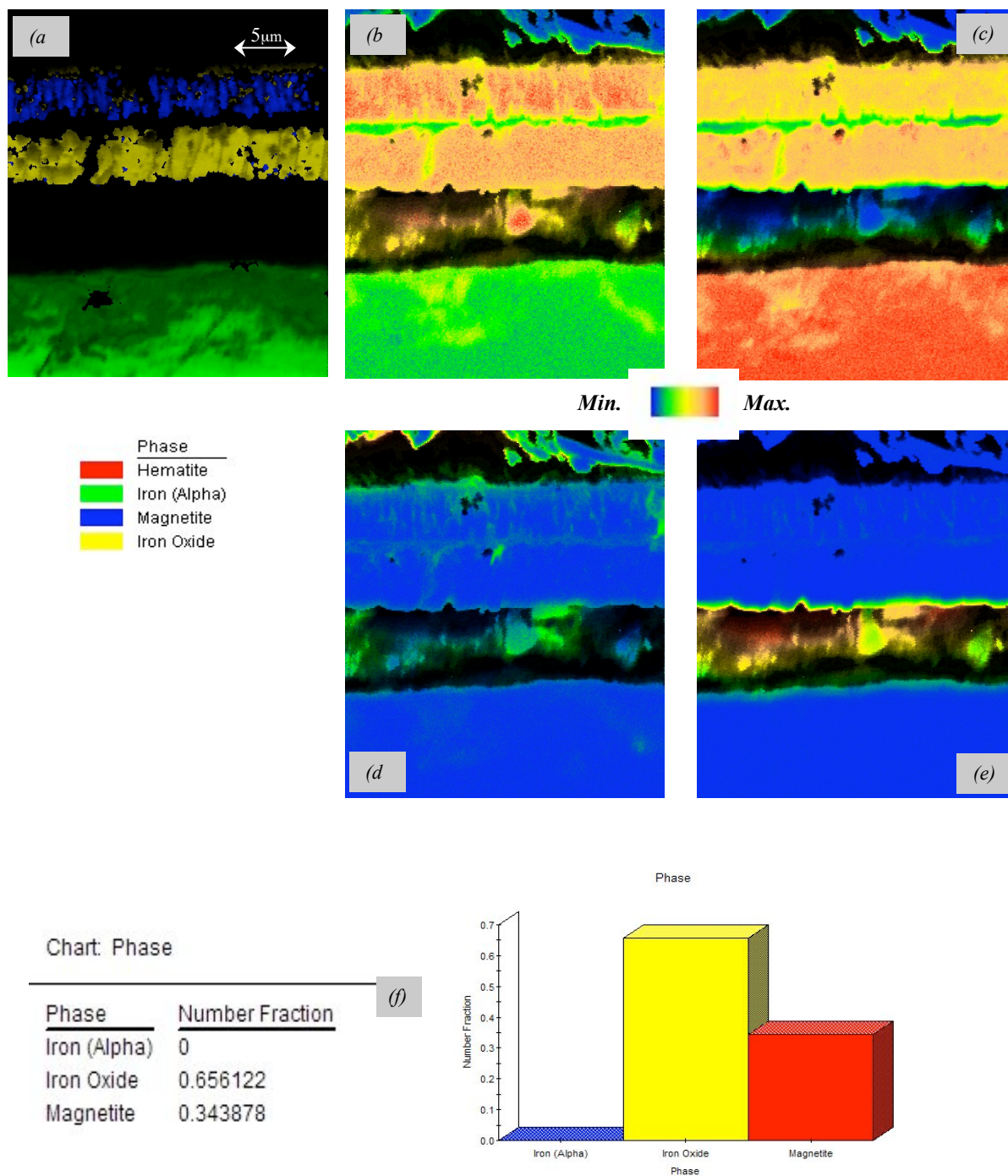
Figure 3.5.12: IF steel oxidised at 650°C for 1800 seconds. (a) phase map, (b) oxygen EDS map, (c) iron EDS map, (d) carbon EDS map, (e) silicon EDS map and (f) phase ratio chart.

Alloy A Related Phase Map Images
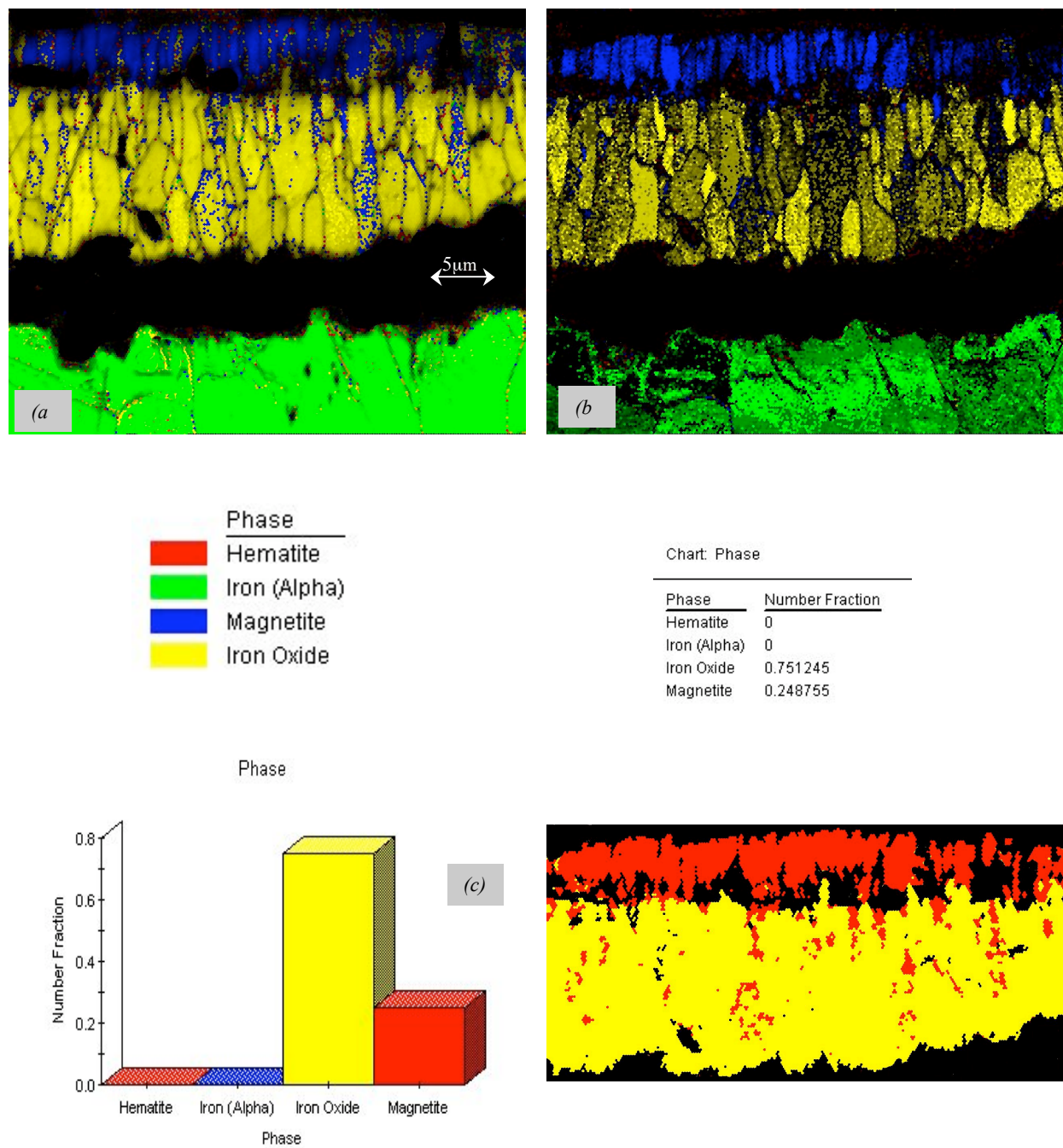
Figure 3.5.13: Alloy A oxidised at 750°C for 1800 seconds. (a) phase and 60% image quality map, (b) phase and 60% confident index map, (c) phase ratio map and chart.
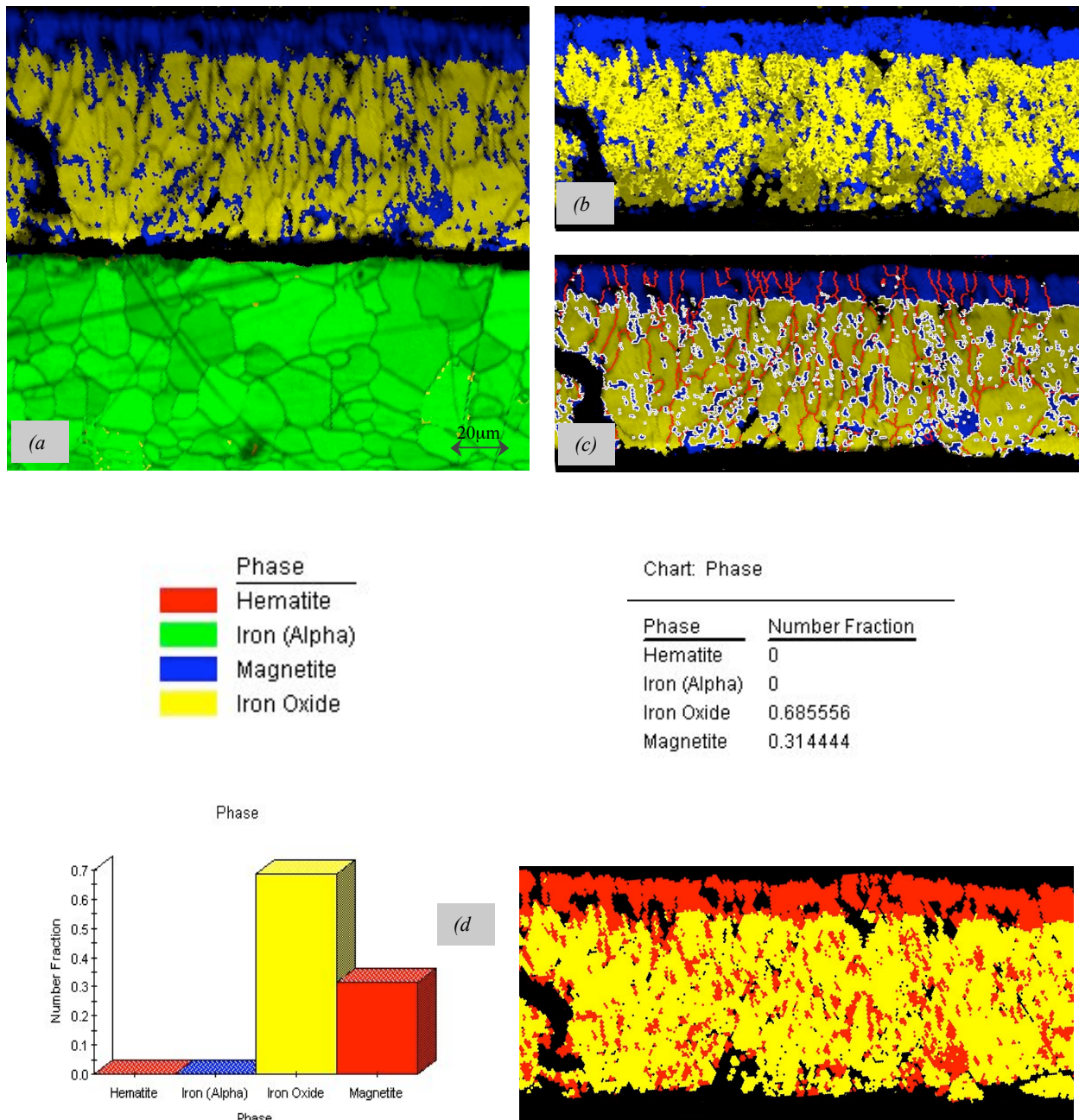
Figure 3.5.14: Alloy A oxidised at 900°C for 1800 seconds. (a) phase and 60% image quality map, (b) phase and 60% confident index map, (c) phase map with grain boundary (red) and phase boundary (white), (d) phase ratio map and chart.
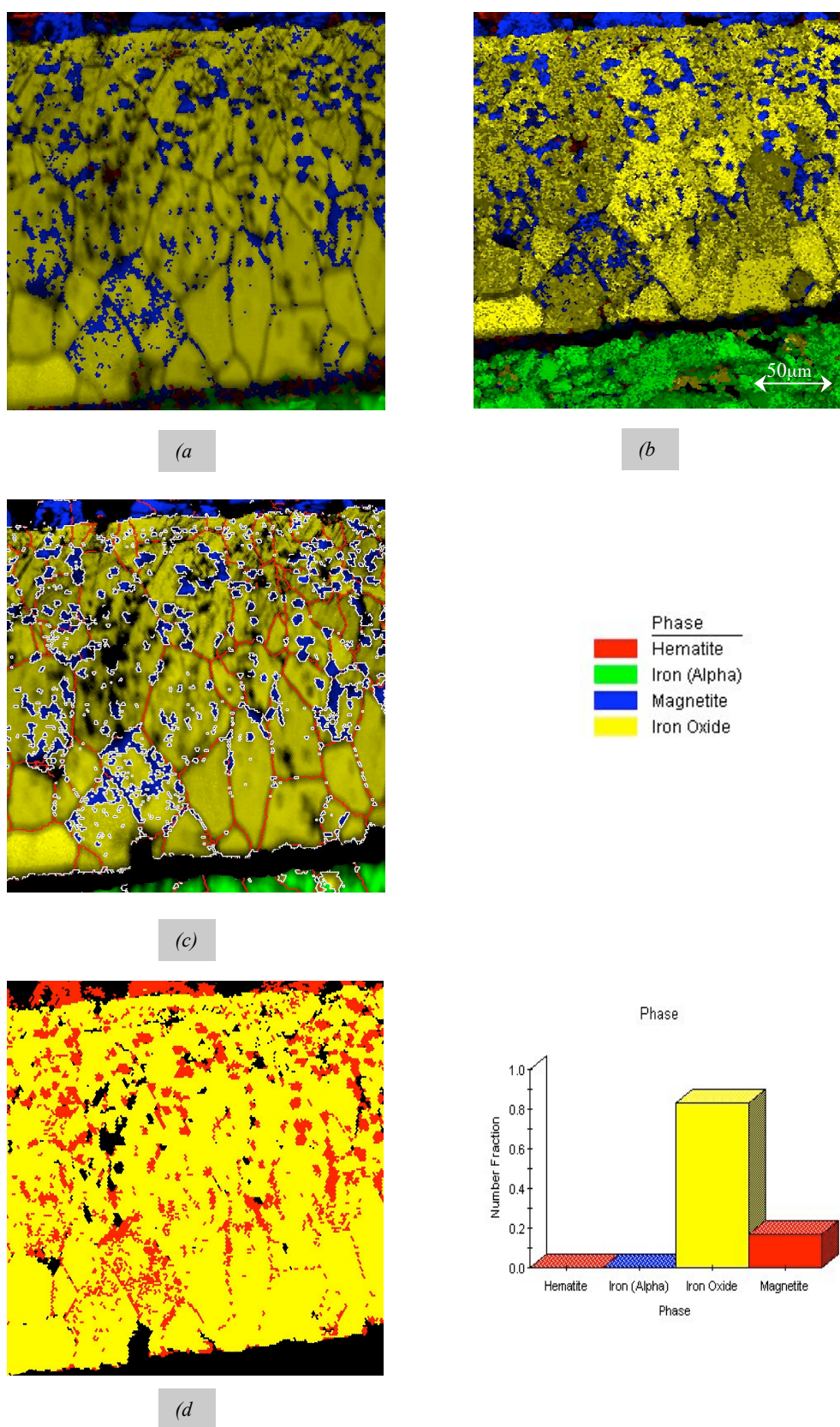
Figure 3.5.15: Alloy A oxidised at 1000°C for 1800 seconds. (a) phase and 50% image quality map, (b) phase and 80% confident index map, (c) phase map with grain boundary (red) and phase boundary (white), (d) phase ratio map and chart.

Phase
- Hematite
- Iron (Alpha)
- Magnetite
- Iron Oxide

Min.   *Max.*

Chart: Phase

Phase	Number Fraction
Iron (Alpha)	0
Iron Oxide	0.882062
Magnetite	0.117938
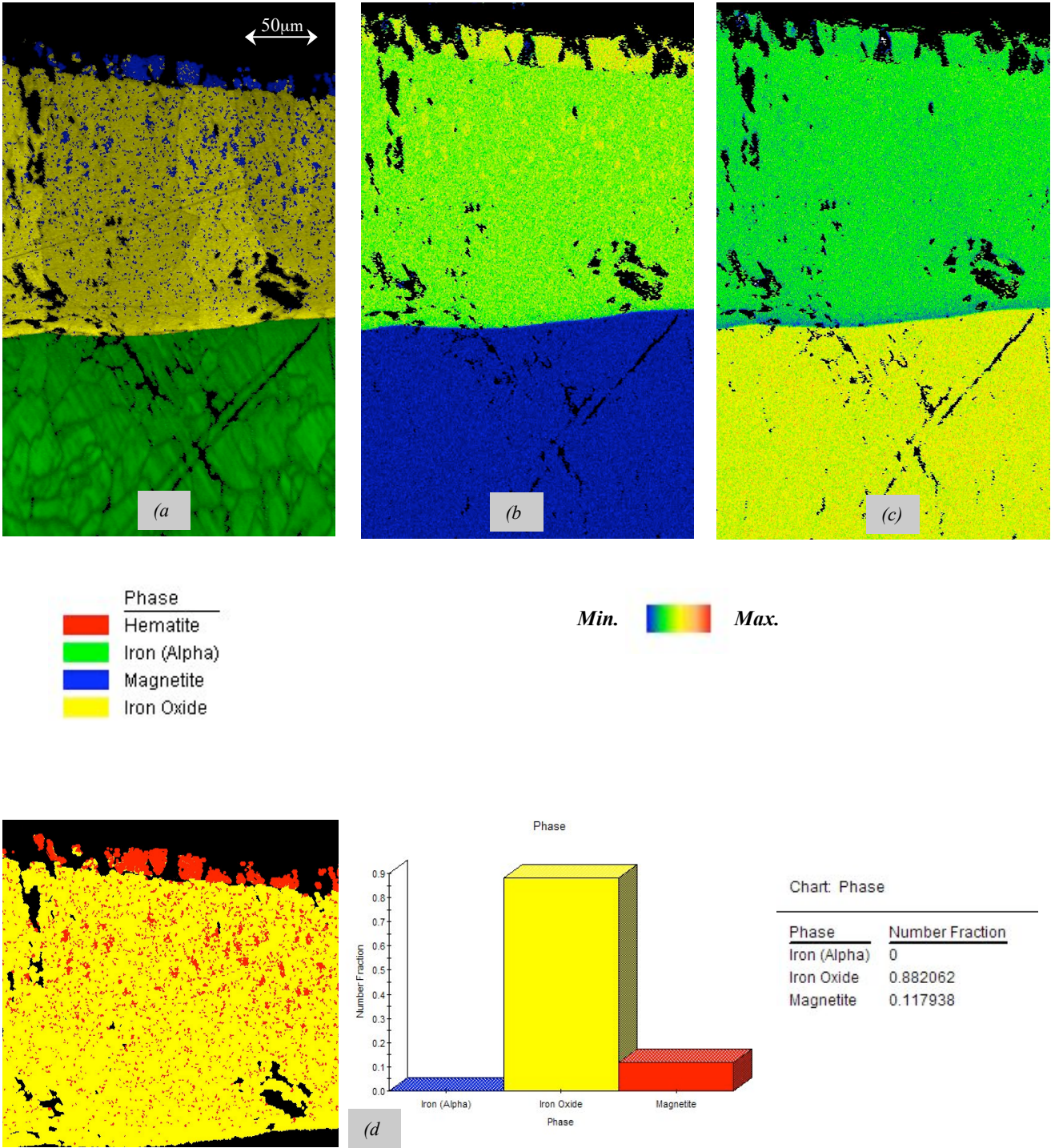
Figure 3.5.16: Alloy A oxidised at 1100°C for 600 seconds. (a) phase map, (b) oxygen EDS map, (c) iron EDS map, (d) phase ratio map and chart.
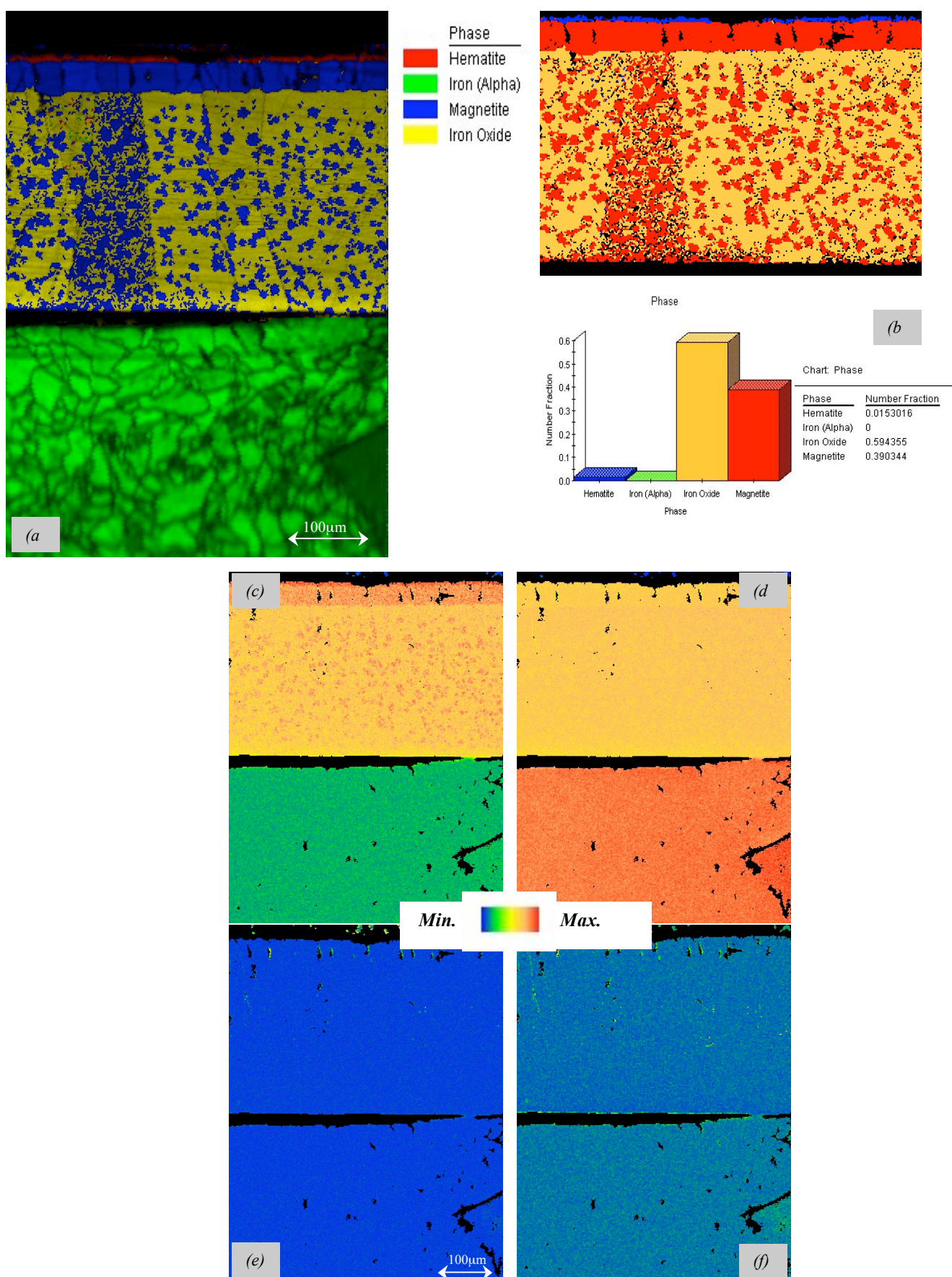
Figure 3.5.17: Alloy A oxidised at 1100°C for 1200 seconds. (a) phase map, (b) phase ratio map and chart (c) oxygen EDS map, (d) iron EDS map, (e) carbon and (f) silicon EDS map.
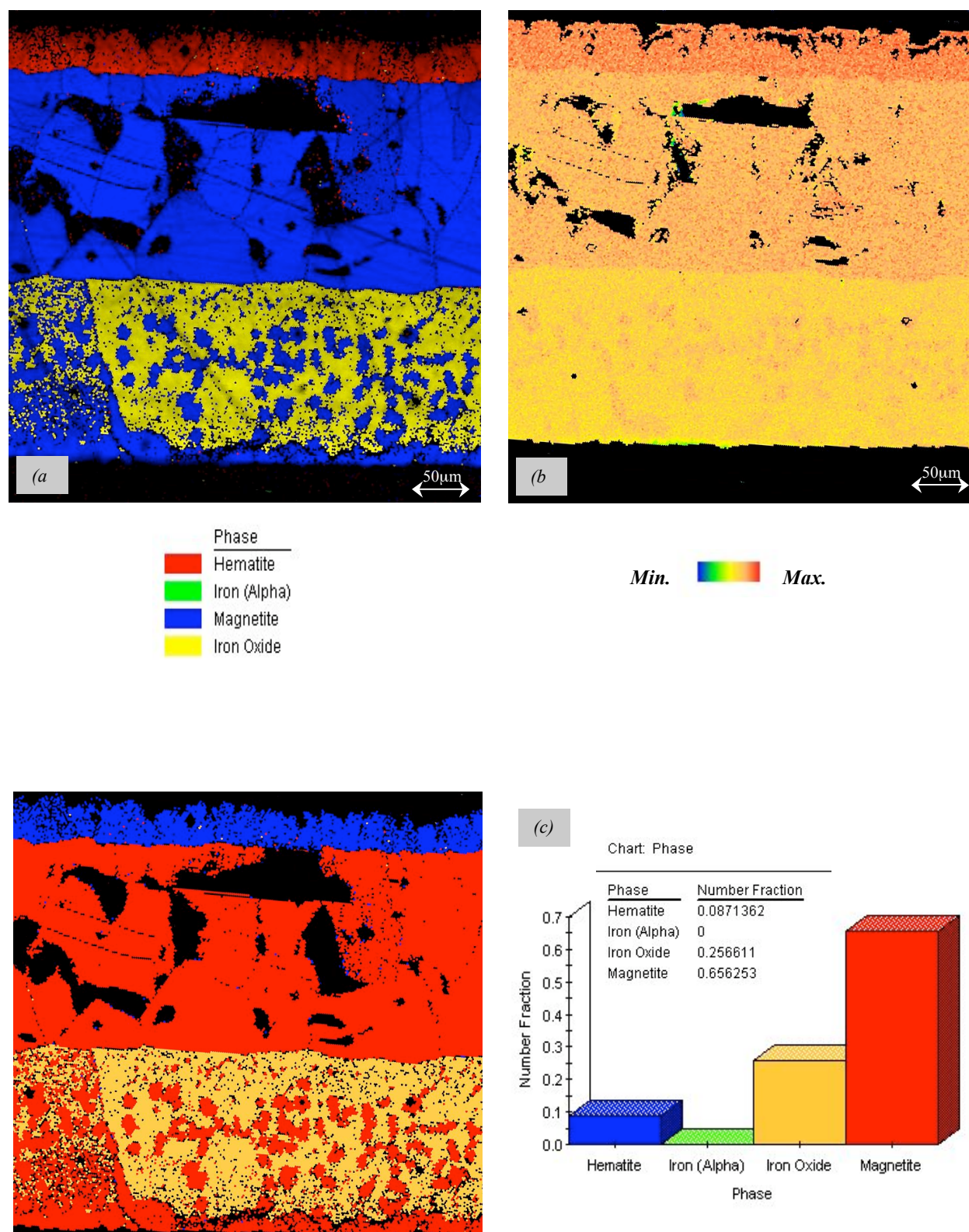
Figure 3.5.18: Alloy A oxidised at 1100°C for 1800 seconds. (a) phase map, (b) oxygen EDS map, (c) phase ratio map and chart.
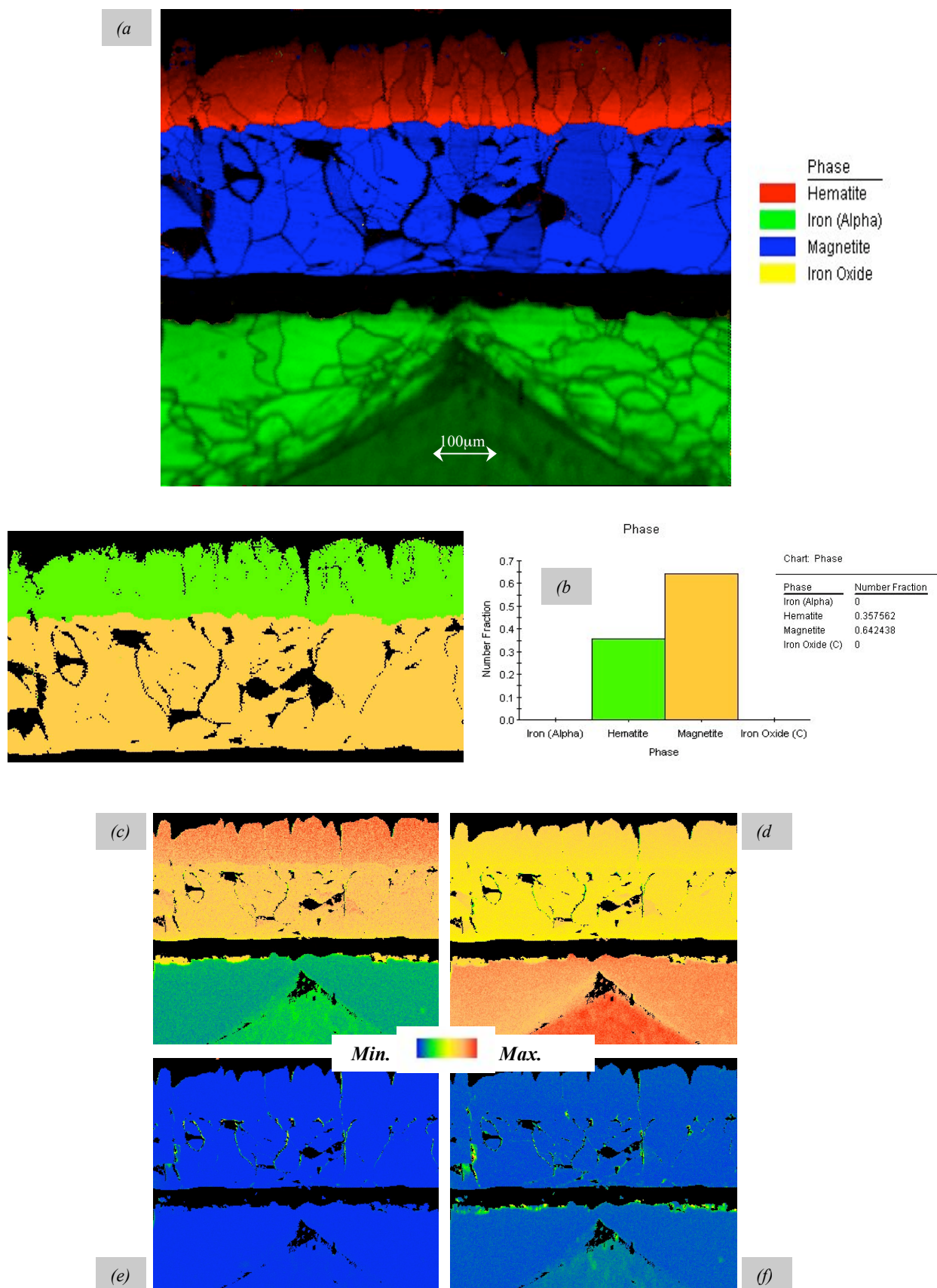
Figure 3.5.19: Alloy A oxidised at 1100°C for 3600 seconds. (a) phase map, (b) phase ratio map and chart (c) oxygen EDS map, (d) iron EDS map, (e) carbon and (f) silicon EDS map.

Alloy B Related Phase Map Images

(a)

(b)

20μm

Phase
- Hematite
- Iron (Alpha)
- Magnetite
- Iron Oxide

Min.   Max.

(c)

(d)

Chart: Phase

Phase	Number Fraction
Hematite	0.0719442
Iron (Alpha)	0
Iron Oxide	0.59354
Magnetite	0.334516

(e)
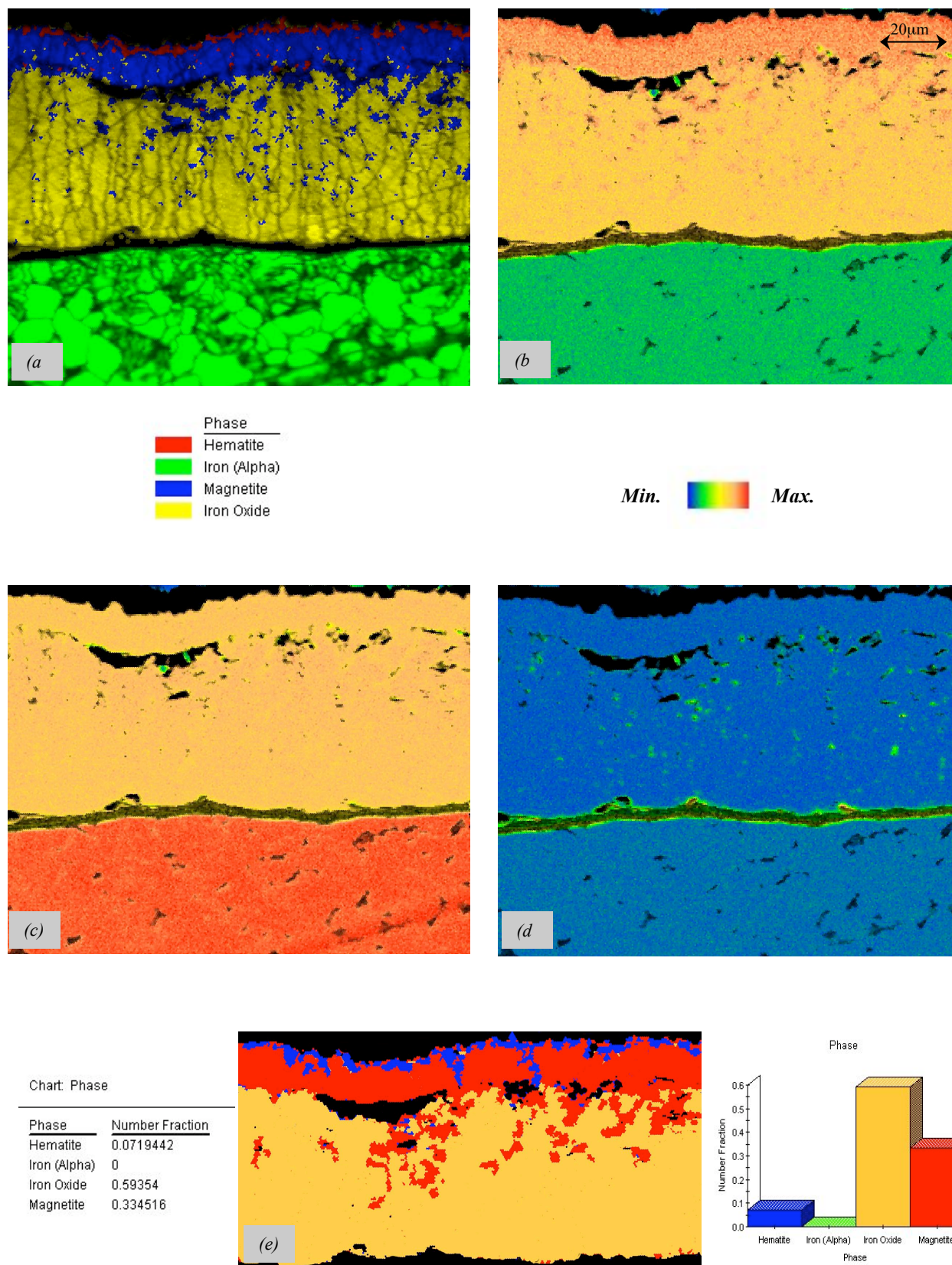
Figure 3.5.20: Alloy B oxidised at 900°C for 1800 seconds. (a) phase map, (b) oxygen EDS map, (c) iron EDS map, (d) silicon EDS map and (e) phase ratio map and chart.
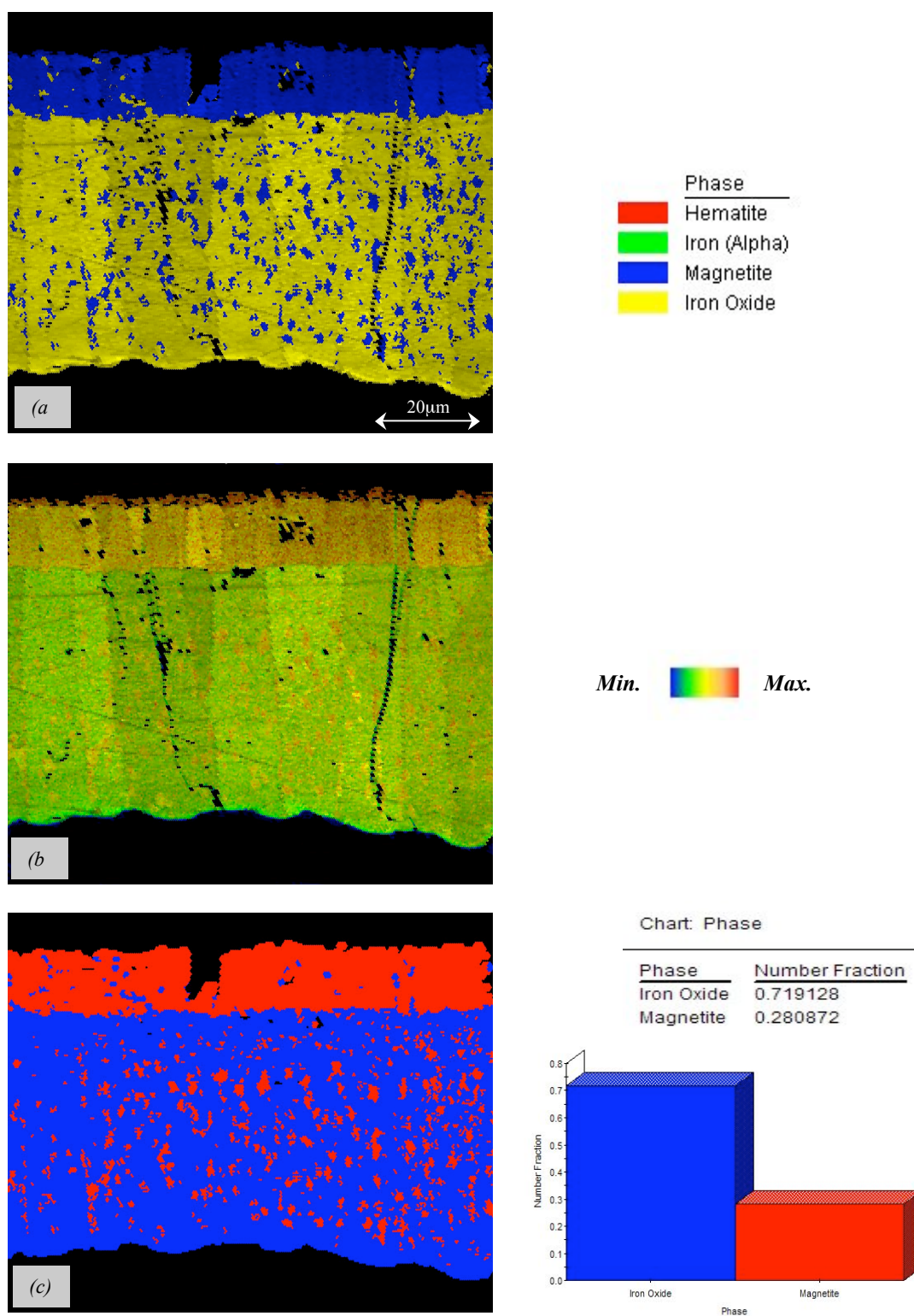
Figure 3.5.21: Alloy B oxidised at 1000°C for 1800 seconds. (a) phase map, (b) oxygen EDS map and (c) phase ratio map and chart.
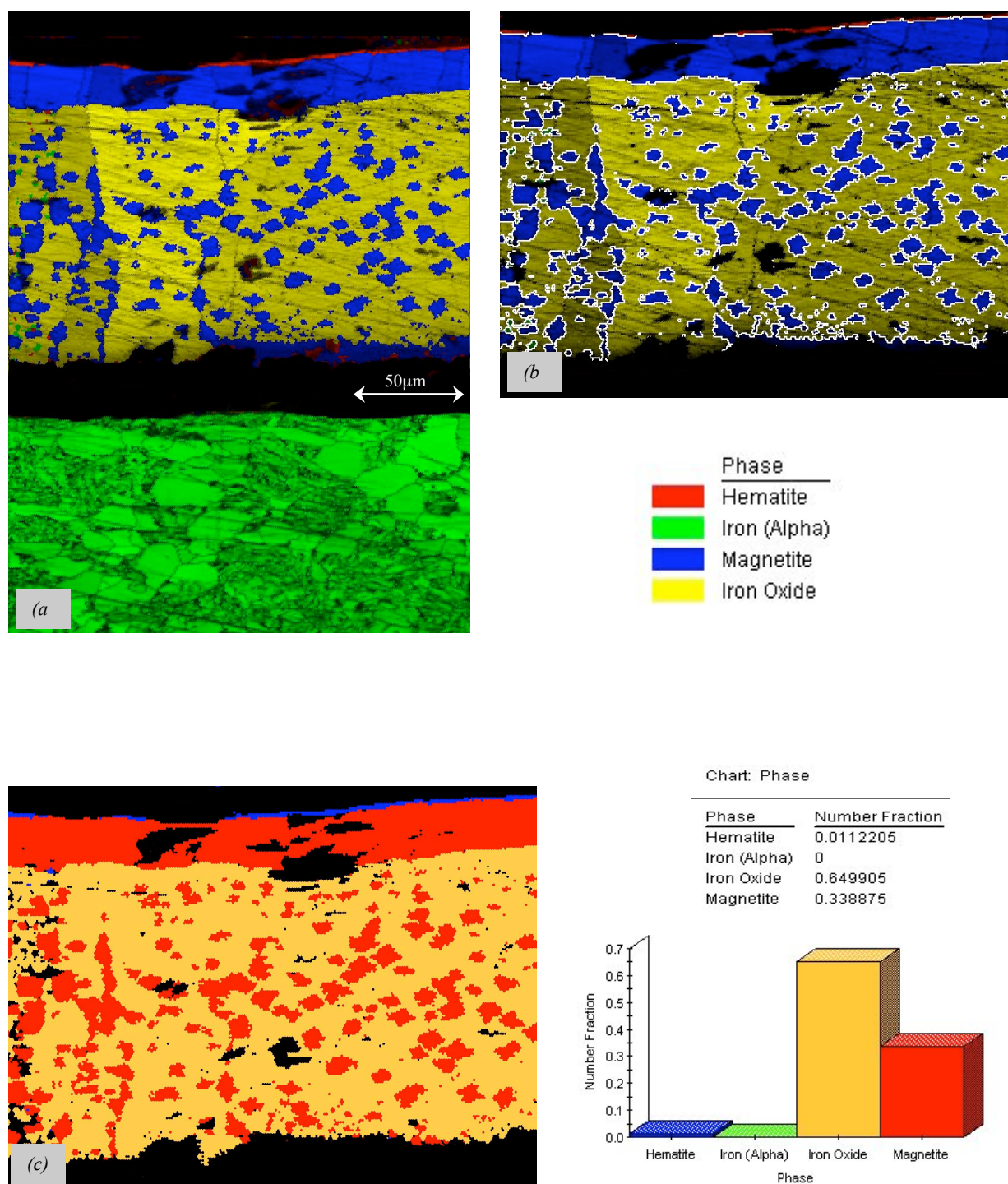
Figure 3.5.22: Alloy B oxidised at 1100°C for 1800 seconds. (a) phase map, (b) phase map with phase boundary (white), (c) phase ratio chart and map.

Temperature (°C)

	650	750	900	1000	1100
■ Heamatite				0.01	0.07
■ Magnetite	0.34	0.6	0.13	0.18	0.62
□ Wustite	0.65	0.39	0.86	0.8	0.3
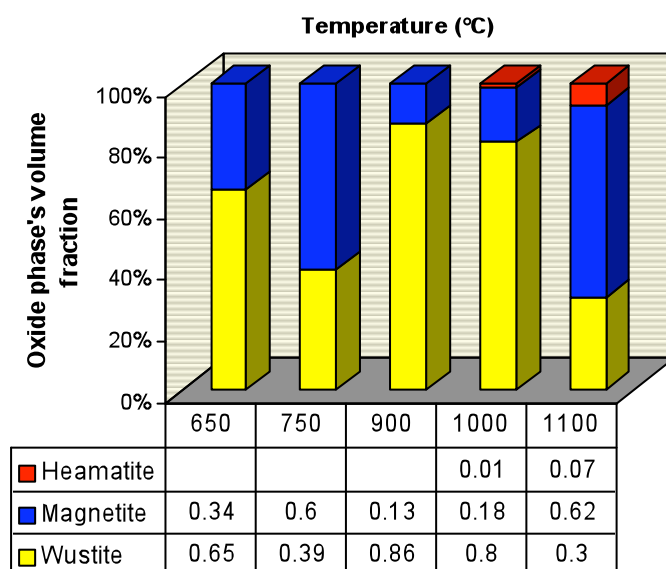
Figure 3.5.23: Oxide phase ratio versus temperature, IF steel oxidised for 1800 seconds.

Temperature (°C)

	750	900	1000	1100
■ Heamatite				0.09
■ Magnetite	0.24	0.31	0.19	0.65
□ Wustite	0.75	0.68	0.8	0.25
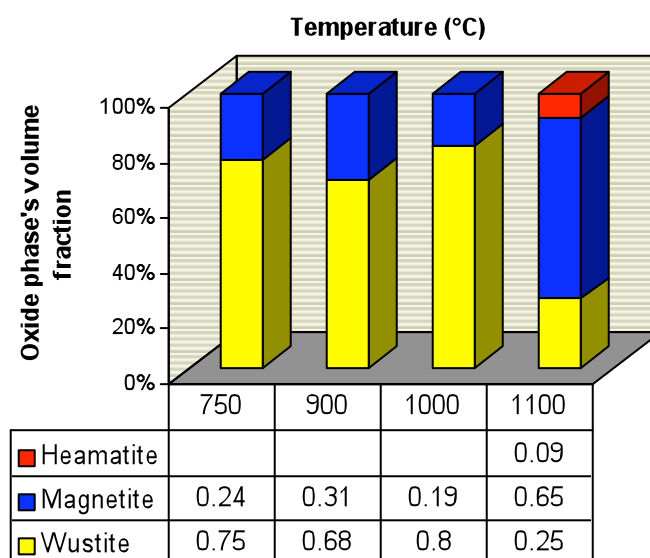
Figure 3.5.24: Oxide phase ratio versus temperature, Alloy A oxidised for 1800 seconds.

	900	1000	1100
Heamatite	0.07	0.01	0.01
Magnetite	0.33	0.33	0.33
wustite	0.59	0.65	0.64
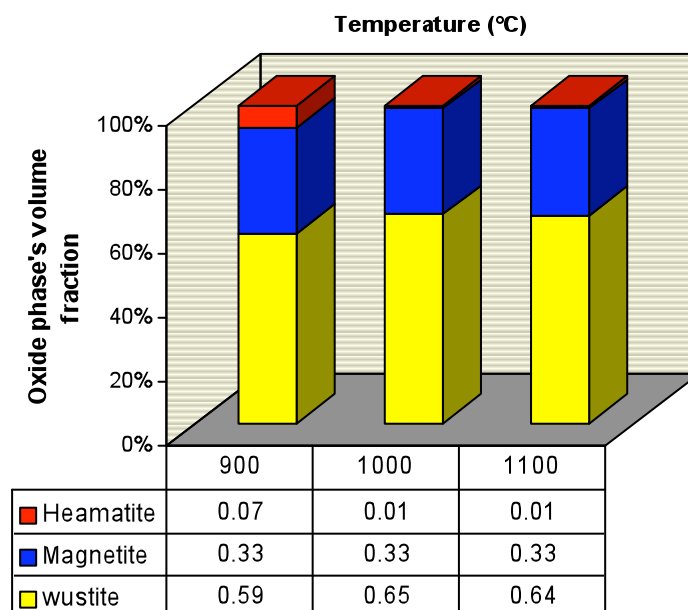
Figure 3.5.25: Oxide phase ratio versus temperature, Alloy B oxidised for 1800 seconds.

	600	1200	1800	3600
Heamatite		0.01	0.09	0.36
Magnetite	0.12	0.39	0.65	0.64
Wustite	0.88	0.59	0.25	
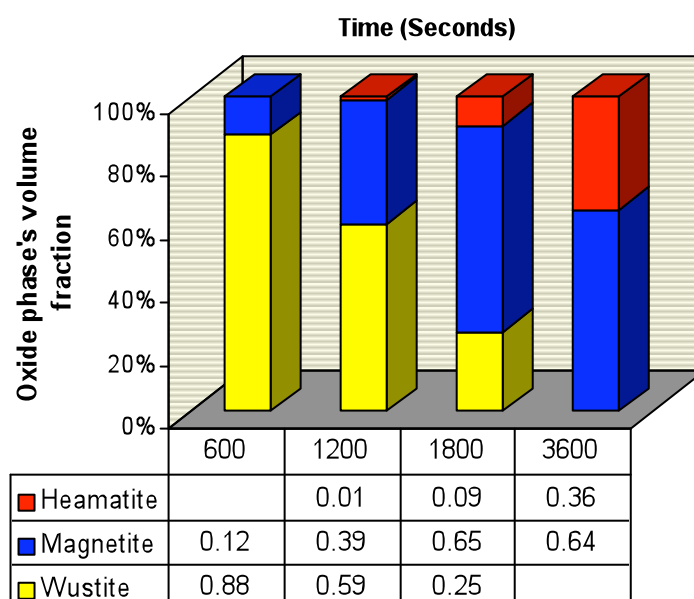
Figure 3.5.26: Oxide phase ratio versus time, Alloy A oxidised at 1100°C.

3.6 Steel Substrate and Oxide Scale Microtexture Analysis

In this section, the microtexture analysis is shown for IF steel, Alloy A and B substrates as well as the oxide scale layers formed on their surfaces. Also, grain orientations of each phase and the misorientations of the grain and phase boundaries have been investigated to give a complete description of the microtexture. The microtextural development of the oxide scales formed on each steel grade are considered in terms of their correlation and development with oxidation temperature and time of exposure. The texture analysis in this study was carried out and relied fully on EBSD data collection and analysis (OIM DC and OIM analysis).

For selected samples, Inverse Pole Figures (IPF) are shown only of Rolling Direction (RD). It should be noted that RD represents the Growth Direction (GD) in this case. The complete description of texture is given in Orientation Distribution Functions (ODF). The intensity of texture components is shown beside each ODF to indicate its strength. The full range of $(0<\varphi_1<360, 0<\phi<180°, 0<\varphi_2<45)$ Euler space is shown where it is necessarily especially where major texture components do not appear in the $(0<\varphi_1<90, 0<\phi<90°, 0<\varphi_2<45)$ Euler space range. It should be noted that φ_2 is constant and only (0 and 45°) are shown for all the samples. Individual misorientation analyses have been carried out for grain and phase boundaries where interesting microstructural features existed in the cross section samples.

Figures 3.6.1 - 3.6.9 show the microtexture analysis of IF steel and oxide scale layers formed on its surface after 1800 seconds at different oxidation temperatures. Some samples were analysed twice for statistical purposes. The EBSD scannings were run at low magnifications to cover relatively large areas for statistical reasons i.e., Figures 3.6.8 and 3.6.9. Figures 3.6.10 – 3.6.13 show the analysis for Alloy A substrate and its oxide scale layers formed after 1800 seconds at different temperatures. Figures 3.6.14 – 3.6.17 show the analysis for Alloy A and oxide scale formed on its surface at constant temperature, 1100°C, for different times of exposures. These EBSD scans were carried out to investigate the relationship between the microtexture developments with time of exposure. Figures 3.6.18 – 3.6.20 show the microtexture analysis of Alloy B and oxide

scale formed on its surface after 1800 seconds of exposure at different temperatures. Generalising the microtexture investigation of all the three steel grades used in this study and their oxide scales is shown in Tables 3.6.1 – 3.6.12 and Figures 3.6.21 – 3.6.24.

The microtexture of IF steel oxidised at 1100°C for 1800°C is shown as a first example in Figures 3.6.1 and 3.6.2. The relatively large thicknesses of oxide scale layers (wüstite, magnetite and haematite) made the microstructure investigation easier than other samples for statistical calculations. However, the larger size of wüstite and iron grains caused difficulty in collecting sufficient orientation data even at very low magnifications, see the same Figures. Thus, only a few grains of iron and wüstite are analysed. Figure 3.6.1 show the ODFs of iron substrate, wüstite layer, magnetite layer, magnetite precipitates and haematite layer. Iron has strong rotated Cube texture. A full range of Euler space are shown in this analysis to show whether the $(0<\varphi_1<90, 0<\phi<90°, 0<\varphi_2<45)$ is showing all the texture components. As shown in Figure 3.6.1 (a), the texture components intensities are distributed in a systematic manner which is repeated throughout $(0<\varphi_1<360, 0<\phi<180°, 0<\varphi_2<45)$ ranges. Thus, $(0<\varphi_1<90, 0<\phi<90°, 0<\varphi_2<45)$ can show all the texture components that exist in the iron phase. The wüstite has a near Cube texture, but the highest texture intensity is (0 1 3) <1 -6 2>, see Figure 3.6.1 (b). The magnetite and haematite texture distribution in Euler space were not symmetric. The $(0<\varphi_1<90, 0<\phi<90°, 0<\varphi_2<45)$ Euler space cannot enclose the major texture components that exist in these phases. In these cases, the texture analyses were shown on $(0<\varphi_1<360, 0<\phi<180°, 0<\varphi_2<45)$ Euler space ranges. As can be seen in Figures 3.6.1 (c) and (e), the highest texture intensity was out of $(0<\varphi_1<90, 0<\phi<90°, 0<\varphi_2<45)$ Euler space ranges. Haematite has the strongest texture among all the other phases, with (0 6- 6- 5) <5 -50 -6> and (0 3 -3 2) <-12 1 11 15> texture components. The major haematite texture intensity is >90 which indicates that haematite has a very strong texture, see Figure 3.6.1 (e). The magnetite precipitates have the same texture components as the wüstite layer. This was the case for all other samples, which is why magnetite precipitates ODF are not shown for further references. As can be seen from Figure 3.6.1, there is no crystallographic texture relationship between the steel substrate and oxide scale layers, nor between the oxide scale layer phases in this sample.

Figure 3.6.2 shows the growth direction Inverse Pole Figures (IPF) map represented in a unit triangle of all the phases and IPF//GD map of the same sample in Figure 3.6.1. As described earlier, the different colour codes in the IPF map represent different orientations, indicated in unit triangles. The steel substrate and wüstite have strong texture as shown in Figure 3.6.1, but this is because only a few grains could be mapped in the EBSD scan due to their large sizes. Otherwise, as shown in the IPF// GD map, the grains have different colours and are orientated in different directions. The magnetite and haematite texture information covers a reasonable numbers of grains. As shown in the same figure, magnetite has weak texture and haematite has very strong texture. Most of the grains in the haematite layer are coloured red which indicates that they are (0001)//GD crystal plane orientated. The magnetite precipitates have the same orientation as the wüstite layer as shown in Figure 3.6.2. This is a confirmation of ODF results; see Figure 3.6.1, where the wüstite layer and magnetite precipitates have the same texture components. The texture correlation between the phases could be considered in a IPF map as well as ODFs. From the ODFs figures, Figure 3.6.1, there is no texture correlation between the substrate and the oxide scale layers. This can be confirmed by showing individual Reconstructed Diffraction Patterns (RDP) and Discrete Pole Figures (DPF) for any grains or points of interest. As shown in the Figure 3.6.2, different grains in the steel substrate (points 1 and 3) have different orientation as shown in RDP and DPF 1 and 3. Furthermore, there was no similarity between the RDPs and PDFs obtained from the innermost wüstite layer in the oxide scale (4, 5, 6, 7 and 8) with the ones obtained in the magnetite layer (points; 9, 10 and 11). The similarity between points 3 and 4 indicates that there is an orientation correlation between steel substrate and wüstite grains. However, this correlation was not found between all the substrate and wüstite grains, see points 1 and 7, 2 and 5. This individual analysis is important for investigating the orientation correlations between neighbouring grains and phase layers.

Other samples of IF steel have analysed, see Figures 3.6.3 - 3.6.7. Because of the limitation of space, only selected maps are shown. The IPF//GD and ODFs are shown for all of the samples and the other related maps shown if there were interesting observations.

To allow a larger area of data to be collected, some EBSD scans were performed at very low magnification, Figure 3.6.8 shows one such scan. Very similar results are obtained from low magnification as high magnification scans. For further confirmation two different scans were carried out. The first scan was only for the steel substrate and another one only of the oxide scale. Figure 3.6.8 shows the microtexture analysis of the steel substrate and Figure 3.6.9 of the oxide scale. The substrate grains are separated by high angles grain boundaries, see Figure 3.6.8 (b). Only 6% and 15% were low angle and CSL boundaries, respectively, which was similar to the results from the high magnification scans. The majority of the steel substrate grains are orientated towards the (101) plane, as indicated by the green colour in the IPF//GD map, see Figure 3.6.8 (a). However, the IPF only shows one direction of the three orientation representation. Looking at the ODFs in Figure 3.6.8 (d), a very weak texture is observed for the iron substrate and the grain boundaries are distributed randomly as shown in 3.6.8 (e). As shown in discrete ODFs in 3.6.8 (c), the grains are orientated randomly and the major texture components distributed randomly across overall sample area. The texture of oxide scale layers were weak as can be seen in Figure 3.6.9 (a) and (b). The majority of the grain boundaries were high angle grain boundaries. Only 18% and 8% were low angles and CSL boundaries, respectively, see Figure 3.6.9 (c). Also the grain and phase boundaries were random as indicated in Figure 3.6.9 (e). An interesting finding was that the texture became stronger with time of oxidation. The textures of the IF iron substrate and oxide scale layers at 750°C- 1200 seconds were very weak (4.1 and 6.5 maximum texture component intensities for iron and wüstite, respectively), see Figure 3.6.8 (d) and 3.6.9 (b). The texture became stronger after 1800 seconds of oxidation at the same temperature (texture components intensities >90 and 20 for iron and wüstite, respectively), see Figures 3.6.5 and 3.6.6. However, as will be discussed in Chapter 4, this example is not a clear indication of strengthening texture with time as only a few grains of steel substrate are sampled.

Alloy A and B as well as their oxide scale layers' microtexture were analysed in the same manner as the IF steel. Figures 3.6.10 - 3.6.20 show the microtexture analysis of Alloy A and Alloy B at different temperatures for 1800 seconds. A discrete phenomenon was found during analysing the Alloy A sample oxidised at 900°C for 1800 seconds. The

magnetite and wüstite layers are separated by very low angle and coherent phase boundaries, see Figure 3.6.11 (a) and (b). In order to double check this result, further individual analyses were carried out, some of them are shown as in Figure 3.6.11 (c). The two points indicated in Figure 3.6.11 (a), have the same orientations, represented by the yellow colour coded grain in IPF//GD and the discrete pole figures in Figure 3.6.11 (c) confirms this result.

Although IPFs do not give a full description of texture in a three dimensional representation, it is very useful for crack investigations. For example in Figure 3.6.12, the vertical crack is of interest to know whether it is intergranular or transgranular crack. As can be seen from the same figure, the orientations on either side of the crack are the same, indicating that the crack is within one grain and it is an transgranular crack. Individual misorientation analysis is shown in Figure 3.6.12 (b), as a double check for the IPF map.

The EBSD microtexture analyses to investigate the time and texture correlation (Figures 3.6.14 – 3.6.17) were carried out in the same manner as for the previous analysis. It should be noted that haematite is always highly textured, see Figure 3.6.16 – 3.6.17. Taking Alloy A-1100°C-3600 seconds as an example, the haematite layer is red colour in IPF//GD, which indicates that the haematite grains were orientated toward (0001)//GD, Figure 3.6.17 (a). As in other examples, here too haematite has strong texture as shown in Figure 3.6.17 (b), see haematite ODF.

Looking at the overall picture of the microtexture analysis of each steel grade used in this study gives a better idea for comparison purposes. Tables 3.6.1 - 3.6.3 show the overall microtexture analysis of the IF steel samples. As shown in Table 3.6.1, the texture intensity varied with temperature for each phase. The haematite was not observed in all the scans which makes the haematite microtextural development observation difficult. Figure 3.6.21 shows the texture strength versus temperature graph. The iron texture strength (green bars in the chart) varied with temperature. At 650 and 750°C the iron exhibits a strong texture which decreases with increasing temperature followed by an increase at 1100°C. No trend of texture strength with increasing temperatures were found

for the IF steel substrates. There is a general trend of wüstite texture strength (yellow bars) with temperature. The wüstite texture strength increased with increasing temperature. The magnetite texture strengths (dark blue bars in the chart) are constant, i.e. weak, excluding at 900°C where it has strong texture.

Table 3.6.2 shows the major texture components of IF steel substrate and the oxide scale at different temperatures. All of the samples were exposed to high temperature oxidation for 1800 seconds in air. The texture correlation between the phases is shown in Table 3.6.3. As shown, there is an iron-wüstite texture correlation at 650 and 1000°C, and iron with magnetite only at 1000°C but a very strong correlation. The texture correlation between the oxide phase layers is stronger than with the steel substrate. The wüstite and magnetite are texturally correlated at 650, 750 and 1000°C.

In the same manner, the texture correlation is generalised in Tables 3.6.4 – 3.6.6 for Alloy A oxidised at different temperatures for 1800 seconds. As shown in Table 3.6.4 and Figure 3.6.22, the wüstite and magnetite texture strength increased with increasing temperature. The steel substrate texture was strong at 650°C and constant (weak) at the rest of the oxidation temperatures indicating no trend with temperature. The major texture components are given in Table 3.6.5. The texture correlation of the phases is shown in Table 3.6.6. The iron and wüstite are texturally correlated at 650, 1000 and 1100°C, iron and magnetite at 1000 and 1100°C. The wüstite and magnetite have a strong texture correlation as shown for the IF steel.

The texture correlation is generalised in Tables 3.6.7 – 3.6.9 for Alloy B oxidised at different temperatures for 1800 seconds. As shown in Table 3.6.4 and Figure 3.6.23, the wüstite texture strength increased with increasing temperatures. The steel substrate texture is weak at 900°C and very weak at 1100°C. The magnetite and haematite texture strengths are constant at all temperatures. The haematite layer has a very strong texture at all temperatures while magnetite has a weak texture. The major texture components are shown in Table 3.6.8. The texture correlation between the phases is shown in Table 3.6.9. The iron-wüstite and iron-magnetite have a strong texture relationship at 1100°C. The wüstite and magnetite are texturally correlated as for the IF steel and Alloy A.

The microtexture development correlation between the phases with time of exposure are generalised in Tables 3.6.10 – 3.6.12. The texture strength of the Alloy A substrate and oxide scale layers at 1100°C for different times of exposure are shown in Table 3.6.10. As shown in the Table and Figure 3.6.24, the iron texture strength is constant at all times of exposure. The wüstite texture strength varies with time. The magnetite texture strengths are constant at all times except at 1800 seconds where it has a strong texture. The haematite which is observed only at 1800 and 3600 seconds, has a strong texture. Overall there is no trend in the texture strengths with time. Table 3.6.11 shows the major texture components of all the phases at different times of exposure. The texture correlation between all the phases is shown in Table 3.6.12. The steel substrate has texture correlation with wüstite at 600 and 1800 seconds, whereas it has correlation with the magnetite layer at all times of exposure. The oxide scale phase's texture correlation clearly can be seen in Figure 3.6.12 at all the times of exposure, especially at 1800 seconds.

Considering only overall phase microtexture correlation with temperature and time, an interesting finding has been discovered. Looking at Tables 3.6.6, 3.6.9 and 3.6.12, the phase's correlations increased with increasing time and temperatures. For examples, at 1000 and 1100°C all of the phases are correlated, but not at lower temperatures. Also at 1800 and 3600 seconds all the phases are correlated but not at shorter time of exposure. However, this trend was not observed fully for IF steel. All the phases are texturally correlated at 1000°C but not at lower or higher temperatures.

Due to space limitation, not all the microtexture analyses and maps could be shown in this study. Further misorientation data are shown in Figure 3.6.25. As the misorientation of grain and phase boundaries is highly related to microtexture, the grain boundary and phase boundaries of the EBSD scanned sample are presented in Section 3.4 and Appendices 9 and10. The grain boundary and overall misorientation maps show the grain boundary angles between selected grains. The complete misorientations analysis should indicate the grain boundary plane as well as their angles to give full description of grain boundary nature and correlation with the microtexture analysis. The EBSD software has unique capabilities in determining the misorientation between individual neighbouring

grains. Figure 3.6.25 (a) shows the individual misorientation analysis between grains and phases that exist within the cross section of IF steel oxidised at 1100°C for 1800 seconds. As indicated in the figure, the iron/wüstite layer misorientation is 25.4° about [-7 -24 8] (dark blue colour coded in the IQ map).

The misorientation between the iron and magnetite seam is much higher than the misorientation between the iron substrate and wüstite layer, see Figure 3.6.25 (a) (dark blue highlighted points). However, that was not the case in all the areas. The differences were wider where the magnetite seam grains have a bigger misorientation difference with the wüstite grains. The magnetite phase boundary misorientation with wüstite layer (red points) was high ~ 59.8, while was very low with haematite ~ 15° (green points). The misorientations between the magnetite precipitates and the wüstite grains were very low ~ 1° at some points. However, the magnetite precipitates are separated from the wüstite grains in the Unique Grain Colour map because of the different phases as can be seen in Figure 3.4.2 (c).

The 750°C-1800 seconds cross section sample is also of interest because the oxide scale was not uniform, see Figure 3.6.25 (b). The general microtexture analysis through IPF//GD and ODFs for each phase was discussed earlier with other samples. The interesting point was in finding grain boundary misorientation correlation with non-uniformability of the scale on the steel surface. Most of the wüstite and magnetite grain boundaries are high angle. More individual analysis was carried out for most of the grain boundaries in the scan area. As indicated in Figure 3.6.25 (b), there are no major differences between the grain misorientations of the smaller thickness and larger thickness areas.

A new approach was followed to discover whether there are any microtexture and misorientation differences in different geometric sides of the samples. Figure 3.6.26 shows an EBSD scan that was carried out to find out more about this approach. The steel substrate has a strong Goss texture as shown in Figure 3.6.26 (a) and IPF//GD in (b) whereas, the grains are orientated towards (001) direction (red colour coded in IPF map). The wüstite has very weak Goss and Cube texture as shown in the same figure. The grain

and phase boundaries are randomly distributed except the iron-iron grains, as shown in Figure 3.6.26 (c). An iron grain (green colour grain orientated (101)//GD), as indicated in the IPF map, Figure 3.6.26 (b), was taken as an example. There is no preferred orientation of the oxide grains in both sample geometric sides around this grain. Furthermore, the thickness of the oxide scale varied along both sides of the grain and there is no indication of sample geometric correlation with oxide scale non-uniformability. A thin oxide scale can be observed in the same figure near the corner of the sample. This phenomenon and the rest of microtexture and misorientation analyses will be discussed in detail in Chapter 4.

IF Steel Microtexture Analysis
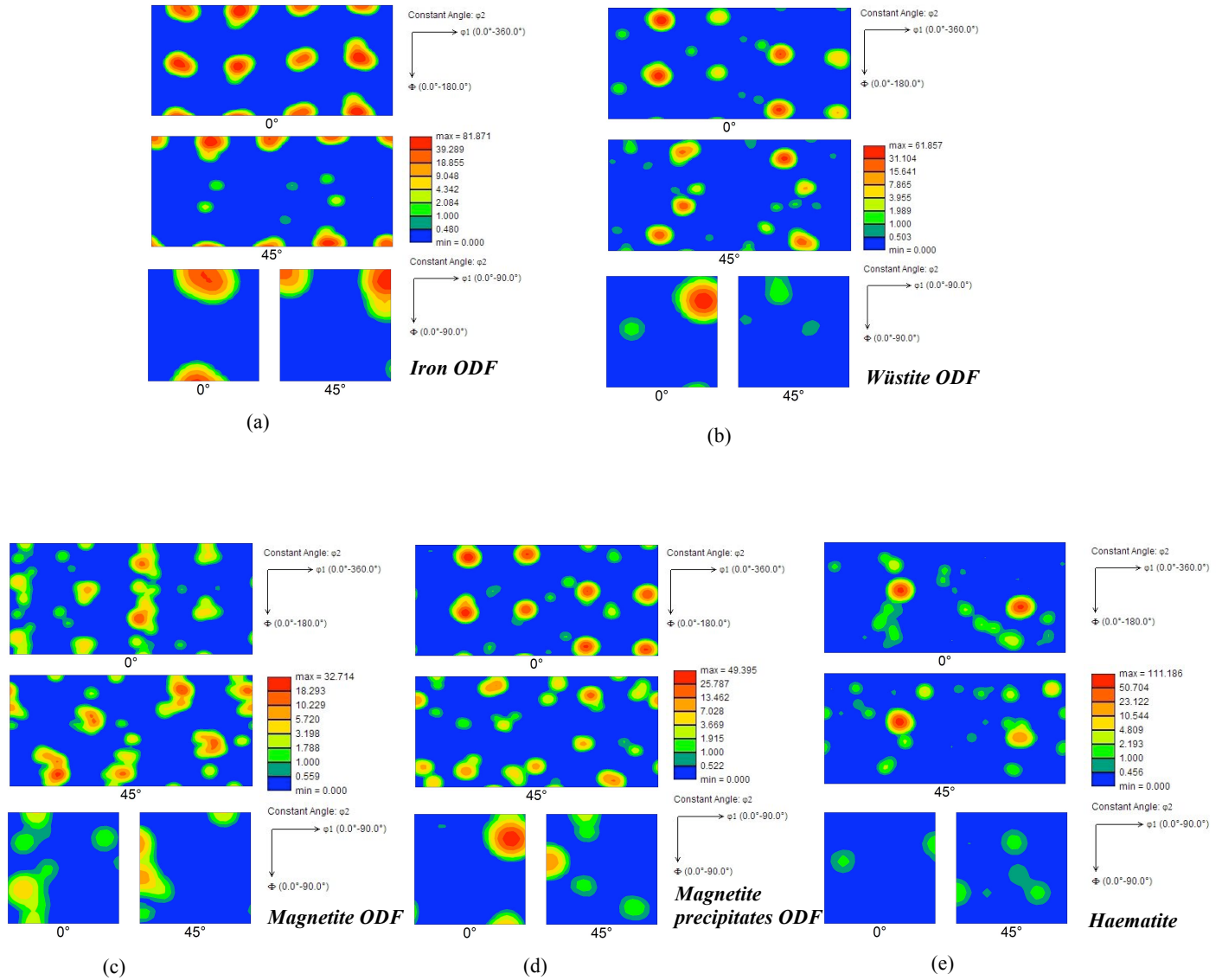
Figure 3.6.1: EBSD-Microtexture analysis of IF steel oxidised at 1100°C for 1800 seconds
    (a) Iron ODFs- strong (001)<110> rotated Cube texture component
    (b) Wüstite ODFs-near Cube texture (100) <001>, highest texture intensity is in (013) <1 -6 2>
    (c) Magnetite ODFs- weak (11-4) <843> texture component
    (d) Magnetite precipitates ODFs- has the same texture components as wüstite layer
    (e) Haematite ODFs-strong (06-6-5) <5-50-6> and (03-32) <-12 1 11 15> texture components
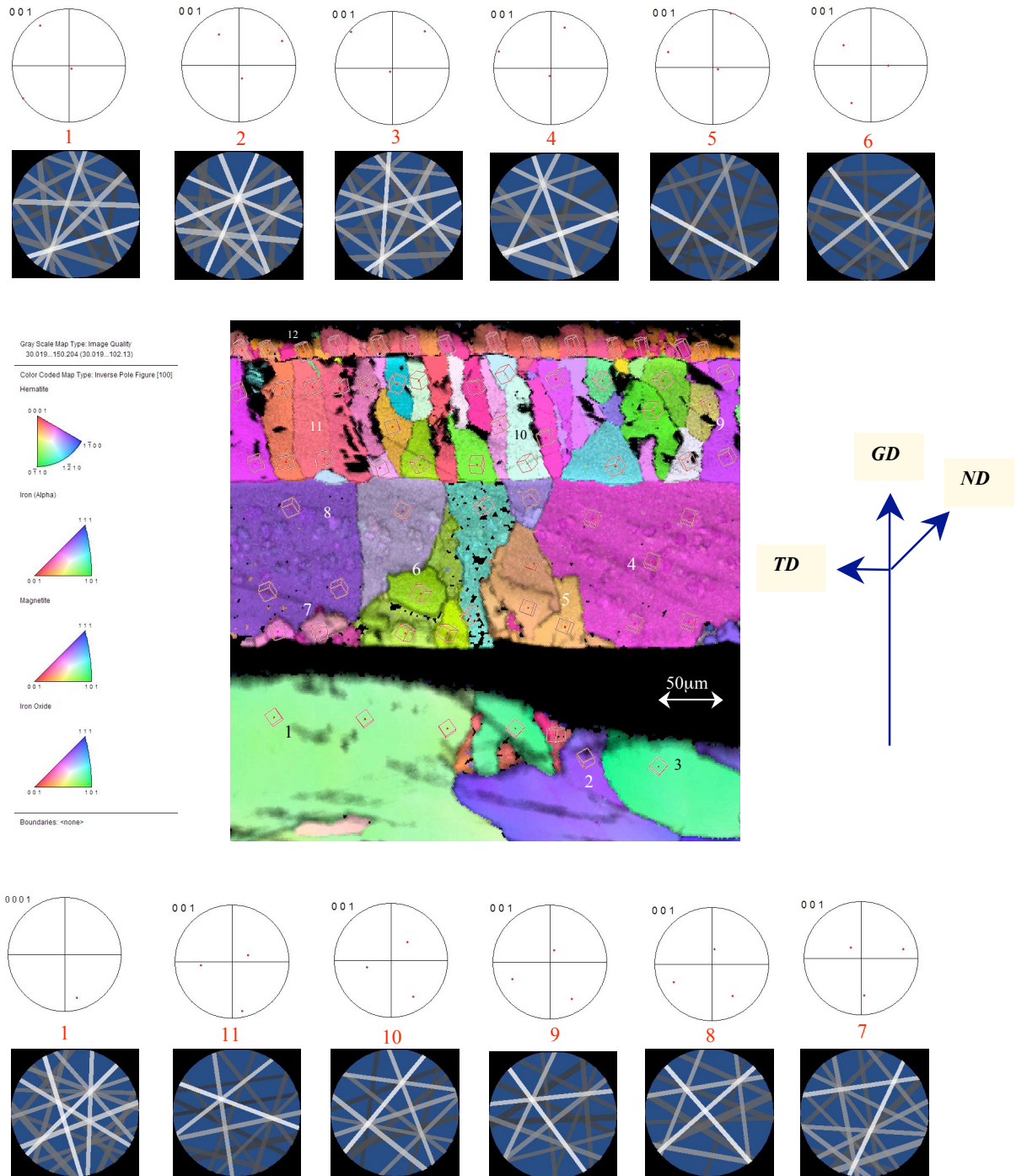
Figure 3.6.2: Highlighted individual grain orientations on IPF of Growth Direction map, discrete pole figure and reconstructed diffraction pattern taken from different grains in the oxide scale layers and substrate.

Constant Angle: φ2

→ φ1 (0.0°-360.0°)

Φ (0.0°-180.0°)

max = 52.094
26.956
13.949
7.218
3.735
1.933
1.000
0.517
min = 0.000

Constant Angle: φ2

→ φ1 (0.0°-90.0°)

Φ (0.0°-90.0°)

Wüstite ODF

(b)

max = 22.308
13.296
7.924
4.723
2.815
1.678
1.000
0.596
min = 0.000

Magnetite ODF

(c)

(a)

50μm

max = 81.750
39.241
18.836
9.042
4.340
2.083
1.000
0.480
min = 0.000

Iron ODF

(d)
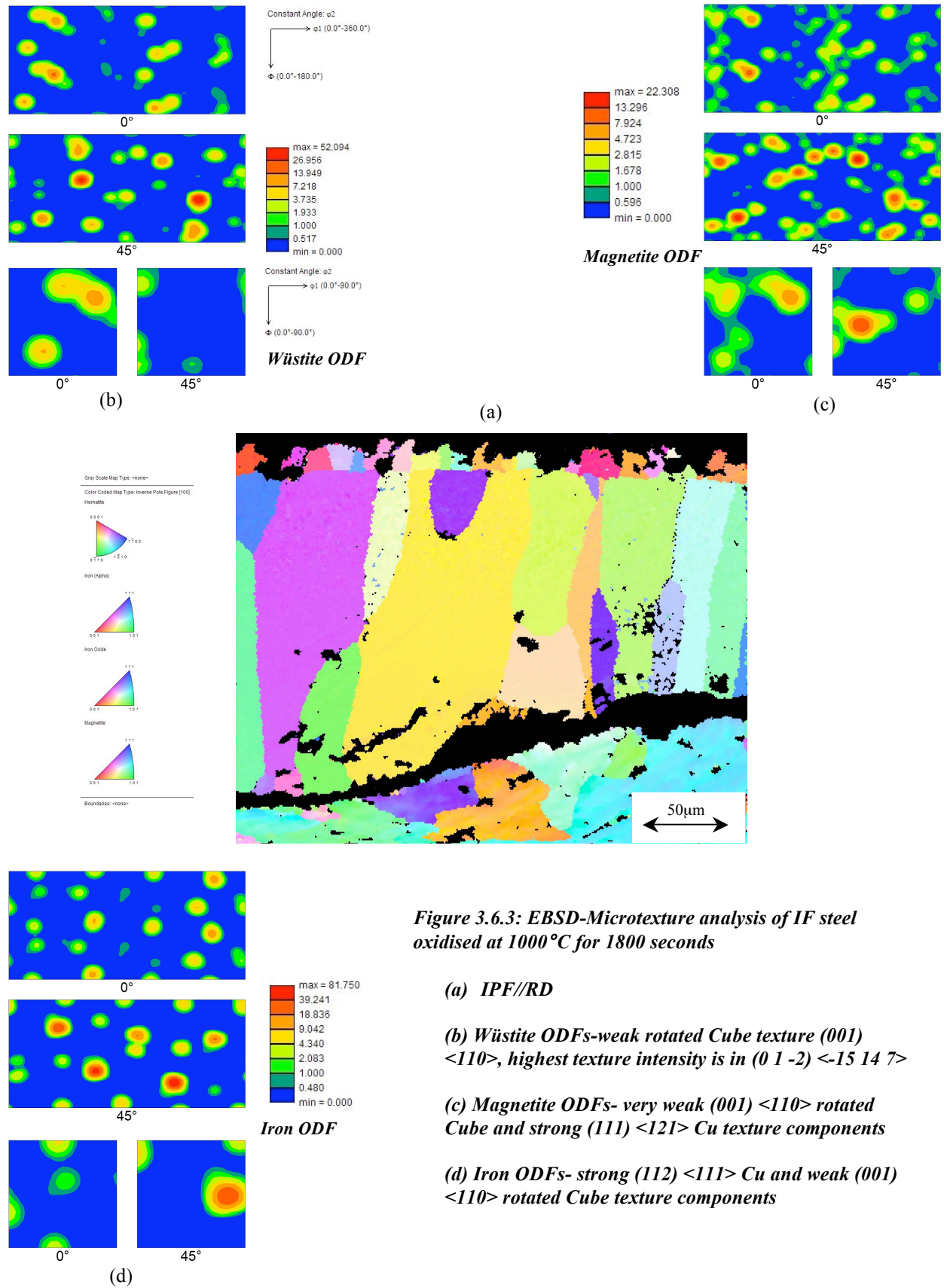
Figure 3.6.3: EBSD-Microtexture analysis of IF steel oxidised at 1000°C for 1800 seconds

(a) IPF//RD

(b) Wüstite ODFs-weak rotated Cube texture (001) <110>, highest texture intensity is in (0 1 -2) <-15 14 7>

(c) Magnetite ODFs- very weak (001) <110> rotated Cube and strong (111) <121> Cu texture components

(d) Iron ODFs- strong (112) <111> Cu and weak (001) <110> rotated Cube texture components

155

max = 45.133
23.919
12.676
6.718
3.560
1.887
1.000
0.530
min = 0.000

(b) Iron ODF

max = 9.354
6.444
4.439
3.058
2.107
1.452
1.000
0.689
min = 0.004

(c) Wüstite ODF

max = 11.316
7.552
5.040
3.364
2.245
1.498
1.000
0.667
min = 0.020
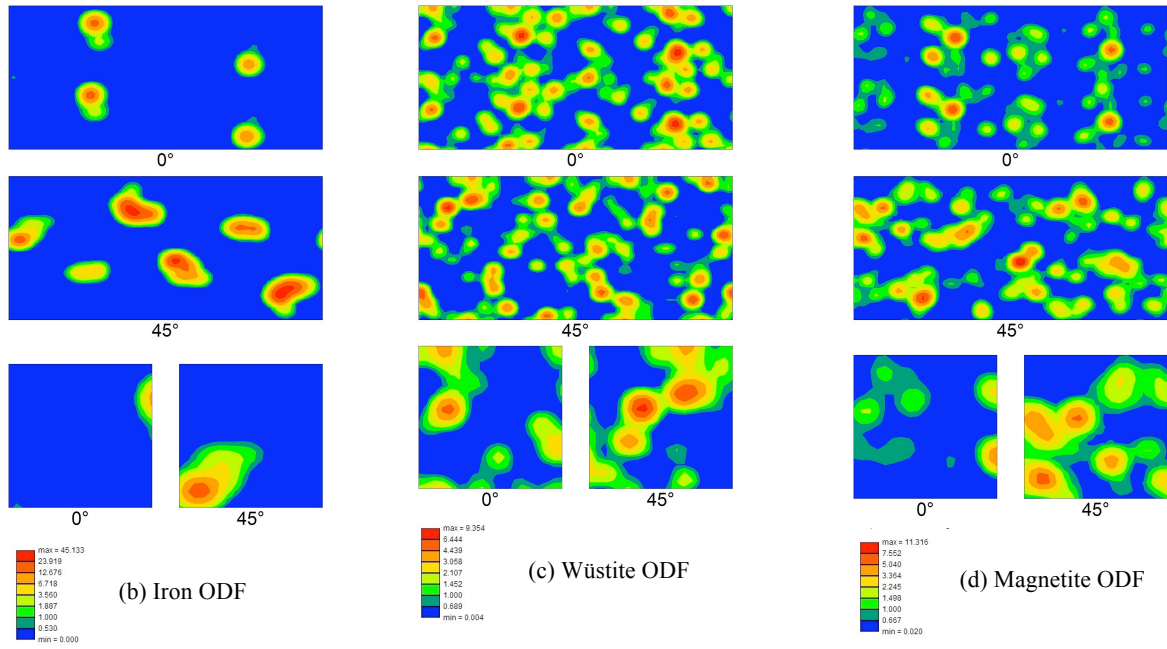
(d) Magnetite ODF

Figure 3.6.4: EBSD-Microtexture analysis of IF steel oxidised at 900°C for 1800 seconds
   (a)   Iron ODFs- strong (110)<011> P and weak (001) <19 -16 0> texture components
   (b)   Wüstite ODFs-weak Cube texture (100) <001>, highest texture intensity is in (0 1 -2) <-15 14 7>
   (c)   Magnetite ODFs- very weak (110) <001> Goss and (335) <1 -1 0> texture components

max = 152.021
65.804
28.484
12.330
5.337
2.310
1.000
0.433
min = 0.001

(a) Iron ODF

max = 20.223
12.252
7.423
4.497
2.724
1.651
1.000
0.606
min = 0.009

(b) Wüstite ODF

max = 21.742
13.014
7.790
4.663
2.791
1.671
1.000
0.599
min = 0.043

(c) Magnetite ODF
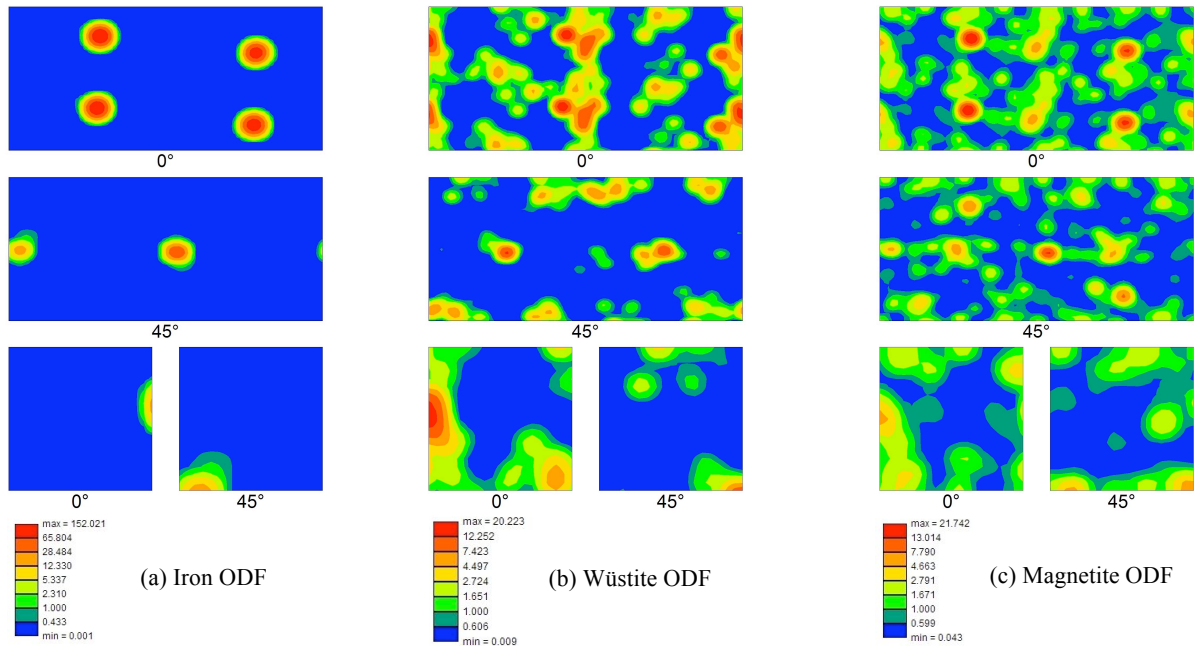
Figure 3.6.5: EBSD-Microtexture analysis of IF steel oxidised at 750°C for 1800 seconds
   (a) Iron ODFs- (110) <122> P texture components, highest texture intensity is in (034) <0 -4 3>
   (b) Wüstite ODFs-strong Goss texture (110) <001> and weak Cube (100) <001> texture components
   (c) Magnetite ODFs- weak (110) <001> Goss and Cube (100) <001> texture components
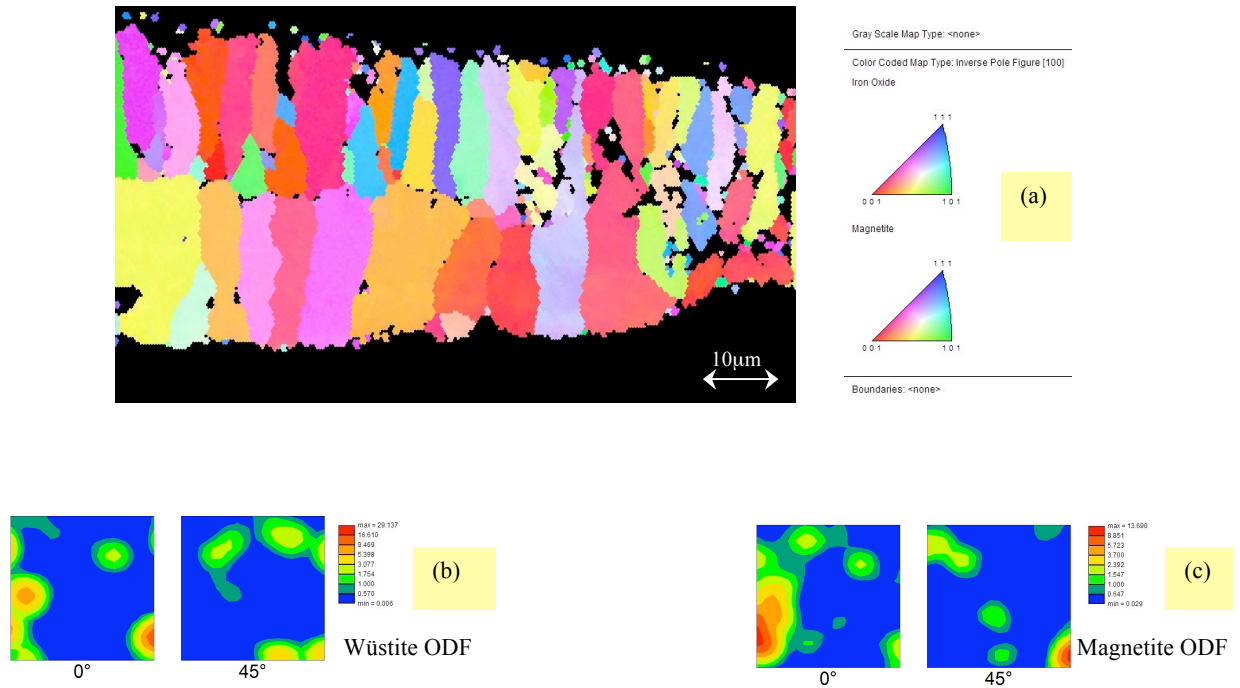
Figure 3.6.6: EBSD-Microtexture analysis of IF steel oxidised at 750°C for 1800 seconds
(a) IPF//RD
(b) Wüstite ODFs-weak Goss texture (110) <001> and Cube (100) <001> texture components
(c) Magnetite ODFs- strong (110) <001> Goss, weak Cube (100) <001> and strong (111) <011> Z texture components
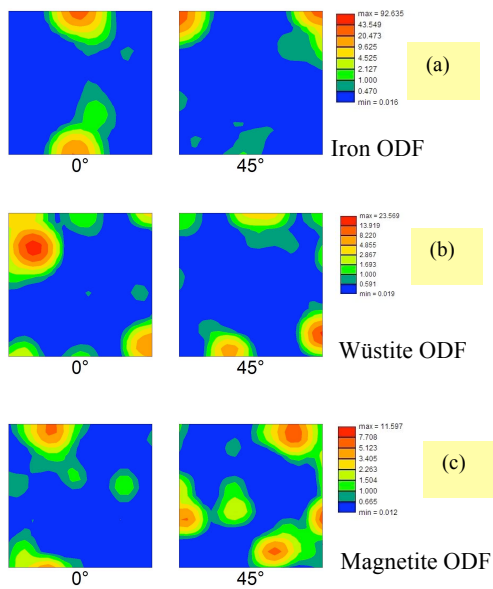
Figure 3.6.7: EBSD-Microtexture analysis of IF steel oxidised at 650°C for 1800 seconds

(a) Iron ODFs- strong rotated Cube (001) <110> texture components

(b) Wüstite ODFs-Cube texture (100) <001> and weak rotated Cube (001) <110> texture components, high intensity is in (331) <-3 -4 21>

(c) Magnetite ODFs- very weak Cube (100) <001> texture component, high intensity is in (001) <2 -1 0>
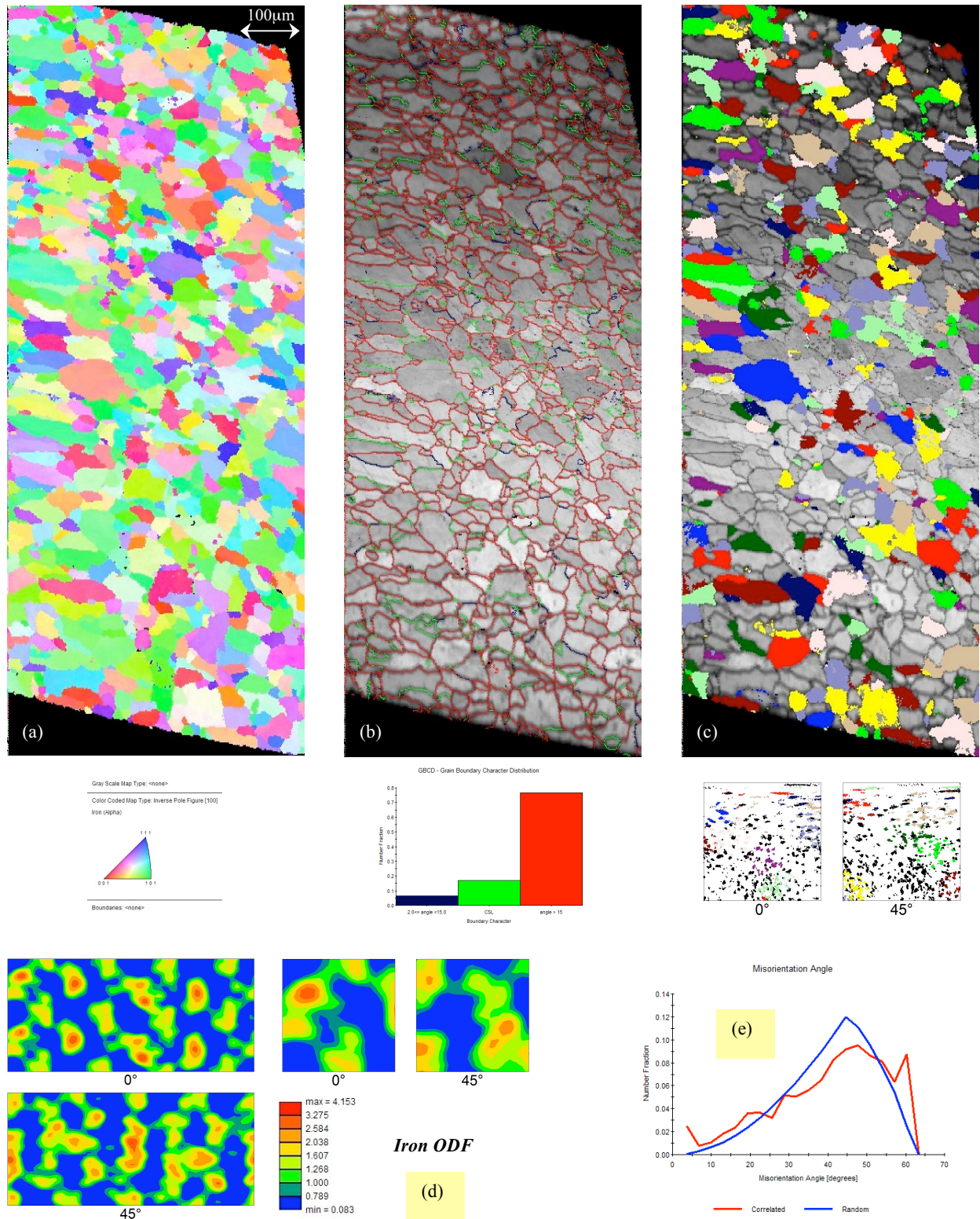
Figure 3.6.8: EBSD-Microtexture analysis of IF steel substrate oxidised at 750°C for 1200 seconds
   (a) IPF//RD, (b) Grain Boundary Character Distribution chart and map, (c) Discrete ODF highlighted on
IQ map, (d) Iron ODFs-weak Goss texture (110) <001> and rotated Cube (001) <110> texture components,
(e) Grain boundaries misorientation chart compared with Mackenzi plot of iron substrate

(a)

(b)

(c)

Wüstite ODF

Magnetite layer ODF

Magnetite precipitates ODF

Magnetite seam ODF

(d)

20μm

The misorientation between magnetite seam and wüstite layer showed 44.4@ [1 27 -7]

The misorientation between wüstite and magnetite precipitates showed 5.1@ [20 -8 17]

The misorientation between wüstite and magnetite layer showed 53.9@ [5 -6 7]

Phase
Iron Oxide
Magnetite

Boundaries: Grain

(e)

Magnetite layer-magnetite layer grain misorientation

Wüstite and magnetite layers boundary misorientation

Wüstite-wüstite grains misorientation

Wüstite and magnetite seam phase boundary

Figure 3.6.9: EBSD-Microtexture analysis of IF steel oxide scale at 750°C for 1200 seconds
(a) IPF//RD, (b) ODFs showing wüstite has Cube (100) <001> and rotated Cube (001) <110> texture components, magnetite has a strong Cube texture, (c) Grain Boundary Character Distribution chart and map, (d) Individual misorientation analysis as indicated on the phase map, (e) Grain boundaries misorientation chart compared with Mackenzi plot

Alloy A Microtexture Analysis

(a)

(b)

Iron ODF

Wüstite ODF

Magnetite layer ODF

Figure 3.6.10: EBSD-Microtexture analysis of Alloy A oxide scale at 750°C for 1800 seconds,

(a) IPF//RD

(b) ODFs showing iron has weak rotated Cube (001) <110> texture with high intensity at (4 4 3) <3 -9 8>, wüstite has very weak rotated Cube, but strong Cube and Goss texture components. Magnetite layer have Cube (100) <001> and Goss texture

(a)

(b)

(c)

(d)
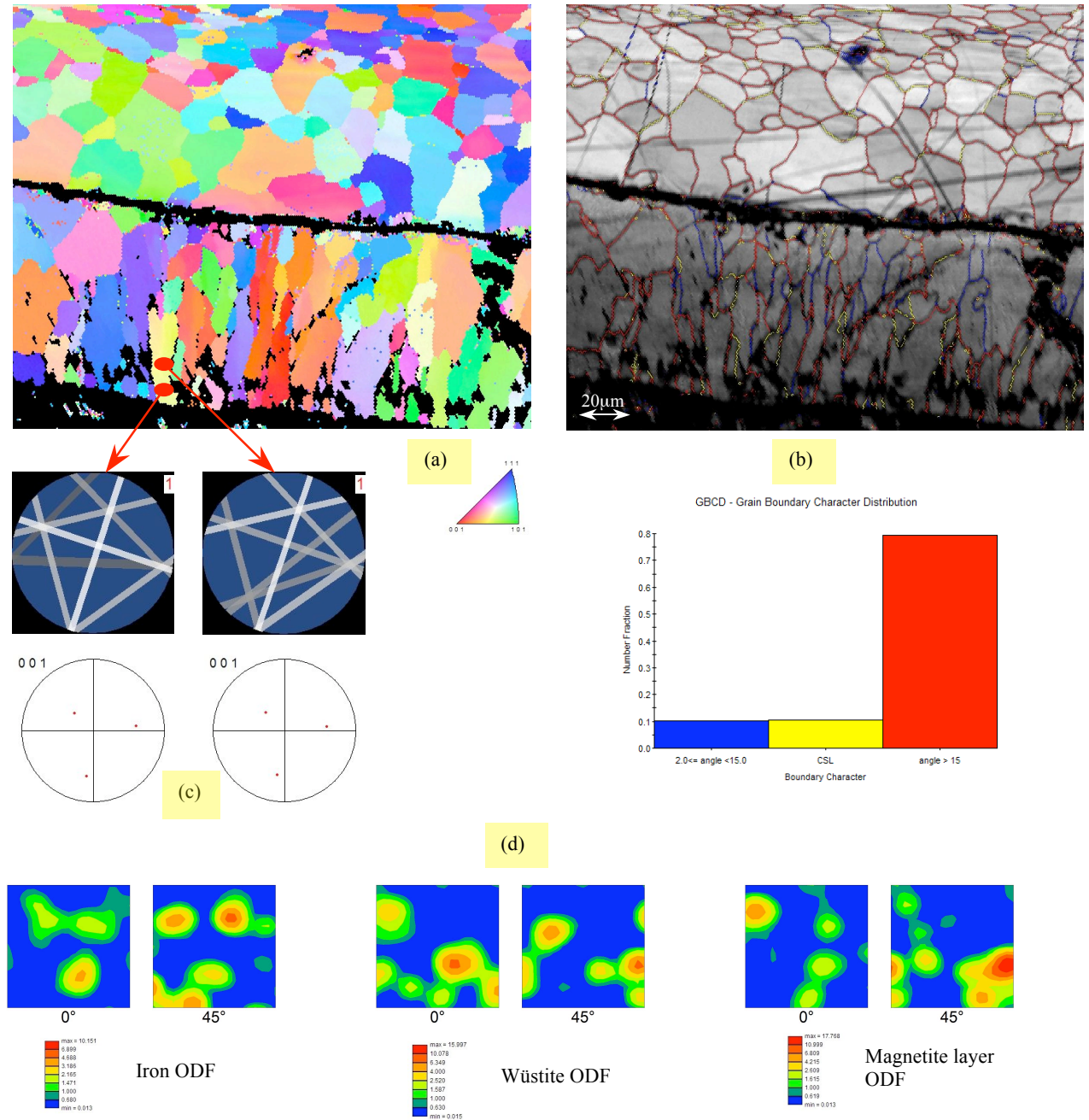
Figure 3.6.11: EBSD-Microtexture analysis of Alloy A oxide scale at 900°C for 1800 seconds

(a) IPF//RD

(b) Grain Boundary Character Distribution chart and map

(c) Reconstructed diffraction patterns and pole figures of neighbouring wüstite and magnetite grains. They have same orientation and the two phases separated by coherent grain boundary in which not appears in (b)

(d) ODFs showing iron has (110) <111> texture, wüstite has weak Goss and Cube texture components, magnetite layer has (111) <112>, weak Goss and rotated Cube texture components

■ Misorientation between the two points showed 0.3 @ [-5 8 11]

■ Misorientation between the two points showed 29.4 @ [-3 14 -15]

■ The substrate and wüstite interface misorientation showed 53.4 @ [-3 2 2]

(b)

Iron ODF

Wüstite ODF

Magnetite layer ODF

(a)

50μm

(c)
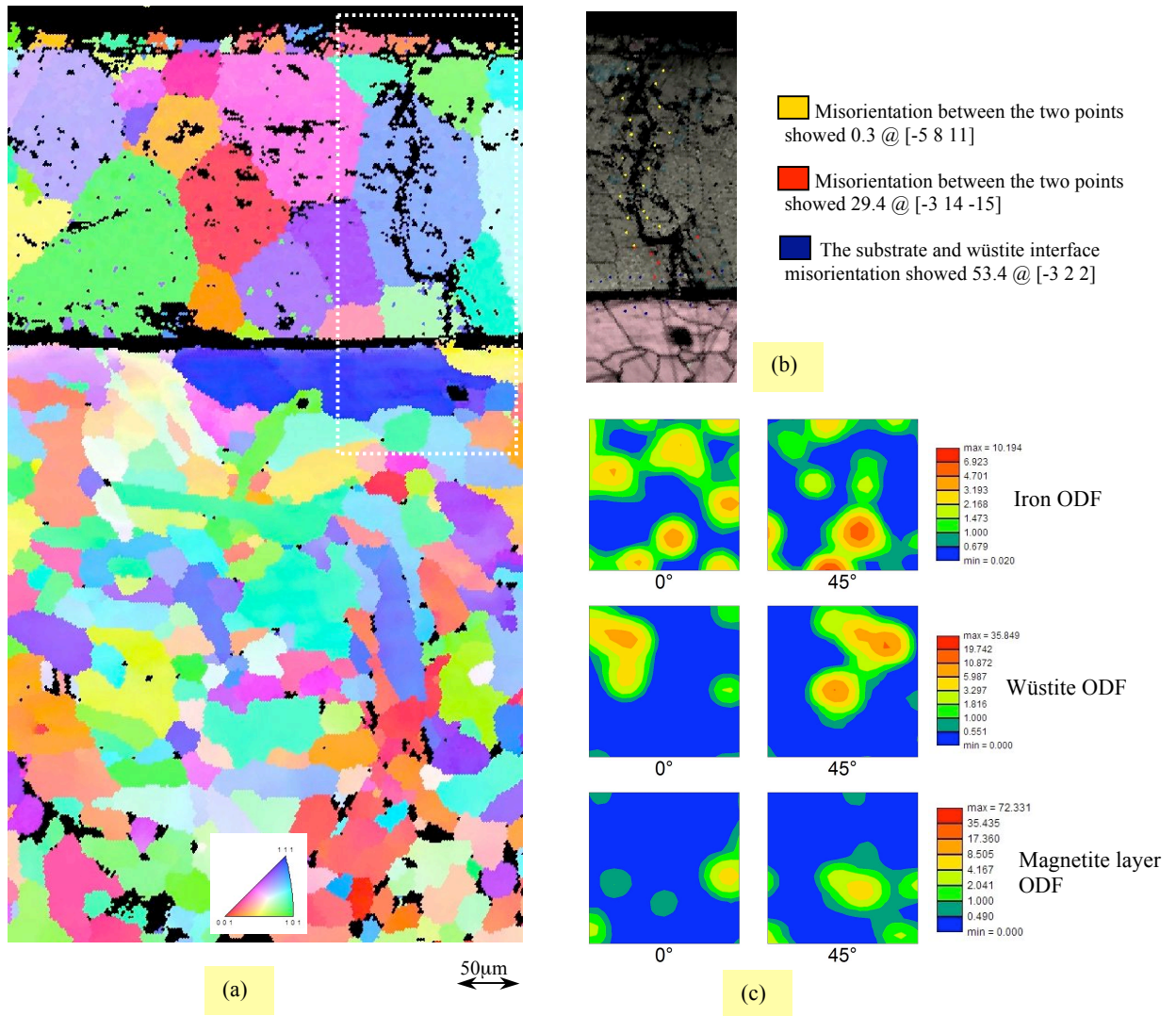
Figure 3.6.12: EBSD-Microtexture analysis of Alloy A oxide scale at 1000°C for 1800 seconds

(a) IPF//RD

(b) Individual misorientation analysis between two selected points in the highlighted IQ map

(c) ODFs showing iron has cube (100) <001> texture, wüstite and magnetite layers have weak Cube and (111) <121> texture components

(a)

(b)

Iron ODF

Wüstite ODF
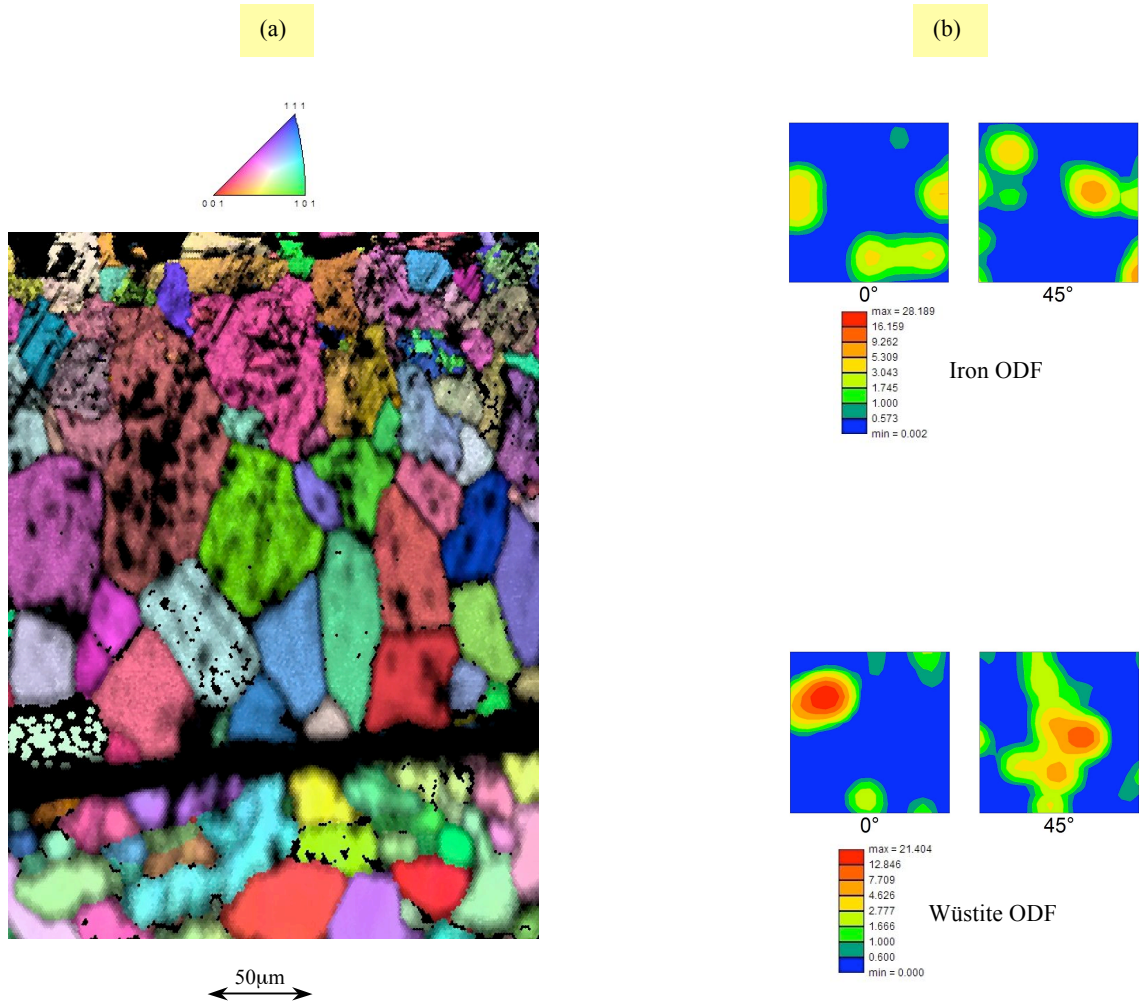
Figure 3.6.13: EBSD-Microtexture analysis of Alloy A oxide scale at 1000°C for 1800 seconds

(a) IPF//RD

(b) ODFs showing iron has weak Goss (110) <001> texture, wüstite has weak Goss and near Cube texture components. Magnetite layer has weak Goss and rotated Cube (001) <110> texture components

Magnetite layer ODF
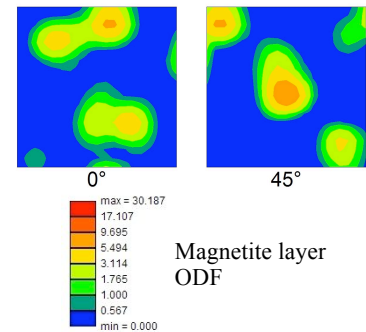
Alloy A Microtexture Analysis Concerning Time-Texture Correlation

(a)

(b)

Iron ODF

Wüstite ODF

Magnetite layer ODF
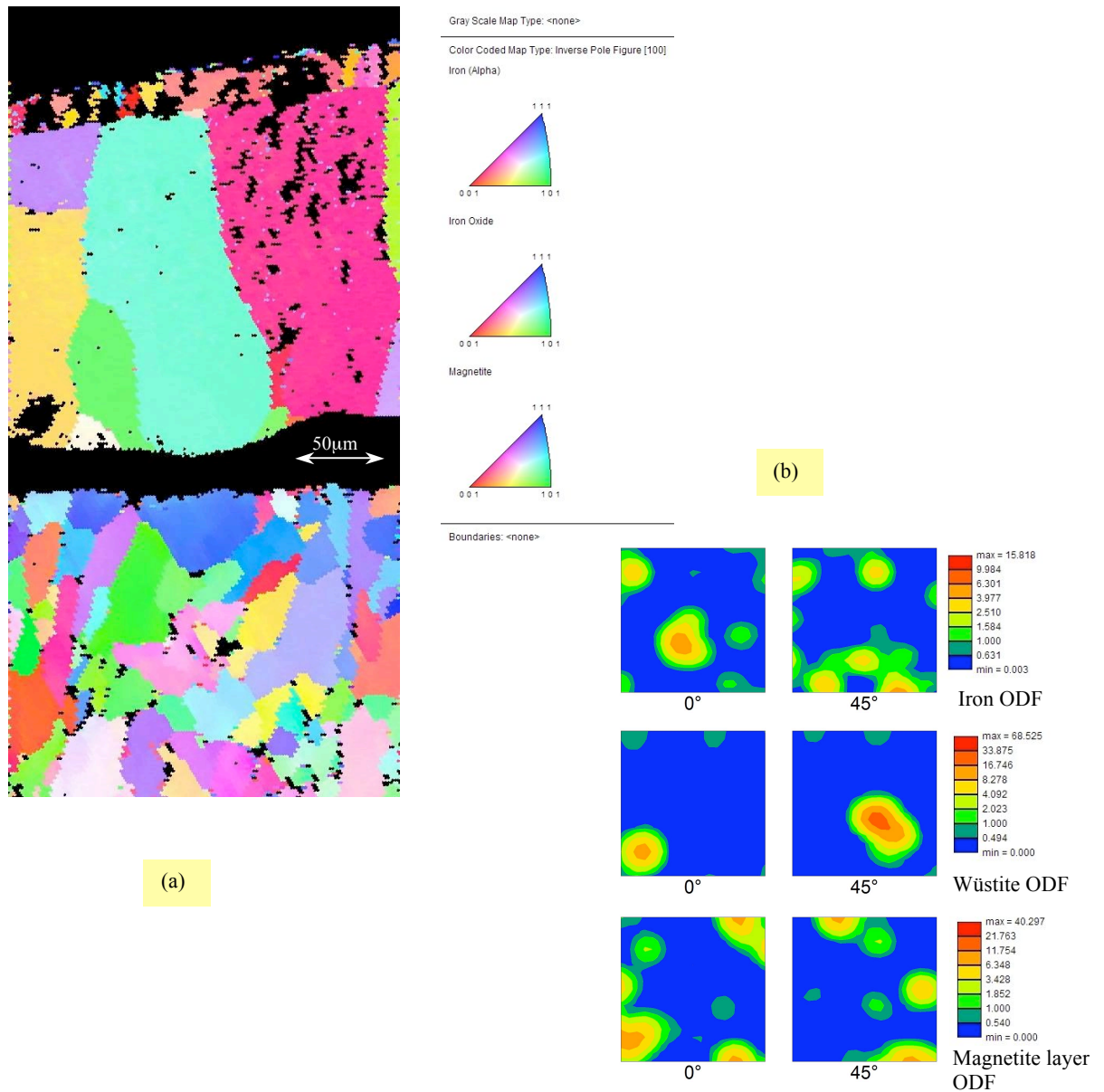
Figure 3.6.14: EBSD-Microtexture analysis of Alloy A oxide scale at 1100°C for 600 seconds

(a) IPF//RD

(b) ODFs showing iron has weak Cube (100) <001> texture, wüstite has very weak Cube and Z (111) <011> texture components, magnetite layer has Cube (100) <001> texture

(a)

(b)

100μm

Iron ODF

Wüstite ODF

Magnetite
precipitates ODF

Magnetite layer
ODF

Haematite layer
ODF

*Figure 3.6.15: EBSD-Microtexture analysis of
Alloy A oxide scale at 1100°C for 1200 seconds*

(a) IPF//RD

*(b) ODFs showing iron has rotated Cube (001)
<110> texture with high intensity in (4 4 3) <-3 -3
8>, wüstite and magnetite precipitates have Cube
and Goss texture components, magnetite layer has
rotated Cube and weak Goss texture, haematite
has (8 3 -11 0) <0 0 0 1>, Goss equivalent texture*

Iron ODF

Wüstite ODF

Magnetite layer ODF

Haematite layer ODF

Figure 3.6.16: EBSD-Microtexture analysis of Alloy A oxide scale at 1100°C-1800 seconds, ODFs showing iron has Cube (100) <001> texture with high intensity in (3 3 5) <0 -5 3>, wüstite and magnetite, layers have Cube texture, haematite has (0 0 0 1) <0 -1 1 0>, Cube equivalent texture

(a)

(b)
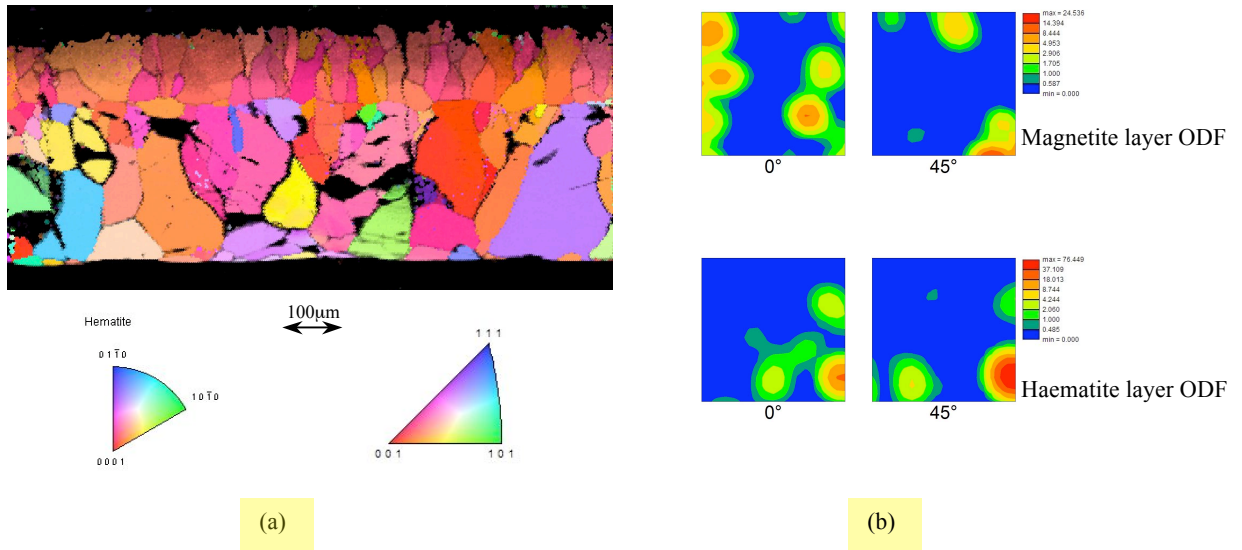
Figure 3.6.17: EBSD-Microtexture analysis of Alloy A oxide scale at 1100°C-3600 seconds
(a) IPF//RD
(c) ODFs showing magnetite has Goss and Cube texture components, haematite layer has Goss equivalent texture

Alloy B Microtexture Analysis
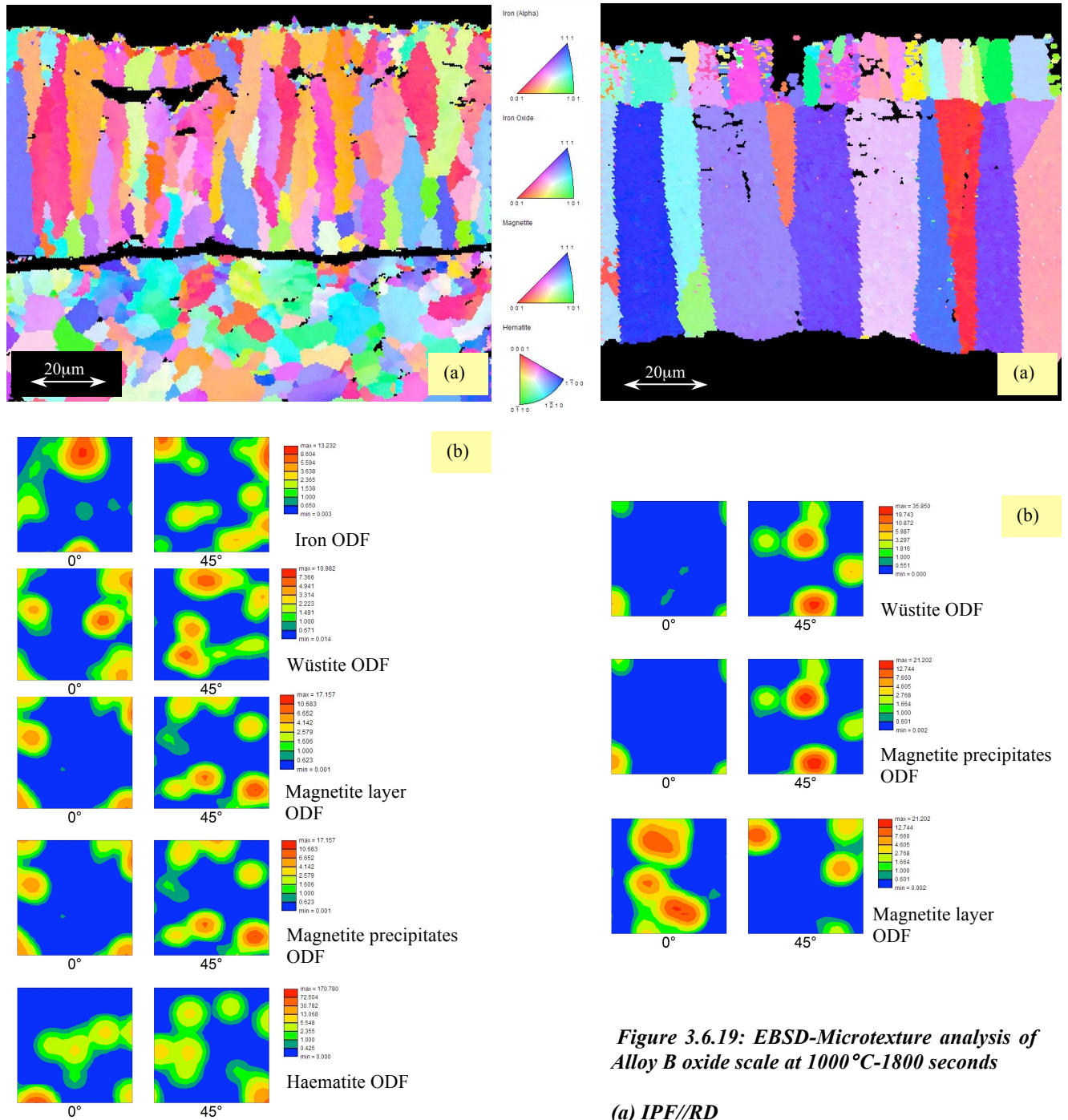
Figure 3.6.18: EBSD-Microtexture analysis of Alloy B oxide scale at 900°C-1800 seconds, (a) IPF//RD, (b) ODFs showing iron has rotated Cube (001) <110> texture, wüstite, magnetite precipitates and magnetite layer have Cube (100) <001> texture, haematite has weak Cube equivalent and Goss equivalent texture components

Figure 3.6.19: EBSD-Microtexture analysis of Alloy B oxide scale at 1000°C-1800 seconds

(a) IPF//RD

(b) ODFs showing wüstite and magnetite precipitates have Cube (100) <001> and strong (110) <112> Bs texture components, magnetite layer has rotated Cube (001) <110> texture and very week Bs texture components

(a)

(b)

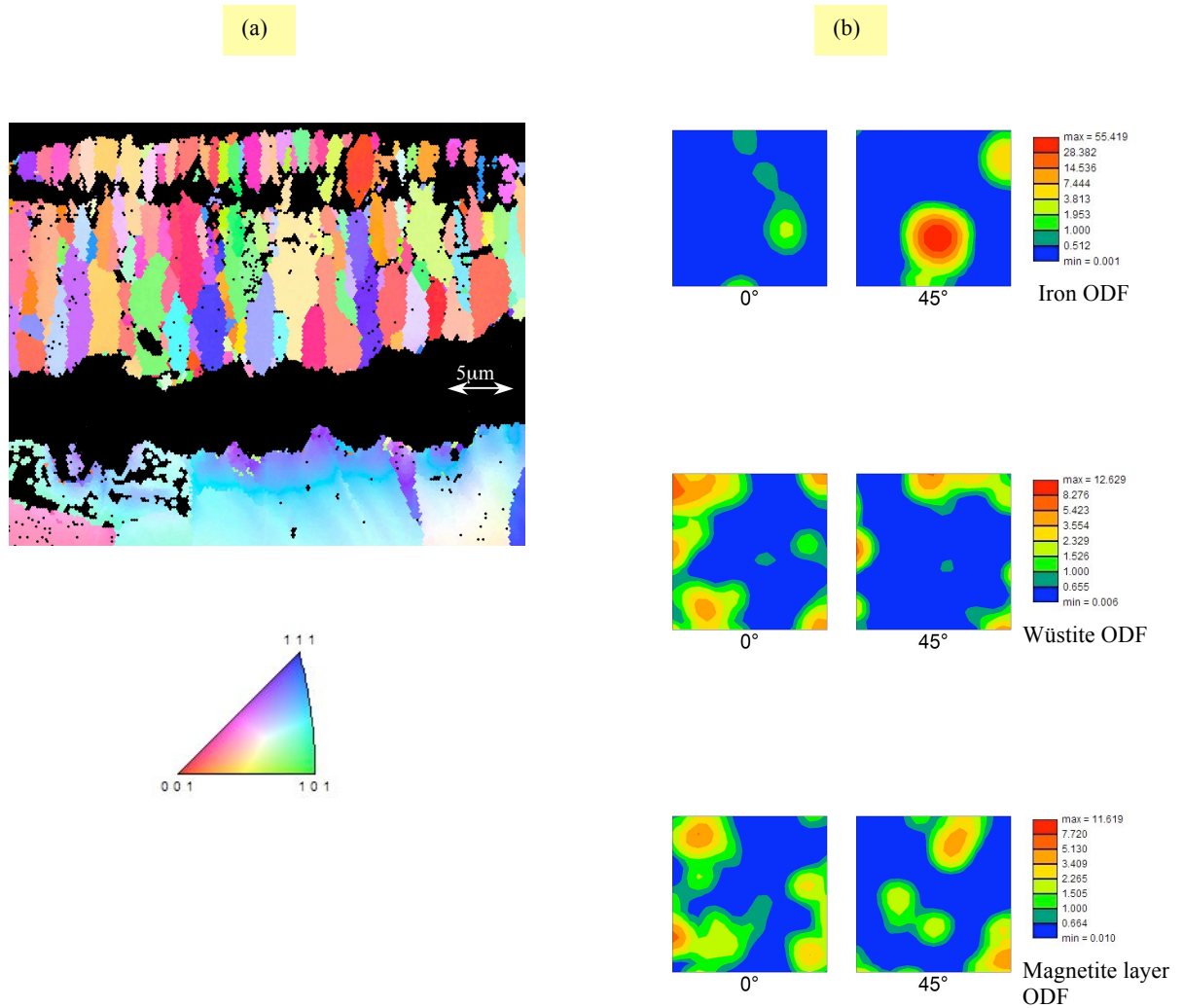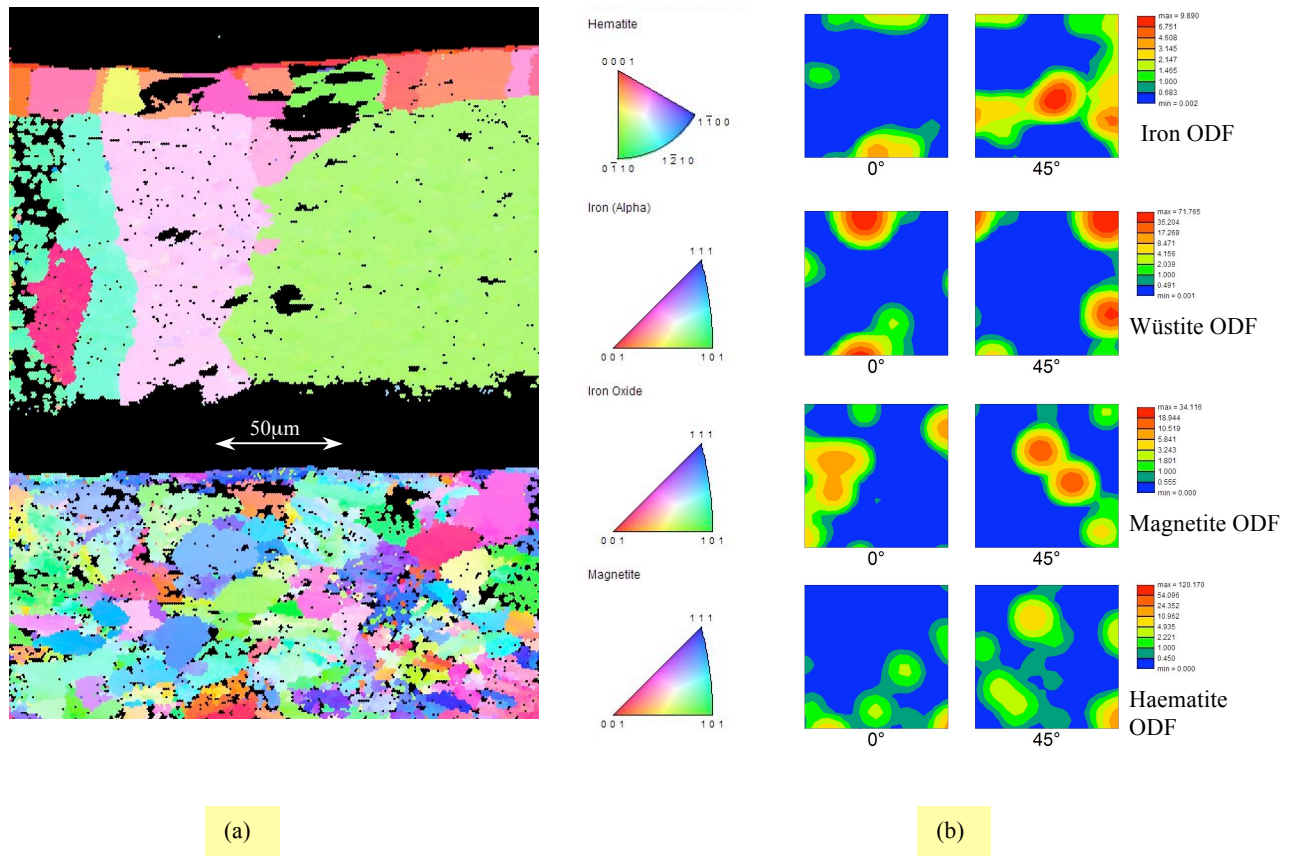*Figure 3.6.20: EBSD-Microtexture analysis of Alloy B oxidised at 1100°C-1800 seconds*

(a) IPF//RD

(b) ODFs showing iron has weak rotated Cube and strong (111) <011> Z texture components, wüstite has strong rotated Cube texture, magnetite layer has weak rotated Cube (001) <110> and strong Z texture, haematite has rotated Cube and weak Cube equivalent texture components

IF Steel Texture Analysis Related Tables

Table 3.6.1: Texture strength of IF steel substrate and oxide scale layers at different temperatures-1800 seconds.

Phase	Temperature (°C)				
	650	750	900	1000	1100
Iron	Strong texture	Strong texture	Weak texture	Weak texture	Strong texture
Wüstite	Weak texture	Weak texture	Very weak texture	Strong texture	Strong texture
Magnetite	Weak texture	Weak texture	Strong texture	Weak texture	Weak texture
Haematite	-	-	-	-	Very strong texture

Texture intensity in range of (5-10) =Very weak texture
Texture intensity in range of (10-50) = weak texture
Texture intensity in range of (50-90) =strong texture
Texture intensity in range of (>90) =Very strong texture

Table 3.6.2: Major texture components of IF steel substrate and oxide scale layers at different temperatures- 1800 seconds.

Phase	Temperature (°C)				
	650	750	900	1000	1100
Iron	Strong Rotated Cube	P texture	Strong P	Strong Cu and weak Rotated Cube	Strong Rotated Cube
Wüstite	Cube and weak Rotated Cube	Strong Goss, weak Cube	Weak Cube	Weak Rotated Cube	Near Cube
Magnetite	Weak Cube	Strong Goss, weak Cube, strong Z	Weak Goss	Strong Cu and Weak Rotated Cube	Weak (11-4) <843>
Haematite	-	-	-	-	Strong (0 6 -6 -5) <5 -5 0 -6> and (0 3 -3 2) <-12 1 11 15>

Table 3.6.3: Texture correlation between IF steel substrate and oxide scale layers at different temperatures-1800 seconds.

Temperature (°C)	Texture correlation		
	Iron-wüstite	Iron-magnetite	Wüstite-magnetite
650	yes	no	yes
750	no	no	yes
900	no	no	no
1000	yes	Yes*	yes
1100	no	no	no

no: no texture relationship, yes: one of the texture components exists in both phases, Yes: strong relationship*

Alloy A Texture Analysis Related Tables

Table 3.6.4: Texture strength of Alloy A substrate and oxide scale layers at different temperatures-1800 seconds.

Phase	Temperature (°C)			
	750	900	1000	1100
Iron	Strong texture	Weak texture	Weak texture	Weak texture
Wüstite	Weak texture	Weak texture	Weak texture	Strong texture
Magnetite	Weak texture	Weak texture	Strong texture	Strong texture

Table 3.6.5: Major texture components of Alloy A substrate and oxide scale layers at different temperatures- 1800 seconds.

Phase	Temperature (°C)			
	750	900	1000	1100
Iron	Weak Rotated Cube	(110) <111>	Cube	Cube
Wüstite	Weak Rotated Cube, strong Cube and Goss	Weak Goss and Cube	Weak Cube	Cube
Magnetite	Cube and Goss	Weak Goss and Rotated Cube	Weak Cube	Cube

Table 3.6.6: Texture correlation between Alloy A substrate and oxide scale layers at different temperatures-1800 seconds.

Temperature (°C)	Texture correlation		
	Iron-wüstite	Iron-magnetite	Wüstite-magnetite
750	yes	no	Yes*
900	no	no	yes
1000	yes	yes	Yes*
1100	Yes*	Yes*	Yes*

no: no texture relationship, yes: one of the texture components exists in both phases, Yes: strong relationship*

Alloy B Texture Analysis Related Tables

Table 3.6.7: Texture strength of Alloy B substrate and oxide scale layers at different temperatures-1800 seconds.

Phase	Temperature (°C)		
	900	**1000**	**1100**
Iron	Weak texture	-	Very weak texture
Wüstite	Weak texture	Weak texture	Strong texture
Magnetite	Weak texture	Weak texture	Weak texture
Haematite	Very strong texture	-	Very strong texture

Table 3.6.8: Major texture components of Alloy B substrate and oxide scale layers at different temperatures- 1800 seconds.

Phase	Temperature (°C)		
	900	**1000**	**1100**
Iron	Rotated Cube	-	Strong Z and weak Rotated Cube
Wüstite	Cube	Cube and strong BS	Strong Rotated Cube
Magnetite	Cube	Rotated Cube and weak BS	Strong Z and weak Rotated Cube
Haematite	Goss and weak Cube (equivalent)	-	Rotated Cube and weak Cube (equivalent)

Table 3.6.9: Texture correlation between Alloy B substrate and oxide scale layers at different temperatures-1800 seconds.

Temperature (°C)	Texture correlation					
	Iron-wüstite	**Iron-magnetite**	**Iron-Haematite**	**Wüstite-magnetite**	**Wüstite-Haematite**	**Magnetite-Haematite**
900	no	no	no	Yes*	yes	yes
1000	-	-	-	yes	-	-
1100	yes	Yes*		yes	yes	yes

no: no texture relationship, yes: one of the texture components exists in both phases, Yes: strong relationship*

Time and Texture Correlation Related Tables

Table 3.6.10: Texture strength of Alloy A substrate and oxide scale layers at different times-1100°C

Phase	Time (Seconds)			
	600	1200	1800	3600
Iron	Weak texture	Weak texture	Weak texture	Weak texture
Wüstite	Strong texture	Weak texture	Strong texture	-
Magnetite	Weak texture	Weak texture	Strong texture	Weak texture
Haematite	-	-	Strong texture	Strong texture

Table 3.6.11: Major texture components of Alloy A substrate and oxide scale layers at different times-1100°C.

Phase	Time (Seconds)			
	600	1200	1800	3600
Iron	Weak Cube	Rotated Cube	Cube	Goss
Wüstite	Weak Cube and Z	Cube and Goss	Cube	-
Magnetite	Cube	Rotated Cube and weak Goss	Cube	Goss and Cube
Haematite	-	Goss equivalent	Cube equivalent	Goss equivalent

Table 3.6.12: Texture correlation between Alloy A substrate and oxide scale layers at different times-1100°C.

Time (Seconds)	Texture correlation					
	Iron-wüstite	Iron-magnetite	Iron-Haematite	Wüstite-magnetite	Wüstite-Haematite	Magnetite-Haematite
600	yes	yes	-	yes	-	-
1200	no	yes	no	yes	yes	yes
1800	Yes*	Yes*	Yes*	Yes*	Yes*	Yes*
3600	-	yes	Yes*	-	-	yes

no: no texture relationship, *yes*: one of the texture components exists in both phases, *Yes**: strong relationship
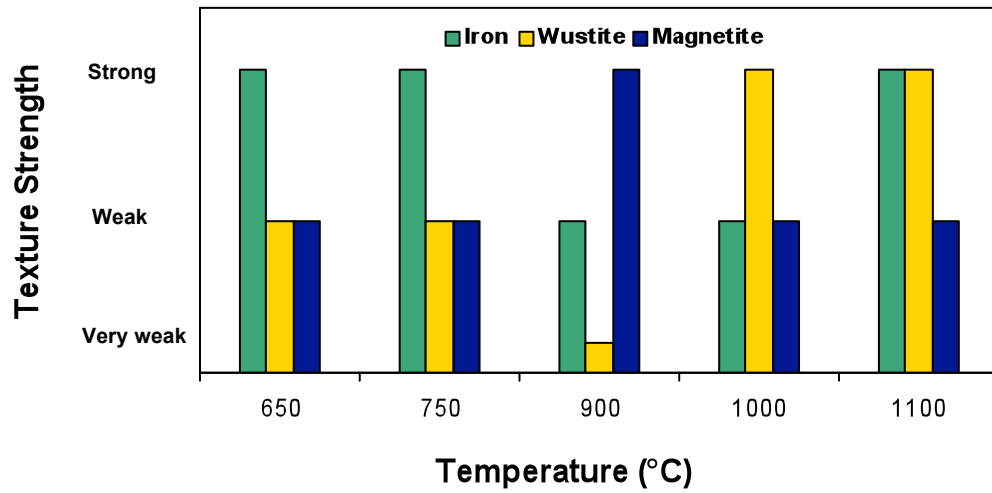
Figure 3.6.21: Texture strength of IF steel substrate and oxide scale layers versus temperature-1800 seconds.
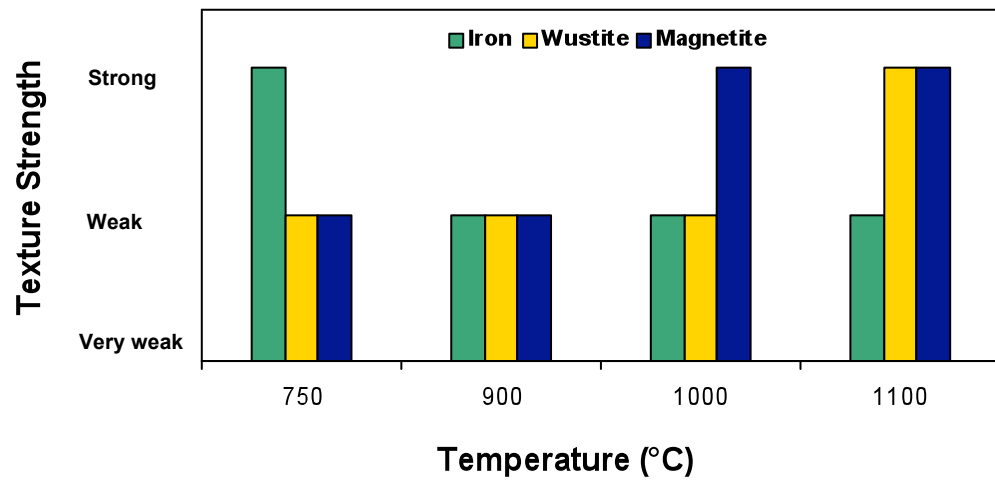
Figure 3.6.22: Texture strength of Alloy A substrate and oxide scale layers versus temperature-1800 seconds.
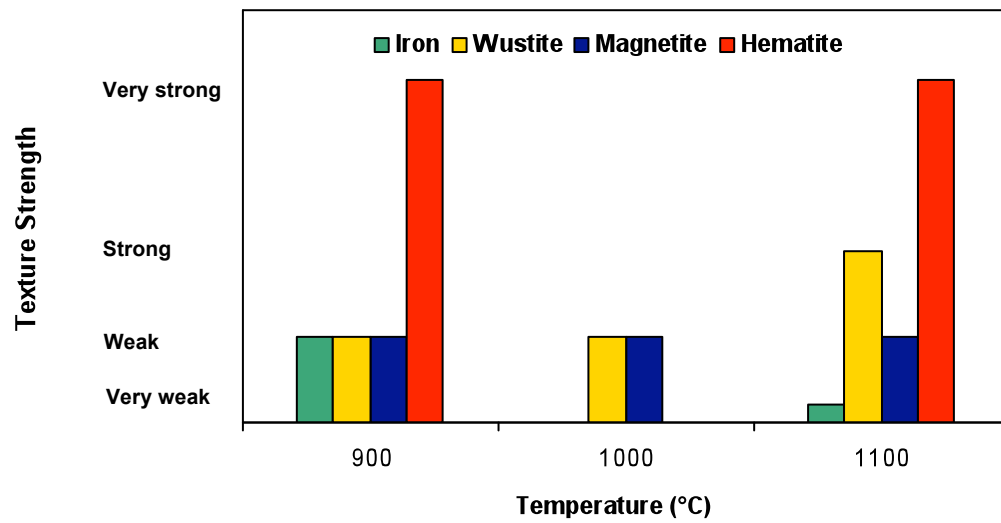
Figure 3.6.23: Texture strength of Alloy B substrate and oxide scale layers versus temperature-1800 seconds.
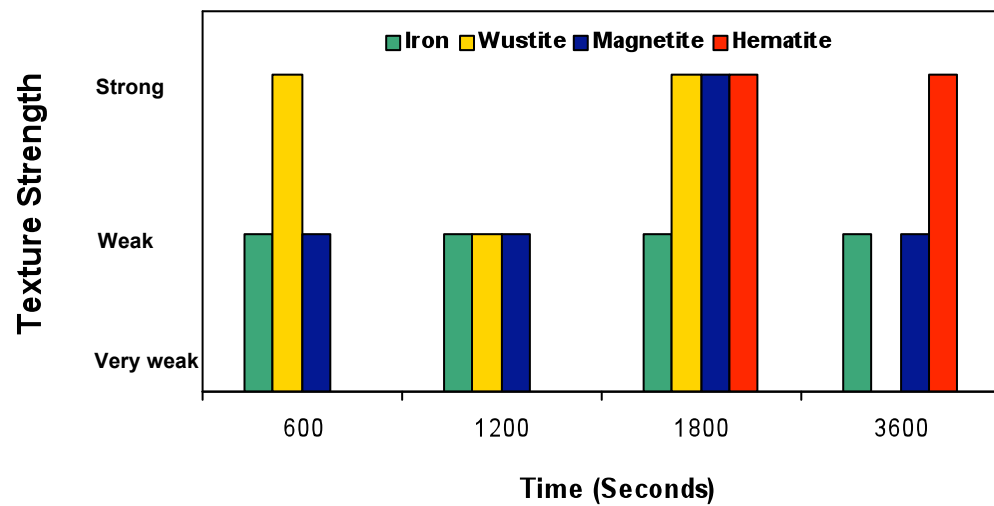
Figure 3.6.24: Texture strength of Alloy A substrate and oxide scale layers versus time, at 1100°C.

174

■ Selected most representing wüstite/magnetite layers misorientation showing 59.8 @ [-4 9 10]

■ Selected most representing magnetite layer/magnetite precipitates misorientation showing 52.7 @ [13 -5 16]

■ Selected most representing iron/magnetite seam misorientation showing 33.9 @ [-7 8 5]

■ Selected most representing iron/wüstite layer misorientation showing 25.4 @ [-7 -24 8]
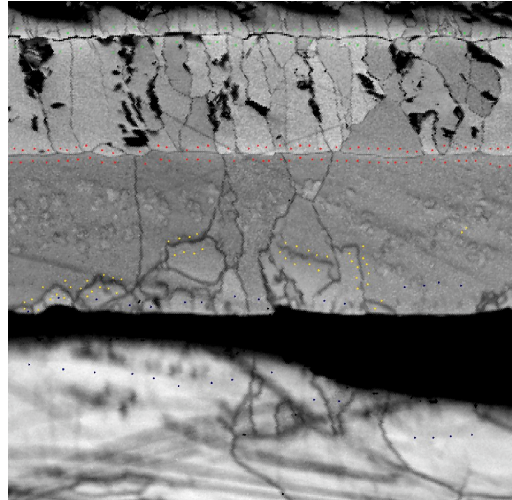
■ Selected most representing haematite/magnetite layers misorientation showing 15.5 @ [1 -2 -4]

■ Selected most representing wüstite/magnetite precipitates misorientation showing 1.1 @ [5 13 -6]

■ Selected most representing magnetite seam/magnetite precipitates misorientation showing 34.1 @ [9 13 2]

■ Selected most representing magnetite seam/wüstite misorientation showing 35.2 @ [-10 7 2]

(a) IF steel oxidised at 1100°C-1800 seconds

■ Misorientation = 39.1@ [-9 9 2]

■ Misorientation = 51.9 @ [8 12 1]

■ Misorientation = 39.9 @ [9 9 17]

■ Misorientation = 11.6 @ [0 0 -1]

■ Misorientation = 37.4 @ [-5 26 1]

■ Misorientation = 42.2 @ [-10 -23 -12]
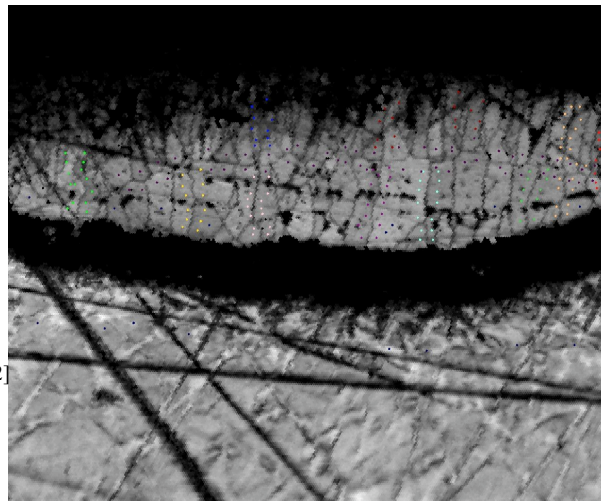
■ Misorientation = 28.6 @ [5 -5 -3]

■ Misorientation = 35.6 @ [-12 -6 25]

■ Misorientation = 17.1 @ [9 -5 6]

■ Misorientation = 30.8 @ [-2 7 1]

■ Misorientation = 48.4 @ [-18 17 8]

(b) IF steel oxidised at 750°C-1800 seconds

Figure 3.6.25 Individual misorientation analysis of the phase and grain boundaries in the oxide layers and steel substrate

(b)

Iron ODF

0°   45°

(a)

Wüstite ODF

0°   45°
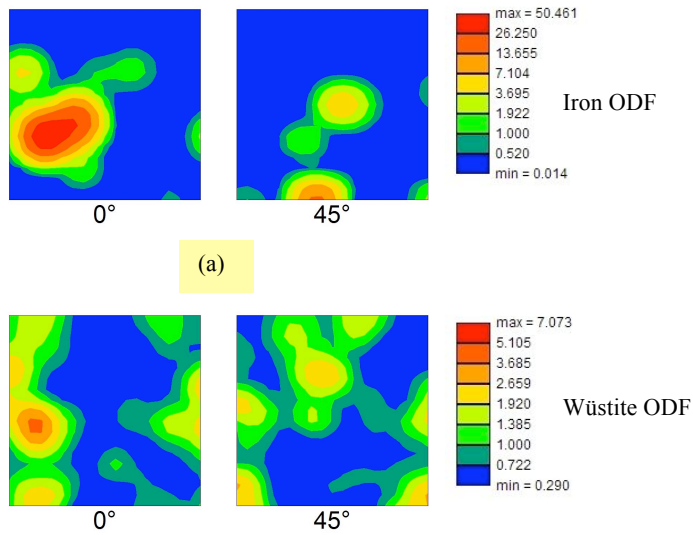
(a) ODFs showing iron has Goss (110) <001> texture with high intensity at (0 5 3) <19 -3 5>, wüstite has Cube and Goss texture components. Magnetite layer texture could not calculate due to difficult indexing on the edges.

(b) IPF//RD

(c) Grains and phase boundaries misorientation charts compared with Mackenzi plot

(c)

Iron-iron grains   Wüstite-wüstite grains   Iron-wüstite phase boundary
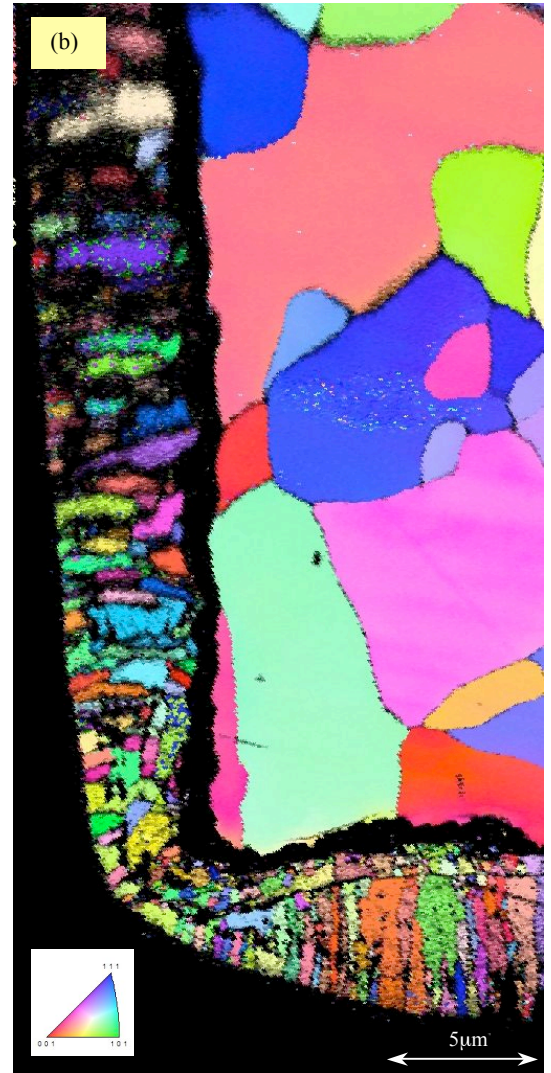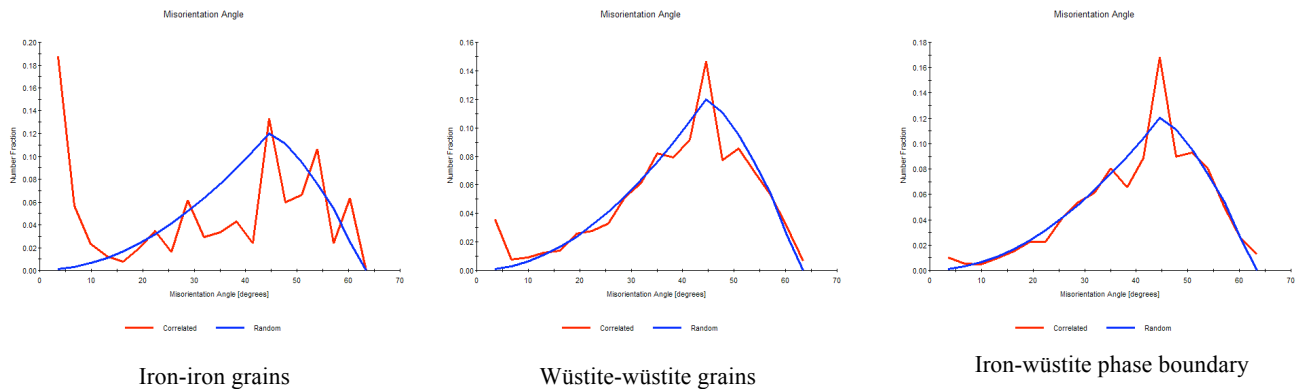
Figure 3.6.26: EBSD-Microtexture analysis of Alloy A oxide scale at 750°C-1800 seconds

3.7 The Mechanical Property of the Oxide Scale Layers

The hardness of the steel substrate and oxide scale layers was measured using a micro-hardness test machine. The aim was to determine the affect of oxidation temperature on the mechanical properties, the differences between the oxide scale layers hardness and if there is any correlation between the grain orientation and the mechanical properties of the oxide scale. An accurate hardness reading is relatively difficult to obtain due to the brittleness of the oxide scale especially the magnetite layer. Furthermore, the magnetite precipitates on wüstite made the measurement more difficult to find a free wüstite area with no magnetite precipitates. To overcome these two problems, the smallest load (10 grams) was used in some areas. However, there were inaccuracies in the measurement when a small load was used due to reading difficulties. Therefore, only reliable data are recorded and averages calculated. It should be noted that at 650 and 750°C, the thin scale makes the micro-indentation difficult therefore, no data could be obtain at those two temperatures. Also due to very the thin layer of haematite seen at only some temperatures, the haematite hardness data could not be obtained at all temperatures. Data is therefore only presented for the wüstite and magnetite layers and other features where it was possible.

The micro-hardness tests were carried out for IF steel, Alloy A, Alloy B and the oxide layers formed on their surfaces after 1800 seconds of oxidation at different temperatures. Figure 3.7.1 shows the micro-indented sample of IF steel-1000°C-1800 seconds. Different loads were used depending on the location and phase tested. The measurements were performed on both thick and thin areas to determine if there were any differences in mechanical properties between the two areas, see Figure 3.7.1 (a). For the steel substrate any load could be used due to its large surface area. The load of 100 grams was mainly used for the substrate because it was easier to measure and readings more accurate than smaller loads, see Figure 3.7.1 (b) also the Table 3.7.1. Furthermore, the steel substrate hardness was measured again using a standard hardness testing machine as a double check of the micro-hardness data. There was a difficulty in finding wüstite areas free from magnetite precipitates especially in the upper layer, Figure 3.7.1 (c). Following the micro-indentations, the samples were observed by optical microscopy at high

magnification. The wüstite hardness readings affected by magnetite precipitates were excluded from the measurements, e.g. (W4) and (W11) in Figure 3.7.1 (c). A load of 25 grams was mainly used in the areas that had high densities of magnetite precipitations in order to avoid indenting them instead of wüstite layer. The magnetite layer was very thin and so the smallest loads (10 and 25 grams) were used. The load of 25 grams always caused a crack around the indenter, which is why 10 grams load was used mainly for the magnetite hardness measurements. However, the results from both loads were close. Figures 3.7.2 and 3.7.3 show other micro-indented samples of IF oxide scales and steel substrates.

Figure 3.7.4 shows the micro-indented sample of Alloy A oxidised at 1100°C-1800 seconds. Following micro-indentations, EBSD scanning was carried over the exact area in Figure 3.7.4, see Figure 3.7.5. The aim was to find any mechanical property correlation with grain orientation of the oxide scale. Figure 3.7.4 shows five areas of interest in which magnified images are shown. Area 1 is the haematite layer where both indentations in the selected area caused cracks around it. It should be noted that fracture toughness is not measured because it is out of the scope of the present study. The haematite layer was thick enough to use a 50 gram load. The hardness values (H1 and H2) differ by 95 Hv, see Table 3.7.2. Looking at IPF//GD in Figure 3.7.5, there is no orientation difference between the two haematite grains. The haematite layer has very strong texture where all the grains are orientated in the (0001)//GD, see RDPs as well as PFs nos; 11, 12 and 13.

Area 2 in Figure 3.7.4 shows the magnetite layer indentions. The hardness value of M1 (386 Hv) is very different from M2 and M3 (530 and 519, respectively). Looking at the magnified image in the same figure, there is cracking in the vicinity of M1, which may have caused the inaccurate reading at the M1 point. The same problem caused the M4 reading (green area) to be excluded from the measurements, see area 4.

Areas 4 and 5 concentrated on the wüstite, magnetite precipitates and magnetite seam. The wüstite hardness values (W1 and W2) are 458 and 432 Hv, respectively. While magnetite precipitates have larger values (MP1, MP2) are 530 and 513, respectively. Looking at IPF//GD in Figure 3.7.5, the grain orientations of W1, MP1, MP2 and MS1

are the same, (111)//GD. Again there was no connection between the hardness and grain orientation. Area 5 confirms this fact again, where, W3, MP3, MP4 and MP5 have different hardness values, but the same orientations, see RDPs and PFs nos.; 1, 2 and 3 in the same figure. Further orientation analyses were carried out, but there was no correlation found between grain orientation and hardness. The magnetite seam has a very similar hardness value with the magnetite precipitates; see MP2 and MS1 in area 3, Figure 3.7.4.

Figures 3.7.6 and 3.7.7 show the micro-indented samples for Alloy B at 1000 and 1100°C, respectively. As shown in Figure 3.7.7, the wüstite indentions were always nearly square and there was no difference between both indentor dimensions. The magnetite indentor dimensions vary with direction, as shown in Figure 3.7.7. However, this did not affect the results as compared with the square indenter in other areas of the magnetite layer. Some of the readings were excluded from the micro-hardness measurements where the indentation covered magnetite precipitates as well as wüstite areas (yellow circles).

Tables 3.7.3 – 3.7.5 show the micro-hardness measurements of IF steel, Alloy A and Alloy B substrates and oxide scale layers on their surfaces at 900, 1000 and 1100°C for 1800 seconds. Figures 3.7.8 – 3.7.10 show the micro-hardness values (Hv) versus temperature for the same alloys. As shown in Table 3.7.3 and Figure 3.7.8, while the IF steel substrate hardness decreased slightly with increasing temperature, the wüstite and magnetite hardness increased. However, the steel substrate hardness values at 900, 1000 and 1100°C are very close. This leads to the conclusion that the hardness of the steel substrate did not change with increasing temperature or there were very small changes. The magnetite precipitates at 900°C were too small to be measured, however, their values were always similar to the magnetite layer hardness as obtained from other samples. At all temperatures, iron was the softest and haematite was the hardest. Moreover, the magnetite was harder than wüstite at all temperatures except 1000°C. It was also noticed that the lower part of the wüstite layer hardness was greater than the upper part at all temperatures, some examples are given below Tables 3.7.3 – 3.7.5. The haematite layer was not observed at 900 and 1000°C.

Table 3.7.4 and Figure 3.7.9 show that the hardness of Alloy A substrate and wüstite increased with increasing temperatures. Also the magnetite hardness increased with increasing temperature except at 1100°C, however, the magnetite hardness values at 1000 and 1100°C are very close. The magnetite precipitates at 900 and 1000°C were too small to be measured. However, their value at 1100°C was similar to the magnetite layer hardness. The relative hardness of the phases was the same as that seen for the IF steel.

Table 3.7.5 and Figure 3.7.10 show that the hardness of the Alloy B substrate, wüstite and magnetite varied with temperature. The hardness of the steel substrate, wüstite and magnetite were the highest at 1000°C with no trend found between the oxide scale hardness with temperature. The magnetite precipitates were too small and the haematite layers were too thin to be measured. At all temperatures, while the steel substrate was the softest, the magnetite layer was harder than the wüstite layer.
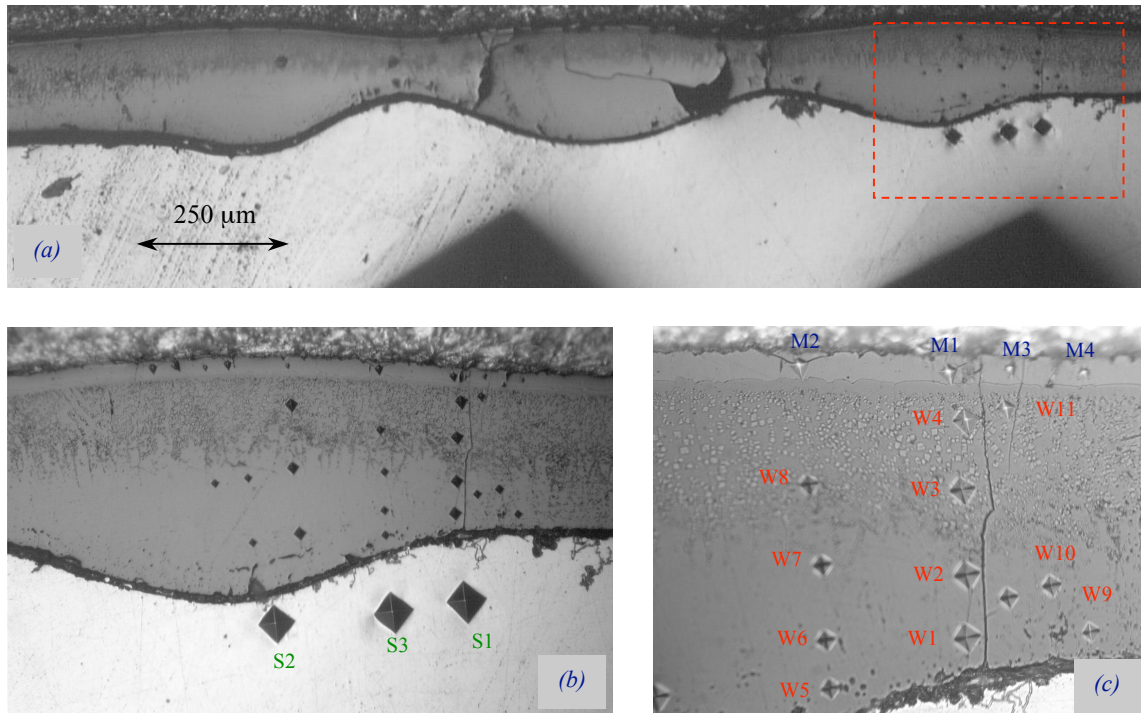
Figure 3.7.1: IF steel-1000°C-1800 seconds, micro-indented in different areas of the oxide phases.(a) low magnification to show non-uniform scale indented, (b) and (c) in higher magnifications

Indentor No.	Load (g)	Dimensions (µm)	Hardness Hv
S1	100	44.2 - 45.9	91.3
S2	100	40.3 - 41.5	110.8
S3	100	43.7 - 44.3	95.5
W1	50	14.8 - 15.3	409.3
W2	50	14.3 - 15.1	429.0
W3	50	14.6 - 14.7	432.0
W4	50	15.0 - 17.1	359.9
W5	25	9.5 - 10.1	482.0
W6	25	10.1 - 10.6	432.0
W7	25	9.6 - 10.2	473.0
W8	25	10.2 - 10.6	428.0
W9	25	10.8 - 11.0	390.2
W10	25	10.0 - 10.3	449.9
W11	25	10.4 - 12.0	369.5
M1	25	9.5 - 12.0	401.1
M2	25	10.0 - 11.7	393.7
M3	10	6.2 - 8.3	352.7
M4	10	5.7 - 7.3	438

S= steel, M= magnetite, W= wüstite.

Table 3.7.1: The micro-hardness data for the indentation points indicated in Figure 3.7.1.
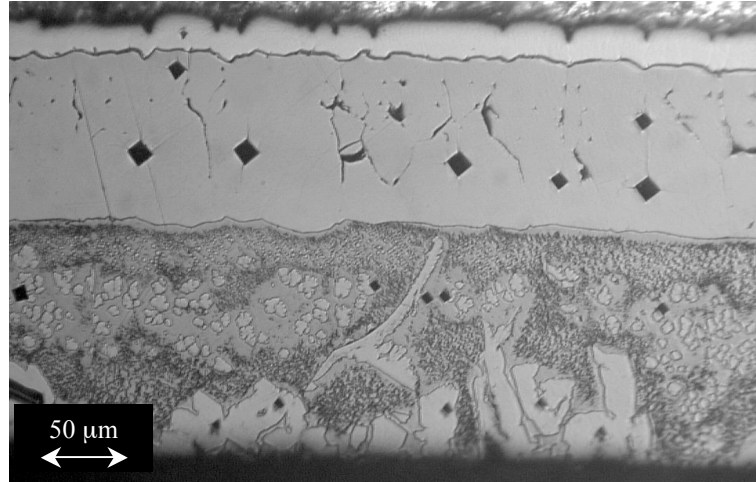
Figure 3.7.2: IF steel-1100°C-1800seconds, micro-indented in different areas of the oxide phases.
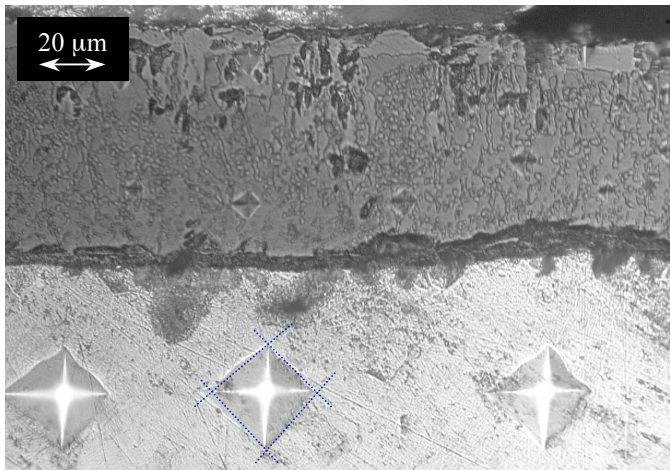
(a)
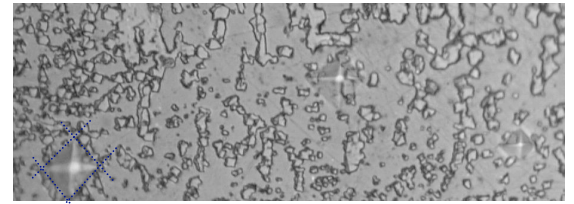
(b)
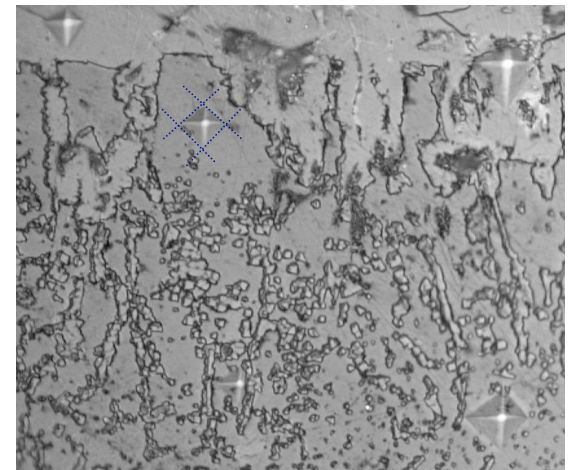
(c)

Figure 3.7.3: Alloy A-900°C-1800seconds, micro-indented in different areas of the oxide phases.(a) low magnification, (b) and (c) in higher magnifications.
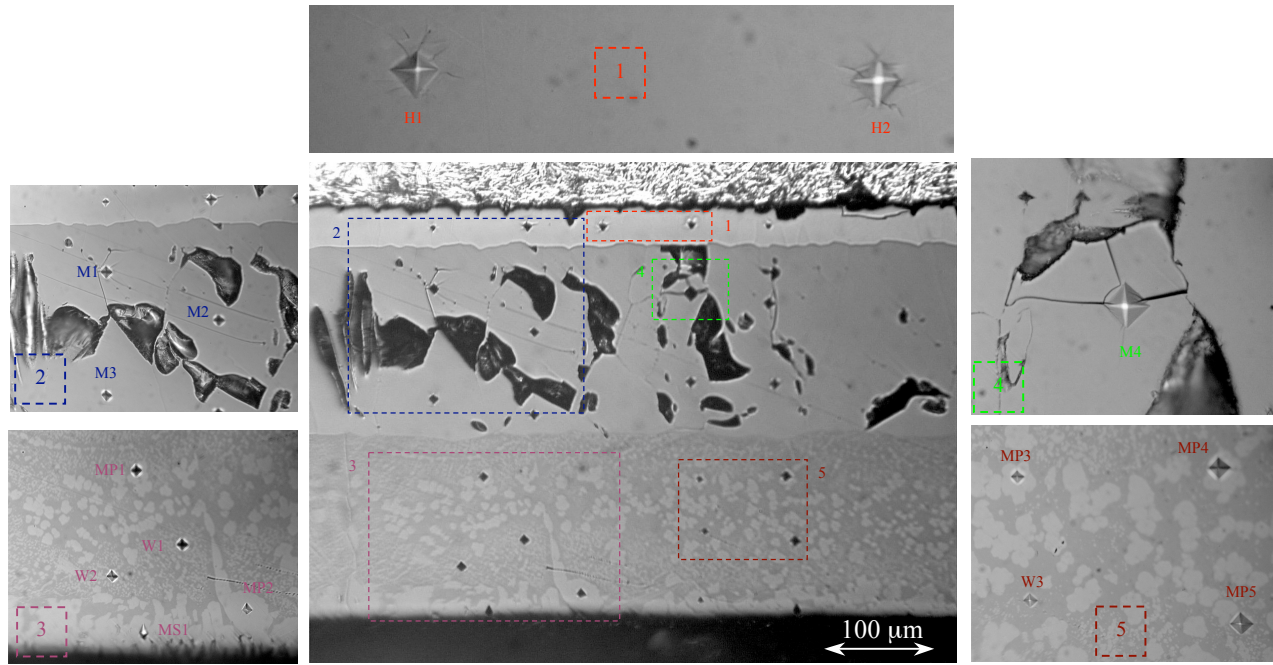
Figure 3.7.4: Alloy A-1100°C-1800 seconds, micro-indented in different areas on the oxide scale.

Areas	Indenter No.	Load (g)	Dimensions (µm)	Hardness Hv
1	H1	50	8.7 – 9.3	1144.6
1	H2	50	9.0 – 9.8	1049.3
2	M1	25	10.8 – 11.1	386.6
2	M2	25	9.1 – 9.2	553.7
2	M3	25	9.3 – 9.6	519.1
3	MP1	25	8.9 – 9.8	530.2
3	MP2	25	9.1 – 9.9	513.6
3	MS1	25	7.8 – 11.1	519.1
3	W1	25	10.2 – 9.9	458.9
3	W2	25	10.3 – 10.4	432.9
4	M4	25	11.6 – 12.4	321.1
5	MP3	10	5.6 – 6.1	541.8
5	MP4	25	9.6 – 9.7	497.8
5	MP5	25	10.1 – 10.2	449.9
5	W3	10	6.3 – 6.7	438.9

H= haematite, M= magnetite, MP= magnetite precipitates, MS= magnetite seam, W= wüstite.

Table 3.7.2: The micro-hardness data for the indentation points indicated in Figure 3.7.4.
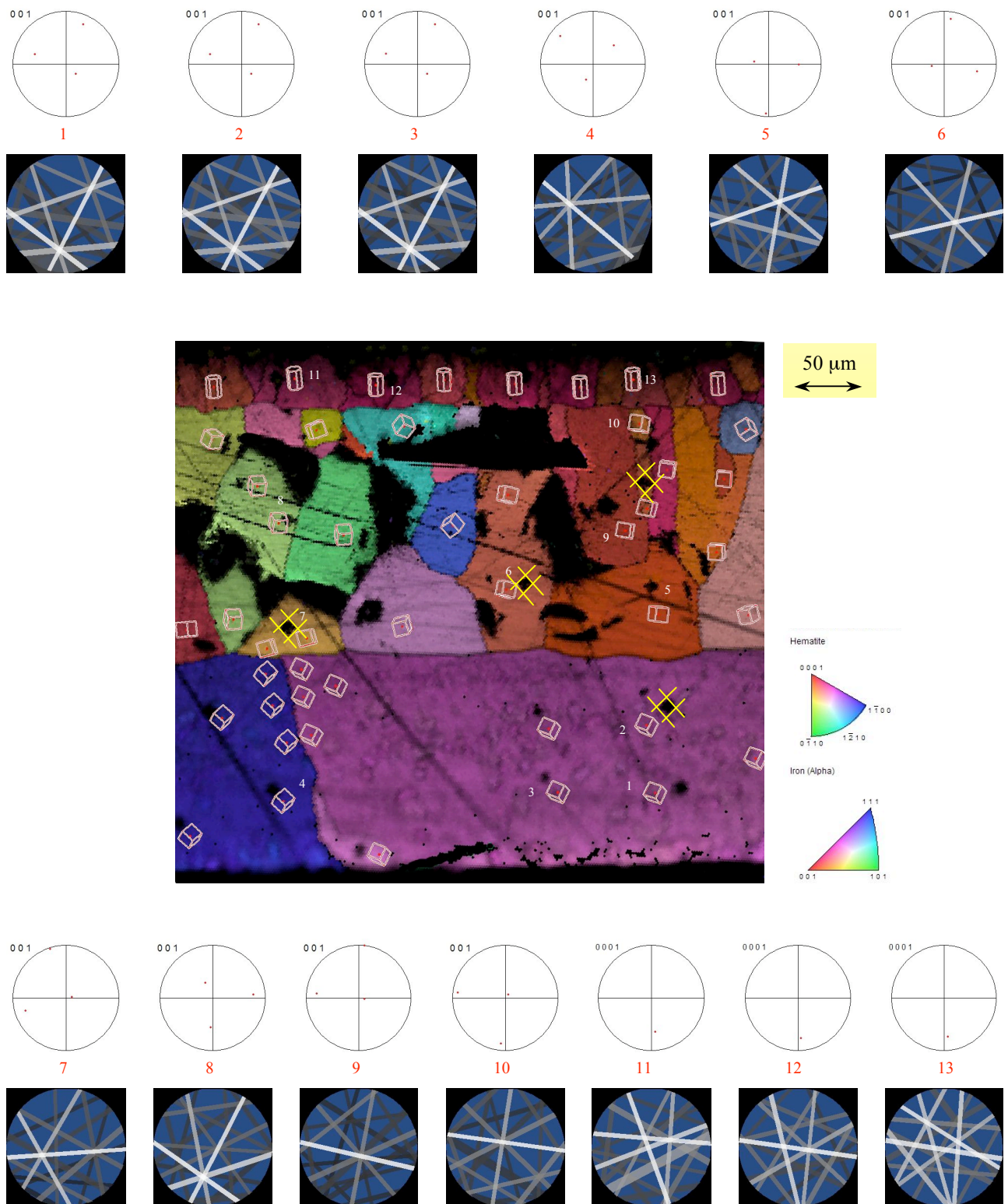
Figure 3.7.5: EBSD IPF//GD map of the same area in Figure 3.7.4. Reconstructed Diffraction Patterns (RDP)s and Pole Figure (PF)s are shown of some points near the indentors.
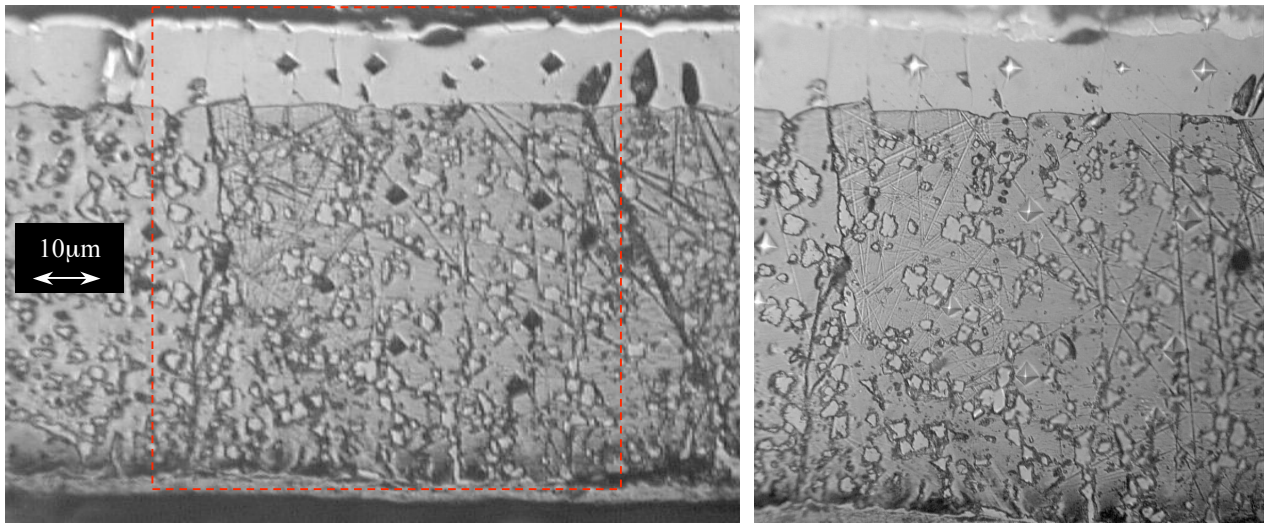
Figure 3.7.6: Alloy B-1000°C-1800 seconds, micro-indented in different areas.
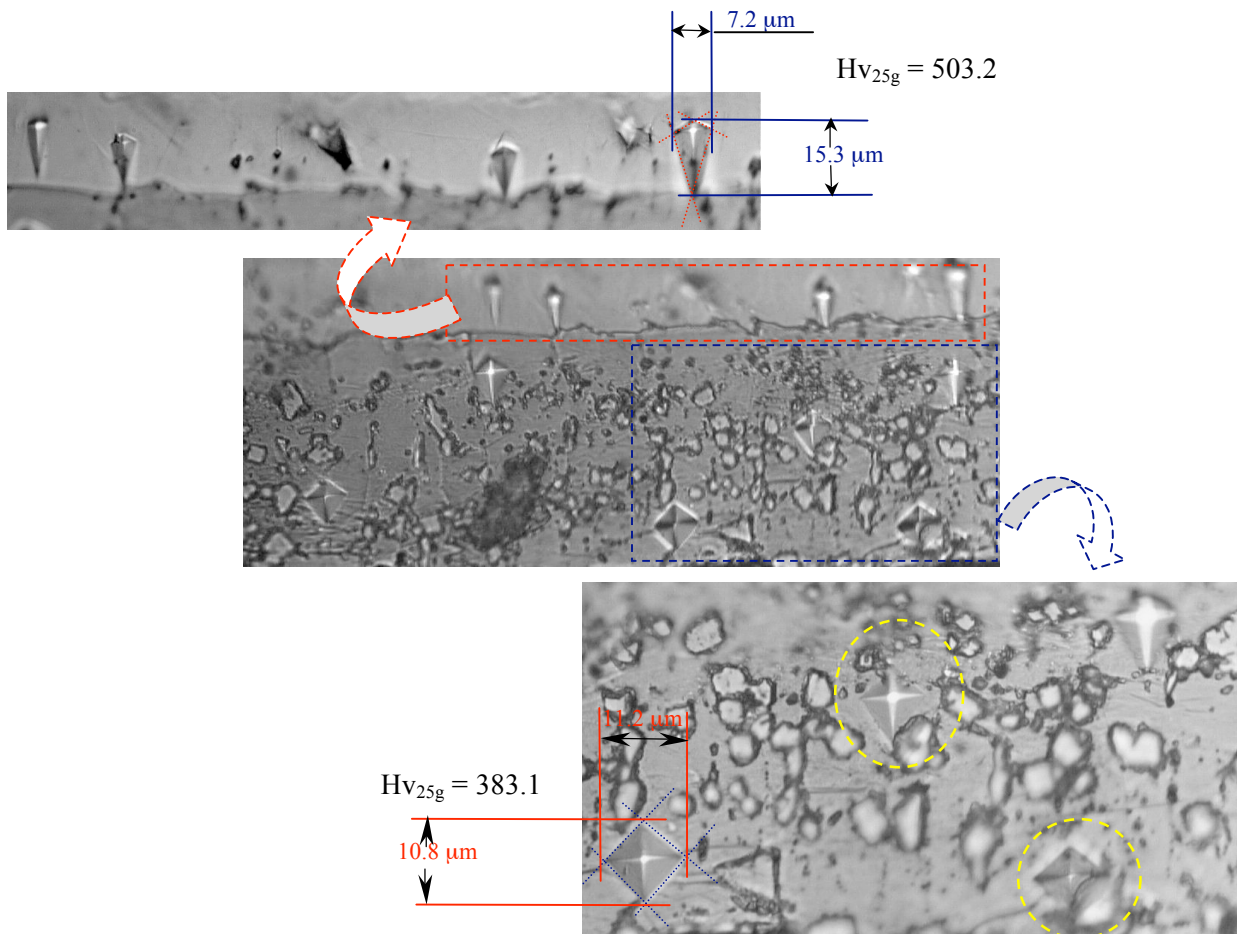
Figure 3.7.7: Alloy B-1100°C-1800 seconds, micro-indented in different areas.

Table 3.7.3: Micro-hardness measurement, IF steel, oxidised at different temperature for 1800 seconds

Temperature (°C)	*Steel Average Hardness*	*Wüstite Average Hardness*	*Magnetite Average Hardness*	*Haematite Average hardness*	*Magnetite precipitate average Hardness*
900	101.9 ± 9.6	387.2 ± 3.2	403.7 ± 2.5	No data	No data
1000	99.2 ± 5.7	426.2 ± 3.7	409.8 ± 2.9	No data	418.9 ± 1.9
1100	96.9 ± 7.8	426.6 ± 1.4	487.4 ± 3.6	993.4 ± 3.6	496.8 ± 8.3

At 900°C: The lower wüstite layer micro-hardness = 389.48
The upper wüstite layer micro-hardness = 383.40

At 1000°C: The lower wüstite layer micro-hardness = 431.40
The upper wüstite layer micro-hardness = 410.44

Table 3.7. 4: Micro-hardness measurement, Alloy A, oxidised at different temperature for 1800 seconds

Temperature (°C)	*Steel Average Hardness*	*Wüstite Average Hardness*	*Magnetite Average Hardness*	*Haematite Average hardness*	*Magnetite precipitation average Hardness*
900	115.5 ± 4.6	423.1 ± 1.3	437.2 ± 3.5	No data	No data
1000	126.6 ± 2.8	435.76 ± 1.9	522.2 ± 8.4	No data	No data
1100	161.9 ± 2.6	445.1 ± 0.8	518.9 ± 3.7	1039.4 ± 2.6	523.2 ± 1.7

At 900°C: The lower wüstite layer micro-hardness =425.45
The upper wüstite layer micro-hardness = 420.85

At 1000°C: The lower wüstite layer micro-hardness = 437.26
The upper wüstite layer micro-hardness = 429.46
The magnetite seam: 483.97

Table 3.7.5: Micro-hardness measurement, Alloy B, oxidised at different temperature for 1800 seconds

Temperature (°C)	Steel Average Hardness	Wüstite Average Hardness	Magnetite Average Hardness
900	246.6 ± 9.6	303.7 ± 3.9	401.0 ± 3.5
1000	285.3 ± 8.2	481.6 ± 11.9	521.2 ± 6.7
1100	219.1 ± 5.4	413.7 ± 7.6	510.3 ± 6.9

At 900°C: The lower wüstite layer micro-hardness = 325.66
The upper wüstite layer micro-hardness = 281.90

At 1000°C: The lower wüstite layer micro-hardness = 486.40
The upper wüstite layer micro-hardness = 478.05
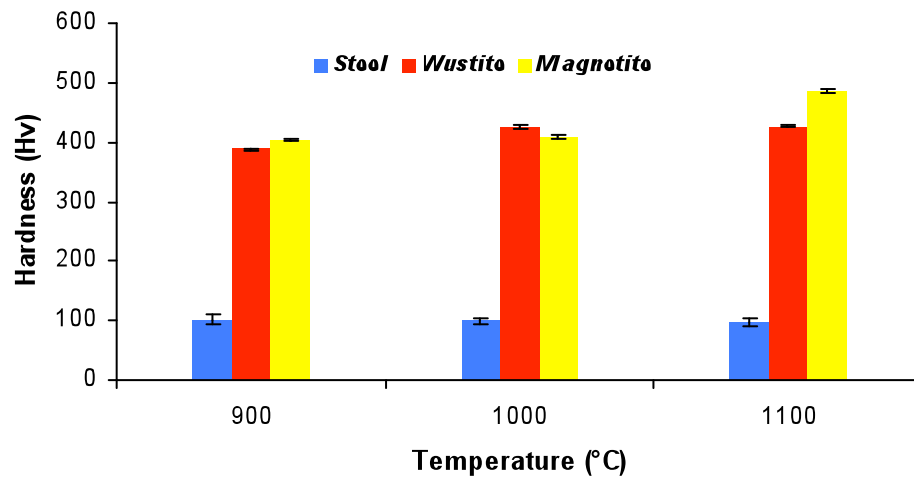
Figure 3.7.8: Micro-hardness versus temperature for IF steel substrate and oxide scale layers at 1800 seconds time of exposure.
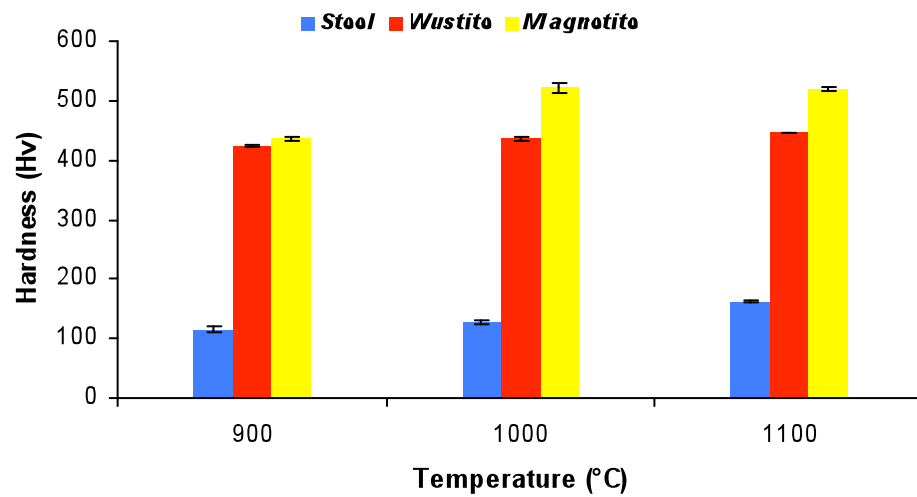
Figure 3.7.9: Micro-hardness versus temperature for Alloy A substrate and oxide scale layers at 1800 seconds time of exposure.
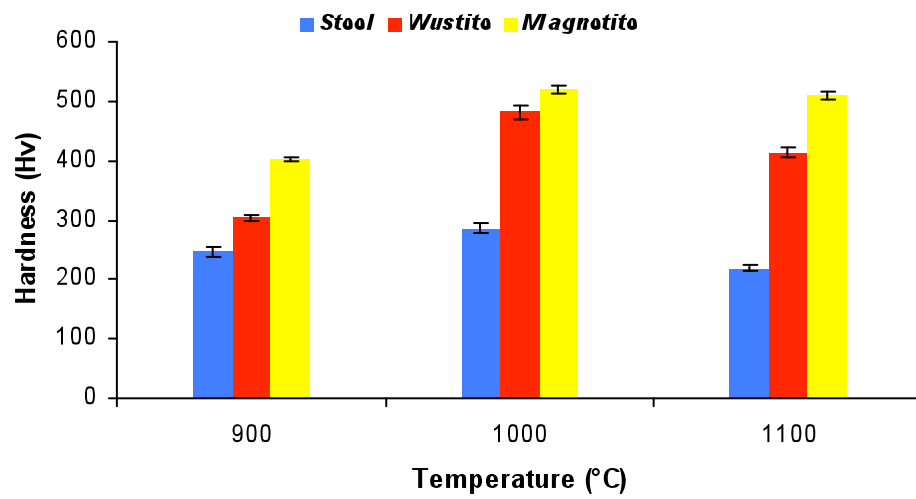
Figure 3.7.10: Micro-hardness versus temperature for Alloy B substrate and oxide scale layers at 1800 seconds time of exposure.

CHAPTER 4 Discussion

The multifactor influence on the oxidation process makes the investigation of individual oxide scale microstructural features and phenomenon difficult. All the factors that affect oxidation phenomenon are involved directly or indirectly in creating a multi process system. Furthermore, microstructural features such as cracks, porosity, adherency, grain size and orientation within the oxide scale have an effect on each other depending on the priority of their development. Therefore, studying the oxidation in the course of "cause and effect" presumption is complex, where each phenomenon is affected by multifactors, making the most influential factor not easily identified. However, attempts have been made here to discuss each feature individually in separate sections. The most important investigations such as oxidation rate, grain size, microtexture and phase ratio are discussed separately and their affect on other microstructural features are discussed throughout this Chapter. Also, the theoretical considerations such as influence of cooling rate, oxidation conditions, sample geometry, surface roughness are discussed in the related sections depending on the results obtained in this study.

4.1 The Oxidation Rate and Kinetics of the Multifactor Manipulated Oxide Scales on Low Carbon Steels

The study of the kinetics of oxide growth on steels is more complex than reported in the literature and is strongly dependant on mathematical considerations. Fitting the experimental data to a standard growth kinetic equations such as; linear, parabolic, cubic or logarithmic equations is useful to know either the behaviour or the trend of the oxidation process for comparison purposes. However, it may lead to a generalisation of the processes without concern for individual observations of each case. As reported in Sections 1.2.4 and 1.2.5, the oxidation rate of the oxide scale on the metal depended on many factors, such as; temperature, time, alloying elements, oxygen partial pressure, cooling rate, healing process after spallation, oxidation environment and geometry of the substrate. Each of those factors has an effect on the oxidation mechanism and oxidation rate, hence on the microstructural development of the scale, such as cracks, porosity,

grain size, orientation, adherency and uniformability of the oxide scale on the steel substrate. Also, it is not evident that repeating experiments under the same oxidation conditions on the same samples leads to the formation of the same pore size or number of cracks, which affect the oxidation rate and kinetics. Thus, each oxidation case should be considered individually in order to identify the main factors affecting the microstructural features in the oxide and hence the oxidation rate.

Depending on experimental and theoretical background, all the recognisable factors that affect the oxidation rate should be considered. In this study effort was made to keep some of the factors constant, such as; environmental composition in which the steel was oxidised (standard laboratory air). Thus, there was no need to consider the oxygen partial pressure, as it was the same for all oxidation experiments. Furthermore, the geometry of the sample and sample preparation methodology was the same for all the samples.

4.1.1 The Effect of Temperature and Time on Oxide Growth Rate

The effect of temperature and time on oxide growth is illustrated in Figures 3.1.1 - 3.1.6. The oxide thickness increased with increasing temperature and time of exposure on all type of steels. The kinetic theory is concerned primarily with the progress of a reaction with time, thus the first task is to find a relationship between oxide thickness and time. It is believed that the diffusion of oxygen in an oxide is much slower than that of iron [Kofstad, 1966]. Therefore, the growth of the oxide scale requires the Fe ions from the substrate to diffuse outward through the scale layers. Since there is an abundance of oxygen at the surface due to the difficulty of reaching the substrate surface through the growing oxide scale, the diffusivity of iron in the oxide determines the growth rate. This means that the temperature/time controls the distance the iron atoms can travel. Moreover, high temperatures in combination with time will allow the iron atoms to travel further and consequently the concentration gradient will decrease with time [Munther, *et al*., 1998]. The kinetics of the scale growth is commonly seen as parabolic with regards to time and exponential with regards to temperature. The "parabolic law" or "square root law" of oxidation was discovered by Tammann and, independently, by Pilling and Bedworth [Kubaschewski, *et al*., 1967, Chen and Yuen, 2002]. The oxidation rates

determined experimentally follow a parabolic relationship between time and oxidation thickness (see Figure 1.2.3 (b)) on IF steel, Alloy A and Alloy B. Appendices 2, 3 and 4 show the thickness of the oxide scale with time at each temperature. The difficulty of fitting data to a parabolic rate equation at 650 and 750°C on Alloy B and IF steels, and at 1100°C on Alloy A, is related to the fact that parabolic kinetics can only be fully suitable for fitting data in the absence of volatile compounds and for growth of coherent films where a diffusion process is the rate determining step throughout the oxidation process [Kubaschewski, *et al*., 1967]. However, the optical micrographs in Figures 3.3.1, 3.3.2, 3.3.13 and 3.3.20 and SEM images in 3.3.26 and 3.3.28 show the scale is not adherent and non-uniform at those temperatures which is why it is difficult to fit this data to a parabolic rate equation. Furthermore, from Appendices 2 - 4, the standard error of the oxide scale measurements at those temperatures is higher than at other conditions, indicating a non-uniform scale growth. In addition, in the literature the oxidation rate is controversial at 650 and 750°C on pure iron and some grades of low carbon steel. Different oxide layer ratios and oxidation behaviour in the range of 600 - 700°C were found from works carried out by Hauffe, 1965, Davies, *et al*., 1951, Chen, *et al.,* 2000 and Kubaschewski, *et al*., 1967. Moreover, in some studies such as Sun, *et al*., 2004, on low carbon steel, the authors were not fully convinced that the oxidation kinetics could be described by either a simple parabolic or logarithmic law.

The parabolic growth of iron oxide scale postulation by Pfeil, 1929 is still valid. As the scale grows thicker, the amount of iron supplied to its outer surface decreases as the transport of iron is by a diffusion process. Eventually the scale becomes so thick that the rate of supply of iron ions to the reaction interface is less than is required for the reaction with the available oxygen ions. At this point the diffusion step is lowest, and beyond this point the reaction is parabolic rather than linear. The parabolic growth mechanism is reported in Sections 1.2.4 and 1.2.5. However, the assumptions made in formulating the parabolic equation should be carefully noted. Whilst it may not be difficult to keep the surface area constant during the oxidation process, the same cannot be said for the diffusion coefficient. The diffusion coefficient depends on the concentration gradient within the layers, which is influenced by the concentration of the diffusing species at the layer interfaces, and may be very sensitive to microstructural changes in the layers [Birks

and Meier, 1983, Kubaschewski, *et al*., 1967]. Therefore, fitting the experimental data to parabolic equation should be considered with its restrictions. Overall the results from this study on IF Steel, Alloy A and B are in agreement with the parabolic growth laws on pure iron within the range of 650 - 1100°C in the literature [Hauffe, 1965, Kubaschewski, *et al*., 1967, Chen, *et al*., 2002, Kofstad, 1966, and recently by Corkovic, *et al*., 2004].

Correlating oxidation rate with oxygen partial pressure is not considered in this study as all the experiments were carried out under zero airflow conditions. However, the dissociation pressure of oxides is influenced by the oxidation temperature, thus, temperature is an important factor to be considered here. As indicated, the oxide thicknesses increased with increasing temperature, as shown in Appendices 2, 3 and 4 and Tables 3.1.1 – 3.1.3. At constant ambient oxygen pressure, the oxidation rate depends on temperature. The surface reaction may be expected to obey the Arrhenius equation (Equation 3.1). Generally, data in a solid straight line in Figures 3.1.4 – 3.1.6 are considered to be representative of the growth of uniform, adherent, and polycrystalline scale layers. Also, the higher K_p values and lower activation energies reflect the fine grain size, [Caplan, *et al*., 1982]. However, as shown in Figures 3.1.4 – 3.1.6, the experimental data from this study are distributed around, not on the straight lines, which is due to the non-uniformability and none adherency of the scale formed on the steel surface at some temperatures. The parabolic constant K_p of IF steel is higher than other steels indicating a higher oxide growth rate on IF steel than on other steels, see Tables 3.1.1 – 3.1.3.

4.1.2 The Factors that Affect Oxidation Mechanism

As the oxidation rate is highly dependant on the growth mechanism and related microstructural features within the oxide, this aspect should be considered in greater detail. The mechanism of parabolic growth was fully elucidated by Wagner [Khanna, 2002]. The mechanism is that of film thickening and is controlled by diffusion due to a concentration gradient. Since the film is composed of cations and anions, the diffusion across the film must be accompanied by simultaneous diffusion of electrons in the same direction as the cations, or in opposite direction to the anions. The details of the parabolic mechanism were discussed in detail in Section 1.2.4. One of the assumptions of the

parabolic law was established by Hauffe, 1965, the mobility of the cation vacancies in wüstite becomes considerably less below 900°C, so that the outward diffusion of Fe^{++} ions becomes slower at higher temperatures, thus, giving the parabolic rate relationship. According to Paidassi, 1955, the growth rate of each layer in the scale such as wüstite, magnetite and haematite is different. It should be noted that, in this study the overall oxide thickness was measured, thus, the oxidation rate has been calculated on the basis of the final scale thickness of all the three layers, not each individual layer within the scale. Therefore the numbers given in Tables 3.1.4 - 3.1.6 of the parabolic rate constant, are related to the total growth rate of all the layers in the scale. As mentioned in Section 3.1, calculating the oxidation kinetics of each individual layer within the oxide scale is based on many different assumptions, for example the phase ratio 95:4:1 for wüstite, magnetite and haematite is not the case at all temperatures, also their thermal coefficients differ. Furthermore, measuring the wüstite layer thickness has to take into consideration the magnetite precipitation which cannot be recognised easily and accurately by conventional techniques and hence should be excluded from the measurements. Also the density of wüstite varies across the wüstite layer as the Fe:O ratio is not constant within the wüstite layer. Thus, as explained previously, in order to avoid any calculation uncertainty, the parabolic rate constant and activation energy were calculated for the entire oxide scale not for individual layers.

A comparison between the results from the present study and the works on similar steel compositions and oxidation conditions is summarised in Appendix 12. The results from this study are different from the others (Appendix 12). As reported by Kubaschewski, *et al*., 1967, Chen, *et al*., 2002 and Kofstad, 1966, iron oxidises faster than steels, where the activation energies of the irons that were oxidised in air or oxygen are higher than for Alloy A and Alloy B. However, this is not the case for IF steel when compared with iron. The experimental conditions in this study differ from the reported data such as gas flow and oxygen partial pressure which makes the comparison difficult. Chen, *et al*., 2001, claimed that the oxidation rate increases with the gas flow rate. As mentioned earlier, in this study the samples were oxidised in a standard furnace in laboratory air at zero flow rate. Sachs and Tuck, 1968, explained that the continuous supplement of oxygen increases the oxidation rate. The activation energy of IF steel is similar to those of works

by Abuluwefa, *et al*., 1996, Chen, *et al.*, 2002 and Hauffe, 1965, however, a small difference may be related to the sample geometry and preparation. As discussed later in this Chapter, different sample preparation may produce different void sizes and micro-holes that affect the surface roughness which in turn influence the oxide growth and kinetics. Also impurities on the scale surface, polishing methodology and furnace conditions can influence the oxidation behaviour.

Blister formation is highly correlated to the cooling rate. Great effort was made here to ensure the cooling rate is the same for all the experiments at approximately 10°C/sec. Also, one of the most important factors that affect the oxidation mechanism is the gap formation between the steel substrate and oxide scale. Furthermore, the gap migration and healing processes that may take place have an influence on the oxide growth mechanism [Mougin, *et al*., 2003].

It is obvious that the gaps have an affect on the oxidation rate by inhibiting diffusion, but understanding the mechanism of the gap formation is crucial in order to prevent or allow it to be formed. There are many theories regarding oxide adherency to the substrate. It was suggested by Pfeil, 1929, that the natural velocity of outwards diffusion of the iron through the scale is greater than the rate of oxidation of the iron core; hence there is a tendency for contact to be lost between the scale and the core. Sachs and Tuck, 1968, suggested that the contact between scale and metal can only be maintained by creep of the oxide. If creep is prevented or inhibited (and this is obviously more likely to occur at lower temperatures) contact is lost, and a gap is formed at the scale/metal interface. Considering these theories the oxidation temperature should be taken into account because the iron diffusion is higher at higher temperatures. From the optical micrographs in Figures 3.3.1, 3.3.2, 3.3.9, 3.3.21 and 3.3.23, the oxide scale is not adherent to the substrate at both low and high temperatures. This indicates that the gap formation is more complex than it is considered in those theories.

Sachs and Tuck, 1968, suggested that a small amount of impurity from the steel substrate might inhibit dislocation movement in the scale, this may lead to the formation of a serious of micropores which form a gap at the steel-scale interface and as a result reduce

the iron flux crossing the interface. Regardless of the validity of those theories, it is obvious that the gap formation would affect the oxidation mechanism. The affect of gaps on the phase ratio and other microstructural features are discussed in later sections in this chapter.

4.1.3 Steel Composition Effects on Oxide Scale Growth

As shown in the Appendices 2 - 4, and the parabolic rate constants in Tables 3.1.1 - 3.1.3, the slowest oxidation rate can be seen on Alloy B and the fastest on IF steel. The oxidation conditions; time, temperature, oxygen gas pressure, surface preparations, geometry of the samples and cooling rate were the same for all the steels used in this study, thus the steel composition results in the different oxidation rates. The activation energy calculation showed that IF steel has the highest value and Alloy B the lowest, Figures 3.1.4 - 3.1.6. This is an indication that the steel composition has a large influence on the oxidation rate.

As shown in the Table in Appendix 12, pure irons have higher activation energies than carbon steels. It is clear that the ratios of the alloying elements within the steel substrate have an influence on the oxide growth [Chen and Yuen, 2003]. Generally, the existence of chromium, aluminium and silicon, which are less noble than iron, provide a certain level of oxidation resistance for steel, but their effect becomes insignificant if their ratios are very low. Residual elements, such as copper, nickel and tin that are more noble than iron, usually accumulate at the scale-substrate interface and have little effect on the steel oxidation behaviour [Geneve, *et al*., 1990]. According to the same reference, the presence of manganese in the steel substrate would result in a lower rather than higher eutectoid temperature, so that wüstite would be expected to form even below 570°C, which is not in agreement of Chen, *et al*., 2001. As shown in Table 2.1, the IF steel contains the lowest amount of alloying elements of the steels used in this study. The tables in Appendices 2 - 4 show that the IF steel oxide thickness is higher than on Alloy A and Alloy B. From Tables 3.1.1 - 3.1.3 it can be concluded that the parabolic rate constant (K_p) of IF steel is the highest at all temperatures. There is an exception to this case as the oxide thicknesses of Alloy A at 1000 and 1100°C are higher than IF steel. The effect of

alloying elements is clear on the oxidation rate as the oxide scale growth decreased with increasing alloying elements. However, each alloying elements affect on oxide growth should be considered individually. The effects of some elements are reviewed in Section 1.2.8. Silicon could produce fayalite ($2FeO.SiO_2$) and this can form a eutectic with wüstite which melts at about 1177°C even at relatively small levels, ~1.8, according to Marston, 2004. However, the experiments carried out in this study did not reach the fayalite formation temperature. Also the highest Si concentration was in Alloy B and is small ~ 0.24%. Generally the effect of that small amount of Si, and being below the fayalite formation temperature, should not affect the oxidation rate. The effect of carbon on the oxide scale is clearer. Carbon due to decarburisation causes the gap formation at the steel substrate and the oxide scale interface. The mechanism of this phenomenon is well known [Marston, 2004, Sachs and Tuck, 1968, Kubaschewski, *et al*., 1967, Chen, *et al*., 2002, Kofstad, 1966]. IF steel contains 0.0026 wt % C, and so the amount of carbon is very small for decarburization to take place. As shown in Figures 3.2.1 - 3.2.4, the IF steel contains only ferrite at all temperatures and times of exposure. From Figures 3.3.1 - 3.3.14, the scale morphology can be seen as it varies in adherency with temperature. While, the pearlite segregation and decarburization occurred in Alloy A as can be seen clearly in Figures 3.2.5 - 3.2.10, the oxide scale on Alloy A varied in adherency with temperature, see Figures 3.3.15 - 3.3.22. Thus, the affect of decarburization on oxide scale adherency with the substrate is not clear.

Caplan, *et al*., 1979 and Chen, *et al*., 2001 stated that carbon in steel can be oxidized to form CO or CO_2 at the scale-metal interface, resulting in loss of contact between the scale and the substrate. However, this was not observed during the current experiments. The work by Kucera and Hajduga, 1998, showed that CO_2 and CO could be measured in the gap and the decarburisation can be observed due to the gas generated during oxidation. However, is not clear in their study how precisely they could measure the gas pressure as the gas could easily escape through the cracks and pores.

Carbon not only affects the oxidation rate through contributing to the gap formation and decarburisation, but also Kucera and Hajduga, 1998, reported that carbon can decrease the oxidation of iron at high temperatures. The oxidation of carbon steel is slower than

pure iron because a residue of graphite is left at the metal surface. This promotes cavity formation at the metal-oxide interface by providing nuclei for the condensation of cation vacancies. The graphite and cavities hinder the transfer of metal to the oxide, thus slowing the oxidation rate. The residue graphite at the steel-metal interface, according to the same reference, is very thin ~ 50-100 nm. The phase maps and carbon EDS maps could not reveal the presence of this layer to prove that hypothesis, see Figures 3.5.5 - 3.5.22 although, silicon is detected, see Figures 3.5.12 (e), 3.5.17 (f), 3.5.19 (f), and 3.5.20 (d), but it is not clear whether it is due to the enrichment of silicon at metal-scale interface or sample preparation. As mentioned in Section 2.2, all the samples examined by EBSD were polished for at least 20 minutes using colloidal silica.

The study of the effect of the small amounts of other alloying elements in steel on oxidation behavior is not well understood. The work by Geneve, *et al*., 1998 on very similar steel to this study showed a distribution of alloying element around the oxide substrate interface in low carbon steel (0.05% C, 0.34% Mn, 0.02% Si, 0.09% Ni, 0.02% Cu and 0.01% S). The presence of alloying and residual elements leads to the modification of the morphology of the oxide layer, adherency, variation in oxidation kinetics and enrichment of some elements around the metal-oxide interface. During oxidation, the evolution of the surface composition of a dilute Fe alloy depends mainly on the solubility of the alloying element in the scale. According to the same reference, the elements that are soluble in the scale such as Mn, behave similarly to iron as they diffuse with iron into the scale during oxidation. Whilst, elements which are not soluble in the scale, do not diffuse with iron and they enrich at the oxide-metal interface, e.g. Ni or Si, which can react with oxygen forming SiO_2 precipitates or probably enrich at oxide-metal interface. Other elements such as Sulphur (S) can produce a volatile oxide SO_2 [Geneve, *et al*., 1998]. There was an attempt in the same reference to show the effect of the small quantity of the alloying element in low carbon steel on oxide thickness. They concluded that the thickness of the oxide scale decreases with increasing concentration of residual elements. They summarised that residual elements generally accumulate around the metal-oxide interface and provide a diffusion barrier for the iron atoms and this causes a decrease in the oxidation rate. Also, they found that Si and Cu strongly segregate at the interface and caused a reduction in the oxide thickness. This explanation may provide the

answer of how the oxidation rate of IF steel is higher than Alloy A and Alloy B which are contain higher alloying elements. However, different alloying elements have different affects on oxidation rate and microstructure of the oxide scale. Also, to what extent each of the alloying elements influence the oxidation rate and which of them dominates is not fully understood. The techniques used in this study such as, SEM, EDS and EBSD, however, are not as capable as other techniques, such as Auger Electron Spectroscopy (AES), of detecting such small amounts of alloying elements at oxide-metal interfaces.

In a multilayer scale such as on steels, the oxidation rate of each layer is different. Therefore, the different phase ratio affected the overall oxidation rate observed in this study. As will be discussed in more detail later, the phase ratio is affected by many factors which in turn make the comparison of oxidation rate with other studies more complex. Also, the phase ratio cannot be manipulated easily through changing one oxidation parameter or another. Thus, not obtaining the same phase ratio within the oxide scale makes the comparison very difficult. The phase ratio may even differ on the same sample in different locations which in turn changes the oxidation rate. Thus, considering every aspect of the oxidation process including all the microstructural features in individual cases is imperative to avoid any misunderstanding conclusions when it is compared with the results from other studies.

As discussed in this section, many factors affect the oxidation rate of steels. The effectiveness of some factors can be monitored and observed by the techniques used in this study, others could not be detected. The difficulties arise where some factors manipulate the growth kinetics indirectly making them difficult to observe. Therefore, it is vital to obtain not only a quantitative analysis but also investigate the microstructural evaluation of the oxide scale. The influence of the other factors such as; microstructure, microtexture and mesotexture of the steel substrate and the oxide scale layers on the oxidation rate will be discussed in the following sections.

4.2 The Oxide Scale Microstructure Evaluation and Investigation into the Factors that Affect Its Development during the Oxidation Process

The study of the oxide microstructure is of great importance in the understanding of the nucleation, growth, kinetics, oxide mechanical properties and descaling properties of the scales. At each oxidation temperature the oxide develops different grain shapes, sizes and orientations, making the oxide scale available with a wide range of mechanical properties which leads to a consideration of microstructural engineering to improve the descaling processes. Furthermore, scale removal and the surface qualities of a steel product are heavily influenced not only by the thickness of the scale formed, but also by the microstructural characteristics of the scale: i.e., the nature and distribution of the different phases present within the scale.

As for the oxidation rate there are many factors that can affect oxide microstructures including time, temperature, oxygen partial pressure, oxidation environment and alloying elements in the steel. In addition it is believed that even the steel texture has an affect on the oxide development and thus oxide microstructure. Therefore the current investigation has studied oxide development at specific temperatures and times to obtain an evaluation of oxide microstructure. The complexity of the microstructural development of the oxide scale and a strong connectivity between the factors that affect the microstructural features within the scale, made the consideration of each phenomenon separately difficult. However, an attempt had been made here to describe and discuss each microstructural feature independently in the subsections below, in the light of the results obtained in this project.

4.2.1 The Observation Techniques Reliability and Their Examination Considerations

As discussed earlier, the simple model of iron oxide scale layers is much more complex in reality and its properties could change with a number of factors. Therefore an understanding of the oxide scale formation and its properties can only be achieved by careful examination of the scale microstructure. However, this is dependant on the reliability of the observation techniques used for the microstructure characterisation.

Traditionally, standard metallographic sample preparation and investigation has been used to characterise the oxide scale by optical or scanning electron microscopy, using etchants containing 0.5-1% hydrochloric acid solutions in ethanol [Chen and Yuen, 2003, Caplan, *et al*., 1981 and Chen and Yuen, 2002]. The microstructure of the oxide scale is, however, not straightforward. For example as in Figure 3.4.1 (a), wüstite appears dark relative to the magnetite, and haematite is the lightest of the etched oxide layers. In contrast to optical microscopy, scanning electron microscopy gives different apparent colour contrast of the oxide phases in the scale, where haematite is the darkest while wüstite is the lightest, as shown in Figure 3.4.1 (b). This traditional method has been used throughout the last century and still in most research centres today. However, it is not an accurate way of identifying the phase's distribution within the scale, as it is not correlated to a crystal structure of the phases. Phase identification by optical microscopy depends on the light reflection from each phase and also from any artefacts generated during sample preparation and etching. Moreover, etching samples does not give any information about the phase grain size, shape, orientation, or grain boundaries. Standard scanning electron microscopy may give more information about the oxide scale at higher magnification than optical microscopy (high magnified magnetite precipitates can be seen in Figure 3.3.29 (b) for the same sample). However, the limitation of the SEM technique is that, as with optical microscopy, it does not give detailed information of oxide microstructure. As shown in Figures 3.4.1 (a and b) the grain boundaries in each phase within the scale are not evident. Generally, the optical, scanning electron microscope, chemical analysis, X-ray diffraction and laser Raman Spectroscopy can give information about the phases present in the oxide scale [Chen and Yuen, 2001, Gleeson, *et al*., 2000 and Raman, *et al*, 1998], but they cannot correlate the phase distribution within the scale microstructure.

In the current study, EBSD was used to eliminate the ambiguity of identifying the phases in the oxide scale and correlating the microstructures. The ambiguities can be eliminated only if the grain and crystallographic structure for each phase in the scale is considered and its microstructure-texture analysis obtained to characterise the scale microstructure. One of the powerful features of the EBSD is the Image Quality (IQ) map, which provides better contrast of the grain boundaries than conventional secondary electron SEM. This occurs because diffraction patterns taken from grain boundary regions result in a poor

pattern quality index, since the EBSD patterns obtained from these regions are generated from both grains. Thus, the pattern quality map is an excellent method of highlighting grain boundaries while still observing the microstructural features [Randle and Engler, 2003]. The image quality map is a greyscale plot where the greyscale level at each point corresponds to the relative intensity of the Kikuchi bands above the background in the EBSD pattern acquired at each point [Dingley and Randle, 1992 and Humphreys, 2001]. Therefore, obtaining grain size, shape and detailed microstructure of the phases using EBSD is more reliable than other techniques. As shown in Figure 3.4.1 (c), the phases and grain boundaries can be seen clearly in the Image Quality map [The details of EBSD capability and accuracy can be found in Randle, 2004, Humphreys, *et al.*, 1998, Randle, 2002, Fukuoka, *et al.*, 2002, Mishin, *et al.*, 1997 and Lee, *et al.*, 2003]. From the grain boundary level map, all the grain boundaries in the sample area can be characterized easily whether low (2 - 15°) or high (15 - 180°) misorientation grain boundaries, Figures 3.4.2 (a and b). Characterizing grain boundary misorientations is important for grain size measurements. The EBSD user can decided which grain boundaries are to be excluded from the grain size measurements (in this study only high angle (15 - 180°) grain boundaries are included).

EBSD is a technique that can also be used to identify unknown crystalline phases while exploiting the excellent imaging capabilities of the SEM. EBSD patterns contain a large amount of information about the crystal structure of the phase such as *d*-spacing, lattice parameters and crystal plane. It is possible to use this information to determine the space group of the phase from the symmetry elements contained in the pattern, see the diffraction pattern indexing for different phases in Figures 3.5.1 - 3.5.4. The combination of EBSD and a crystallographic database is becoming a standard technique for the identification of unknown crystalline phases [Randle and Engler, 2003]. To distinguish between phases, the selected crystals must either have different structures or have a unit cell parameter difference greater than 10%. When these conditions are met, a mapping program can distinguish between the phases (phase discrimination) [Dingley and Randle, 1992]. For instance, it was easy for the EBSD system to recognise haematite among the rest of the phases within the scale as it have trigonal crystal structure, on the other hand iron, wüstite and magnetite have cubic crystal structures. It should be noted that there was

no need to consider γ-haematite as it is not stable at temperatures above 400°C [Kofstad, 1966]. The working temperature in this study was from 650°C and above. As mentioned earlier the diffraction patterns produced by EBSD not only containing crystal structure information but also the *d*-spacing and lattice parameters, thus, EBSD could distinguish between iron and wüstite and magnetite on this basis. The determination of *d*-spacing, identifying the axis zone associated with the poles in the diffraction pattern and indexing parameters are shown in Figures 3.5.1 - 3.5.4 for all the phases within the scale plus α-iron in the steel substrate. Having said that, the accurate indexing of each phase was not an easy process as the lattice parameter and *d*-spacing are very similar for these cubic phases.

There are many different approaches to phase identification using EBSD. It is important to make the distinction between phase identification and phase verification. The main difference between these two terms is the number of candidate phases that are to be searched to find the correct match to the unknown. In phase verification, the operator is sure of the phases present in the sample and thus very small numbers of choices are given (usually less than 5 for the case of iron, wüstite, magnetite and haematite). In true phase identification, a large database of crystalline compounds is searched for the correct identification with little input from the operator [Michael, 2000]. Randle, 2004, stated that EBSD is not at a stage to identify phases but had great potential in usability for phase verification. However, in this study the term of phase identification is used as it is recognised by EBSD system providers and developers in a wide range of publications. Moreover, comparing the phase identification by EBSD with conventional techniques, EBSD can identify the phase in a better way. In this study the term phase identification is used as a phase verification or phase discrimination in order to be compatible with the standard terms used by others and not cause confusion for the reader. It should be noted that the phase discrimination carried out through crystallographic identification of the crystal structure for each phase has been compared with EDS results. Nowell and Wright, 2003, stated that it can be difficult and/or time intensive to differentiate phases within materials by crystallography alone. The crystallographic information is extracted from the diffraction patterns and then compared with the crystallographic information from the

candidate phases in the database, and a best-fit match is determined. Problems rise when two phases have similar crystal structures and lattice parameters, e.g., wüstite, magnetite and iron. The phase differentiation process can be improved by collecting chemical information through energy dispersive X-ray spectroscopy (EDS) simultaneously with the crystallographic information and then using the chemical information to filter the crystallographic phase candidates using "Chi-scan" in the OIM-DC software. This technique improved both the overall speed of the data collection and the accuracy of the final characterisation. However, through optimisation of the indexing parameters (as explained in section 2.4.3) there was no need to use Chi-scan for all the scans. Examples of the Chi-scan are shown in Figures 3.5.9, 3.5.12, 3.5.16 and 3.5.20. It should be noted that collecting chemical information alone is not enough to distinguish between magnetite and wüstite, as the oxygen concentration difference is not large. However, combining crystallographic and chemical information could overcome this problem even near edges or in porous areas, see Figures 3.5.9, 3.5.10, 3.5.12 and 3.5.16.

Figure 3.5.5 shows the phase distribution in the oxide scale layer grown on the IF steel at 1100°C for 1800 seconds. As can be seen from the figure, the three existing phases within the scale can be clearly identified as well as the magnetite precipitate distribution within wüstite grains. Figure 3.5.6 (a) shows the EBSD-EDS oxygen map for the same scanning area in Figure 3.5.5. As expected the haematite phase contains the highest oxygen concentration, while wüstite the lowest. The contrast EBSD and EDS maps are very similar, indicating that the diffraction patterns from each oxide phase in the scale were accurately indexed.

4.2.2 The Phase Identification and Transformation within the Oxide Scales

Smuts and Villiers, 1966, described the phase ratio, oxide thickness and distribution of oxide phases as the main factors governing the descaling properties. It is therefore important to use reliable techniques to identify the phases within the oxide scales in order to avoid misleading conclusions. Recognising the phases within the scale accurately helps to determine the affect of temperature, time, steel composition as well as microstructural

features on the phase ratio and related phase transformations which occur during oxidation and cooling.

As explained in Section 4.2.1, haematite with the highest oxygen content and the highest hardness, is the least soluble in acid and appeared white relative to other two phases under the light microscope. Magnetite has an intermediate oxygen content, intermediate hardness, and an intermediate solubility in acid, appeared as light grey. Wüstite has the lowest oxygen content, is the softest and is the most acid soluble phase among the three iron oxides, also it is appear as a dark grey. It is easy for the observer to recognise the magnetite precipitates as they have the same colour as magnetite layer. However, the colour gradient in the wüstite layer from very dark grey to less dark should be carefully considered. Smuts and Villiers, 1966, reported that stoichiometric wüstite etches lighter than non-stoichiometric wüstite but darker than magnetite. Non-stoichiometric wüstite represents equilibrium wüstite, which is stable above 570°C as in the wüstite field of the equilibrium phase diagram for Fe-O, see Figure 1.2.4. Normally its composition in the presence of excess iron does not differ appreciably from $Fe_{0.95}O$, the lattice parameter being $a = 4.304$Å. Whereas the stoichiometric wüstite is the metastable wüstite phase obtained by limited decomposition of non-stoichiometric wüstite below 480°C and has a composition very close to $Fe_{1.00}O$ with a lattice parameter $a = 4.332$Å.

The wüstite which forms is iron deficient and generally has a range of 5-16 percent Fe defect structure [Pickens, 1984]. As explained in Section 1.2.7 the chemical composition of wüstite is more accurately written as $Fe_{1-y}O$ where y defines the degree of variation from the stoichiometric ratio. The values of y generally increase with distance away from the metal/scale interface. The $Fe_{1-y}O$ formed at high temperatures undergoes a eutectoid decomposition at lower temperature around 570°C as shown in the Figure 1.2.4. This eutectoid reaction can be written as in Equation 1.10. In practice, however, the reaction products may be magnetite and wüstite of lower oxygen and higher iron content with no precipitation of metallic iron [Barlow, *et al.*, 1965 and Tominaga, *et al.*, 1982]. Gleeson, *et al.*, 2000, showed some images indicating that the very white particle within the oxide was Fe produced from above equation. The iron particles were the brightest phase within the scale.

Recognising metallic Fe within the oxide scale is not an easy task using any of the techniques used in this study. This is related to the fact that the metallic iron precipitates in very small amounts at different locations within the scale. Thus, it is difficult to recognise by EBSD especially at low magnification. Furthermore, iron EDS maps as in Figures 3.5.6 (b), 3.5.7 (d)…etc., are not sensitive enough to identify the metallic Fe within the scale. Also the iron content within the scale layer varies which makes the task more difficult to distinguish between the Fe metallic precipitates and Fe concentration variations across the scale. The colour contrast of iron by optical microscope or SEM is not accurate as it can be affected by the sample preparation.

The exact phase transformation reaction can vary depending on the cooling rate and the oxygen content of the parent wüstite. During rapid cooling the reaction may take place only partially or not at all and as such wüstite can exist at room temperature [Kofstad, 1966 and Chen, *et al*., 2001]. The cooling rate in this study of 10°C/seconds was rapid enough to allow some wüstite to be retained to room temperature and some to transform to magnetite. However, the amount of magnetite precipitates within wüstite at different time and temperatures is a matter of consideration and will be discussed later.

During cooling from temperatures above the wüstite eutectoid, proeutectoid magnetite crystals can nucleate and grow [Pickens, 1984]. Again, the degree of development is dependant upon the oxygen content of the wüstite and the cooling rate. In theory this reaction should begin and be most advanced in the more oxygen rich wüstite near the magnetite/wüstite interface and occur last in the more iron-rich, oxygen deficient wüstite near the wüstite/metal interface [Tominaga, *et al*., 1982]. From both reactions eutectoid and proeutectoid magnetite is formed during cooling as can be seen from Figures 3.3.9 and 3.3.10. The magnetite precipitate shape was also considered in this study. The highly magnified SEM images in Figures 3.3.29 (b), 3.3.30 (d) and 3.3.31 (a) show the square or rectangular shapes of the precipitates. Schimd, *et al*., 2001 suggested that the oxide scale establishes a pyramidal growth structure. This explanation may be valid for magnetite precipitates were the pyramidal shape appears as a square or triangles in the oxide scale cross section. Kyung, *et al*., 2000 and Kim, *et al*., 2000 related the shape of the magnetite precipitates to the differences in the surface diffusion and coalescence of the phase's

species which results in the surface morphological development. Generally, the square or triangular grains that appear in the Figures 3.5.29 - 3.3.31 indicate cubic structure of the magnetite phase.

Smuts and Villiers, 1966, stated that the presence of Fe and magnetite is very important in considering the speed of decomposition. An isolated magnetite nuclei acts as a nucleus for further growth of magnetite. For the magnetite to grow it has to expel the excess iron atoms which then diffuse into the adjacent wüstite to form iron saturated stoichiometric wüstite as a layer adjacent to the magnetite. According to the same authors, the stoichiometric wüstite is always found together with magnetite. This is clearly illustrated in Figures 3.3.29 and 3.3.30 where the magnetite is present as islands in a wüstite matrix surrounded by stoichiometric wüstite. In addition there is an intermediate layer at the magnetite-wüstite interface present in some images (e.g. as indicated in Figure 3.3.10). In some references this intermediate layer is called the "transition layer" and is simply described as a wüstite of higher oxygen content [Pickens, 1984]. This is in agreement with the observation in this study, as the colour of the transition layer at the magnetite/wüstite interface always has same contrast as the wüstite layer. This intermediate layer was observed in some but not all cases especially at high temperatures i.e. above 900°C; see Figures 3.3.9, 3.3.10, 3.3.11 and Appendix 8. It has been noticed that where magnetite precipitates were very small in size and highly concentrated in some areas, the wüstite around them appears darker than the rest of the layer, see Figures 3.3.11 and 3.3.12. Is should be noted that EBSD cannot recognise the different wüstite oxygen contents (i.e. stoichiometric and non-stoichiometric wüstite) as the diffraction patterns obtained from both wüstites are the same. Furthermore, in the TSL and ICCD crystallographic data bases used only, cubic FeO is available with a fixed lattice parameter regardless of the lattice parameter changes which might occur due to oxygen content variations. The wüstite and magnetite lattice parameter variations are reported by Goldschmidt, 1942. He claimed that the wüstite lattice constant decreases with decreasing iron content. EDS is also not sensitive enough to differentiate these small differences in oxygen content within wüstite layer, for example see Figure 3.5.6 (a).

4.2.2.a The Phase Ratio and Distribution within the Oxide Scale Layers

The phase ratio within the oxide scale must be related to the factors that affect microstructural development of the scales. The factors that affect microstructure of the oxide scale would affect the phase ratio in the same way. As shown in Figures 3.5.23 - 3.5.26, the oxidation temperature and time of exposure influence the phase ratio. The haematite and magnetite on IF steel that was oxidised for 1800 seconds increased with increasing temperature from 900°C to 1100°C, whereas, wüstite decreased. The magnetite volume fraction at 900°C was 0.13, which increased dramatically to 0.62 at 1100°C, whereas the wüstite volume fraction was 0.86, then decreased to 0.3 at 1100°C, see Figure 3.6.23. The volume fraction of the oxide phases on Alloy A changed less significantly, see Figure 3.6.24. On Alloy B, the magnetite volume fraction remains constant at all temperature, where as the wüstite and haematite changed slightly, see Figure 3.6.25. The predominance of wüstite at all temperatures is clear because the diffusion coefficient of iron in wüstite is much higher than in magnetite and the diffusion coefficient of oxygen and iron in haematite are extremely small [Chen, *et al.,* 2002]. However, this case would change as the extent of the transformation depends on the cooling rate and composition of the parent FeO. For instance, oxygen-rich FeO transforms much faster than iron-rich FeO [Gleeson, *et al*., 2000]. Kubaschewski and Hopkins, 1967, claimed that above 700°C, the relative thickness of the three oxide layers is independent of temperature and the ratio is near 95:4:1 for wüstite: magnetite: haematite. This is in agreement, but not fully, with the results in this study where the thickness of individual layers remains constant on Alloy B and varied without any trend with temperature on Alloy A. The phase ratio is highly dependant of the mechanism of growth of each phase within the multilayer scale. The details of this mechanism are reported in detail in Section 1.2.5; the oxidation rate of each layer is different and is dependant on its structure. FeO, is a p-type metal deficit semiconductor which can exist over a wide range of stoichiometry. Thus it contains a high cation vacancy concentration and the mobility of the cations and electrons is extremely high. However, this is not the case for magnetite and haematite. Therefore the diffusion of the iron in wüstite is very high and the rate controlling step.

From the phase diagram of the iron-oxygen system, Figure 1.2.4, it is clear that the wüstite does not form below 570°C. Above this temperature the multi scale layer will form with wüstite as the greatest part with a thin outer layer consisting of magnetite and haematite. The results from this study agreed with a phase ratio calculation by Tominaga, *et al*., 1982, Figure 1.2.6 (a), especially for IF steel where the wüstite decreased with increasing temperature after 900°C, while magnetite increased, see Figure 3.5.23. However, Hauffe, 1965, illustrated a different phase ratio as shown in Figure 1.2.6 (b), where the wüstite, magnetite and haematite remain constant after 750°C. The work by Hauffe, 1965, is more in agreement with the results in this study for Alloy B than the work by Tominaga, 1982, see Figure 3.5.25. It should be noted that both work by Tominaga and Hauffe were carried out on iron, however, the phase ratio of oxide scale is affected by many factors as previously described. The oxidation rate of iron is very similar to low carbon steel as reported by Chen, *et al*., 2002. Therefore the phase ratio of iron and low carbon steel oxide scales would be similar, which is why the results from this study on IF steel and Alloy B are in agreement with Tominaga and Hauffe. However, the differences between IF steel, Alloy A and Alloy B phase's ratio and their differences with the work by Hauffe and Tominaga is related to the factors that affect the oxidation mechanism such as, steel composition, sample preparation, porosity, crack formation and oxidation conditions.

From the phase maps of all the three types of steel it is clear that wüstite dominates large areas of the oxide scale especially below 1000°C, see Figures 3.5.5 - 3.6.22. However, this changes at higher temperatures as the magnetite layer formed at high temperatures may grow into the wüstite because the wüstite becomes supersaturated with oxygen during cooling [Hauffe, 1965 and Kofstad, 1966]. Figures 3.4.1 - 3.4.6 and Appendix 9 and 10 show the number of the grain boundaries in magnetite is always more than in wüstite at all times and temperatures. The results also show increasing magnetite precipitation with temperature contributing to the overall increase of fraction of the magnetite phase within the scale. Increasing magnetite precipitate volume fraction was explained by Pickens, 1984. He stated that the magnetite precipitation increases with temperature and is related to increasing proeutectoid decomposition within wüstite at higher temperatures. Sachs and Jay, 1960, stated that it is very difficult to prevent the

decomposition of FeO during cooling when the temperature is above 980°C. This is in agreement with the observation in this study, where magnetite precipitation is lower at lower temperatures, i.e., 750°C, Figures 3.5.9, 3.5.10, 3.5.12 and 3.5.13., but increases above 900°C, Figures 3.5.5, 3.5.7 and 3.5.14. Furthermore, increasing porosity and the formation of fissures and voids with increasing temperature allows more decomposition of wüstite.

The effect of time on the phase ratio was clearer than that of temperature. Figure 3.5.26 shows the oxide phase ratio versus time graph for Alloy A oxidised at 1100°C. As shown, the wüstite volume fraction decreased with increasing time, and at 1100°C wüstite does not appear in the scale, while magnetite and haematite increased with increasing time, occupying the whole scale at 1100°C. This is in agreement with the work by Abuluwefa, *et al.*, 1996 (see Figure 1.2.7), where the magnetite has the highest volume fraction after 3000 seconds while wüstite has the lowest. Kucera and Hajduga, 1998, stated that long times of exposure will lead to complete saturation of the oxide scale. They called complete oxidation where the entire oxide scale is haematite. This is in agreement with the results in this study where the haematite volume fraction increased from 1% at 1200 seconds to 36% at 3600 seconds, see Figure 3.5.26. It should be noted that complete saturation did not occur in this case and magnetite also exists in the scale at 3600 seconds. Gleeson, *et al.*, 2000, claimed that the entire transformation of wüstite to magnetite and iron eutectoid mixture had been observed after holding the sample for 7200 seconds at 425°C. According to Garber, 1959, complete (90 - 100%) wüstite transformation to magnetite took 2400 - 3000 seconds at 800°C. In this study the wüstite completely transformed to magnetite after 3600 seconds, see Figure 3.5.19. It is clear that the longer times can increase haematite and magnetite volume fractions in all studies. Generally, it is agreed that in the absence of a wüstite layer, the haematite can expand inwardly as the iron can be supplied through magnetite layer easier and oxygen from the air, where wüstite has fully transformed to magnetite.

It is not only the oxidation time that affects the phase ratio within the oxide scale, but also the microstructural features influence the ratio, i.e. porosity, fissures, uniformability, adherency, blister formation and most importantly the alloying elements. Figures 3.3.13,

3.3.20, 3.6.21 and 3.3.22 show the effect of blister formation and uniformability of the oxide scale microstructure including the phase ratio. The wüstite volume fraction is higher in the thicker rather than thinner oxide scale areas (see also Figures 3.5.9 and 3.5.10). From Figure 3.3.21, the wüstite phase does not exist in the blistered area, while occupying large areas in the adherent oxide (see also SEM images in Figure 3.3.30). Caplan, 1981, confirmed the fact that at those areas where the scale was still in contact with the substrate, the scale comprised of three layers, but the thickness ratios between the three layers tended to vary at different locations. Due to the expansion of the detached area as a result of blister growth and coalescence, the scale formed after longer times of oxidation comprises of haematite and magnetite, with much less wüstite being present. Caplan, 1981 and Chen, 2001 – 2003, results are in agreement with the present study, see Figures 3.3.21 and 3.3.22. They also showed that at locations where the scale remains in contact, the scale is relatively thick, whereas at locations where scale-steel contact was lost, it was very thin. The iron ions supply is determined as a result of the scale detachment from the substrate, and the wüstite will oxidise at the later stages to form magnetite. The thin layer in the blister, Figure 3.3.21 (c), went through oxygen saturation to transform to magnetite. At those areas where the scale is still in contact with the substrate, the scale comprises three layers, Figure 3.3.21 (b) and 3.3.30 (c), but the thickness ratios between the three layers tend to vary at different locations, Figures 3.3.21 (c) and 3.3.30 (b). The study of blister formation is out of the scope in this study, but it was important to know how blistering can change the phase ratio and other microstructural features in the scale.

It is clear now that it is not only time and temperature that are responsible for phase transformation and ratio variations within the scale, but they also influenced by others factors such as microstructural features. Other factors such as alloying elements, substrate phase transformation, pores, cracks, uniformability and adherency on oxidation rate, phase ratio and other microstructural features are discussed in the following subsections.

4.2.2.b The Magnetite Seam Formation during Oxidation of Low Carbon Steels

Through the same eutectoid reaction in Equation 1.10, the wüstite layer at the metal/oxide scale interface would transform to magnetite. The magnetite precipitates are likely to join together creating a magnetite seam at the metal-scale interface. The nucleation and growth of magnetite precipitates at that interface are discussed in this section. The magnetite seam on IF steel was only observed clearly at 750°C-1200 second and at 1100°C-1800 seconds where the magnetite precipitates did not join together to create a complete magnetite seam at the interface, see Figures 3.5.11 and 3.5.5 respectively. On Alloy A, the magnetite seam is only observed at 1100-1800 seconds, see Figure 3.5.18, whereas, it is not observed at any temperature on Alloy B, see Figures 3.5.20 - 3.5.22.

One of the explanations by Sachs and Jay, 1959, is that after the formation of the gap between the steel substrate and the oxide scale, the oxygen diffuses inward from the outer surface but no iron enters the scale at the interface with the metal. This has two effects: oxidation of iron is interrupted so the scale layer is thinner; and the oxygen content of the scale increases so that the proportion of higher oxides increases and the wüstite is saturated with oxygen. This causes a "sandwich structure", in which wüstite is bordered by magnetite on the both sides. A year later the same authors, Sachs and Jay, 1960, claimed that the iron-rich wüstite is more stable than oxygen-rich wüstite, thus, wüstite decomposition to magnetite near the substrate is highly improbable. This is in agreement with some of the observations in this study as at some temperatures the majority of the magnetite precipitates accumulated in the wüstite upper layer, see Figures 3.5.7, 3.5.8, 3.5.15, 3.5.16 and 3.5.25. However, these are distributed randomly at some temperatures, see Figures 3.5.5, 3.5.11, 3.5.14, 3.5.17, 3.5.21 and 3.5.22.

It is believed that the gap between the scale and metal is necessarily for the formation of a continuous magnetite seam beneath the wüstite later as a main supplier of oxygen for the wüstite decomposition reaction. Furthermore, Barlow, *et al.*, 1965, explained that the separation of the scale from the substrate does not upset the three-layer structure unless the atmosphere can penetrate into the crack; all that happens is a change in the relative

proportions of the phase and saturation of the wüstite layer with oxygen. In practice, however, cracking of the scale often allows oxygen to penetrate into the gap between the metal substrate and the scale. In this way the inner layer of wüstite is enriched in oxygen and the gap surface may even be oxidized to magnetite. However, as in the Figures 3.5.11 and 3.5.18, the magnetite seam is only observed where the oxide scale separated from the substrate.

Those postulations concerning the sandwich structure formation or magnetite seam formation are in agreement with the present observations, where the scale was adherent to the substrate there was no evidence of magnetite seam, see Figure 3.5.8 for IF steel, Figure 3.5.16 for Alloy A and Figure 3.5.20 for Alloy B. However, there is also no magnetite seam in most of the non-adherent oxide scales; see Figures 3.5.9, 3.5.12, 3.5.13, 3.5.14 and 3.5.21. Further observations showed that there is magnetite precipitation within the wüstite, regardless of whether the scale was adherent to the substrate or not. Thus, the effect of the scale/metal adhesion on the phase transformation within the oxide scale is not clear. However, cracks, gap migration and healing processes should be considered in this investigation. The existence of a magnetite seam at adherent scale-metal interfaces relates to the healing process which might take place during the oxidation or cooling process after the magnetite seam formation. Sachs and Jay, 1960, considered that the existence of the magnetite seam at adherent steel scale interface as an indication of the occurrence of a healing process. Theoretically, in the absence of a large amount of oxygen and iron ions, the healing process will not take place and that amount is sufficient enough to form magnetite. However, the magnetite can transform again to wüstite through dispersion of oxygen ions and dilution of iron ions if the sample is oxidised for a longer time. The mechanism of gap migration and healing and related phase changes was explained by Sachs and Jay, 1960. However, these phenomena are very difficult to observe. In this study only the final structures (i.e., after oxidation and cooling processes) of the oxide scale have been investigated.

In general, the phase transformation within the scale is important for descaling purposes. Smuts and Villiers, 1966, claimed that magnetite seam formation is undesirable for mechanical descaling purposes. They also reported that rapid cooling is good to avoid

wüstite transformation to magnetite because mechanical cracking is easier in the absence of the magnetite seam. Other studies preferred the retention of wüstite within the scale for chemical descaling purposes [Tominaga, *et al.*, 1982]. Although the descaling process is not carried out in this study, but its consideration is discussed throughout this chapter.

4.2.2.c The Steel Phase Transformation Correlation with the Oxide Scale Phases

The correlation between the phase transformations in the steel substrate with phase transformation within the oxide scale is not well understood and highly complex. The phase transformation investigation within the steel substrate itself is out of scope in this study, however, it was necessarily to consider it with reference to what is known as the thermal-equilibrium diagram. By reference to that diagram (Figure 1.1), for an alloy of any composition, its structure or physical condition can be determined at any given temperature [Sinha, 1989].

Generally, there were only three important phases to be considered for all the steels studied under these experimental conditions, namely, austenite, ferrite and carbide. Austenite is the solid solution which is formed when carbon dissolves in fcc iron, whilst ferrite is a very weak solid solution produced when carbon dissolves in bcc iron below 910°C. Cementite is a carbide Fe_3C, formed by combination of the carbon with some of the iron [Higgins, 1994].

In the light of the thermal-equilibrium diagram in Figure 1.1, the transformation from ferrite (bcc structure) to austenite (fcc structure) at a temperature of 912°C is possible for IF steel as it is contain very low carbon content of oxygen. Due to the low carbon content (0.0026%C) and other alloying elements in IF steel, only ferrite phase was present in the final structure at room temperature, see Figures 3.2.1 - 3.2.4. Referring to the Figure 1.1., the amounts of 0.1 and 0.17% carbon content in Alloy A and Alloy B, respectively, was sufficient for a pearlite formation depending on the cooling rate during oxidation process, see Figures 3.2.5 - 3.2.10 for Alloy A and 3.2.11 - 3.2.22 for Alloy B. The 0.1% carbon content in Alloy A was sufficient for the formation of a ferrite + pearlite structure, at 750

- 1100 °C. The 0.17%C content in Alloy B could form bainite at 1000°C and martensite at 1100°C depended on cooling rate [Higgins, 1968].

There are many hypotheses with regards to the affect of the steel phase transformation on the oxide scale microstructure including its phase ratio. The close structural relation between γ-Fe and wüstite was claimed by Goldschmidt, 1942, as the atoms occupy the same fcc lattice in both phases. There is a pronounced parallelism between the relative atomic volumes of γ-Fe and wüstite on the one hand and α-Fe and Fe_3O_4 on the other. The expansion associated with the γ→α change seems to be simulated by that occurring during the transformation FeO→ Fe_3O_4 (the α-γ change at 912°C is coupled with the decomposition of FeO at 570°C: $4FeO \rightarrow Fe + Fe_3O_4$). The change from γ→α iron is determined by temperature, the change from FeO to Fe_3O_4 by composition as well as temperature (eutectoid decomposition). It should be remembered that γ-iron is stable above 912°C; wüstite is stable above 570°C. He also claimed that the solubility of oxygen is probably somewhat higher in γ-iron than in α-iron. He also connected magnetite with ferrite as the magnetite is stable at all temperature up to its melting point, and so is bcc iron. His work was confirmed by Sack and Jay, 1959. They stated that it is conceivable that the presence of wüstite influences the γ-α transformation at the surface and that the freshly formed ferrite affects the wüstite produced by the continued oxidation at the interface. Overall, these hypotheses could not be confirmed in this study as only the final structures of the oxide scale and steel substrates were investigated, therefore, the austenite could not be observed. Thus, γ-Fe correlation with wüstite remains only in a theoretical frame. The phase transformation influence on the oxide microstructure needs in-situ investigation rather than theoretical consideration. Tholence and Norell, 2001, claimed that thinner oxides formed on ferrite grains while thicker oxide formed on carbide network on the steel samples. However, his work was on high carbon steel, thus, comparison with this study is not appropriate.

Overall, as discussed earlier the phase ratio determined on IF steel, Alloy A and Alloy B were very similar to that of pure iron. It should be noted that the similarity between iron and low carbon steel oxidation rate and phase ratio are confirmed in many other studies

[Sachs and Jay, 1960, Kofstad, 1966, Kubaschewski and Hopkins, 1967, Chen, *et al.,* 2002, Kucera and Hajduga, 1998, Khanna, 2002, Hauffe, 1965, Tominaga, *et al*, 1982 and Abuluwefa, *et a*l., 1996]. It is clear that there was no pearlite, cementite, bainite or martensite formation in pure iron after the oxidation process. As explained earlier there was a considerable amount of these phases in Alloy A and Alloy B. However, the phase ratios on Alloy A and Alloy B were very similar with that on pure iron. Furthermore, their trend with time and temperature was also very similar. Therefore, it appears that the phases produced through the phase transformation in the steel substrate have limited influence on the phase ratio of the oxide scale on steel. The phase transformation of the substrate and the changes in ferrite grain size affects the oxide grain size as discussed further in the following sections.

4.2.3 The Influence of Oxidation Conditions on the Size and Shape of Oxide Grains

As described earlier, conventional techniques and traditional sample preparation are unable to reveal grain boundaries within the oxide scale. Thus, measuring grain size in absence of reliable techniques such as EBSD is not being possible. Therefore, measuring grain size for each individual phase within the oxide scale relied completely on EBSD grain boundary characterisation and measurements. The most obvious example of the differentiation between grain and phase boundaries by EBSD and optical microscopy can be seen in Appendix 13. It is not uncommon to see such optical micrographs of the oxide scale as in Appendix 13 in many of the published studies on oxidation. As can be seen from the Figures, the phase boundaries are clearly revealed by optical microscopy. However the grain boundaries cannot be seen even when the sample is etched for more than 30 seconds with 1% HCl. EBSD scanning was carried out on the selected area as shown in the same Appendix. The EBSD IQ map reveals the grain boundaries making the measurement of grain sizes easier and more accurate. It should be noted that the linear intercept method was selected for measuring grain size in the TSL-EBSD OIM Analysis software and not the reconstructed grain boundary method as suggested by Humphreys, 2001. As the definition of a grain in OIM can vary depending on user-specified values, the grains separated by 15° angles are accounted and the Grain Tolerance Angle (GTA) used in this study was 3 degree for all the measurements. Moreover, the phases within the

scale are clearly identified as shown in Figures 3.5.9 and 3.5.10. Another problem arose where, due to high concentrated magnetite precipitates in some areas, it was difficult to recognise phase from grains boundaries. The unique capability of EBSD overcomes this problem; hence the grain size measurement could be carried out, see Figures 3.5.14 (c) and 3.5.15 (c), where the phase boundaries are white and grain boundaries red.

Considering grain growth of the phases within the scale and correlating it to the steel substrate grain size, time, temperature, microstructural features such as porosity, crack is a new area because of the limitations of conventional techniques. However, in the light of the theoretical background in the literature and the results in the present study those factors that affects grain size and shape will be discussed it the following subsections.

4.2.3.a The Affect of Oxidation Temperature and Time of Exposure on the Oxide Grain Size

Tables 3.4.1, 3.4.2 and 3.4.3 show the grain sizes of oxide scale developed on IF, Alloy A and Alloy B, respectively, exposed to different temperatures for 1800 seconds. The effect of the oxidation temperature on the oxide grain size is very clear. As shown in Figures 3.4.7, 3.4.9 and 3.4.11, the wüstite and magnetite grain sizes on all the steels increased with increasing temperature. This is in an agreement with Kyung, *et al*., 2000, who claimed that the oxide grain size significantly increases with increasing steel substrate temperature, however, no indication of what phase grain size was given.

The effect of time on the oxide scale grain size on Alloy A formed at 1100°C is shown in Tables 3.4.4 (a) and (b). The wüstite grain size increased in the growth direction until 1200 seconds and then started to decrease, whilst in the transverse direction the wüstite grains grow with time, see Figure 3.4.17 and Appendix 11 (Table 4). The magnetite grains are equiaxed at 600 and 1200°C, and then grow laterally making the shape elongated at 1800 seconds. The magnetite grain shape became columnar where the wüstite phase was completely transformed, allowing the magnetite grains to grow

vertically at ~ 3600 seconds. The same phenomenon was observed for haematite, see Table 3.4.4 (a and b).

The overall conclusion was, as shown in Figures 3.4.13 - 3.4.16, that the wüstite grain size increases with increasing temperature on IF steel, Alloy A and B. The magnetite grain size also increases but less dramatically than the wüstite, which may be why descaling oxide scale at higher temperature is more difficult because less grain boundaries exist in the scale due to enlargement of the grains. It is believed that grain boundaries act as a diffusion path and in some cases, due to internal stress, change to vertical or lateral cracks that help in the mechanical and chemical descaling processes [Birks and Jackson, 1970, Schutze, 1988, Tominaga, *et al*., 1982]. The trend of oxide grain size to increase with temperature and longer time of exposure indicates grain growth. The theory of grain growth can be applied to oxide scale as well as metal substrate. It is believed that at temperatures above that of recrystallisation, the newly formed crystals will tend to grow by absorbing each other. This will results in the formation of a relatively coarse-grained structure, the ultimate grain size depending jointly upon the time and the temperature employed [Higgins, 1994]. The grain growth of the oxide phases with time and temperature also have confirmed by Schmid, *et al*., 2001, using in-situ ESEM experiments.

Theoretically, at high temperatures the grain boundaries in a sample will migrate so as to reduce the total number of grains and thereby increase the mean grain diameter. The haematite and magnetite grain growth is called Normal Grain Growth (NGG) [Porter and Easterling, 1981] where the grain growth was due to increasing the grain boundary mobility at high temperature. The same reference stated that the growth of just a few grains growth to very large diameters is called Abnormal Grain Growth (AGG). These grains then expand consuming the surrounding grains, until the fine grains are entirely replaced by a coarse grained array. This can occur when normal grain growth ceases due to the presence of a fine precipitate array. It seems that wüstite grain growth followed the AGG mechanism as above 900°C the wüstite grain size is very large and magnetite precipitates were distributed across the wüstite layer, see Figures 3.4.1 - 3.4.4 for IF steel, Appendix 9 for Alloy A and Appendix 10 for Alloy B. Whereas, below 900°C the wüstite

grain size increased steadily and followed NGG and magnetite precipitates were significantly less. This could explain the dramatic increase of wüstite grain size above 900°C. The mechanism and types of grain growth are out of the scope of this study but it is important when considering oxide scale growth. It should be noted that there are no reports detailing the oxide grain growth at high temperatures in the literature.

4.2.3.b The Affect of Alloying Elements on the Oxide Grain Size

The effect of alloying elements on grain growth within the steel substrates is well understood. However, the presence of alloying element in the steel substrate and oxide scale and their affect on grain growth of the oxide is not clear. The effects of steel composition on grain size are shown in Figures 3.4.13 - 3.4.16. While on IF steel; wüstite grains grow steadily in the growth direction, a dramatic growth can be seen in the transverse direction at 1000°C, Figures 3.4.13 and 3.4.14. The more dramatic increase at 1100°C in the transverse direction on Alloy A makes the shape elongated. Alloy B did not show any dramatic changes in grain size in either direction. The same phenomenon can be seen in Figures 3.4.15 and 3.4.16 for Alloy A magnetite grains at 1100°C. However, this phenomenon can be related to oxidation kinetics and rates which will be discussed later in this section. Throughout this study an attempt has been made to find any grain size correlation between steel substrate and oxide scale. This assumption was based on many studies in this area. The effect of the grain size and phase transformation within the steel substrate regarding its connections with the oxide scale microstructure is very complex. Caplan, *et al.*, 1981, stated that the $FeO-Fe_3O_4-Fe_2O_3$ oxide scale that formed on annealed or cold-worked, fine-grained iron was uniform, adherent, and thickened with normal parabolic kinetics. Coarse-grained iron behaved similarly when cold-worked, but when in the annealed condition it oxidized more slowly and formed non-uniform, less adherent scales. They connect this to the grain boundaries, as they claimed that the dislocations and grain boundaries suppress cavity nucleation by providing sinks for the cation vacancies arriving at the metal surface and monocrystalline FeO remains monocrystalline as it thickens. Cold worked metal might be expected to oxidize faster than annealed iron because of the many easy diffusion paths provided by the finer FeO grain size. They concluded that the polycrystalline FeO remained in good

contact with the steel substrate, however, this is not observed in this study as wüstite formed polycrystalline oxide and its adherency with the steel substrate is varied, see Figures 3.4.1 - 3.4.6. It appears, that, with the lack of a reliable technique to reveal and characterise grain boundaries, the wüstite appeared as a one big grain in their study and that lead to this misleading conclusion. Furthermore, the influence of finer grains, within the substrate, on oxide grain size is not clear in this study. Thus, their hypotheses on the affect of grain size and grain boundaries on the oxide grain size cannot be proven in this study.

Considering the different oxide grain sizes formed on different phases in the substrate is rather complicated. The IF steel and Alloy B ferrite grain size varied with temperatures as shown in Figures 3.2.23 and 3.2.25, whereas, increased in Alloy A, see Figure 3.2.24. The ferrite grain size in IF steel is bigger than in Alloy A, whereas, Alloy B ferrite grain size is the smallest at all temperatures (e.g. at 1800 seconds, IF steel; 85μm at 650 and 109μm at 1100°C, Alloy A; 21μm at 650°C and 31μm at 1100°C, Alloy B; 10μm at 650°C), see also Appendices 5 - 7. The wüstite and magnetite grain size on Alloy B is smallest, while on IF steel and Alloy A varied and was not very different in either directions, see Tables 3.4.1 - 3.4.3, also Figures 3.4.13 – 3.4.16. This indicates that the ferrite grain size influence on the wüstite and magnetite grain size is not clear, where the IF steel ferrite grain size is bigger than in Alloy A, but wüstite and magnetite grain sizes were similar and varied with temperature. In the absence of any correlation between the ferrite and oxide phase grain size, the study focused on the phase transformation within the steel substrate rather than the grain size. It should be noted that ferrite is the only phase present in IF steel at room temperature due to its very low level of carbon and other alloying elements. However, that was not the case for Alloy A and Alloy B, where pearlite was always present in the final structure at all temperatures, plus bainite and martensite formation in Alloy B above 1000°C. Furthermore, the pearlite colony sizes and volume fraction in Alloy A were bigger than in Alloy B at all temperatures, see Appendices 6 and 7. It is believed that the alloying elements in the substrate have an affect on the phase ratio within the oxide scale. Thus, as explained earlier the phase transformation within the oxide scale has a great influence on oxide grain size and shape. There are a few studies that have considered this aspect. Chen, *et al*., 2003, reported that

higher carbon content in the steels increased the oxidation rate. This is because the magnetite that formed over pearlite had a finer grain size than that formed on ferrite and hence, a higher growth rate. As a result, the average oxidation rate of the alloy was found to increase with increasing carbon content because of the increased volume fraction of pearlite in the alloy. This contradicts with the higher oxide growth of IF steel than Alloy A which contains higher carbon content and also the results from Alloy B which contains the highest carbon content but has the lowest oxidation rate as discussed in Section 4.1. However, the decarburisation that occurred in Alloy B might explain this as the oxide formed only on the ferrite phase as pearlite was absent at the substrate surface. Kucera and Hajduga, 1998, explain this in another way; as they reported that fine-grained scale thicken faster because the oxide grain boundaries act as preferential diffusion paths. They also claimed that pearlite oxidised faster than ferrite because the oxide grain sizes are finer over pearlite. The haematite layer, they reported, is fine grained in all cases and it is thicker where the scale is thin, that is, where the magnetite is coarse-grained, because of the lower diffusivity of iron in coarse-grained magnetite. However, there was no evidence of a different oxide growth on ferrite and pearlite in this study due to the decarburisation that occurred in Alloy A and Alloy B.

4.2.3.c Consideration of Oxide Grain Size Aspect Ratios

One of the important features in high temperature oxidation is the change in the aspect ratio of the grains. This was investigated through calculating the oxides grain size aspect ratio and observing its change with temperature. As shown in Figure 3.4.8 and Appendix 11 (Table 1), the aspect ratio of the wüstite grains on IF steel is ~ 1 only at 1100°C, at the rest of the temperatures the wüstite grain shape was columnar. The magnetite grain shape on Alloy A was columnar at 750°C and becomes equiaxed at 900 and 1000°C, then grows laterally making the elongated shape at 1100°C, see Figure 3.4.10 and Appendix 11 (Table 2). As shown in Figure 3.4.10 the aspect ratio value decreased with increasing temperature, which indicates that the grain shape changes from columnar to equiaxed to elongated with increasing temperature. The aspect ratio of wüstite grains on Alloy B were larger than 1 at all temperatures, see Figure 3.4.12, which indicates that the shape of the grain is columnar, see also Appendix 11 (Table 3). The magnetite grain aspect ratio was

~ 1 only at 900°C. The grains then started to grow laterally becoming elongated in shape at higher temperatures.

Carpenter, *et al.*, 1973 investigated the oxide scale microstructure using optical and scanning electron microscopy. They came to the conclusion, after experiments on low carbon steel, that haematite has an equiaxed grain structure, magnetite is columnar and wüstite due to magnetite precipitation is not clear but looked to be columnar. However, throughout this study different ideas about grain shape of the oxide phases have been obtained by EBSD as it is considered as an important tool for quantitative metallography [Randle, 2005]. As a first example, haematite was detected by EBSD at 1100°C on IF steel and Alloy A which consists of multigrain of varying size and shapes as shown in Figure 3.4.3 (a). The haematite, like the other phases in the oxide scale, consists of multiple grains which are equiaxed, columnar or elongated; see also Appendix 11 (Table 4). This is not consistent with the work of Caplan, *et al.*, 1981, who claimed that the haematite layer consisted of one thick grain at the top of the oxide scale or with Carpenter, *et al.*, 1973, that haematite exists only in equiaxed grain shape. However, the author of this study believes that the grain shape depends on the conditions of the oxidation process, i.e. time and temperature for all the phases on the steels and not only on the crystal structure. The oxide grain shape development with temperatures is not well understood as it is related and affected by many factors such as oxidation rate, stress development, oxidation conditions and microstructural features within the oxide. Initially the oxide scale grows as the result of competition between growing grains making the grain shape columnar rather than equiaxed. As can be seen at low temperature, the wüstite grains have a columnar shape at 750 to 1000°C for IF steel, and then grow further in the transverse direction making the shape equiaxed at 1100°C. The more dramatic growth in the transverse direction on Alloy A make the shape elongated, see Figure 3.4.10 and Appendix 11. As the rate of oxidation is parabolic, the rate of growth of the oxide scale decreases with time. At this point the grains will grow in the transverse direction not in the growth direction. As the grain growth continues due to increasing temperature or time the only direction for the wüstite grains to grow is the transverse direction. The same phenomenon can be seen for magnetite grains. This can be observed clearly in Figure 3.4.17 and Appendix 11 (Table 4). The wüstite grains grow faster in the

growth direction than in the transverse direction at 600 and 1200 seconds. At 1800 seconds the shape becomes elongated where the oxide growth slows down, thus, the wüstite grains grow laterally (in the transverse direction). The magnetite grains are equiaxed at 600 and 1200 seconds, through the same mechanism by which wüstite is changed to elongated shape at 1800 seconds. At 3600 seconds, the complete wüstite transformation to magnetite allows the magnetite and haematite layers to grow in the growth direction as described earlier. Thus, the shape of magnetite and haematite grains changes to columnar at 3600 seconds in the absence of the wüstite layer. Therefore, it is not only the oxidation rate and oxide scale thickness that affect the grains, but also the phase transformation within the scale plays a vital roll in the oxide grain shapes.

It is clear now that the oxide grain shape is affected by oxidation conditions such as oxidation temperature and time of exposure. Furthermore, the microstructural features within the oxide scale can influence the grain size and shape to some extent. Kofstad, 1966, reported that the columnar grain shape of oxide scale developed as a result of competition between grains during the oxidation process. Moreover, the author of this study believes that cracks and porosity also affect the grain shape. Any assumption as to the effect of cracks and pores on the grain shape should consider whether the cracks and pores are formed during the oxidation processes or the cooling period. Currently, the microstructure images obtained from EBSD can only reveal the final stage of the oxidation after cooling is completed. Thus, it is very difficult to determine when the cracks and pores are formed, moreover, how they affect the microstructure development of the oxide scale. In the absence of a suitable technique to monitor the oxide development during the oxidation process, only morphology observations have been reported during this study regardless at what stage the pores and cracks have formed. As shown in Figures 3.4.4 (d) and 3.4.6 (a), the grains near the cracks are more columnar than equiaxed. This could be explained by accumulating oxygen in the crack which promoted further oxidation of the area beside the crack which makes the grains grow alongside the crack direction, making their shape columnar. This assumption is only valid if the crack is considered to have formed during the oxidation period. Porosity has a different affect on the grains' shape. It has been noted that the grains surrounded by pores in all directions, are more equiaxed than columnar. In some areas within the scale pores

are distributed around some grains. This can be explained by the accumulating reactant gas around the grains causing equal growth in all directions. Whilst, the grains which were bordered by pores on only one side look rather columnar and in this case pores have the same affect as cracks on the grain shape, see Figures 3.4.1 (c), Appendix 9 (F and G).

Overall, it is clear that the grain size and shape are affected by many factors during the oxidation process including time, temperature, oxidation rate, microstructural features, and phase ratio. As well as these factors, it is not clear as to whether the substrate grain size and phase transformations, porosity and cracks within the scale or adherency affect the scale. However, there are other factors which have not been considered in this study, such as sample geometry, oxidation environment, oxygen partial pressure which also affect the grain growth of the oxide scale. Due to the large number of the factors that might affect the oxide grain growth directly or effectively, the study of this aspect is very difficult unless further techniques are utilised.

4.2.4 Porosity Measurement

There is generally contradictory and inaccurate data of oxide scale porosity measurements in the literature. It is not uncommon in the open literature that some scale structures are presented with preparation damages, which in some cases were treated as porosity in the scale, and explained in great depths of their fundamental mechanism of formation, these example can be seen in [Hussey and Graham, 1981, Abuluwefa, 1997, Caplan, *et al*., 1978 and Tuck, *et al*., 1979]. It is related to the fact that the scale is brittle and metallographic sample preparation is difficult and time consuming. In some studies the porosity and grain pull out during sample preparation were referred to as fissures without referring to the differences in physical appearance between them [e.g., Pickens, 1984]. As shown in Figure 2.2, the artefacts generated during sample preparation decreased through the polishing procedures without being eliminated entirely. Effort was made to eliminate the artefacts entirely, but increasing the time of polishing caused secondary problems as explained in Section 2.2. This problem was addressed by Chen, *et al*., 2005, however, without providing suitable experimental solution in this regards. Furthermore, measuring porosity requires high magnification images of the oxide scale,

which makes statistical accuracy of the measurement much more difficult as the porosity concentration is different from one area to another. The large number of samples oxidised at different times and temperatures made the task of collecting accurate data which can be accepted statistically impossible. The problem further arises when the porosity differs across the normal direction of the cross section, i.e., the porosity at the top of the cross section surface is different from the porosity below the surface. In other words, measuring porosity in two-dimensional areas does not give accurate and adequate porosity concentration data. In this study the porosity influence on the microstructural features within the oxide scale is considered rather than its concentration. However, the same problem remains to differentiate between pores and polishing artefacts. Any microstructural feature changes such as phase changes, grain size and shape or oxide layer thickness which occurred near what were thought to be pores have been considered. The porosity influence on oxidation rate and kinetics, grain size and shape, phase ratio and phase transformation is discussed throughout this chapter as well as those factors which might influence porosity formation and concentration.

4.2.5 The Consideration of Uniformability of the Oxide Scale and Its Affect on Other Microstructural Features

The non-uniform oxide scale formation on steel substrate is not well understood. There are many hypotheses regarding its occurrence and affect on the many microstructural features of the oxide scale. The main factors that are responsible for non-uniformability of the oxide scale on steel substrates are not clear. The surface quality, alloying elements, time, temperature and oxidation environment are the main considerations reported in the literature. As the optical micrographs shown in Figures 3.3.1, 3.3.2, 3.3.8, 3.3.13, 3.3.20 and 3.3.22, the oxide on IF steel, Alloy A and B is not uniform at some oxidation temperatures and times of exposure. It should be noted that the majority of the oxide at high temperatures (i.e. above 900°C) were uniform. Most of the oxide scales on all the three type of steels used in this study were not uniform at lower temperatures, i.e., under 900°C.

For the oxide scale to be uniform and remain intact during the course of the oxidation the chemical equilibrium between the oxides must be maintained. However, if oxygen has access to the lower layers of the oxides, through porosity and cracks within the scale, the relative growth rates are then controlled by the local equilibrium [Abuluwefa, *at al.*, 1996]. Therefore, various phases at random locations within the scale can exist, giving rise to the faster growth of the higher oxides with their proportions depending on the accessibility of oxygen to the various reaction sites. Sachs, *et al.*, 1968, suggested that a small amount of impurity from the steel substrate might inhibit dislocation movement in the scale, favour the formation of a series of micropores or gaps at the steel-scale interface and as a result reduce the iron flux crossing the interface. Other studies [Caplan, 1979] observed a thin layer of graphite at the scale-steel interface at some steel surface locations during oxidation in the range of 600 to 800°C which might lead to the non-uniform scale. However, the most probable postulation is in the early stage of oxidation the scaling rate is so rapid that the vacancy-annihilation processes could not take place with the vacancy-generation processes. As a result, a larger number of the vacancies were left at the scale-steel interface, eventually causing localised scale-steel separation at the later oxidation stage through a vacancy condensation process [Chen, *et al.*, 2001].

The uniformability of the oxide scale may also be connected to the sample geometry. The oxide scale at the edges and the corners is thinner and some phase transformations take place due to their accessibility to oxygen. However, cooling rate influences the phase ratio and structure at the edges and corners as described earlier. This can explain the phase changes and different oxide thicknesses at the edges in the sample in Figure 3.3.22. The phase ratio at the edge on the sample clearly changes with distance from the edge. Furthermore the thickness of the oxide at the edge is much smaller than in the centre of the sample. Chen, *et al.*, 2001, reported and confirmed again in 2003 that because of the presence of oxygen at the edge region, the unstable wüstite layer will gradually be oxidised to magnetite during cooling (Equation 1.9) or where the temperature is very high forming magnetite and haematite, e.g., above 720°C. Chen, *et al.*, 2001 and 2003, reported that the oxides at the edges were thinner than in the centre of the steel plate or strip. Because of the access of ambient air to these regions, the haematite layer is always present at the edges and continues to grow, depending on cooling rate.

The phase ratio and thickness changes at the edge, as in Figure 3.3.22, are explained by different mechanism by Kucera and Hajduga, 1998. They stated that when an iron atom is transferred from the metal into the oxide, oxide formation takes place at the external surface and metal vacancies are left behind at the metal/scale interface. The adherence of the scale to the metal is retained by plastic readjustment of the oxide scale. Since wüstite exhibits plasticity an adherent compact scale can be observed. However, in many cases, voids and cavities, caused by vacancy condensation, are formed. This feature becomes pronounced above a certain thickness, which is dependant of the exposure condition, the shape and the grade of the steel specimens. A critical degree of vacancy super-saturation at the metal/scale interface is required to account for the condensation of voids. This degree of super-saturation is approached more easily near the edges of the specimens where the curvature of the scale restricts the plastic flow of the wüstite. When these cavities enlarge to a distinct blister, oxygen can possibly be transported across a scale. The voids and vacancies formation and condensation is more probable the cause of different thicknesses of the oxide scale at the edges and corners seen in this study. However, the first mechanism could explain the phase ratio changes at the edges due to accessibility of oxygen.

At the early stage of this study, it was thought that the grain boundary misorientation may affect the uniformability of the oxide scale on the steel substrate. Therefore, a complete grain boundary characterisation was preformed in order to see whether the grain boundaries in the thin areas differed from the thick areas. The general microtexture analysis through IPF//GD and ODFs for each phases are discussed in Section 4.3. The grain boundary misorientation can be seen in Figure 3.6.25 (b). Most of the wüstite and magnetite grain boundaries are high angles. More individual analysis was carried out for most of the grain boundaries in the scan areas. As indicated in Figure 3.6.25 (b) there was no major differences between the grain misorientations of the thinner and thicker areas. Cropping small oxide thickness area from the rest of the scan area as well as the large thickness area gave the same results. Therefore, relating grain boundary misorientation at different location of the scale with the uniformability of the scale on the steel surface did not lead to any solid conclusion.

4.2.6 Investigation into the Crack Initiation within the Oxide Scale on Steels

The crack initiation and progress are described in Section 1.2.9.6. The study of oxide scale microstructure must consider crack investigation because cracks can influence the mechanism of the oxide development and its growth rate depending on the crack types and initiation time. It is imperative to know the initiation time of the crack in the scale to investigate its effect on the mechanism of the scale development. A crack is observed after complete oxidation and cooling procedures, Figure 3.3.10. As the final structure of the scale was investigated, it is not clear when this crack formed and developed. EBSD can give clarification of the initiation of those cracks through misorientation analysis and orientation map. As shown in Figure 3.6.12, the vertical crack was of interest and investigated with a view to determine whether it is an intergranular or transgranular crack. As can be seen from the same figure, the orientations before and after the crack were the same, indicating that the crack is within one grain and hence a transgranular crack. As the mechanism of crack initiation described in Section 1.2.9.6, most of the cracks in the oxide scale should be intergranular as the grain boundaries act as diffusion paths and depending on the range of internal stresses and thermal expansions the boundaries create micro-channels and then cracks. Thus, there is less probability of the formation of transgranular crack within the oxide scale. As suggested by Gourgues, 2002, random grain boundaries are highly sensitive and coherent grain boundaries are most immune to brittle cracking. As described in Section 3.6 and discussed later in this Chapter, the majority of the grain boundaries within the oxide scales are high angle and are expected to form cracks. The cracks found in this study were transgranular, indicating they are not formed during the oxidation process but were created during cooling and sample handling. Except for the samples in Figures 3.6.12 and 3.4.4, all the other samples were free from vertical cracks. Hidaka, *et al*., 2003, stated that the probable reason for finding an oxide scale without cracks might be due to extremely pure grain boundaries, which may have minimised grain boundary fracture. It is not clear, however, what exactly the authors in that study mean by pure grain boundaries. It may be that the magnetite precipitation on the wüstite grain boundary may improve the crack resistance of the wüstite layer. Figures 3.5.14 (c), 3.5.15 (c), 3.5.17 (a), 3.5.18 (a) and 3.5.22 (b) show some examples of magnetite precipitation on the grain boundaries in support of this

theory. As Gourgues, 2002, explained grain boundary segregating species or precipitation can be beneficial to the resistance to intergranular cracking. However, they may increase the possibility of transgranular cracking.

Lateral cracking was found in some oxide scales on IF steel, Alloy A and B, see Figures 3.5.13 and 3.5.20. These lateral cracks could have a significant affect on the oxidation rate and oxide growth. It is believed that vertical cracks work as a short circuit for iron and oxygen ions diffusion through the oxide scale, but when a lateral crack forms, it works as a barrier, which would inhibit the diffusion between the surface and the outer layers of the scale. Tominaga, *et al*., 1982, reported that cracks inevitably form due to differences in thermal contraction between the iron base and the scale upon cooling, i.e. internal residual stresses. The amount of these stresses depends on whether a transformation takes place or not. The condition of the crack formation depends on the scale thickness, scale strength, and other factors such as cooling rate. The number and interval of such cracks are important factors for the descaling process. There are many sources for developing stress in oxide scales. As Birks, *et al*., 1983, explained one of them is haematite growth. As mentioned in the literature review haematite is an n-type semi-conductor, when the oxygen diffuses inwardly to the metal surface, and reacts with iron ions at the magnetite/haematite interface, the haematite will form a new oxide which expands against the resistance of the existing layer, stress develops and eventually leads to eruption of the film. Nagl, *et al.*, 1993, classified the sources of stresses as oxide growth stresses and thermal stresses. Growth stresses arise mainly from the volume change during formation of the oxide. Grosskreutz, *et al*., 1969, showed that the most common sources of stresses in oxides are thermal stresses due to cooling/heating or thermo-cycling as a result of differences in thermal expansion coefficients of metal and oxide. Thermal stresses are also induced under thermal shock conditions or when the heat flow is removed. Similarly the substrate geometry can cause stresses, in particular at corners.

4.3 The Oxide Scale Layers and Steel Substrate Microtexture

   Correlations

The role of texture in improving high temperature oxidation and corrosion resistance is essential [Szpunar, 1999 and Hualong, *et al*., 1999]. An understanding of the oxide texture formation is therefore critical to the understanding of how and to what extent the oxide film can protect the alloy from further oxidation during processing and in service. It is believed that the substrate texture has an affect on the oxide nucleation and its growth, kinetics, microstructure and mechanical properties through its affect on the oxide texture. Sewell and Cohen, 1964, studied the oxidation of iron single crystals at ~ 200°C by means of electron diffraction, electrochemical, and gravimetric methods. They found that both the oxide composition and thickness was highly dependant on the iron crystal orientation. The effect of the steel substrate texture on the oxide texture has not been studied extensively, most studies so far have been carried out on other metals, such as nickel and copper.

It would be obvious to suggest that the substrate grain orientation must influence the orientation of the oxide scale grown on its surface. But how far this correlation is valid at all temperatures, times and oxidation conditions and to what extent it would affect the oxidation rate and kinetics and the microstructural features of the oxide scale, has not been studied in great detail. In the absence of a reliable technique to fully investigate the microtextural development of the oxide scale, some attempts have been made as mentioned in Section 1.2.10 without studying a full range of oxidation temperatures and times. Most of the studies investigate the microstructure only on one or a few samples. In this study great efforts have been made to investigate the microstructure correlation over a wide range of temperatures and times.

The idea of establishing a texture relationship between steel with its oxide is not universally accepted as for grain orientations, e.g. Kim, *et al.*, 2001. However, a different approach of studying microtexture correlations has been followed here. The factors that affect texture development in the oxide scale should be considered fully before making any conclusion in this regard. Those factors such as steel composition, temperature, time,

sample preparation, oxidation condition and microstructural features in the steel substrate and oxide scale are highly important and may change the whole mechanism of texture development. The current studies have shown that there is a crystallographic texture correlation between the oxide and substrate depending on the factors mentioned above. Also individual microtexture analysis was carried out for each phase within the scale and the steel substrate to find more aspects of the involvement of the microtexture evaluation. This approach is in agreement with that of Corkovic, *et al*., 2004, as they stated that the texture of the oxide layers on polycrystalline specimens in general depends on a multitude of factors such as the grain size of the substrate, surface roughness, surface geometry, local chemical concentration, precipitation state, as well as the temperature and time. Thus due to favoured directions of crystal growth, the texture of the oxide layers differ significantly from those expected from epitaxial growth. Their results, obtained using EBSD, showed that the {100}-fibre texture was observed for wüstite and magnetite at 950°C and the texture strength increased with increasing time. They claimed that the time was the biggest factor for developing fibre texture for both the wüstite and magnetite layers at the same temperature.

It is believed that the strength of the crystallographic texture within the scale increases as the oxidation temperature increases in a low carbon steel [Higginson, *et al*., 2003]. This is in disagreement with the investigation for IF steel where the texture strength of the phases varied with temperature and that there was no trend with temperatures, see Figure 3.6.21. The texture correlation between the phases is shown in Table 3.6.3. The texture correlation between the oxide phase layers is stronger than that with the steel substrate. The wüstite and magnetite are texturally correlated at 650, 750 and 1000°C. This is in agreement with previous work on a similar alloy by Higginson, *et al*., 2002. They showed that at 760°C there was a texture correlation between the wüstite and magnetite layers. The texture components in iron, wüstite and magnetite differ with temperature, see Table 3.6.2. This is in disagreement with Kim, *et al.*, 2001, who claimed the wüstite and magnetite have cube texture regardless of the texture of the steel substrate. These disagreements with Kim, *et al.*, 2001, about texture component and texture strength correlation with temperature are valid for Alloy A and Alloy B as well, see Tables 3.6.5 and 3.6.8. But there is agreement with Higginson, *et al.,* 2002 about the texture

correlation between the oxides phases with increasing temperature. As shown in Table 3.6.4 and Figure 3.6.22, the wüstite and magnetite texture strength increased with increasing temperatures on Alloy A. However, this was not the case for the substrate texture. There is always a wüstite-magnetite, wüstite-haematite and magnetite-haematite textural relationship at all temperatures.

Kim, *et al.*, 2001, claimed that certain elements such as carbon and silicon in low carbon steel may distort the orientation relationship, but their role is not significant. However, it was very difficult to prove the validity of those hypotheses in this study. As explained earlier, the steel phase transformation affects on the phase transformation within the oxide scale is not clear, also its affect on texture correlation is much more complex. As discussed earlier, the steel composition and microstructural features affect the phase ratio within the oxide scale, which in turn changed the grain size and migration of the grain boundaries. However, this particular consideration would require a very high magnified scan area on individual samples or in-situ experiments are needed. The strength of the steel substrate crystallographic texture correlation with time and temperature is not clear. Also the effect of the phase present within the substrate on the substrate texture strength is not clear. For example, where only ferrite is present in IF steel, see Figures 3.2.1 - 3.2.4, the texture strengths fluctuate with increasing temperature, see Figure 3.6.21. Also, the carbide segregation and decarburisation that occurred within Alloy A did not affect the texture strength; see Figures 3.2.5 - 3.2.10 and the graph in Figure 3.6.22. Moreover, the ferrite grain size increase with temperature did not appear to have any affect on the texture strength; see also Figure 3.2.24. It should be noted that the texture strength for Alloy A substrate is constant at all the times of oxidation exposure, see Figure 3.6.24. The only change observed is where the bainite was present in Alloy B at 1100°C, see Figure 3.2.21, as the texture became very weak. This can be explained as the bainite formation changes the structure of the steel substrate making the orientation of the grains random and weak. However, the effect of the phases present within the substrate on the texture strength of the oxide layers is not clear as the haematite and magnetite textures remain constant and wüstite strengthened, see Figure 3.6.23. It can be suggested that the oxide scale separation from the steel substrate may reduce the affect of the phases present within the steel substrate on the oxide scale microtexture, for example see Figure 3.6.20.

Also the strong relationship between the phases at that temperature (1100°C) can be seen, see Table 3.6.9. This is in agreement with Hauffe, 1965 and Kofstad, 1966, where they stated that the oxide scale orientation is affected by the substrate orientation at the early stage of the oxide nucleation and growth. Thus, later bainite formation may have no an affect on the oxide scale orientation. Therefore, the effect of the oxidation temperature and time appears to be a much greater influence than the phase present within the steel substrate on the texture strength and their correlations.

The overall phase microtexture correlation with temperature and time are shown in Tables 3.6.3, 3.6.6, 3.6.9 and 3.6.12. The phase's correlations increased with increasing times and temperatures. However, this trend was not observed fully for the IF steel. As far as the author of this study is aware there is no explanation in literature about the texture correlation strengthening between the oxide phases at evaluated temperature. Smuts and Villiers, 1966, realised that longer heating of the steel plate does not alter the composition of the scale but results only in the orientation of the various oxides with their (001) planes predominantly parallel to the surface of the plate. However, they did not explain why the increasing time and temperature encouraged the oxide on the plate to grow in that particular direction. It would be safe to suggest that increasing time and temperature will allow the phases within the oxide scale to be oriented similarly towards a particular direction as phase transformation and further atomic arrangement is more likely to occur.

There have been a few attempts to investigate the oxide microtexture correlation with microstructure. Kim, *et al*., 2001, carried out some experiments on commercial low carbon steel oxidised at 950°C in air characterised using EBSD. They showed that wüstite could be characterised as having a columnar cellular structure and the grains of magnetite showed a cell structure. Small wüstite grains were observed close to the substrate where more equiaxed grains were formed in the early stages of nucleation. Those grains were textured. In this study the grain size correlation with orientation and its location within the scale substrate have been studied through superimposing Image Quality onto orientation maps for each sample. As IPF//GD for all the samples of IF steel Alloys A and Alloy B, is shown in Section 3.6, no specific orientation were found to be

related to the size of the grains. The grain orientations are distributed randomly within different grain sizes in all the three oxide layers. Furthermore, the misorientation angles between the grains from each individual layer as compared to Mackenzi plot were distributed randomly regardless of their size.

It is important to know where the major components concentration in the steel substrate and the oxide scale layers in order to ascertain if there is any orientation relationship at the steel-oxide scale interface. Furthermore, most of the studies reported that if there is correlation between the substrate texture and the oxide scale, it would be only between the connected layers and the substrate [Kofstad, 1966, Kubaschewski and Hopkins, 1967, Hauffe, 1965]. In the light of the literature it might be expected that the grains on the steel surface have strong orientation correlation with the innermost grains of the oxide scale. This has been investigated by considering the misorientation between the grains at the interface and highlighting the major texture components in each phase, an example is shown in Figure 3.6.8 (c). Individual orientation analysis carried out for the grains at the top surface of the substrate and the inner most grain of the oxide, showed no strong relationship. A relationship between the phases exists when considering the overall ODFs, however, the major texture components in iron, wüstite, magnetite and haematite are distributed randomly across the sample. Overall there is weak orientation correlation between the grains at the metal-oxide interface whether there was a texture correlation between the phases or not. Furthermore, the gap between the steel substrate and oxide scale did not change this fact, i.e., the same observation was seen whether the oxide scale was adherent to the steel substrate or not, see Figures 3.6.2, 3.6.12, 3.6.18, 3.6.20 and 3.6.25. This can be confirmed by showing individual Reconstructed Diffraction Pattern (RDP) and Discrete Pole Figure (DPF) in any grains or points of interest. As shown in the Figure 3.6.2 different grains in steel substrate (points 1 and 3) have different orientation as shown in RDP and DPF 1 and 3. Furthermore, a larger sample area was scanned, see Figures 3.6.8 and 3.6.9 respectively, and the same conclusions have been obtained.

The geometry of the sample was also considered as to whether it had any effect on the orientation of the oxide scale grains. Figure 3.6.26 shows an oxide scale formed on Alloy A at 750°C-1800 seconds. It appears that the grains from both sides of the sample are

oriented randomly without preference to any side of the sample. The oxide scale grains on both sides of the green grain (101//GD) in Figure 3.6.26 are orientated randomly around it regardless of their location. It appears here that the geometry of the sample therefore has little effect on the crystallographic orientation.

Higginson, *et al.*, 2002, concluded that there appears to be a correlation between the porosity of the scale and the preferred orientation of the oxide layers, i.e. as the porosity decreases the strength of the orientation in the scale layers increase (the lower the porosity the stronger the texture). This could not be proved in the current study. The affect of pores and cracks on phase ratio and grain size are discussed earlier, however, their effects on grain orientation was not clear, see Figures 3.6.1 - 3.6.20. Also increasing and decreasing porosity with time and temperature could not be confirmed in this study.

Further consideration of the adherence between the steel substrate and the oxide revealed that the gap between substrate and the oxide layers did not have any affect on the oxide grain orientation. For example, Alloy A at 1100°C-1800 seconds shows that the all the phases have a strong cube texture even though the oxide is not adherent to the substrate surface, Figure 3.6.16 and Appendix 9 (F). While at 900°C there is no texture relationship between the steel substrate and the oxide scale, the oxide layer is adherent to the substrate surface, Figure 3.6.11. At 750°C and 1000°C, Figures 3.6.10, 3.6.12 and 3.6.13, a texture correlation between the phases exists whether the scale is adherent to the substrate surface or not. The miscorrelation between the gap and the texture is related to the fact that development of texture in the oxide scale layers is started at an early stage of oxide nucleation and growth. Thus, later separation of the oxide scale from the substrate may not influence the oxide grain orientations. This result agrees with the work of Kofstad, 1966, who discovered that the orientation of the oxide started from whisker development on the substrate surface, or at the initiation of oxide scale formation. However, this does not agree with Kim, *et al*., 2001, when they claimed that the relationship between substrate and oxide orientations become weaker when an oxide grain nucleates and grows away from the substrate. In fact, at 1100°C the gap between the substrate and the oxide scale is highest than at all other temperatures, but it has the strongest orientation relationship, whereas at 900°C, the minimum gap can be seen and

the weakest orientation relationship exists. The same results were seen for Alloy B and IF steel. Morawiec, 2000, also confirms this, as he indicated that the orientation selection sets in at a very early stage. Thus, the gaps formed latterly have no or very little affect on the orientation of the oxide grains.

From the Figures in Section 3.6, the magnetite precipitates have the same orientation as the wüstite layer at all temperatures and times of exposure on all three types of steel used in this study. This is shown and indicated in IPFs and OFDs, Figures 3.6.1 and 3.6.2. As expected the misorientation angles between the magnetite precipitates and wüstite layer are very low, see Figure 3.6.25 (a). However, magnetite precipitates are separated from wüstite grains in the Unique Grain Colour map because of the difference in phase as can be seen in Figure 3.4.2 (c). These results lead to the conclusion that wüstite transformation to magnetite during cooling occurs without a change in orientation. Therefore the magnetite is separated from surrounding wüstite grains by very low angles boundaries. This is in agreement with Goldschmidt, 1942, who claimed that there is a close connection between the three phases' structure (iron, wüstite and magnetite), which are all cubic. While the transition $Fe \rightarrow FeO$ is considered as a true oxidation, the change $FeO \rightarrow Fe_3O_4$ is not, because the number of oxygen ions per crystal volume remains constant, only iron ions being lost. From the current work it is believed that segregation of crystallites Fe_3O_4 from primary FeO may well take place without causing a physical disruption. Supporting this assumption is that the orientation of wüstite and magnetite precipitations were the same or very similar. This magnetite and wüstite correlations were fully explained by Goldschmidt, 1942, as he proved that α-Fe forms FeO or Fe_3O_4 by the gaining of oxygen and loss of iron atoms, while FeO forms Fe_3O_4 by loss of iron atoms only. Thus, the relation between FeO and Fe_3O_4 is founded on a mechanism of atomic movements and a fundamental relation between the FeO and Fe_3O_4 structures exists. Starting from the ideal composition FeO of fully occupied lattice points, the wüstite lattice loses iron atoms, until the sodium chloride type of structure becomes unstable. With more oxygen an atomic rearrangement takes place (changing to magnetite), which does not alter the cubic symmetry or the basic framework of the structure. Therefore, it is not surprising that the grain boundaries between wüstite and

magnetite precipitates were coherent grain boundaries as indicated in individual misorientation analysis and IPF//GD, see Figure 3.6.2 and 3.6.25 (a).

Overall, the affect of time, temperature and microstructural features on texture correlation between the oxide scale and steel substrate have been investigated. However, other factors that affect oxidation rate and related microstructure development of oxide scale should be considered as well to obtain solid conclusions about texture interconnection. The multifactor influence of the oxide scale growth on steel, ultimately has an affect on the texture correlation. Factors that may cause uncertainty of oxidation rate and growth outcome, as explained in this chapter, might affect the orientation interconnection between the phases to some extend.

4.4 Oxide Scale Grain Boundaries and Misorientation Considerations

Randle, *et al*., 2003, stated that the orientation analysis should be combined with misorientation analysis to give a full description of the microtexture of the material. The orientation of the grain boundaries (misorientation) within the oxide scale and the substrates are important to the investigation of many aspects of the oxidation process such as diffusion through grain boundaries, uniformability of the scale, and phase transformation. The importance of grain boundaries in oxide scales is well reported in the literature but without real investigation into misorientation in great detail. As Kofstad, 1966, stated the grain boundaries represent regions of lattice mismatch and disorder, which, in turn, cause enhanced diffusion. Further influence of the grain boundaries on oxidation processes is that vacancies move towards and condense at the grain boundaries and that, due to chemical and potential gradients [Carpenter and Ray, 1973], have a significant affect on oxidation rate. Kofstad, 1985, demonstrated the formation of micro-channels from grain boundaries. As he illustrated in detail, the oxide grain boundaries might be opening up during oxidation to form small micro-channels which allow a sufficient amount of oxygen to diffuse inwardly to the metal surface, hence affecting the oxidation mechanism and rate. This illustrates the importance of studying grain boundaries in the oxidation process. Some of these aspects have already been discussed

in the previous sections in this chapter and more mesotexture considerations are discussed here.

The misorientation analysis has been carried out for all the samples. Due to space restrictions only a few examples are shown in this report. The IF steel oxidised at 1100°C for 1800 seconds are discussed here as an example of this analysis. The misorientation angles between iron and the magnetite seam layer is much higher than the misorientation angles between the iron substrate and wüstite layer, see Figure 3.6.25 (a), note the dark blue highlighted points, however, that was not the case in all of the areas. The differences were wider where the magnetite seam grains had a bigger misorientation difference with the wüstite grains. This is probably where the temperature was high enough to allow wüstite decomposition to occur faster and the magnetite precipitates to grow and join together at the interface, hence separated by higher misorientation angles with the wüstite matrix. The magnetite phase boundary misorientation with the wüstite layer (red points) was high ~ 59.8, but low with the haematite ~ 15° (green points). The magnetite/wüstite and magnetite/magnetite precipitates grain boundary misorientations (red points) were very close (59.8° and 52.7°, respectively). It is expected that the magnetite layer will have a bigger misorientation angle with the wüstite layer than the haematite layer as the growing direction of magnetite is inward at the expense of the wüstite layer. As Kofstad, 1966, stated that the grain growth is not same on all surface areas, different directions might cause different rates of growth of the scale. When multilayer oxide scales form; wüstite, magnetite and haematite, the sequence of interfaces and the difference in growth rate mechanism of the different layers may have deleterious effects on the microstructural features and could lead to cracks between the layers.

It is expected that the magnetite grains within the magnetite layer have high misorientation angels, because it has a weak texture, see Figure 3.6.1 (c). Haematite grains have very low misorientation angles whereas they have very strong texture as indicated in ODF maps, see Figure 3.6.1 (e). The grain boundaries are also influenced by the phase ratio, grain size and shape as discussed in previous sections. Thus, the types, migration of the grain boundaries and misorientation variations were also affected by microstructural features within the oxide scale.

The magnetite precipitates' misorientation angles were very low (0.5 - 2°) with the wüstite matrix and appear to have coherent grain boundaries. The magnetite precipitates can grow without increasing the misorientation angles with the wüstite matrix, thus the small or large magnetite precipitates have very similar misorientation angles with the wüstite matrix. See Figure 3.6.25 (a) for some individual misorientation analysis carried out for small and large magnetite precipitates. This is further confirmed by Gleeson, *et al.,* 2000, as they stated that the kinetics of Fe_3O_4 precipitation are not controlled by diffusion in the FeO matrix but by the motion of the coherent FeO/ Fe_3O_4 interphase boundary.

The magnetite and wüstite phases are not always separated by high angle grain boundaries as previously discussed. For example, the magnetite and wüstite layers are separated by very low angle and coherent phase boundaries at 900°C-1800 seconds, see Figure 3.6.11 (a) and (b). In order to double check this result, more individual analysis was carried out. The two points indicated in Figure 3.6.11 (c) have the same orientations; one of the points was taken from wüstite side and another from the magnetite side. This indicates that the yellow colour coded grain in IPF//GD are correct, see indicated area in Figure 3.6.11 (a). The phase boundary at that area is very coherent which is why it does not appear in Figure 3.6.11 (b). This may be related to the absence of the haematite layer on this sample where the magnetite layer is in direct contact with the environment and could grow outwardly rather than inwardly as in the previous sample. Thus, the internal stress between the wüstite and magnetite layer is much less because the two phases might be growing in the same direction. As discussed previously the magnetite intermediate layer can grow outwardly or inwardly. Where haematite is an n-type (anion deficiency semi-conductor), wüstite is a p-type (cation deficiency semi-conductor) and magnetite can be a cation or anion deficient semi-conductor [Sachs and Tuck, 1967, Birks and Meier, 1983].

The random distribution of the phase boundaries and grain boundaries within the phase layers is expected as shown throughout the grain and phase boundaries misorientation charts when compared to the Mackenzi plot in Figures 3.6.8 (e) and 3.6.9 (e). This is

because the majority of the phase and grain boundaries within the layers differ from one location to another and depend on the interconnection between the phases and other microstructural features within the scale such as grain size and shape. There was also a non-random distribution of the phase and grain boundaries found in other samples. However, because of the different scanning surface area from different samples it is not accurate for comparison purposes in terms of statistical consideration because the number of the grain boundaries characterised in each scan is different. Furthermore, in some scans where the steel substrate and the oxide scale layer contained very small number of grain boundaries, the grain misorientation chart as compared with the Mackenzi plot is meaningless. A few scans were carried out at low magnification to collect more grain boundaries, as in Figure 3.6.8, for only the steel substrate and Figure 3.6.9 for only the oxide scale layer where sufficient numbers of grain boundaries were collected. The results were similar to that in other scanning areas at higher magnifications.

Overall, the misorientation analysis carried out throughout this study was to correlate and affirm the microtexture analysis. As explained earlier the majority of oxide scale on IF steel, Alloy A and Alloy B were crack free, thus, the investigation of misorientation did not lead to any solid conclusion in that aspect. However, it has led to a better understanding of the magnetite precipitates correlation with the wüstite matrix, and also between other phases within the scale. Most importantly, the individual misorientation analysis could contribute to the analyses of specific locations within the scale to understand the exact correlation between the neighbouring grains within that area.

4.5 The Oxide Scale Mechanical Properties and Its Correlation with Oxide Microstructure

The mechanical properties of the oxide scale on steel have the largest effect on the descaling properties. The mechanical properties with other microstructural features in the oxide scale have been extensively studies. It is important to assess the correlation between microhardness of the oxide scale layer with the results of orientation, phase identification and their trends with temperatures.

The results from this study are in agreement with other studies where, at all temperatures, wüstite was the softest and haematite was the hardest, with the magnetite harder than wüstite at all temperatures. Also the lower wüstite layer was harder than the upper layer at all temperatures, see Tables 3.7.3 – 3.7.5 and Figures 3.7.8 – 3.7.10. This result is in agreement with Garber, 1959, when he claimed that wüstite hardness is of the order of 270-350 Hv, magnetite 40-500 Hv and haematite is over 1000 Hv. The difference between the wüstite upper and inner layer harnesses could be related to composition. As Sachs and Jay, 1960, claimed that the iron-rich wüstite is more stable than oxygen-rich wüstite. Thus, more stability and closer correlation with magnetite might cause a harder inner-wüstite layer than the upper part.

As described in Section 1.2.11, it is important to consider the mechanical properties of the oxide scale for both chemical and mechanical descaling. As Krzyzanowski, *et al.*, 2002, and Nagel, *et al.*, 1993, explained the mechanical properties of the scale are important in the scale-breaking process. The wüstite present is very effective in the descaling process, as wüstite is porous and easy to penetrate by the chemical solvents. This mechanism was described by Garber, 1959. He stated that once the acid has access to the metal and inner parts of the scale, the removal of a layered oxide scale by pickling is fastest when the innermost layer in contact with the metal is wüstite (because wüstite is easier to remove than the magnetite seam if formed under the wüstite layer, making the removal of the scale more difficult). Furthermore, when the acid comes into contact with the two adjacent phases, an electrochemical cell is created which rapidly dissolves the wüstite. Also the sandwich structure (magnetite-wüstite-magnetite) is not ideal for pickling, which is why the steel manufactures prefer rapid cooling to avoid wüstite transformation to magnetite.

Garber, 1959, used microhardness to identify the oxide phases. In fact difficulties arose in his test when there was a close similarity between the wüstite matrix and magnetite precipitates. The detailed experimental procedure and micrographs were not given in that study, however, he confirmed that the magnetite proeutectoid has the same microhardness value as magnetite layer is some areas. As mentioned in Section 3.7 and illustrated in Figures 3.7.3, 3.7.6 and 3.7.7, there was a difficulty in finding wüstite areas

free from magnetite precipitates especially in the upper wüstite layer. This may cause inaccurate readings of wüstite hardness values, e.g., (W4) and (W11) in Figure 3.7.1 (c). A load of 25 grams was mainly used in the areas that had high densities of magnetite precipitations in order to avoid indenting them instead of the wüstite layer.

From Figures 3.7.8 - 3.7.10, generally, with increasing temperature, wüstite and magnetite hardness increased on both IF steel and Alloy A but no trend was found on Alloy B. The microhardness of the oxide phases in this study are similar to those obtained by Munther and Lenard, 1999, (460Hv for wüstite, 540Hv for magnetite and 1050Hv for haematite at room temperature). Their work is in agreement with this study as they observed that the hardness of the oxides is temperature dependant. It is not clear in the literature the reason for increasing hardness with increasing temperature. As discussed in Section 4.3, the microtexture correlation between the phases within the scale also increased with temperature. There is the possibility of a connection between both findings. In technical terms; as explained earlier the descaling is more difficult at higher temperatures which might be connected to the harder oxide scale layers at evaluated temperatures. It should be noted this is only connected to mechanical properties of the oxide scale regardless of other microstructural features such as adherency, phase ratio, scale thickness and cracking which also affect the descaling process.

Correlating the mechanical properties of the oxide scales on steel with orientation is rather complex due to the anisotropy of the grain properties. However, effort was made to find the mechanical properties in regards to the orientation in one direction, as in this case, this was against Growth Direction (GD). Following the microhardness test, an EBSD scan was carried out for the same indented sample area as shown in Figure 3.7.5 with the optical micrograph shown in Figure 3.7.4. As explained in Section 3.7, no connection between the hardness and grain orientation was found in the three oxide layers. For example, the hardness values (H1 and H2) differ by 95 Hv, see Table 3.7.2. Looking at IPF//GD in Figure 3.7.5, there is no orientation difference between the two haematite grains. The haematite layer has very strong texture where all the grains are orientated (0001)//GD, see Figure 3.7.5 and RDPs as well as PFs nos; 11, 12 and 13. The same results were obtained from other layers within the scale as explained in Section 3.7.

It appears that the mechanical properties, particularly hardness, are affected by other factors rather than orientation, such as the phase distribution, grain size, time, temperature and vacancies especially in the wüstite layer as the oxygen concentration varies from area to area. The complete correlation between mechanical properties and orientation needs to be through nano-hardness tests where the stress, strain and modulus can be recorded and highly accurate creep monitoring during the experiment, and then followed by microtexture analyses. However, this aspect is not considered further as it was outside of the scope of this project.

In many studies it has been suggested that increasing CSL boundaries have an influence on improving the mechanical properties of the materials [Christopher, *et al*., 2002, Mukul, *et al*., 2002, Ian and Randle, 2002, Davies, *et al*., 2002, Morawiec, 2000]. Also CSL boundaries are believed to be much more sensitive to cracking than others [Gourgues, 2002]. However the CSL volume fraction, as measured in this study, for example see Figures 3.6.9 (c) and 3.6.11 (b), was not significant and so the affect could not be observed in terms of increasing hardness within the oxide scale with increasing CSL grain boundaries.

The consideration of mechanical properties of the steel oxide scale need more tests such as 4-points bend tests, tensile test, rupture consideration or measuring adhesion strength. This aspect was out of the scope of this project and can be found elsewhere, Echsler, *et al*., 2003, Krzyzanowski, *et al*., 2002, Li and Sellars, 1998, Hidaka, *et al*., 2002, Nagel and Evans, 1993, Schtze, 1988, Hancock and Nicholls, 1988. Generally, the results in this study confirmed the microhardness data in the literature as explained earlier with the benefit of confirming the phase identification by EBSD for the samples micro-indented.

CHAPTER 5   Conclusions

In this chapter, the conclusions of the results obtained throughout this project are summarised. In this study the oxidation process of low carbon steel has been reviewed and compared with the literature in the light of examining the oxide scale microstructures using EBSD as a new technique. The validity of the theories or postulations reported in the literature regarding the microstructural features and oxidation phenomenon are examined on the basis of the new observations acquired from EBSD. The multifactor influence on the complex system such as oxide scale makes characterising and investigating specific phenomenon and features individually complicated. Moreover, recognising the most influential parameter on distinctive aspects in a mixed process such as oxidation is delicate. Adjusting and fixing some parameters during oxidation experiments assisted in the understanding the effect of individual parameters on distinctive characteristics. On this basis, the main conclusions from the investigation of different phenomena and features of the oxide scale are bulleted below:

Oxidation Rate and Kinetics

- The oxidation rate of low carbon steel at 650, 750, 900, 1000, and 1100°C has been studied. At all of temperatures the oxide reached a plateau level after relatively short oxidation times with higher temperatures leading to greater oxide thicknesses.

- The oxide thicknesses of Alloy B are less than on the IF steel and Alloy A samples at all temperatures. Furthermore, the oxide scale thicknesses of Alloy A are less than on the IF steel at 650, 750 and 900°C, but greater in thicknesses at 1000 and 1100°C. The thicknesses of the scale reach a maximum value after 1800 seconds after which there is a little further growth of the scale layers.

- As expected the activation energy for IF steel has the highest value (-145 J/mol), while the Alloy B is the lowest value (-214.178 J/mole). This indicates that the highest thickness of the oxide scale should be found on the IF steel.

⬤ The oxidation rate of the scale on metal depends on many factors, such as; temperature, time, alloying elements, oxygen partial pressure, cooling rate, healing process after spallation, oxidation environment and geometry of the substrate. Each of these factors influence the oxidation mechanism and oxidation rate, hence on the microstructural development of the scale, such as cracks, porosity, grain size, orientation, adherency and uniformability of the oxide scale on the steel substrate. Also, it is not evident that repeating experiments under the same oxidation conditions on the same samples leads to the formation of the same pore size or number of cracks which affect the oxidation rate and kinetics to a great extent. Therefore, optimising experimental procedure such as sample preparation and oxidation conditions is very difficult for repeatability and duplication purposes, and that makes comparison difficult. Thus, each oxidation case should be considered individually in order to identify the main factors affecting the microstructural features in the oxide and hence the oxidation rate.

Comparison of Observation Techniques

⬤ Optical and scanning electron microscopy can give valuable information about some of the oxide scale microstructure features. However, sample preparation artefacts, etching methodology and their limitation may affect the results which might mislead the observer. To avoid unreliable results, the optical and SEM observations should be compared with those obtained from other techniques, such as EDX and EBSD.

⬤ Optical and SEM microscopy cannot reveal complete grain boundaries in the oxide scale layers. Furthermore, it is difficult to distinguish between the grain and phase boundaries as well as small micro-cracks or scratches due to artefacts generated during the sample preparation. Electron Backscatter Diffraction (EBSD) could disclose complete microstructure characteristics as it can expose grain boundaries as well as phase boundaries in the oxide scale. The unique features in EBSD facilitate grain size measurement for each phase within the oxide scale.

⬤ EBSD patterns contain a large amount of information about the crystal structure of the phases. In the current study, EBSD could eliminate the ambiguity of existing phases in the oxide scale and correlate it to microstructure. The ambiguities can be eliminated only if the crystallographic structure for each phase within the scale is considered and its microstructure-texture analysis obtained to characterise the scale microstructure.

⬤ EBSD is shown to be a valuable tool in the study of oxide scale layers. The microstructure of the scale can be easily imaged and the phases identified. Furthermore, complete microtexture and misorientation analysis can be carried out using EBSD.

The Microstructural Development of Steel Oxide Scale

⬤ It appeared that the magnetite and haematite volume fractions increased with increasing temperatures while wüstite decreased on IF steel. On Alloy A there were no trends in the variation of the oxide scale phase's volume fraction with temperature. On Alloy B, the phase volume fraction in the oxide scale changed slightly with temperature. The magnetite phase volume fraction remained constant at all temperatures, while slight changes occurred for haematite and wüstite. The oxide layer thickness and overall thickness increased with temperature, but the phase ratio remains constant or very small changes have been noted. Furthermore, the magnetite precipitations increased with increasing temperatures on all the steels used in this study.

⬤ As expected the phase ratio was affected by oxidation time. The wüstite phase volume fraction decreased with increasing time. As full wüstite saturation occurred at 1100°C-3600 seconds, the magnetite and haematite increased with increasing time, occupying the whole layer of the oxide scale.

⬤ The oxidation time and temperature are not the only factors that affect the phase ratio and distribution within the oxide scale, but also the microstructural features

such as porosity, fissures, uniformability, adherency, blister formation and alloying elements influence the phase ratio to some extent.

◉ It appears that the phases produced through phase transformation in the steel substrate have very limited influence on the phase ratio of the oxide scale.

◉ The wüstite and magnetite grain size increases with increasing temperature on the IF steel, Alloy A and Alloy B. Furthermore, the exposure time affects the grain size and shape. At constant temperature the grain boundary number decreases with increasing time.

◉ Generally, the majority of the oxide scales at high temperatures, i.e., above 900°C were uniform on all three type of steels used in this study.

◉ The oxide scale at the edges or corners was thinner than at the centre of the sample and some phase transformations take place due to their accessibility to oxygen. Voids and vacancies formation and condensation may cause the different thickness of the oxide scale at the edges and corners.

◉ Relating grain boundary misorientation at different locations on the scale with the uniformability of the scale on the steel surface did not lead to any solid conclusions in this study.

◉ EBSD can give clarification of the initiation of cracks within the oxide scale through misorientation analysis and orientation maps. The results showed that the oxide scale on IF steel Alloy A and Alloy B were generally free from cracks.

Microtexture Correlation between Oxide Scale Layers and Steel Substrate

◉ The texture strength with increasing temperatures were investigated for IF steel substrates. The wüstite texture strength increased with increasing temperature and

the magnetite texture strengths were constant. The wüstite and magnetite are texturally correlated at 650, 750 and 1000°C.

⚬ On Alloy A, the wüstite and magnetite texture strength increased with increasing temperature. The steel substrate texture was strong at 650°C and constant (also weak) at the rest of the oxidation temperatures indicating no trend with temperature. While, iron and wüstite are texturally correlated at 650, 1000 and 1100°C, iron and magnetite at 1000 and 1100°C.

⚬ On Alloy B, the wüstite texture strength increased with increasing temperatures. The steel substrate texture is weak at 900°C and very weak at 1100°C. The magnetite and haematite layer texture strengths are constant at all temperatures. The haematite layer has a very strong texture at all temperatures while magnetite has a weak texture. Iron-wüstite is texturally correlated at 1100°C, but not at 900°C. The iron-magnetite has a very strong texture relationship at 1100°C, whilst the wüstite and magnetite are texturally correlated as for the oxide on IF steel and Alloy A. As for IF steel and Alloy A, Alloy B oxide scale layers have strong texture relationships between the phases. There were always wüstite-magnetite, wüstite-haematite and magnetite-haematite textural relationship at all temperatures.

⚬ The texture correlation between the oxide phase layers is stronger than they have with the steel substrate. Furthermore, texture correlation between the oxides phases strengthened with increasing temperature.

⚬ Considering only overall phases' microtexture correlation with temperature and time, the phases' correlations within the oxide scale increased with increasing time and temperatures.

⚬ A closer examination showed that there is a weak orientation correlation between the grains at the metal-oxide interface whether there was a texture correlation between the phases or not. Further considerations about the adherence between the steel substrate and the oxide revealed that the gap between substrate and the oxide layers

did not have any affect on the oxide grain orientation. A texture correlation between the phases might exists regardless of if the scale was adherent to the substrate surface or not. The correlation between the gap and the texture is related to the fact that development of texture in the oxide scale layers is started at an early stage of oxide nucleation and growth. Thus, later separation of the oxide scale from the substrate would not influence the oxide grain orientations.

● Generally, the results showed that higher misorientation angles caused weaker texture compounds. E.g., Haematite grains have very low misorientation angles whereas they have very strong texture.

● The multifactor influence of the oxide scale growth on steel, ultimately have an affect on the texture correlation. Therefore, only controlling time, temperature and oxidation conditions can not led to the formation of specific orientations of the oxide scale grains on steel substrate. So that the factors that caused uncertainty of oxidation rate and growth outcome, might affect the orientation interconnection to some extent.

Mechanical Properties of the Oxide Scale

● The results from this study were in agreement with other studies where, at all temperatures, wüstite was the softest and haematite was the hardest layer within the oxide scale. Moreover, the magnetite was harder than wüstite at all temperatures. The difference between the wüstite upper and inner layer hardness could be related to composition.

● With increasing temperature, the wüstite and magnetite hardness increased on both the IF steel and Alloy A but no trend was found on Alloy B. The haematite layer could not be observed on most of the samples, thus, no hardness data was available.

● It appears that the mechanical properties, particularly hardness, are affected by other factors rather than orientation such as the phase distribution, grain size, time,

temperature, vacancy and voids especially in the wüstite layer as the oxygen concentration is variable from one area to another.

●   No connection between the hardness and grain orientation is found in the three oxide layers. Future work would be needed to fully investigate this aspect.

CHAPTER 6   Suggestions for Further Work

The effect of the oxidation temperature, time of exposure, environmental conditions and alloying elements on the nucleation, growth, kinetics, microstructural development and mechanical properties of the oxide scale on steels are studied throughout the current work. Also, the steel crystallographic texture influence on the oxide scale formation leads to review the oxidation mechanism hypotheses and establishing a new method of descaling processes. Further work has to be carried out in order to develop a mechanism for the complete characterisation of the oxide scales relating microstructure and microtexture to the mechanical properties of the oxide scale. On this base, the main suggestions for further work are bulleted below.

- Further experiments would be needed at different oxidation temperatures and times of exposure as well as at various environmental conditions to collect more microstructural and microtextural data of the oxide scale.

- Other grades of steel should be used for microtexture and microstructure investigations to obtain more evidence on their correlations and also for comparison purposes.

- Further work would be needed to investigate the affect of the microstructure on the mechanical properties of oxide scale on the steels.

- The microtexture analysis has to be continued on other grades of steel to obtain further information about the steel and oxide texture correlation.

- The affects of alloying elements in steel such as carbon, silicon, chromium, nickel and manganese on the oxide microstructure and microtexture should be considered in greater detail which may need in-situ experiments at high temperatures.

- Through relating microstructure and microtexture of the oxide scale with the mechanical properties of the scale, the descaling process and its mechanism

would need further work to determine the best microstructure for ease of descaling, especially mechanical descaling.

⚫ The phase transformation occurring during oxidation and cooling within the steel substrate and the oxide scale and their correlation may require future work. The investigation of the final structure, as in this study, cannot give adequate answers to the phase correlations and their affect on each other, hence the whole oxide structure.

⚫ Further work may be required to ascertain whether there is a correlation between steel substrate with wüstite and magnetite grain size.

⚫ Further work would be needed in relating grain boundaries misorientation at different locations on the scale with the uniformability of the scale.

⚫ Understanding the trend of texture strength with time and temperature, also the affect of the phase transformation during oxidation on texture strength require future work to consider this aspect fully.

⚫ In this study, no interconnection between the hardness and grain orientation is found in the steel oxide layers. Future work would be needed to fully investigate this aspect.

⚫ No significant affect was observed of improving the mechanical properties with increasing CSL grain boundaries within the steel oxide scale. Therefore, correlating CSL boundary within the scale with the mechanical properties may need further study.

References

Abuluwefa H., Guthrie R. I. L. and Ajersch F., The effect of oxygen concentration on the oxidation of low carbon steel in the temperature range 1000 to 1250°C, Oxidation of Metals, Volume 46, No; 5/6, p; 423, 1996.

Abuluwefa H., Root J. H., Guthrie R. I. L. and Ajersch F., Real-time observation of the oxidation of mild steel at high temperature by neutron diffraction, Metallurgical and Materials Transactions B, Volume 27 B, p; 993, 1996.

Adam B. L. and Field D. P., Measurement and representation of grain boundary texture, Metallurgical Transaction, Volume 23 A, p; 2501, 1992.

ASM, Metal Hand book, Volume 7, edition 8, ASM, Metals Park, Ohio, USA, 1972.

Audery G. M., Practical methods in electron microscopy, Volume 1, part 2 "Electron diffraction and optical diffraction technique, Elsvier/North-Holland Biomedical press, Amsterdam, 1979.

Baba-Kishi K. Z. and Dingely D. J., Backscatter Kikuchi diffraction in the SEM for identification of crystallographic point group, Scanning Electron Microscopy, Volume 11, p; 303, 1989.

Baik S. K. and Kwon O. S., Effect of composition on anisotropy and texture of continuously low carbon steels sheets, International conference on texture of materials-12th:, Montreal, Canada, NRC Research Press, Volume 2, p; 1043, 1999.

Barlow J., Jay G. T. F. and Sachs K., Laboratory simulation of industrial scale, Journal of the Iron and Steel Institute, Volume 203, p: 983, 1965.

Benard J. P., Adsorption of oxidant and oxide nucleation, American Society For Metals, Oxidation of Metals and Alloys, Ohio, USA, 1970.

Birks N. and Jackson W., A quantitative treatment of simultaneous scaling and decarburisation of steel, Journal of the Iron and Steel Institute, Volume 208, p; 81, 1970.

Birks N. and Meier G. H., Introduction to high temperature oxidation of metals, Edward Arnold, London, 1983.

Bobeth M., Pompe W., Schumann E. and Ruhle M., Out-diffusion of the noble component during the initial stage of the oxidation of γ-Ni_3Al, Acta Materialia, Volume 40, No; 10, p; 2669, 1992.

Brich F. and Spicer H. C., Handbook of physical constants, Geological Society of America, 1942.

Brundle C. R., Chuang T. J. and Wandelt K., Core and valence level photoemission studies of iron oxide surfaces and the oxidation of iron, Surface Science, Volume 68, p; 459, 1997.

Burke D. P. and Higginson R. L., Characterisation of multicomponent scale by electron backscatter diffraction (EBSD), Scripta Materialia, Volume 42, p; 277, 2000.

Bunge H. J. and Esling C., Quantitative texture analysis, Informationsgesellschaft. Verlag, Germany (FRG), 1986.

Camus P., Hardware and software optimisation for orientation mapping and phase identification, Chapter 11, from "Electron backscatter diffraction in materials science" Kluwer Academic/ Plenum Publishers, New York, USA, 2000.

Caplan D., Hussey R. J., Sproule G. I. and Graham M. J., The effect of FeO grain size and cavities on the oxidation of Fe, Corrosion Science, Volume 21, No; 9, p; 689, 1981.

Carpenter D. and Ray A., The effect of metallurgical pre-treatment on the kinetics of oxidation of iron at 700°C in pure gaseous oxygen, Corrosion Science, Volume 13, p; 493, 1973.

Caul M. and Randle V., Microtexture analysis of interstitial free steel, Material Characterisation, Volume 38, p; 155, 1997.

Caudron E. and Buscail H., In-situ temperature X-ray diffraction characterisation of yttrium implanted extra low carbon steel and pure iron, Materials Chemistry and Physics, Volume 64, p; 29, 2000.

Chan R. W. and Haasen P., Physical Metallurgy, North-Holland Physics Publishing, Amsterdam, 1983.

Chen R. Y. and Yuen W. Y. D., Oxide scale structures formed on commercial hot-rolled steel strip and their formation mechanism, Oxidation of Metals, Volume 56, No; 1/2, p; 89, 2001.

Chen R. Y. and Yuen W. Y. D., Oxidation of low carbon, low silicon mild steel at 450-900 under conditions relevant to hot-strip processing, Oxidation of Metals, Volume 57, No;1/2, p; 53, 2002.

Chen R. Y. and Yuen W. Y. D., Review of the high temperature oxidation of iron and carbon steels in air or oxygen, Oxidation of Metals, Volume 59, No; 5/6, p; 433, 2003.

Chen R. Y. and Yuen W. Y. D., Examination of oxide scale of hot rolled steel products, the paper presented at the annual meeting of the Iron and Steel Institute of Japan, accepted for publication, 2005.

Chiang Y., Birnire D. P. and Kingery D. W., Physical ceramics, John Wiley & Sons Inc., Canada, 1997.

Chiba M., Morio K. and Koizumi Y., Microstructure and magnetic of iron oxide thin films by solid reaction, Journal of Magnetism and Magnetic Materials, Volume 239, p; 457, 2002.

Cho C., Wang C. M., Chan H. M., Rickman M. J. and Harmer M. P., A study of grain boundary structure in rare-earth doped alumina using EBSD technique, Journal of Materials Science, Volume 37, p; 59, 2002.

Corkovic S. and Pyzalla A. R., In-situ stress analysis during high temperature oxidation of mild steel and grey cast iron, Materials and Corrosion, Volume 55, No; 5, p; 341, 2004.

Cross I. J., Randle V. and Daniel S. R., Microtexture development in high strength interstitial free steels, Proc. International conference on texture of materials-12th: edited by Szpunar J. A, Montreal, Canada, NRC Research Press, Volume 2, p; 1202, 1999.

Cross I. J. and Randle V., Lowest angle solution versus low-index axis solution for misorientations, Scripta Materialia, Volume 48, p; 1587, 2003.

Czerwinski F. V. and Szpunar J. A. V., The surface texture of nickel for high temperature oxidation prevention, Proc. International conference on texture of materials-12th: edited by Szpunar J. A, Montreal, Canada, NRC Research Press, Volume 2, p. 1397. 1999.

Czerwinski F. V., Li H. And Szpunar J. A. V., A model of NiO texture formation on single crystal substrate, Proc. International conference on texture of materials-12th: edit by Szpunar J. A, Montreal, Canada, NRC Research Press, Volume 2, p; 1391, 1999.

Davies P. J., Randle V., Watkins G. J. and Davies H. J., Triple junction distribution profiles as assessed by electron backscatter diffraction, Journal of Materials Science, Volume 37, p; 4203, 2002.

Diggle J. W. and Vijh K., Oxide and oxide films, Volume 4, Marcel Dekker INC, New York, 1976.

Dingley D. J. and Baba-Kishi K. Z, Use of the electron backscatter diffraction patterns for determination of crystal symmetry elements, Scanning Electron Microscopy, Volume 11, p; 383, 1986.

Dingley D. J. and Randle V., Review; Microtexture determination by electron backscatter diffraction" Journal of Material Science, Volume 27, p; 4545, 1992.

Dingley D. J., Electron backscatter diffraction in materials science, Chapter 1, Kluwer Academic/ Plenum Publishers, New York, USA, 2000.

Donald A. R., The science and engineering of materials, third edition, Chapman and Hall, UK, 1996.

Edington J. W., Electron diffraction in the electron microscope, Volume 2, Department of Metallurgy and Materials Science, University of Cambridge, Philips Technical Library, UK, 1975.

Echsler H., Ito S. and Schutze M., Mechanical properties of oxide scales on mild steel at 800 to 1000°C, Oxidation of Metals, Volume 60, No; 3/4, p: 241, 2003.

Flewitt P. E. J. and Wild R. K., Microstructural characterisation of metals and alloys, Institute of Metals, London, 1985.

Fukuoka C., Morishima K, Yoshizawa H. and Mino K., Misorientation development in grains of tensile strained and crept 2.25% Cr-1% mo steel, Scripta Materialia, Volume 46, p: 61, 2002.

Gaskell D. R., Introduction to the thermodynamics of material, Third edition, Taylor & Francis, USA, 1995.

Garber S., Fundamental aspects of scale on mild steel strip, Journal of the Iron and Steel Institute, Volume 192, p; 153, 1959.

Geneve D. K., Confete M. K., Rouxel D. K., Pigeat P. K. and Weber B. K, Distribution around the oxide-substrate interface of alloying elements in low carbon steel, Oxidation of Metals, Volume 51, No; 5/6, p; 527, 1999.

Gemundo F. M. and Viani F. M, The formation of multilayer scales in the parabolic oxidation of pure metals-II., Temperature and pressure dependence of the different rate constant, Corrosion Science, Volume 18, p; 231, 1978.

Gleeson B. A., Hadavi M. and Young D., Isothermal transformation behaviour of thermally-grown wüstite, Materials at High Temperature, Volume 17, No; 2, p; 311, 2000.

Goldschmidt J., The crystal structures of Fe, FeO and Fe_3O_4 and their interrelations, Journal of Iron and Steel Institute, Volume 146, p; 157, 1942.

Gonser U., Microscopic methods in metals, Topic in Current Physics, Volume 40, Speinger-Varlag, Germany, 1986.

Gourgues A. F., Flower H. M. and Lindley T. C., Electron backscatter diffraction study of acicular ferrite, bainite, and martensite steel microstructures, Material Science and Technology, Volume 16, No; 1, p; 26, 2000.

Gourgues A. F., Overview; Electron backscatter diffraction and cracking, Materials Science and Technology, Volume 18: p; 119, 2002.

Graham M. J. L. and Hussey R. J. L., Characterisation and growth of oxide films, Corrosion Science, Volume 44, p; 319, 2002.

Guinier A., X-Ray crystallographic technology, Hilger and Watts Ltd. London, 1952.

Gwathmey A. T. and Lawless K. R., The surface chemistry of metals and semiconductors, John Wiley & Sons, New York, 1960.

Hancock P. and Nicholls J. R., Application of fracture mechanics to failure of surface oxide scale, Materials Science and Technology, Volume 4, p; 398, 1988.

Harkins P. C., Dissolution of iron oxide under potential control, PhD thesis, Loughborough University, UK, 1984.

Hatherley M. and Hutchinson W. B., An introduction to textures in metal, The Institution of Metallurgists, Monograph No; 5, Chameleon Press Ltd, London, 1979.

Hauffe K., Oxidation of metals, Plenum Press, New York, 1965.

Hearle J. W. S., Sparrow J. T. and Cross P. M., The use of the scanning electron microscope, Pergamon Press Ltd, Great Britain, 1972.

Hidaka Y. P., Anraku T. P. and Otsuka N., P. Deformation of iron oxides upon tensile tests at 600-1250°C, Oxidation of Metals, Volume: 59, No; 1/2, p; 97, 2002.

Higgins R. A., Properties of Engineering Materials, Second edition, Edward Arnold, London, 1994.

Higginson R. L., Roebuck B. and Palmiere E. J., Texture development in oxide scales on steel substrates, Scripta Materialia, Volume 47, p; 337, 2002.

Higginson R. L. and Sellars C. M., Worked examples in quantitative metallography, Maney-IOM[3], London, 2003.

Hill R. E., Physical metallurgy principle, Brooks & Cole Engineering Division, Monterey, California, 1973.

Honeycombe R. W. K., Steels; microstructure and properties, Edward Arnold, London, 1981.

Hsun H., Cline R. S. and Goodman S. R., Recrystallization, grain growth and textures, Paper presented at a seminar of the American Society for Metals, , Metal Park, Ohio, USA, 1965.

Hualong L., Glavicic M. G. and Szpunar J. A., Simulation of texture formation in ZrO_2 film grown, International conference on texture of materials-12th, Montreal, Canada, NRC Research Press, Volume 2, p; 1303, 1999.

Humphreys J. F., Encyclopaedia of Materials Science and Engineering, Pergamon Press, Oxford, 1986.

Humphreys J. F., Huang Y., Brough I. and Harris C., Electron backscatter diffraction of grain and subgrain structures - resolution considerations, Journal of Microscopy, Volume 195, Part 3, p; 212, 1999.

Humphreys J. F., Determination of microstructure by EBSD at high spatial resolution in a FEGSEM, Proc. International conference on texture of materials-12th: edit by Szpunar J. A, Montreal, Canada, NRC Research Press, Volume 1, p; 74, 1999

Humphreys J. F., Review; grain and subgrain characterisation by electron backscatter diffraction, Journal of Materials Science, Volume 36, p; 3833, 2001.

Hussey R J. H. and Graham M. J. H., Some observation on void formation in Fe_3O_4 layers on Fe., Corrosion Science, Volume 21, No. 3, p; 255, 1981.

Hutchinson B. and Lindh E., On the determination of textures from discrete orientation measurements, Proc. International conference on texture of materials-12th: edit by Szpunar J. A., Montreal, Canada, NRC Research Press, Volume 1, p; 34, 1999.

International union of crystallography web site (ICSU), 2002. http.//www.iucr.org/iucr-top.html, viewed in March, 2003.

Ilschner B. and Mlitzke E., The kinetics of precipitation in wüstite ($Fe_{1-x}O$), Acta Materialia, Volume 13, p; 855, 1965.

Johnson M., Carter B. and Michael J., SEM analysis of oxide thin film and reaction, American Ceramic Society Journal, Volume 82, No; 6, p; 1644, 1999.

Khan E. U., Dix R. C. and Kalpakjian S., Thermal contact resistance of thick oxide layers on steel, Journal of the Iron and Steel Institute, Volume 39, p; 4578, 1969.

Khanna A. S., Introduction to high temperature oxidation and corrosion, The Materials Information Society, ASM International, USA, 2002.

Kim B. K. and Szpunar J. A., Orientation imaging microscopy for the study on high temperature oxidation, Scripta Materialia, Volume 44, p; 2605, 2001.

Kim B. K. and Szpunar J. A., Anisotropic microstructure of iron oxides formed during high temperature oxidation of steel, Materials Science Forum, Volume: 408-412, No; 2, p; 1711, 2002.

Kofstad P., High temperature oxidation of metals, John Wiley & Sons, Inc, USA, 1966.

Kofstad P., On the formation of porosity and microchannels in growing scales, Oxidation of Metals, Volume 24, No; 5/6, p; 265, 1985.

Kolosov V. Y. and Tholen A. R., Transmission electron microscopy studies of the specific structure of crystals formed by phase transition in iron oxide amorphous films, Acta Materialia, Volume 48, p; 1829, 2000.

Krzyzanowski M., and Beynon J. H., Measurement of oxide properties for numerical evaluation of their failure under hot rolling conditions, Journal of Materials Processing Technology, Volume 125-126, P; 398, 2002.

Krzyzanowski M., Yang W., Sellars C. M. and Beynon J. H., Analysis of mechanical descaling; experimental and modelling approach, Materials Science and Technology, Volume, 19, p; 109, 2003.

Kubaschewski O. and Hopkins B. E., Oxidation of metals and alloys, Second edition, Butterworths, London, 1967.

Kubaschewski O., Cibula A. and Moore D. C., Gases and metals, Morrison and Gibb Ltd, London, 1970.

Kucera J. and Hajduga M., High temperature and long time oxidation of iron and steel, Wydawnictwo PL Filia w Bielsku- Bbialej, 1998.

Kumar M., Schwartz A. J. and King W. E., Microstructural evolution during grain boundary engineering of low to medium stacking fault energy fcc materials., Acta Materialia, Volume 50, p; 2599, 2002.

Kurosawa k., Li H., Ujihira Y., Nomura k., Mochizuki E. and hayashi H., Characterisation by CES, XRD and XPS of oxidised layers formed on the surface of carbonitrided low carbon steel, Materials Characterisation, Volume, 34, p; 241, 1995.

Kunze, K., Wright S. I., Adams B. L. and Dingley D. J., Advanced in Automatic EBSD Single Orientation Measurement, Texture and Microstructure, Volume 20, p; 41, 1993.

Kyung K., Moon D., Lee S. and Jung K., Formation of highly orientated FeO thin film by phase transition of Fe_3O_4 and Fe nanocrystallines, Thin Solid Films, Volume 360, p; 118, 2000.

Lassen K., Conradsen K. and juul-jensen D., Image processing procedures for analysis of electron backscattered patterns, Scanning Microscopy, Volume 6, p; 115, 1992.

Lee K. T. and Szpunar J. A., The influence of texture on the oxidation kinetic of copper, Proc. International conference on texture of materials-12th: edit by Szpunar A., Montreal, Canada, NRC Research Press, Volume 2, p; 1415, 1999.

Lee S., Chun Y., Han W. and Hwang S., Effect of thermomechanical processing on grain boundary characteristics in two-phase brass., Materials Science and Engineering, Volume A363, p; 307, 2003.

Li Y. H. and Sellars C. M., Comparative investigation of interfacial heat transfer behaviour during hot forging and rolling of steel with oxide scale formation, Journal of Materials processing Technology, Volume; 80-81, p; 282, 1998.

Li Y. S., Niu Y., Gesmundo F. A. and Wang F. H., Grain size effects on the oxidation of two-phase Cu-Fe alloys, Corrosion Science, Volume 44, p; 1457, 2002.

Liu W., Bayerlien M., Mughrab H., Day N., Quested, Acta Materialia, Volume 40, p; 1763, 1992.

Llewellyn D., Steels: Metallurgy and Application, Butterworth-Heinemann Ltd, Oxford, UK, 1995.

Loretto M. H., Electron beam analysis of materials, second edition, Chapman & Hall, London, 1994.

Lowenheim F. A., Modern electroplating, third edition, published by Wiley International, 1974.

Mao W. and Chen N. and YU. Y., Relationship between texture, magnetic induction and maximum magnetic permeability of steels, Proc. International Conference on Texture of Materials-12th: edit by Szpunar A., Montreal, Canada, NRC Research Press, Volume 1, p; 511, 1999.

Marston H., Influence of scale structure on the effectiveness of descaling", Corus research and development, Swinden Technology Centre, UK. September 2003 (Paper accepted for publication).

Mckie D. and Mckie C., Essentials of crystallography, Blackwell Scientific Publication, London, 1986.

McLean D., Grain boundaries in Metals, Oxford, Clarendon Press, 1957.

Michael J. R., Phase identification using electron backscatter diffraction in the scanning electron microscopy, Proc. Chapter 7, from "Electron backscattered diffraction in materials science" Kluwer Academic/ Plenum Publishers, New York, USA, 2000.

Militzer M., Hawbolt E. B., and Meadowcroft T. R., Microstructure model for hot strip rolling of high-strength low-alloy steel, Metallurgical and Material Transactions A, Volume 31 A, p; 1247, 2000.

Mishin O. V., Gertsman V. Y. and Gottstein G., Distribution of orientations and misorientations in hot-rolled copper, Materials Characterisation, Volume 38, p; 39, 1997.

Modin H. and Modin S., Metallurgical Microscope, revised English version, C. Tinling & Co Ltd, London, Butterworths, 1968.

Morawiec A., Grain misorientation in theories of abnormal grain growth in silicon steel, Scripta Mater, Volume 43, p; 275, 2000.

Mougin J., Dupeux M., Antoni L. and Galerie A., Adhesion of thermal oxide scales grown on ferritic stainless steels measured using the inverted blister test, Materials Science and Engineering, Volume A359, p; 44, 2003.

Mrowec S., On the mechanism of high temperature oxidation of metals and alloys, Corrosion Science, Volume 7, p; 563, 1967.

Munther P. A. and Lenard J. G., The effect of scaling on interfacial friction in hot rolling of steels, Journal of Material Processing Technology, Volume 88, p; 105, 1999.

Nagl M. M. D., and Evans W. T. D., The mechanical failure of oxide scales under tensile or compressive load, Journal of Materials Science, Volume 28, p; 6247, 1993.

Nowell M. M and Wright S. I., Phase differentiation via combined EBSD and XEDS, Journal of Microscopy, Volume 213, part 3, p; 296, 2004.

Paidassi J., The precipitation of Fe_3O_4 in scales formed by oxidation of iron at elevated temperatures, Acta Materialia, Volume 3, p; 447, 1955.

Pfeil L. B., The oxidation of iron and steel at high temperature, The Journal of the Iron and Steel Institute, Volume CXIX, No; 1, p; 501, 1929.

Pfeil L. B., The constitution of scales, Journal of Iron and Steel Institute, Volume; CXXIII, No; 1, p; 237, 1931.

Phillips F. C., An introduction to crystallography, Longmans Green and Co. Ltd, University press, Glasgow, 1949.

Pickens J. W., The microstructural characteristics of oxide scales formed during bar processing, Mechanical Working and Steel Processing; 25th Conference proceeding paper, Iron & steel Society, UK less Current Serials, volume 21, p; 39, 1984.

Pollack W. H, Materials science and metallurgy, Fourth Edition, Englewood, New Jersey, USA, 1988.

Poter D. A. and Easterkings K. E., Phase transformations in metals and alloys, Van Nostrand Reinhold Ltd, Alden Press, oxford, 1981.

Powell G. A. and Randle V., The effect of Si on the relationship between orientation and carbide morphology in high chromium white irons, Journal of Materials Science, Volume 32, p; 561, 1997.

Ralph G. Wyckoff, Crystal structure, Interscience Publishers, New York, USA, Volume 1-3, 1963.

Rajan K., Presentations of texture in orientation space, Proc. Chapter 3 from "Electron backscattered diffraction in material science" Kluwer Academic/ Plenum Publishers, New York, USA, 2000.

Rajan K., Prodrigues-Frank representations of crystallographic texture, Proc. Chapter 4 from "Electron backscattered diffraction in materials science" Kluwer Academic/ Plenum Publishers, New York, USA, 2000

Raman R. K. S., Gleeson B and Young D. J., Laser Raman Spectroscopy: a technique for rapid characterization of oxide scale layers, Materials Science and Technology, Volume 14, p; 373, 1998.

Randle V. and Brown A., Development of grain misorientation texture, in term of coincident site lattice structures, as a function of thermomechanical treatments, Philosophical Magazine A, Volume 59, No; 5, p; 1075, 1989.

Randle V., Microtexture determination and its application, Institution of Materials, Bourne Press, Bournemouth, London, 1992.

Randle V., The measurement of grain boundary geometry, Institution of Physics Publication. Bristol, 1993.

Randle V., Guidebook Series-Electron backscatter diffraction, Oxford Instrument plc. Publication, Microanalysis Group, UK, 1996.

Randle V., Theoretical framework for electron backscattered diffraction, Proc. Chapter 2 from, "Electron backscattered diffraction in material science" Kluwer Academic/ Plenum Publishers, New York, USA, 2000.

Randle V., The coincidence site lattice and the sigma enigma, Materials Characterisation, Volume 47, p; 411, 2001.

Randle V. and Engler O., Introduction to texture analysis, macrotexture, microtexture and orientation mapping, Taylor & Francis Ltd, UK, 2003.

Randle V., Microtexture determination and its applications, Second edition, Maney Publication, London, 2003.

Randle V., Application of electron backscatter diffraction to grain boundary characterisation, International Materials Review, Volume 49, No; 1, p;11, 2004.

Restoker W. and Dvorak J. R., Interpretation of metallographic structure, Academic Press INC, London, 1965.

ResMat corporation web site, Montreal, QC CANADA 2002, http.//www.resmat.com/Course.htm. The website viewed in April, 2003.

Rolland P. and Dicks K. G., An automated EBSD acquisition and processing system, Proc. Chapter 12 from "Electron backscattered diffraction in materials science", Kluwer Academic/ Plenum Publishers, New York, USA, 2000.

Rosiere C. A., Siemes H., Quad H., Brokmeier H. G. and Jansen E. M., Microstructures, textures and deformation mechanism in hematite, Journal of Structural Geology, Volume 23, p; 1429, 2001.

Sachs K. and Brown R., A theory of decarburisation by scale, Journal of the Iron and Steel Institute, Volume 190, p; 169, 1958.

Sachs K. and Jay F., Scale on mild steel in various stages of rolling wire rod, Journal of the Iron and Steel Institute, Volume 193, p; 344, 1959.

Sachs K. Jay F., A magnetite seam at the scale/metal interface on mild steel, Journal of the Iron and Steel Institute, volume 195, p: 180, 1960.

Sachs K. and Tuck C. W., Surface oxidation of steel in industrial furnaces, Proc. Conf. Reheating for Hot Working, The Iron and Steel Institute, p; 17, 1967.

Sachs K. and Tuck C. W. Werkst. Korros Journal "werkstoffe und korrosion-materials and corrosion", Volume 21, p; 945, 1970.

Sand D. E., Introduction to crystallography, W. A. Benjamin INC, university of Kentucky, New York, 1969.

Schmid B. L., Aas N. L., Grong Q. and Qdegard R., High temperature oxidation of iron and the decay of wüstite studied with in situ ESEM, Oxidation of Metal, Volume 57, No; 1-2, p; 115, 2001.

Schutze M., Stresses and decohesion of oxide scales, Materials Science and Technology, Volume 4, P; 407, 1988.

Schuh C. A., Kumar M., and King W. E., Analysis of grain boundary networks and their evolution during grain boundary engineering., Acta Materialia, Volume 51, Number 3, p; 687, 2003.

Schwarzer R., Automated electron backscattered diffraction: present state and prospects, Proc. Chapter 9, from "Electron backscattered diffraction in materials science" Kluwer Academic/ Plenum Publishers, New York, USA, 2000.

Senkevich J. J., Jones D. A. and Chatterjee I., Measuring the growth of oxide films on low carbon steel at 500 °C by impedance spectroscopy, Corrosion Science, Volume 42, p; 201, 2000.

Sewell P. B. and Cohen M., Journal of electrochemistry Society, Volume 111, p; 501, 1964.

Shaw R. and Rolls R., The calculation of relative layer thickness in a two-component scale, Corrosion Science, Volume 14, p; 433, 1974.

Sheasby J. S., Boggs W. E. and Turkdogan E. T., Scale growth on steels at 1200 °C: rationale of rate and morphology" Metal Science, Volume 18, p; 145, 1984.

Shigeji T., Yamamoto K., Megumi D. and Shibata T., Characterisation of scale/substrate interface area of Si-containing low-carbon steels at high temperatures, Materials Science and Engineering, Volume, A308, p; 250, 2001.

Sinha. A. K., Ferrous Physical Metallurgy, Butterworths, Stoneham, USA, 1989.

Siebert C. A. and Upthegrove C., Transaction American Society of Metal, Volume 23, p; 187, 1923.

Smallman R. E. and Bishop R. J., Metals and Materials; Science, Processes and application, Butterworth-Heinemann Ltd, Oxford, UK, 1995.

Smith F., Principle of Materials Science and Engineering, McGraw-Hill, New York, USA, 1986.

Smuts J. and De Villiers P., Scale on heat-treated hot-rolled steel plate, Journal of Iron and Steel Institute, Volume 204, p; 787, 1966.

Stack M. M., Stott F. H. and Wood G. C., Erosion-corrosion of pre-oxidized Incoloy 800H in fluidised-bed environments, Materials Science and Technology, Volume 7, p; 1128, 1991.

Steadman R., Crystallography, university of Bradford, Van Nostrand Reinhold Company Ltd, the Thetford press limited, UK, 1982.

Stott F. H., The protective action of oxide scales in gaseous environments at high temperature, Reports to Progress in Physics, Volume 50, P; 861, 1987.

Stott F. H., Methods of improving adherence, Materials Science and Technology, Volume 4, p; 431, 1988.

Sun W., Tieu A. K., Jiang Z. Y., Zhu H. T and Lu C., Surface characterisation of oxide scale in hot strip rolling, Journal of Materials Processing Technology, Volume 140, p; 76, 2003.

Sun W., Tieu A. K, Jiang Z. Y., Zhu H. T. and Lu C., Oxide scales growth of low carbon steel at high temperatures, Journal of Materials Processing Technology, Volume 155-156, p; 1300, 2004.

Szpunar J. A., Texture design for new application, Proc. International conference on texture of materials-12th: edit by Szpunar J. A, Montreal, Canada, NRC Research Press, Volume 1, p; 6, 1999.

Taniguchi S., Yamamoto K., Megumi D. and Shibata T., Characteristics of scale/substrate interface area of Si-containing low carbon steels at high temperatures, Materials Science and Engineering, Volume A 308, P; 250, 2001.

TexSEM Laboratories Inc, Incorporated, TSL and EDAX Manual Users, Part 1 OIM DC and Analysis, USA, 2001

Tien K. and Davidson M., Proceedings of the symposium on stress effects and the oxidation of metal, edited by J. V. Cathcart, AIME, USA, 1974.

Tholence F. and Norell M., High temperature corrosion of cast irons and cast steels in dry air, Materials Science Forum, Volume: 369-372, p; 197, 2001.

Toft O., Nonstoichiometric Oxides, Academic Press, New York, USA, 1972.

Tomellini M. G. L. and Mazzarano A. G., High temperature oxidation under time-dependent gas pressure: an application to steel oxidation, Oxidation of Metal, Volume 29, part 3-4, p; 179, 1998.

Tominaga J., Wakimoto K., Mori T. Murakami M. and Yoshimura T., Manufacture of wire rods with good descaling property, Transactions ISIJ, Volume 22, p; 646, 1982.

Turney A, oxidation mechanism, Butterworths, London, 1965.

Vainshtein B., Structure Analysis by Electron Diffraction, Pergamon Press Ltd, Oxford, 1964.

Venables A. and Harland C. J., Electron backscatter patterns-a new technique for obtaining crystallographic information in the scanning electron microscopy, Philosophical Magazine, Volume 2, p; 1193, 1973.

Wan Y., Tan J. and Shi Z., Characterisation of the rust on carbon steels pre-corroded by different gaseous pollutants, journal of Materials Science, Volume 38, p; 3597, 2003.

William D. and Callister, R., Fundamentals of Materials Science and Engineering, Fifth Edition, John Wily & Sons Inc., USA, 2001.

Wilson A. W. and Spanos G., Application of orientation imaging microscopy to study phase transformation in steels, Materials Characterization, Volume 46, p; 407, 2001.

Wright S. I., Fundamentals of Automated EBSD, Chapter 5, from "Electron backscattered diffraction in materials science" Kluwer Academic/ Plenum Publishers, New York, USA, 2000.

Wright S. I., Field D. P. and Dingley D. J., Advanced software capabilities for automated EBSD, Proc. Chapter 13 from "Electron backscattered diffraction in materials science" Kluwer Academic/ Plenum Publishers, New York, USA, 2000.

Yangchun Y. and Lenard J. G., Estimating the resistance to deformation of the layer of scale during hot rolling of carbon steel strips, Journal of Materials Processing Technology, Volume 121, p; 60, 2001.

Zhilyaev A. P., Czerwinski F. and Szpunar J. A., On the calculation of grain boundary character distribution in textured nickel oxide layers, Proc. International conference on texture of materials-12th: edit by Szpunar J. A, Montreal, Canada, NRC Research Press, Volume 2, p; 1403, 1999.

Zhang J., Rong L., Liu Y. and Dong B., SAXS study on the microstructure of Fe_2O_3 nanocrystal, Materials Science and Engineering, Volume A351, p; 224, 2003.

The fourteen types of unit cells, grouped in seven crystal system. Characteristics of the crystal systems are summarised in the Table below.

The Figure and the Table are reproduced from (Donald, 1996)
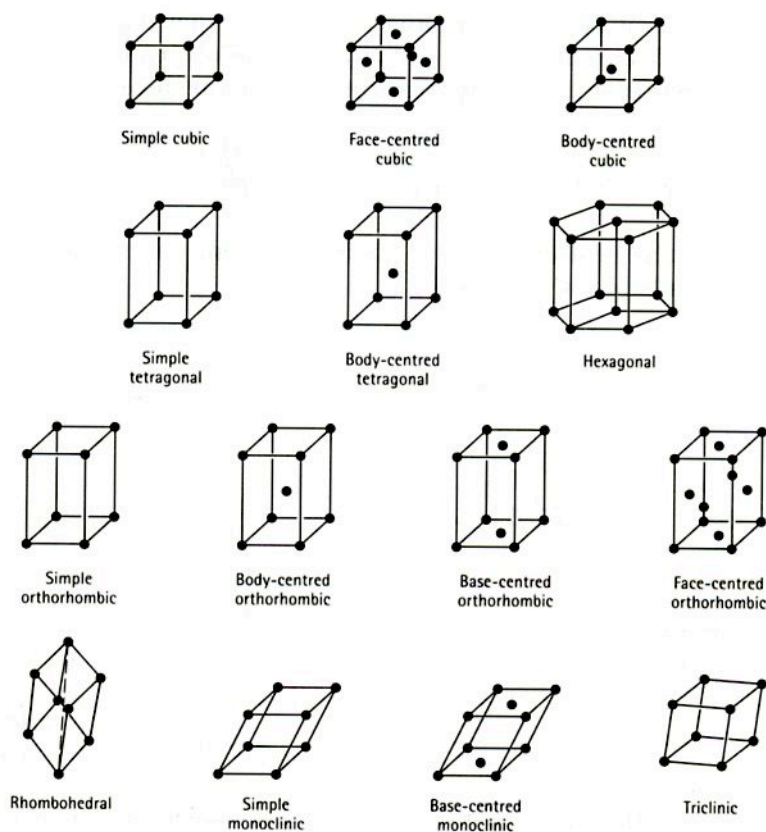
Structure	Axes	Angles between Axes
Cubic	$a = b = c$	All angles equal 90°.
Tetragonal	$a = b \neq c$	All angles equal 90°.
Orthorhombic	$a \neq b \neq c$	All angles equal 90°.
Hexagonal	$a = b \neq c$	Two angles equal 90°. One angle equals 120°.
Rhombohedral	$a = b = c$	All angles are equal and none equals 90°.
Monoclinic	$a \neq b \neq c$	Two angles equal 90°. One angle (β) is not equal to 90°.
Triclinic	$a \neq b \neq c$	All angles are different and none equals 90°.

Appendix 2

Oxide scale thicknesses of IF steel at different times and temperatures

Temperature	Time (Second)	Oxide Scale Thickness (µm)	Standard Error with 95% CI (Confidence interval)
650 °C	600	6.40	± 1.67
650 °C	1200	8.00	± 0.44
650 °C	1800	13.20	± 1.22
650 °C	3600	17.30	± 1.58
750 °C	600	47.67	± 4.02
750 °C	1200	51.00	± 2.10
750 °C	1800	53.45	± 4.10
750 °C	3600	55.52	± 10.17
900 °C	600	16.36	± 1.14
900 °C	1200	88.60	± 12.60
900 °C	1800	168.90	± 4.67
900 °C	3600	195.00	± 9.00
1000 °C	600	97.20	± 4.14
1000 °C	1200	211.00	± 11.93
1000 °C	1800	252.00	± 4.47
1000 °C	3600	260.40	± 3.50
1100 °C	600	220.00	± 43.00
1100 °C	1200	265.00	± 10.00
1100 °C	1800	308.00	± 61.40
1100 °C	3600	328.00	± 4.47

Oxide scale thicknesses of Alloy A at different times and temperatures

Temperature (°C)	Time (Second)	Oxide scale thickness (µm)	Standard Error with 95% CI
650	600	4.20	± 2.08
650	1200	4.60	± 0.76
650	1800	4.60	± 0.53
650	3600	6.76	± 2.18
750	600	6.60	± 1.14
750	1200	15.31	± 2.24
750	1800	21.42	±13.12
750	3600	25.61	± 8.90
900	600	61.00	± 5.35
900	1200	82.84	± 18.50
900	1800	90.84	± 2.64
900	3600	133.56	± 4.35
1000	600	131.42	± 6.42
1000	1200	221.42	± 9.28
1000	1800	285.71	± 9.27
1000	3600	346.71	± 11.70
1100	600	249.99	± 9.28
1100	1200	374.98	± 23.64
1100	1800	432.14	± 6.55
1100	3600	444.51	± 46.69

Appendix 4

Oxide scale thicknesses of Alloy B at different times and temperatures

Temperature	Time (Second)	Oxide Scale Thickness (μm)	Standard Error with 95% CI (Confidence interval)
650 °C	600	1.78	± 1.13
650 °C	1200	2.14	± 1.21
650 °C	1800	4.64	± 2.85
650 °C	3600	4.62	± 2.93
750 °C	600	4.58	± 3.68
750 °C	1200	4.64	± 1.13
750 °C	1800	7.49	± 2.86
750 °C	3600	7.56	± 7.09
900 °C	600	13.23	± 1.43
900 °C	1200	64.23	± 5.04
900 °C	1800	79.66	± 9.35
900 °C	3600	81.50	± 16.37
1000 °C	600	47.01	± 4.12
1000 °C	1200	75.09	± 7.99
1000 °C	1800	82.20	± 2.34
1000 °C	3600	92.53	± 10.88
1100 °C	600	181.62	± 7.20
1100 °C	1200	230.36	± 10.88
1100 °C	1800	157.14	± 9.28
1100 °C	3600	389.28	± 6.32

Appendix 5

Ferrite grain size and aspect ratio of IF Steel at different times and temperatures

Sample No.	Temperature (°C)	Time (Second)	Ferrite Grain Size (µm)	Ferrite Grains Aspect Ratio
1	650	600	78.98 ± 1.22	0.84
2	650	1200	82.53 ± 0.91	0.92
3	650	1800	85.23 ± 2.07	0.98
4	650	3600	93.87 ± 2.22	0.81
5	750	600	97.35 ± 3.27	0.92
6	750	1200	104.65 ± 2.17	0.89
7	750	1800	110.04 ± 1.12	1.00
8	750	3600	146.36 ± 1.27	0.93
9	900	600	110.67 ± 1.18	0.95
10	900	1200	115.72 ± 2.12	0.96
11	900	1800	106.49 ± 4.10	0.84
12	900	3600	131.47 ± 1.34	0.93
13	1000	600	123.53 ± 2.46	0.96
14	1000	1200	128.30 ± 2.14	0.89
15	1000	1800	126.80 ± 1.25	0.86
16	1000	3600	129.53 ± 4.23	0.98
17	1100	600	107. 91 ± 2.95	1.25
18	1100	1200	107.44 ± 1.87	0.90
19	1100	1800	109.51 ± 3.11	1.11
20	1100	3600	107.73 ± 2.19	0.94

Appendix 6

Ferrite and pearlite grain sizes of Alloy A at different times and temperatures

Sample no.	Temperature (°C)	Time (Second)	Ferrite grain size (µm)	Pearlite volume fraction	Pearlite colony size (µm)	Ferrite grains aspect ratio
1	650	600	26.08 ± 2.15	0.12 ± 0.03	14.12	0.82
2	650	1200	21.73 ± 1.04	0.11 ± 0.02	17. 65	0.91
3	650	1800	21.64 ± 1.28	0.13 ± 0.09	16. 92	0.93
4	650	3600	20.25 ± 2.54	0.27 ± 0.09	24.08	0.89
5	750	600	25.86 ± 2.13	0.16 ± 0.05	15.13	0.91
6	750	1200	22.66 ± 1. 22	0.14 ± 0.07	14.49	1.05
7	750	1800	22.50 ± 1.78	0.12 ± 0.09	06.29	0.87
8	750	3600	20.29 ± 4.86	0.10 ± 0.08	09.69	0.93
9	900	600	19.95 ± 0.72	0.13 ± 0.07	3.68	1.12
10	900	1200	19.01 ± 1.29	0.34 ± 0.02	10.17	1.08
11	900	1800	22.92 ± 1.92	0.33 ± 0.07	12.42	1.00
12	900	3600	21.84 ± 3.45	0.31 ± 0.06	11. 53	1.01
13	1000	600	28.38 ± 4.12	0.16 ± 0.08	5.64	0.98
14	1000	1200	29.35 ± 2.36	0.13 ± 0.01	6.74	0.93
15	1000	1800	31.25 ± 2.05	0.11 ± 0.01	15.35	0.91
16	1000	3600	30.52 ± 1.25	0.13 ± 0.04	16.74	0.94
17	1100	600	31.21 ± 2.84	0.15 ± 0.03	17.36	0.95
18	1100	1200	30.22 ± 3.08	0.14 ± 0.02	16.35	0.92
19	1100	1800	31.35 ± 3.76	0.21 ± 0.07	15.62	0.83
20	1100	3600	29. 44 ± 2.98	0.21 ± 0.09	6.35	0.86

Grain sizes and volume fractions of the phases in Alloy B

Sample no.	Temperature (°C)	Time (Second)	Ferrite Volume fraction	Ferrite grain size (μm)	Pearlite volume fraction	Bainite Volume Fraction	Pearlite colony size (μm)	Ferrite grains aspect ratio
1	650	600		8.86 ± 0.18	0.45 ± 0.025		7.24	0.70
2	650	1200		8.32 ± .23	0.29 ± 0.025		5.45	1.00
3	650	1800		10.40 ± 1.02	0.20 ± 0.022		7.11	0.97
4	650	3600		9.89 ± 1.32	0.27 ± 0.012		6.97	0.99
5	750	600		9.19 ± 0.67	0.35 ± 0.012		9.49	1.01
6	750	1200		11.05 ± 1.36	0.18 ± 0.022		6.54	1.00
7	750	1800		11.10 ± 2.45	0.33 ± 0.067		8.26	1.66
8	750	3600		10.23 ± 0.09	0.16 ± 0.067		6.71	0.82
9	900	600		10.53 ± 1.56	0.25 ± 0.022		5.94	0.84
10	900	1200		7.79 ± 0.08	0.18 ± 0.071		7.11	0.90
11	900	1800		11.92 ± 1.87	0.08 ± 0.055	0.41 ± 0.004	7.49	0.82
12	900	3600		13.42 ± 2.66	0.12 ± 0.038	0.45 ± 0.025	9.18	0.89
13	1000	600		9.51 ± 0.45	0.04 ± 0.025	0.49 ± 0.051	3.69	1.07
14	1000	1200		7.22 ± 0.31	0.14 ± 0.012	0.62 ± 0.77	4.06	1.04
15	1000	1800	0.25 ± 0.026		0.14 ± 0.025	0.63 ± 0.001		
16	1000	3600	0.25 ± 0.132		0.01 ± 0.028	0.76 ± 0.001		
17	1100	600	0.24 ± 0.003		0.041 ± 0.036	0.76 ± 0.002		
18	1100	1200	0.22 ± 0.012		0.01 ± 0.023	0.77 ± 0.005		
19	1100	1800	0.16 ± 0.001		0.10 ± 0.051	0.78 ± 0.003		
20	1100	3600	Martensite structure					

Optical micrographs of the oxide scales formed on Alloy A at different times and temperatures
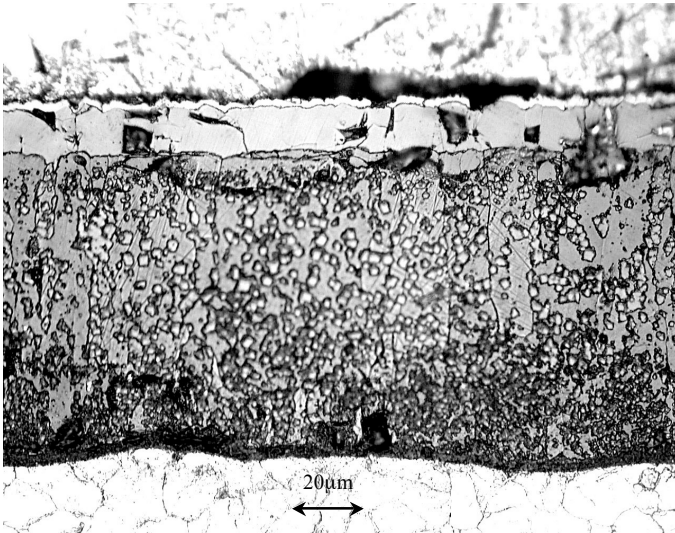
A: Oxide scale formed on Alloy A, 900°C-3600 seconds, etched with 2% Nital.
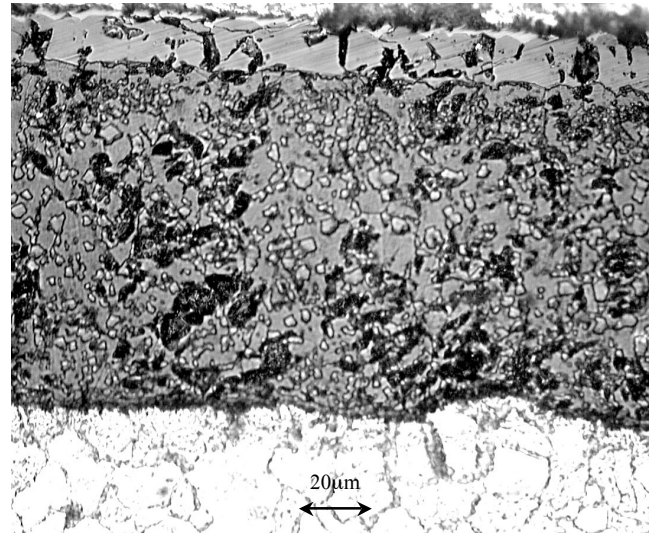
B: Oxide scale formed on Alloy A, 1000°C-600 seconds, etched with 2% Nital.
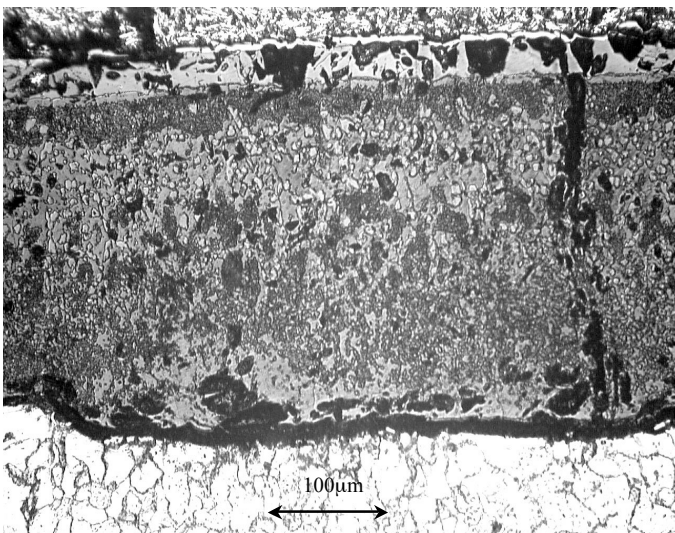
C: Oxide scale formed on Alloy A, 1000°C-1800 seconds, etched with 2% Nital.
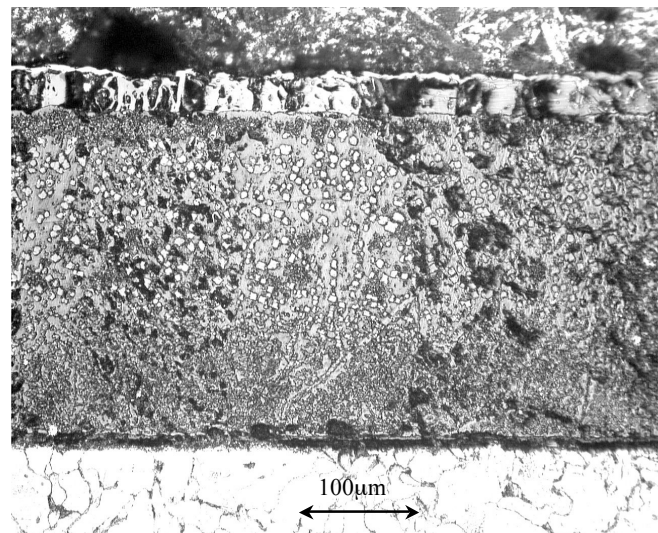
D: Oxide scale formed on Alloy A, 1000°C-3600 seconds, etched with 2% Nital.
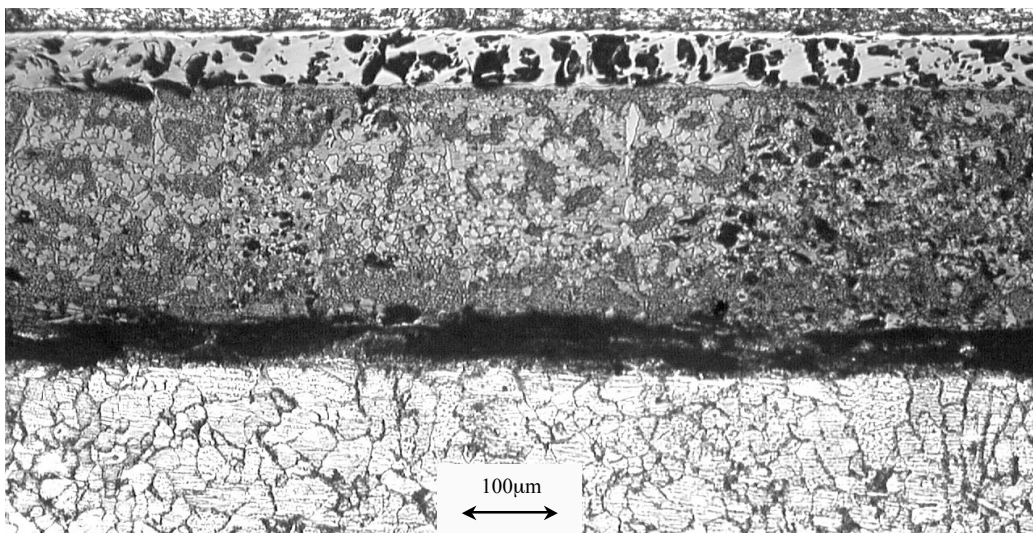
E: Oxide scale formed on Alloy A- 1100°C-1200 seconds, etched with 2% Nital.
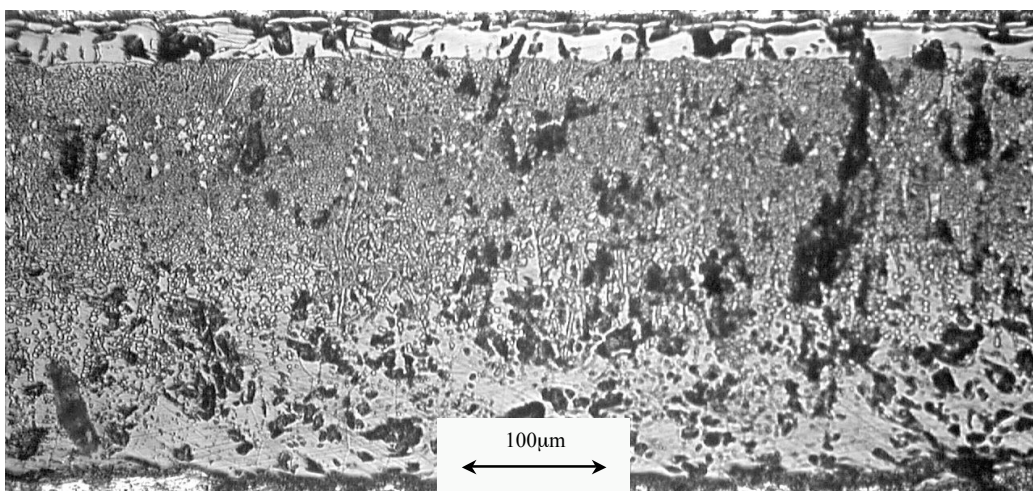
F: Oxide scale formed on Alloy A at 1000°C-1800 seconds, etched with 2% Nital.
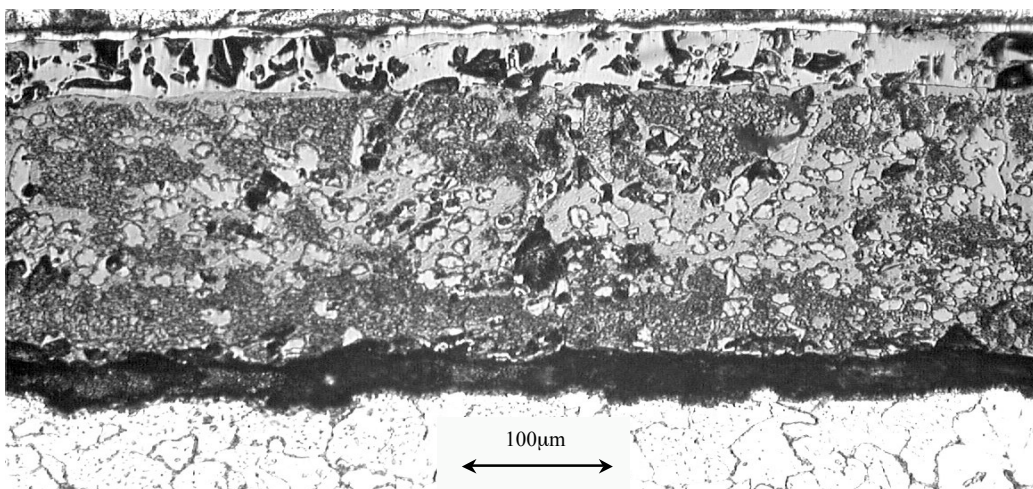
G: Oxide scale formed on Alloy A at 1100°C-600 seconds, etched with 2% Nital.

EBSD selected images of Alloy A oxide scale at different times and temperatures (arranged in order from low to high temperatures)
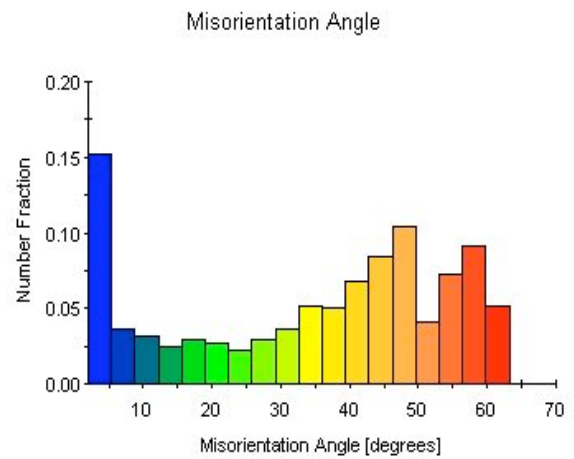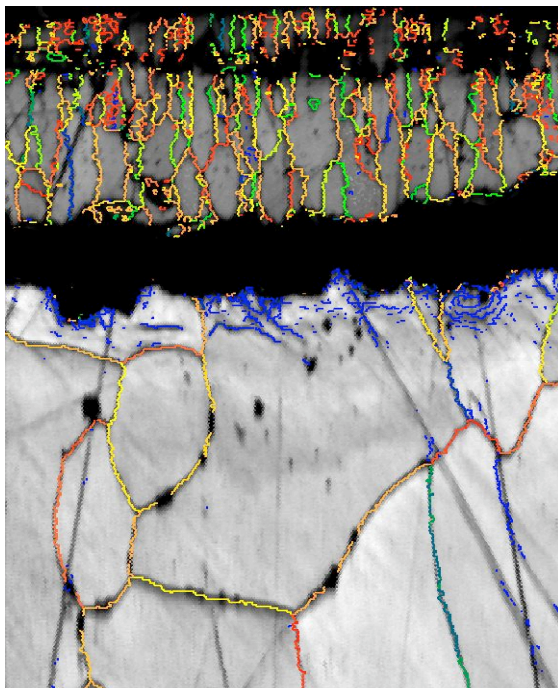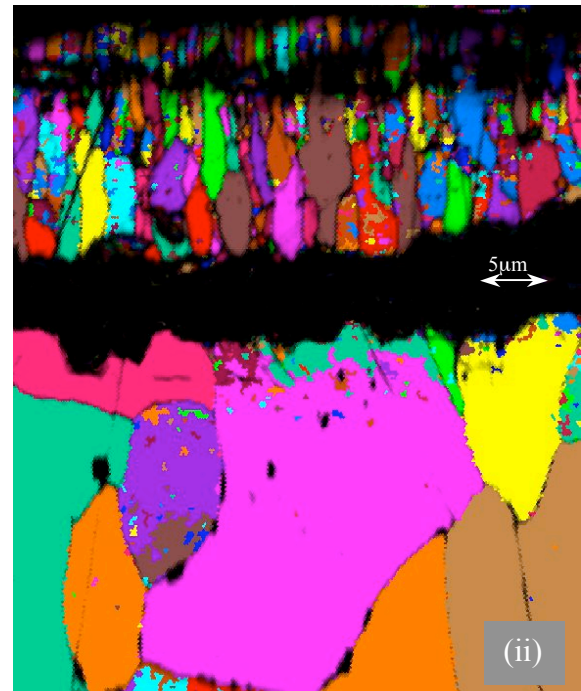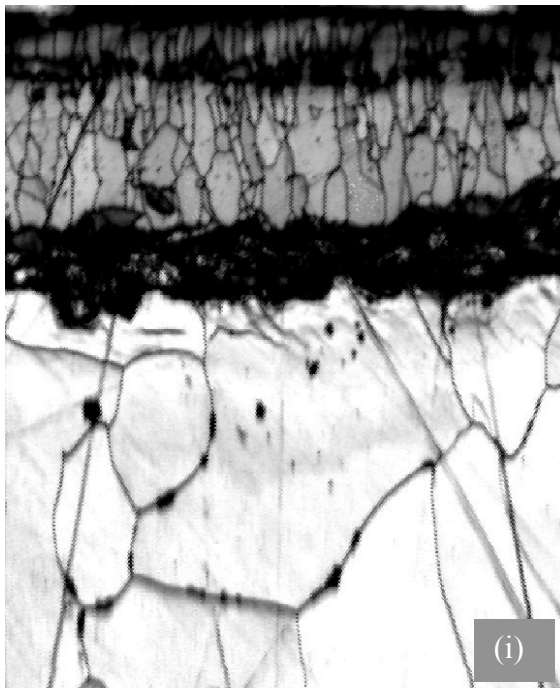
*A: EBSD maps of Alloy A oxidised at 750°C for 1800 seconds, 0.05 step size. (i) EBSD Image Quality map, (ii) EBSD-Unique Grain Colour map, (iii) EBSD-Misorientation map and misorientation volume factions v angles graph showing misorientation distribution within the map.*
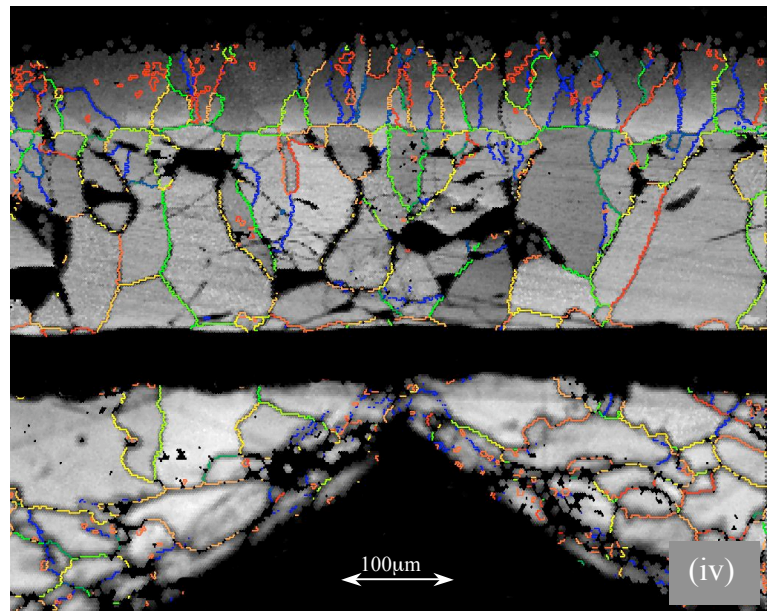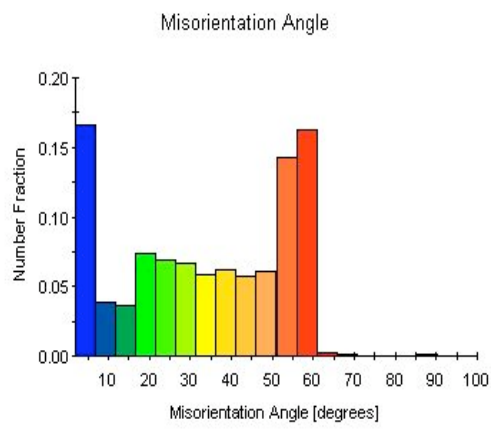
(i)

(ii)

Misorientation Angle
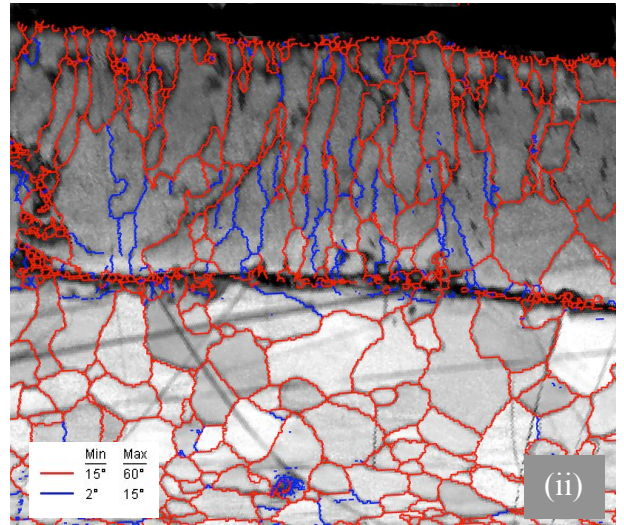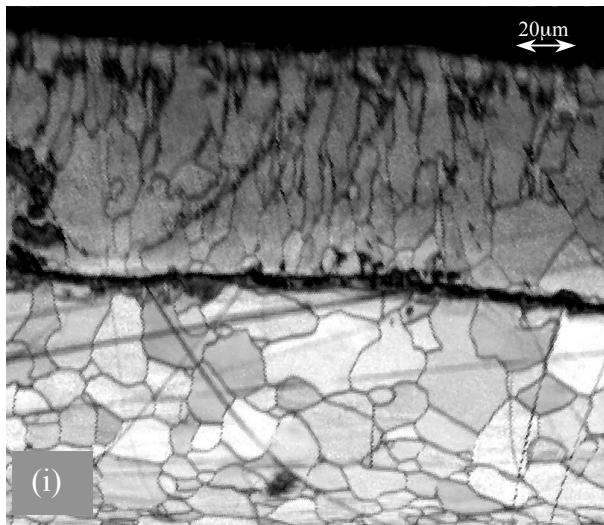
B: EBSD maps of Alloy A, oxidised at 900°C for 1800 seconds, 0.03 step size. (i) EBSD Image Quality map, (ii) EBSD-Grain boundary Level map, characterising low and high grain boundary levels in the map, (iii) EBSD-Unique Grain Colour map, (iv) EBSD-Misorientation map and misorientation volume factions v misorientation angles graph showing misorientation distribution within the map.
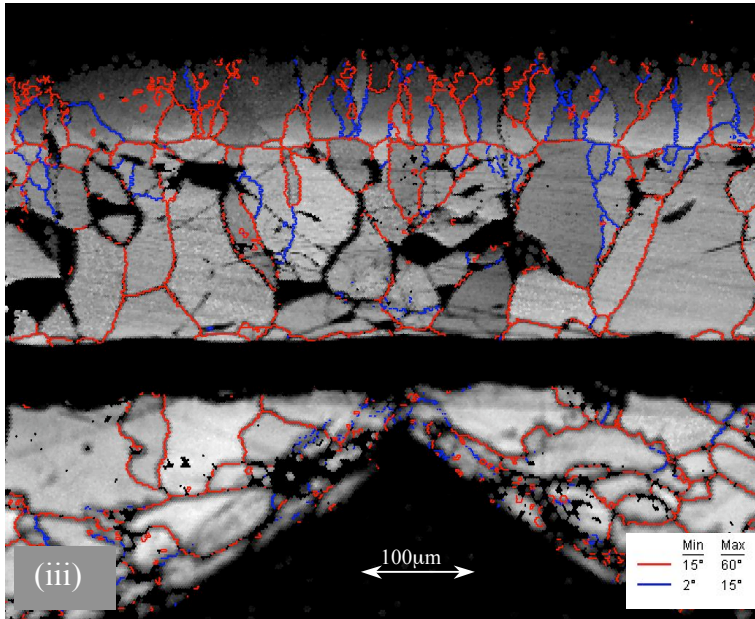

(iii)

(iv)

272
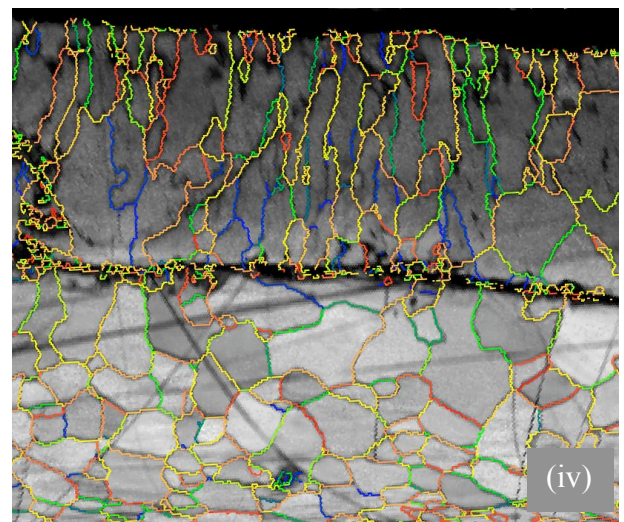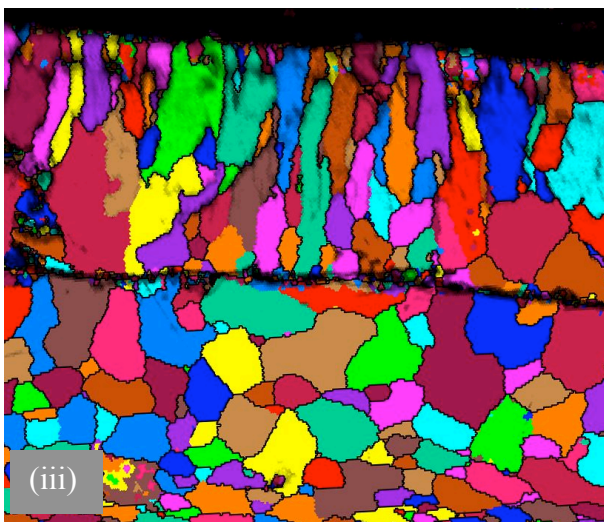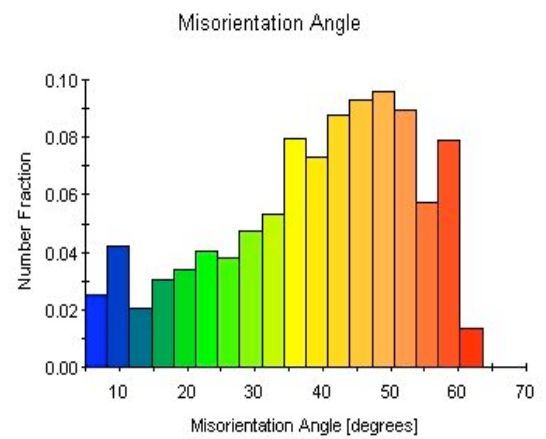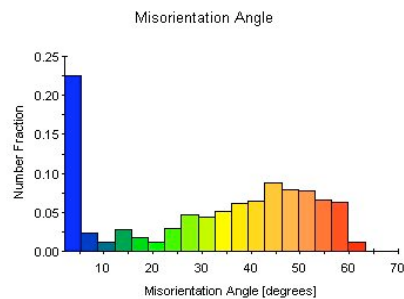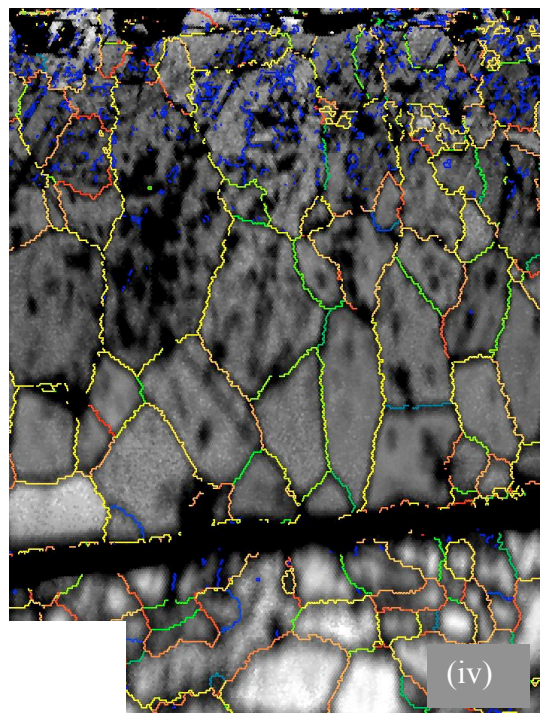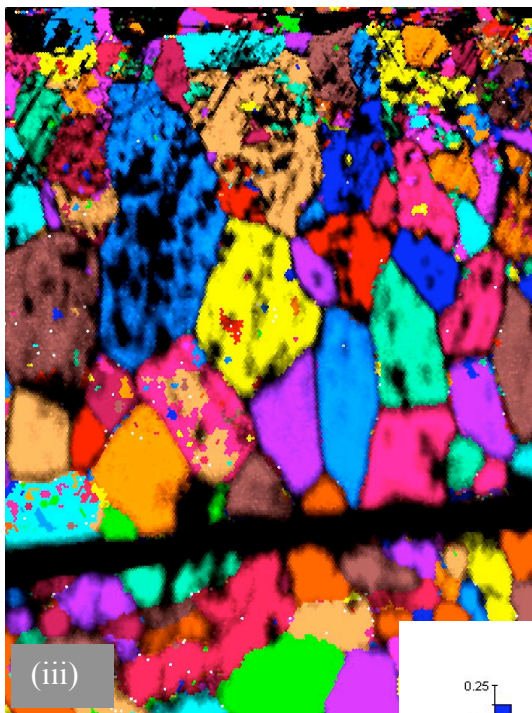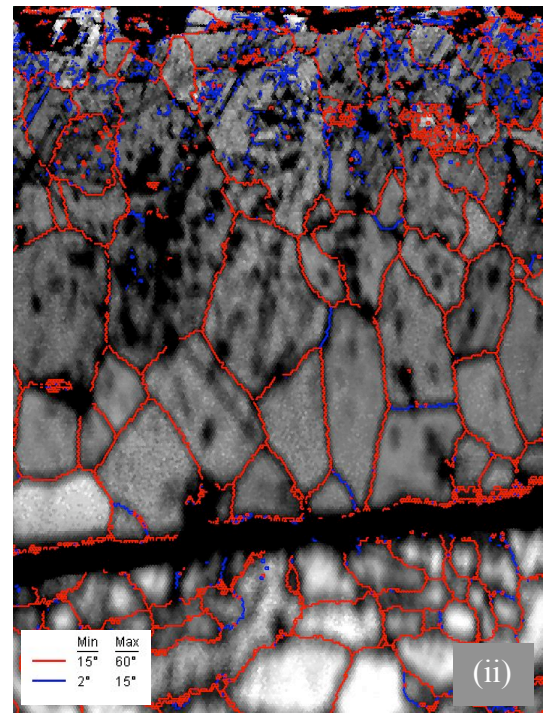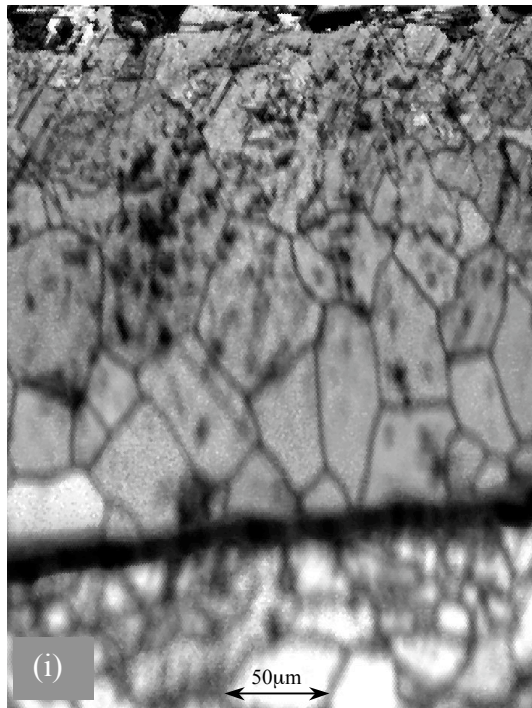
C: EBSD maps of Alloy A, oxidised at 1000°C for 1800 seconds, 0.1 step size. (i) EBSD Image Quality map, (ii) EBSD-Grain boundary Level map, characterising low and high grain boundary levels in the map, (iii) EBSD-Unique Grain Colour map, (iv) EBSD-Misorientation map and misorientation volume factions v misorientation angles graph showing misorientation distribution within the map.

D: EBSD maps of Alloy A, oxidised at 1100°C for 600 seconds, 0.1 step size. (i) EBSD Image Quality map, (ii) EBSD-Grain boundary Level map, characterising low and high grain boundary levels in the map, (iii) EBSD-Misorientation map and misorientation volume factions v misorientation angles graph showing misorientation distribution within the map.
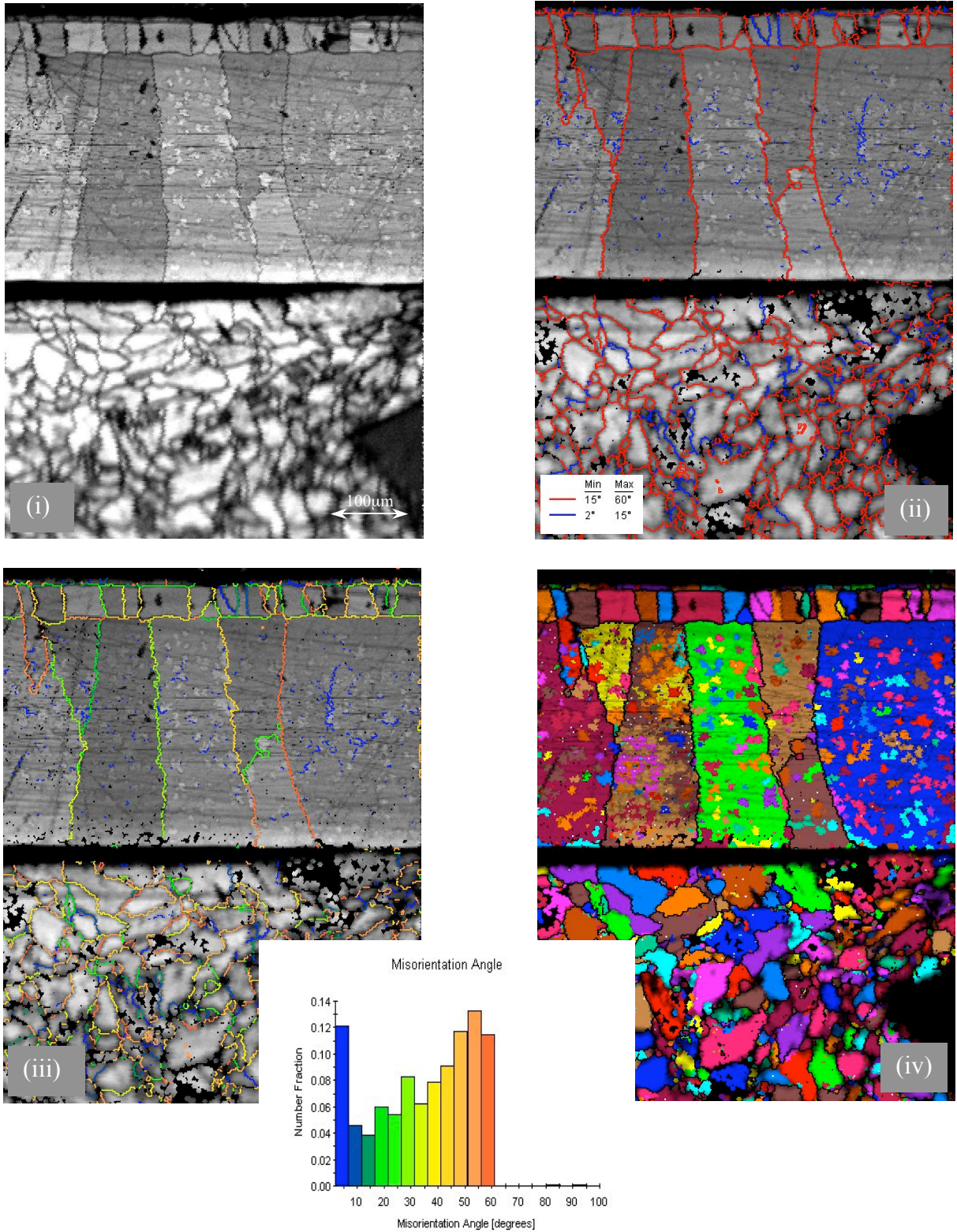
E: EBSD maps of Alloy A, oxidised at 1100°C for 1200 seconds, 0.05 step size. (i) EBSD Image Quality map, (ii) EBSD-Grain boundary Level map, characterising low and high grain boundary levels in the map, (iii) EBSD-Misorientation map and misorientation volume factions v misorientation angles graph showing misorientation distribution within the map, (iv) EBSD-Unique Grain Colour map.
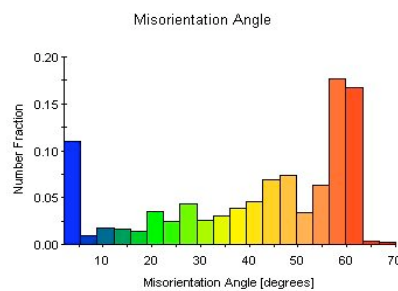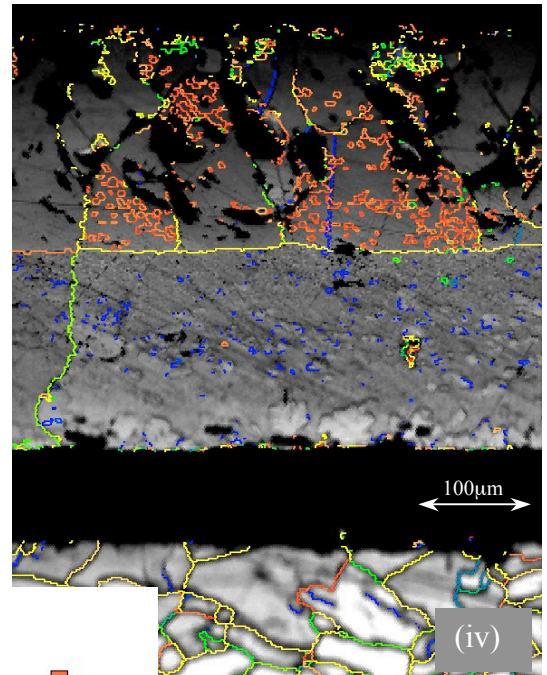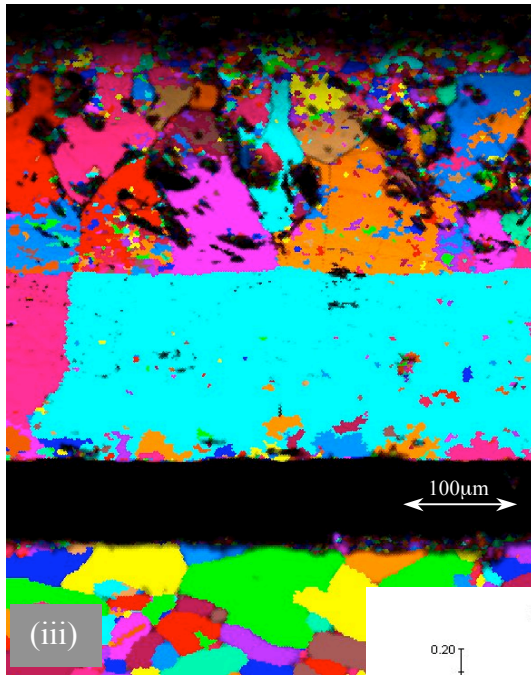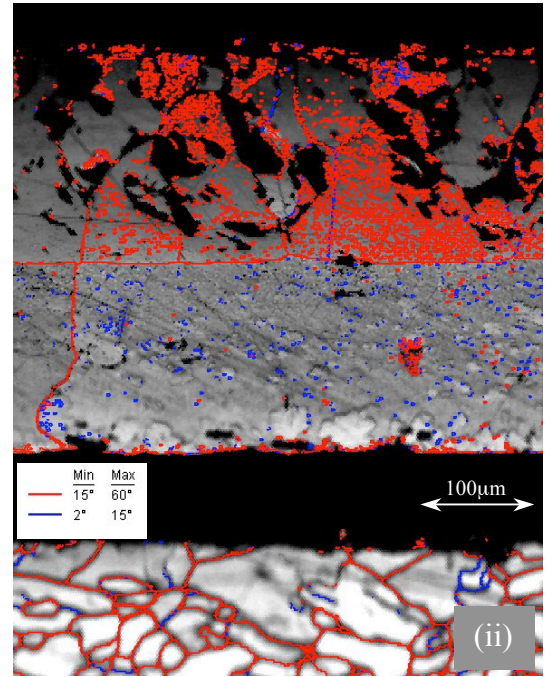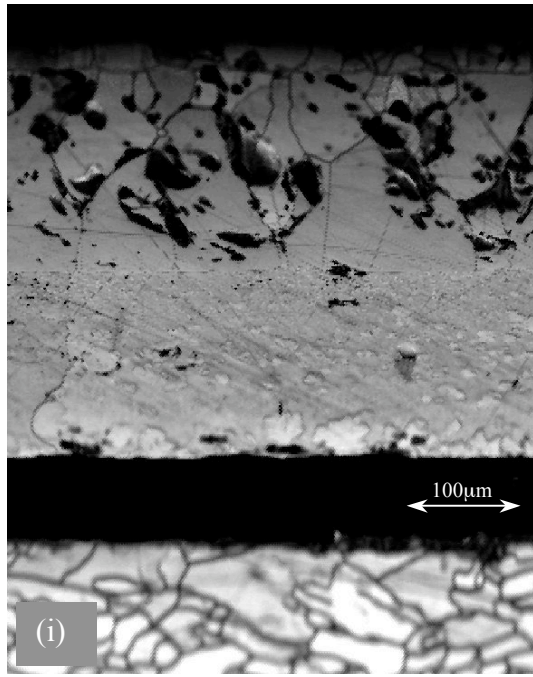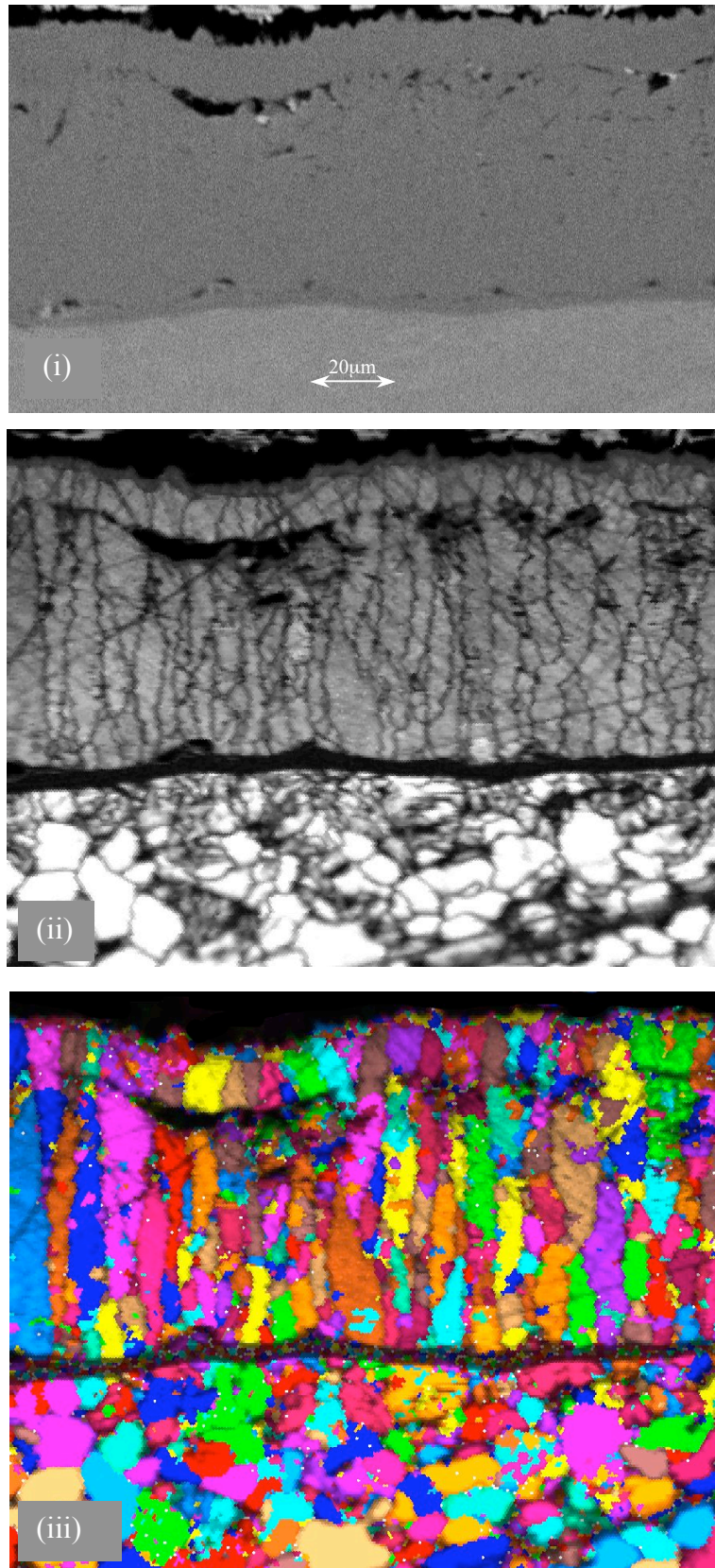
F: EBSD maps of Alloy A, oxidised at 1100°C for 1800 seconds, 0.08 step size. (i) EBSD Image Quality map, (ii) EBSD-Grain boundary Level map, characterising low and high grain boundary levels in the map, (iii) EBSD-Misorientation map and misorientation volume factions v misorientation angles graph showing misorientation distribution within the map, (iv) EBSD-Unique Grain Colour map.
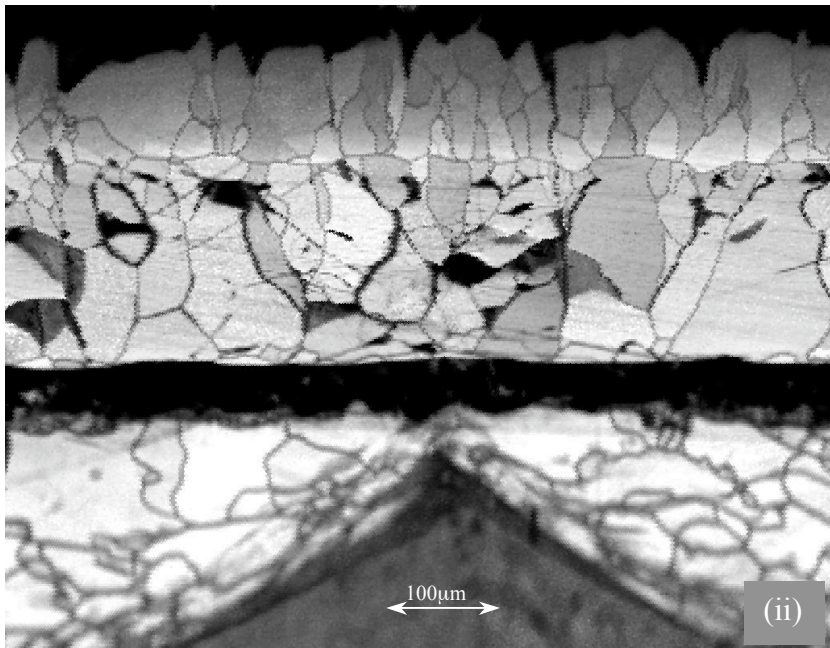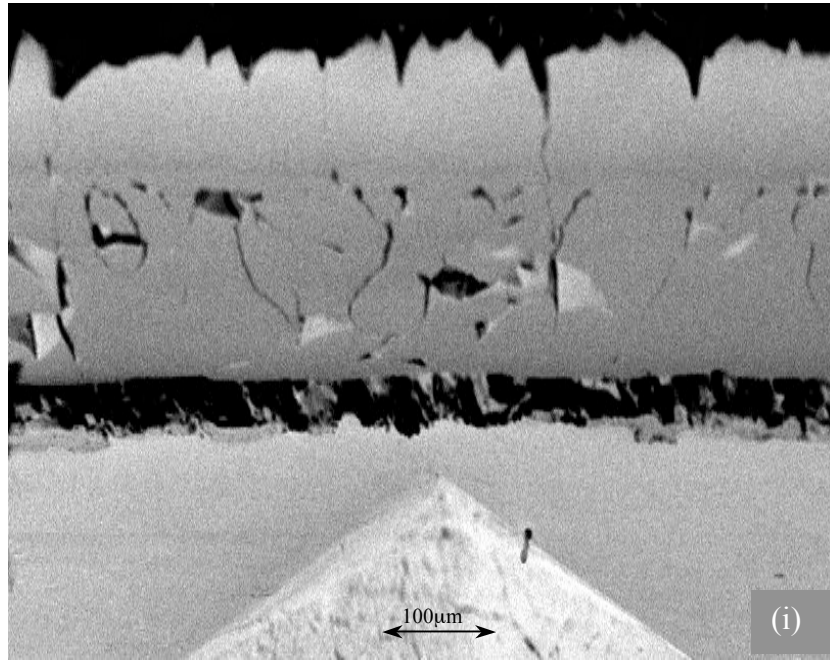
G: Alloy A, oxidised at 1100°C for 3600 seconds, (i) SEM-SE detector image, 20kV, 16 mm WD, (ii) EBSD Image Quality map, 0.5 step size, (iii) EBSD-Grain boundary Level map, characterising low and high grain boundary levels in the map, (iv) EBSD-Misorientation map and misorientation volume factions v misorientation angles graph showing misorientation distribution within the map, (v) EBSD-Unique Grain Colour map. The rest of the images (iii, iv and v) are in the next page.

(iii)

Misorientation Angle

(iv)

(v)
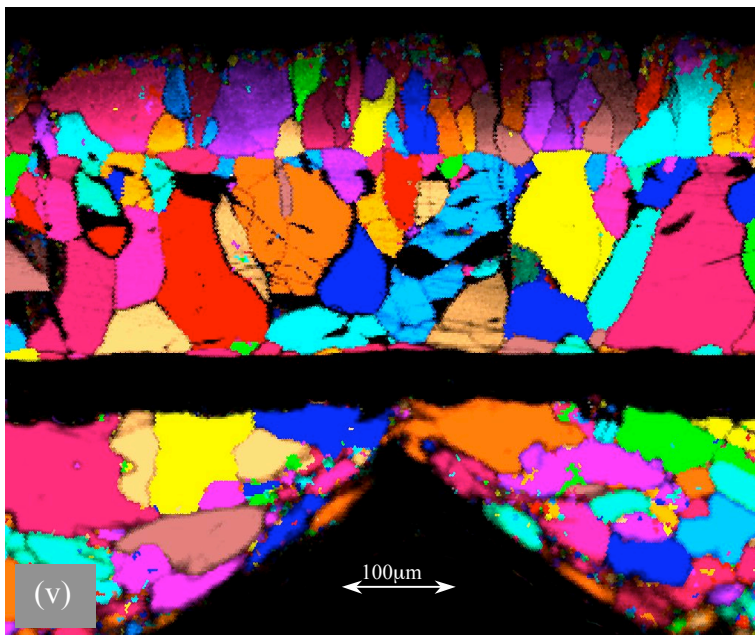
EBSD selected images of Alloy B oxide scale at different times and temperatures (arranged in order from low to high temperatures)

A: Alloy B, oxidised at 900°C for 1800 seconds, (i) SEM-SE detector image, 20kV, 16 mm WD, (ii) EBSD Image Quality map, 0.5 step size, (iii) EBSD-Unique Grain Colour map.
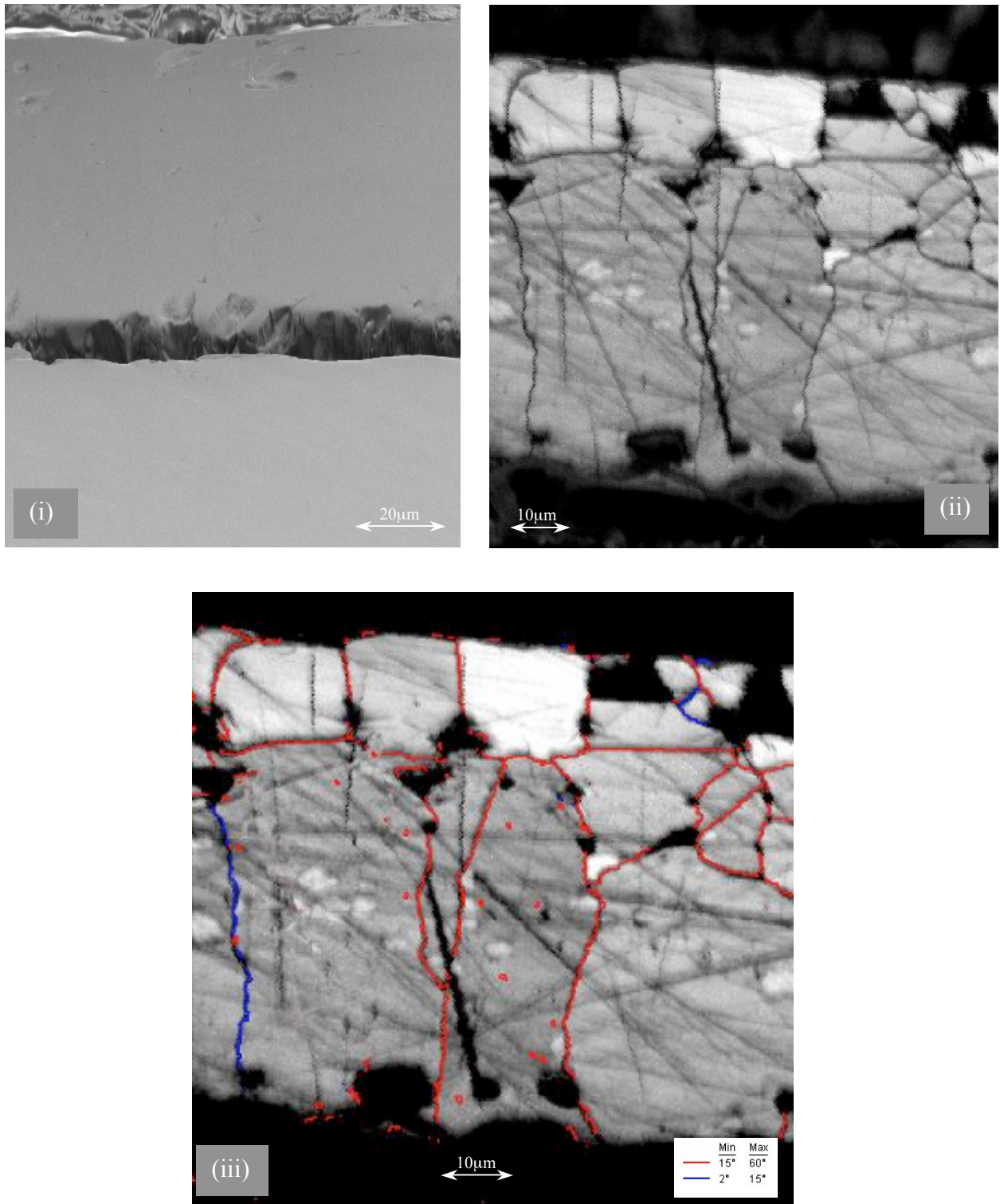
B: Alloy B, oxidised at 1000°C for 1800 seconds, (i) SEM-SE detector image, 20kV, 17 mm WD, (ii) EBSD Image Quality map, 0.5 step size, (iii) EBSD-Grain boundary Level map, characterising low and high grain boundary levels in the map.
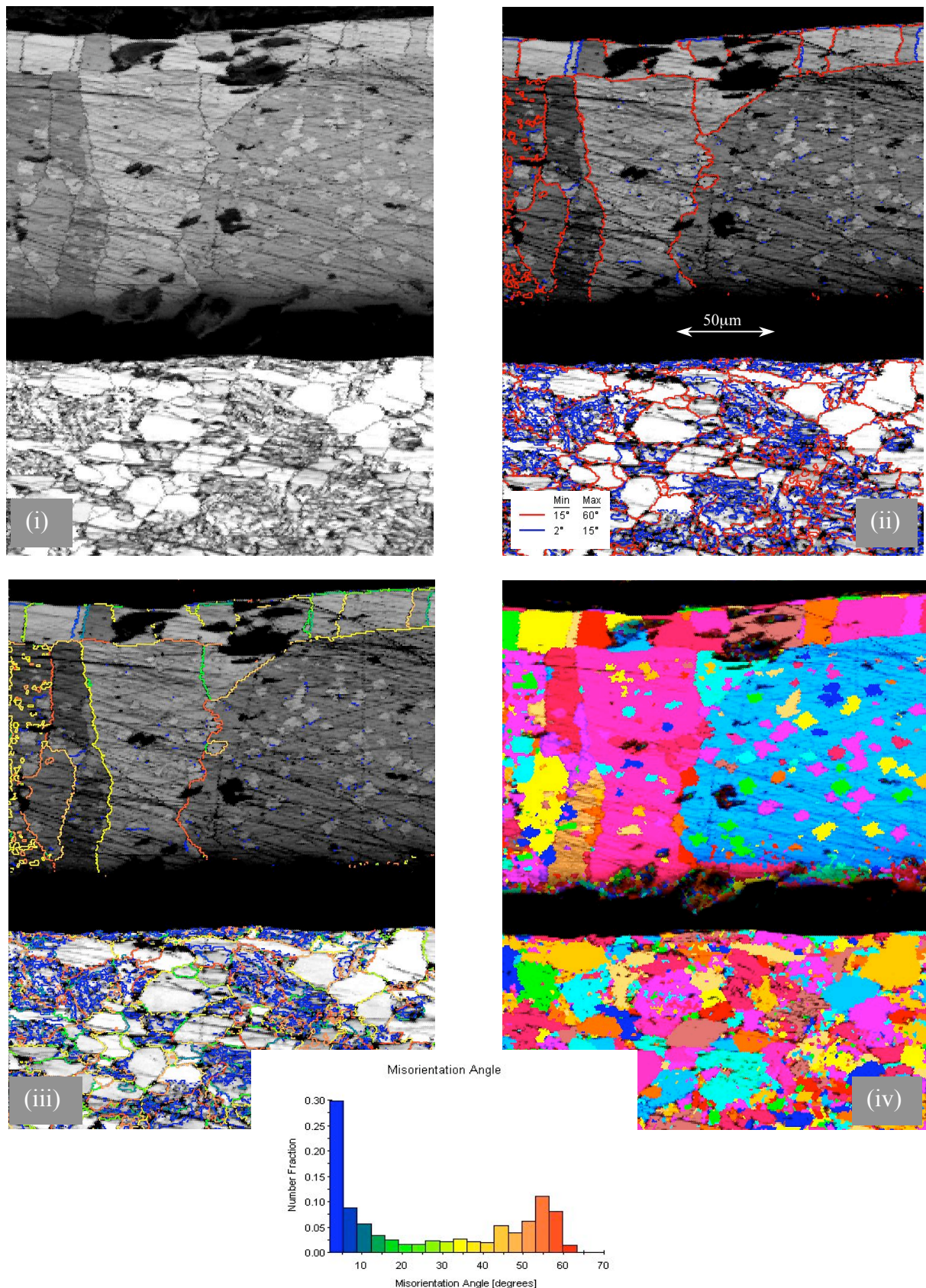
C: EBSD maps of Alloy B, oxidised at 1100°C for 1800 seconds, 0.05 step size. (i) EBSD-Image Quality map, (ii) EBSD-Grain boundary Level map, characterising low and high grain boundary levels in the map, (iii) EBSD-Misorientation map and misorientation volume factions v misorientation angles graph showing misorientation distribution within the map, (iv) EBSD-Unique Grain Colour map.

Tables of the Oxide Scale Grain Shape versus Time and Temperature

Table 1: grain shapes of the oxide scale on IF steel exposed for 1800 seconds to different temperatures.

Temperature (°C)	Wüstite	Magnetite	Haematite
650	columnar	columnar	-
750	columnar	columnar	-
900	columnar	elongated	-
1000	columnar	~ equiaxed	-
1100	~ equiaxed	columnar	~ equiaxed

Table 2: grain shapes of the oxide scale on Alloy A exposed for 1800 seconds to different temperatures.

Temperature (°C)	Wüstite	Magnetite	Haematite
750	columnar	columnar	-
900	columnar	~equiaxed	-
1000	columnar	~ equiaxed	-
1100	elongated	elongated	elongated

Table 3: grain shapes of the oxide scale on Alloy B exposed for 1800 seconds to different temperatures.

Temperature (°C)	Wüstite	Magnetite
900	columnar	~equiaxed
1000	columnar	elongated
1100	columnar	elongated

Table 4: gain shapes of the oxide scale on Alloy A at 1100°C for different time.

| Time	Wüstite	Magnetite	Haematite
600	columnar	equiaxed	-
1200	columnar	equiaxed	elongated
1800	elongated	elongated	columnar
3600	not observed	columnar	columnar

Appendix 12

Activation energy comparison between the results from current study and the other works on similar steel compositions and oxidation conditions.

Materials	Temperature °C	Activation energy KJ/mole	Reference
Iron in air	1000-1100	-138	Hauffe, 1965
Iron in oxygen	700-1250	-169	Paidassi, 1955
Iron in air	700-1250	-157	Chen and Yuen, 2003
Iron in air	600-1250	-170	Sheasby, *et al.*, 1984
Carbon steel in air	900-1200	-120	Munther, *et al.*, 1999
Mild steel (0.04C-0.2 Mn-0.02Si)	700-1250	-143	Abuluwefa, *et al.*, 1996
99.96% Fe in purified oxygen	640-805	-192	Caplan, *et al.*, 1981
Iron in oxygen	700-1200	-196	Davies, *et al.*, 1951
Low carbon steel (0.04C-0.2 Mn, 0.02Si) in mix oxygen and nitrogen	1000-1250	-127	Abuluwefa, *et al.*, 1996
IF steel in air	650-1100	-145	This study
Alloy A in air	650-1100	-214.18	This study
Alloy B in air	650-1100	-214.17	This study

Optical micrographs and EBSD images of IF steel oxide formed at 750°C after 1800 seconds
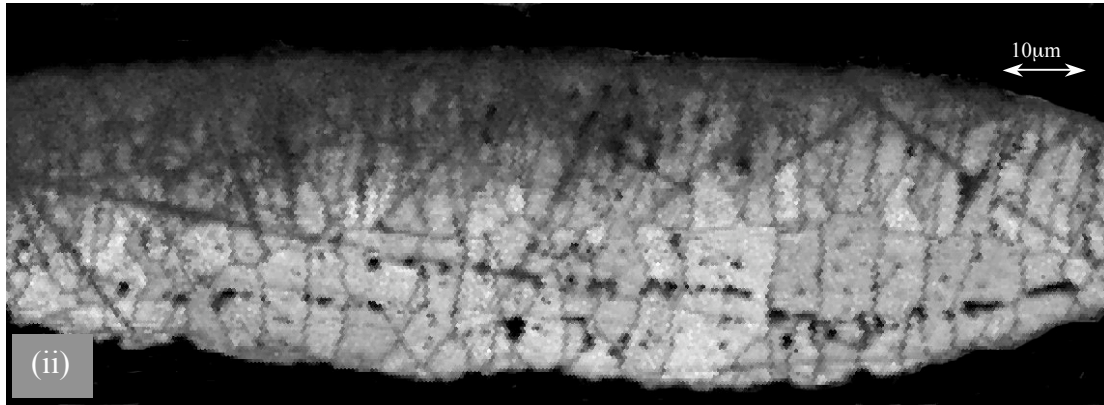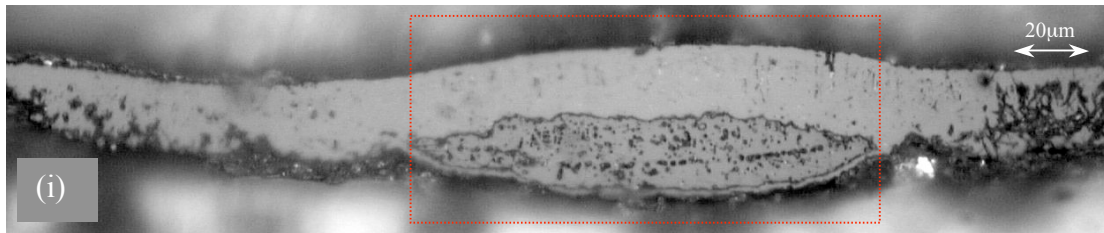

A: IF steel oxidised at 750°C for 1800 seconds. (i) Optical micrograph of etched cross section with 1% HCl in ethanol-10 seconds, (ii) EBSD Image Quality map for the same area in (i), 0.1 step size
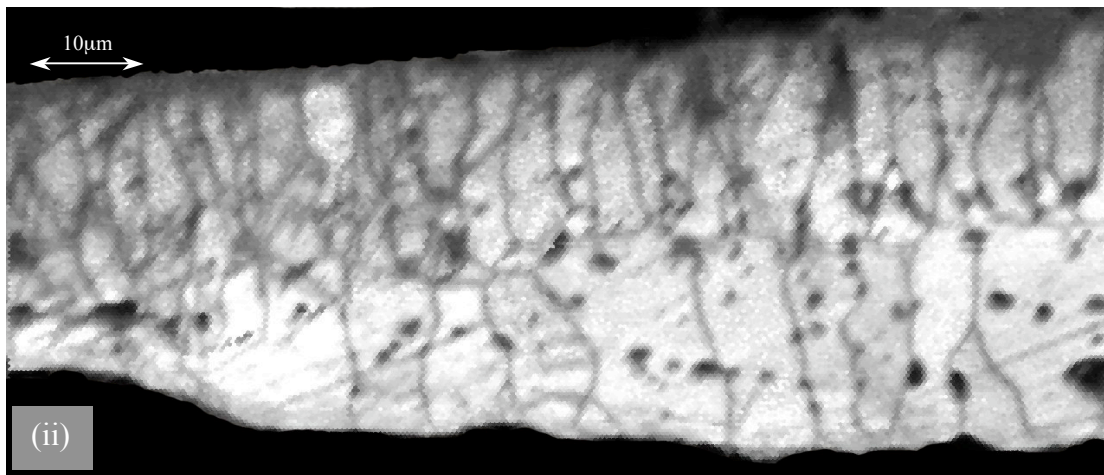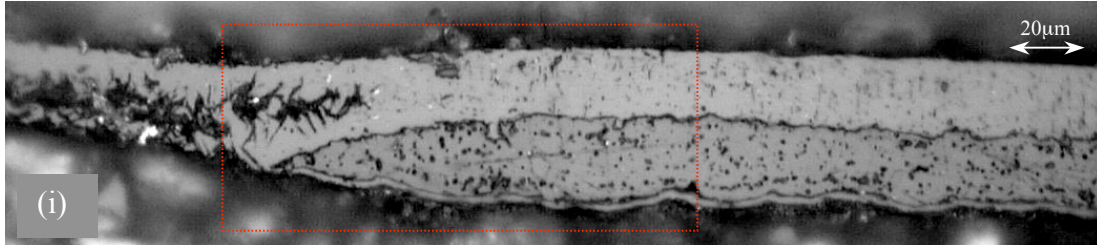
B: IF steel oxidised at 750°C for 1800 seconds (i) Optical micrograph of etched cross section with 1% HCl in ethanol-10 seconds, (ii) EBSD Image Quality map for the same area in (i), 0.1 step size. (Different area of the same sample in A)

Standard Texture Components (Reproduced from Randle and Engler, 2003)
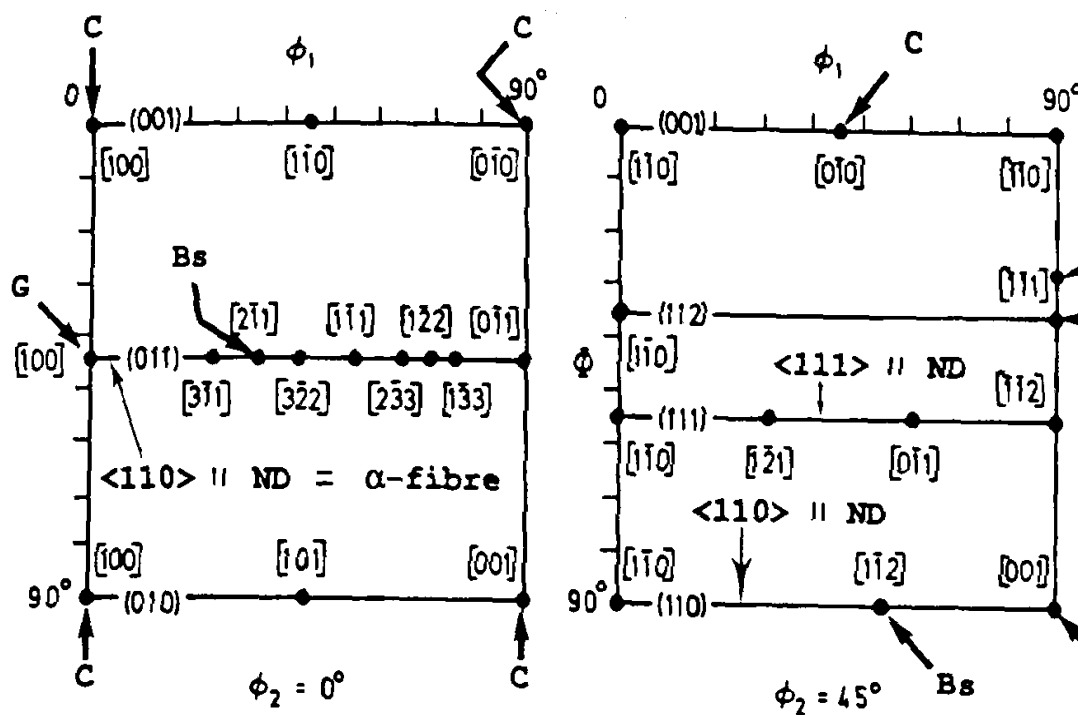
C = Cube	{100}<001>	
G = Goss	{110}<001>	
Bs = Brass	{110}<112>	
Cu = Copper	{112}<111>	
T = Taylor	{4 4 11}<8 8 11>	